Elastic Photoproduction of J/ψ Vector Mesons at high Photon-Proton Centre-of-Mass Energy at the H1 Experiment at HERA

Dissertation der Fakultät für Physik
der
Ludwig-Maximilians-Universität München

vorgelegt von

Ludger Janauschek

aus München

angefertigt am
Max-Planck-Institiut für Physik München
Werner-Heisenberg-Institut

München, den 12.11.2004

1. Gutachter: Prof. Dr. Chr. Kiesling

2. Gutachter: Prof. Dr. M. Faessler

Tag der mündlichen Prüfung: 17. Januar 2005

Kurzzusammenfassung

Die elastische Photoproduktion von J/ψ Vektormesonen wird bei hohen Werten der Photon-Proton-Schwerpunktsenergie $135\,\mathrm{GeV} < W_{\gamma p} < 305\,\mathrm{GeV}$ untersucht. Der elastische Photoproduktionswirkungsquerschnitt $\sigma(W_{\gamma p})$ wird als Funktion von $W_{\gamma p}$ gemessen. Der differentielle Wirkungsquerschnitt $\frac{\mathrm{d}\sigma}{\mathrm{d}t}$ wird im Bereich $|t| \leq 1.2\,\mathrm{GeV}^2/\,\mathrm{c}^2$ bestimmt. Diese Analyse weitet den Bereich von H1-Messungen bis zu den höchsten Werten von $W_{\gamma p}$ nahe an der kinematischen Grenze, die durch die Beschleunigerparameter festgelegt ist, von $\approx 318\,\mathrm{GeV}$ aus.

Die Daten für zwei verschiedene Ereignistopologien wurden mit dem H1-Detektor am ep-Speicherring HERA in den Jahren 1999 und 2000 genommen. Die analysierten Daten entsprechen einer integrierten Luminosität von $30.26\ \mathrm{pb}^{-1}$ und $26.90\ \mathrm{pb}^{-1}$ für die zwei Ereignisklassen. Der Neuronale-Netzwerk-Trigger auf Triggerstufe 2 und der rückwärtige Siliziumspurdetektor sind wichtige Detektorkomponenten des H1-Experiments, die diese Analyse ermöglichen.

Aus der $W_{\gamma p}$ Abhängigkeit des Wirkungsquerschnittes $\sigma(W_{\gamma p}) \propto {W_{\gamma p}}^{\delta}$ wird der Parameter $\delta = 1.17 \pm 0.11 \pm 0.16$ aus den Resultaten dieser Analyse bei hohem $W_{\gamma p}$ bestimmt und $\delta = 0.76 \pm 0.03 \pm 0.04$ unter zusätzlicher Verwendung von Daten aus dem ganzen, H1 zugänglichem $W_{\gamma p}$-Bereich. Der exponentielle Steigungsparameter b des differentiellen Wirkungsquerschnittes $\frac{\mathrm{d}\sigma}{\mathrm{d}t} \propto \mathrm{e}^{-b|t|}$ wird im Bereich hoher Werte von $W_{\gamma p}$ gemessen: $b(\langle W_{\gamma p}\rangle = 180.6\,\mathrm{GeV}) = (5.1 \pm 0.3 \pm 0.2)\,\mathrm{GeV}^{-2}\,\mathrm{c}^2$, $b(\langle W_{\gamma p}\rangle = 250.7\,\mathrm{GeV}) = (5.4 \pm 0.4 \pm 0.2)\,\mathrm{GeV}^{-2}\,\mathrm{c}^2$. Der Achsenabschnitt α_0 und der Steigungsparameter α' einer effektiven Pomerontrajektorie werden bestimmt. Die $W_{\gamma p}$-Abhängigkeit des Steigungsparameters b führt zu $\alpha'_b = (0.17 \pm 0.04 \pm 0.01)\,\mathrm{GeV}^{-2}\,\mathrm{c}^2$. Die $W_{\gamma p}$-Abhängigkeit des differentiellen Wirkungsquerschnittes $\frac{\mathrm{d}\sigma}{\mathrm{d}t}$ liefert beide Parameter: $\alpha_0 = 1.21 \pm 0.01 \pm 0.01$ und $\alpha' = (0.14 \pm 0.03 \pm 0.03)\,\mathrm{GeV}^{-2}\,\mathrm{c}^2$. Die beiden Steigungsparameter α'_b und α' sind im Rahmen der Fehler miteinander verträglich.

Unterschiedliche theoretische Vorhersagen werden mit den Daten verglichen. Das Ein-Pomeron-Modell basierend auf der Reggetheorie beschreibt nicht den starken Anstieg des Wirkungsquerschnittes $\sigma(W_{\gamma p})$ als Funktion von $W_{\gamma p}$. Das Zwei-Pomeron-Modell beschreibt die $W_{\gamma p}$-Abhängigkeit des Wirkungsquerschnittes $\sigma(W_{\gamma p})$ innerhalb der kinematischen Bereichs von HERA. Es ist aber nicht fähig die kombinierten Resultate von HERA und "fixed-target"-Experimenten bei niedrigen Werten von $W_{\gamma p}$ zu beschreiben.

Vorhersagen der QCD werden mit dem gemessenen Wirkungsquerschnitt $\sigma(W_{\gamma p})$ verglichen. Die Vorhersagen verwenden verschiedene Parametrisierungen der Gluonverteilung im Proton und zeigen eine starke Abhängigkeit von der verwendeten Gluonverteilung, da diese quadratisch in den Wirkungsquerschnitt eingeht. Der Vergleich der Vorhersagen mit den gemessenen Werten des Wirkungsquerschnittes $\sigma(W_{\gamma p})$ ist daher ein sensitiver Test für die verwendeten Gluonverteilungen, die indirekt aus inklusiven Messungen bestimmt werden. Während einige dieser Analysen Gluonverteilungen bestimmen, die mit den hier vorgestellten J/ψ-Messungen verträglich sind, können einige andere gemessene Gluonverteilungen ausgeschlossen werden.

Abstract

The elastic photoproduction of J/ψ vector mesons at large values of the photon-proton centre-of-mass energy $135\,\mathrm{GeV} < W_{\gamma p} < 305\,\mathrm{GeV}$ is studied. The elastic photoproduction cross section $\sigma(W_{\gamma p})$ is measured as a function of $W_{\gamma p}$. The differential cross section $\frac{\mathrm{d}\sigma}{\mathrm{d}t}$ is determined in the range $|t| \leq 1.2\,\mathrm{GeV}^2/\,\mathrm{c}^2$. This analysis extends the measurements of $\sigma(W_{\gamma p})$ and $\frac{\mathrm{d}\sigma}{\mathrm{d}t}$ using H1 data up to highest $W_{\gamma p}$ near the kinematic limit given by the parameters of the accelerator of $\approx 318\,\mathrm{GeV}$.

Data for two different event topologies were collected with the H1 detector at the ep-collider HERA during the years 1999 and 2000 resulting in an integrated luminosity of 30.26 pb^{-1} and 26.90 pb^{-1} for the analysed data. The level 2 neural network trigger and the backward silicon tracker are important components of the H1 experiment which make this analysis possible.

From the $W_{\gamma p}$ dependence of the elastic cross section $\sigma(W_{\gamma p}) \propto {W_{\gamma p}}^{\delta}$ the parameter δ is extracted to be $\delta = 1.17 \pm 0.11 \pm 0.16$ for the high $W_{\gamma p}$ results of this analysis alone and $\delta = 0.76 \pm 0.03 \pm 0.04$ including data of the complete kinematic range of the H1 experiment. The exponential slope b of the differential cross section $\frac{\mathrm{d}\sigma}{\mathrm{d}t} \propto \mathrm{e}^{-b|t|}$ is determined in the high $W_{\gamma p}$ regime: $b(\langle W_{\gamma p}\rangle = 180.6\,\mathrm{GeV}) = (5.1 \pm 0.3 \pm 0.2)\,\mathrm{GeV}^{-2}\,\mathrm{c}^2$, $b(\langle W_{\gamma p}\rangle = 250.7\,\mathrm{GeV}) = (5.4 \pm 0.4 \pm 0.2)\,\mathrm{GeV}^{-2}\,\mathrm{c}^2$. The intercept α_0 and slope α' of an effective pomeron trajectory are determined. The $W_{\gamma p}$ dependence of the b-slope gives $\alpha'_b = (0.17 \pm 0.04 \pm 0.01)\,\mathrm{GeV}^{-2}\,\mathrm{c}^2$. The $W_{\gamma p}$ dependence of the differential cross section $\frac{\mathrm{d}\sigma}{\mathrm{d}t}$ yields both parameters: $\alpha_0 = 1.21 \pm 0.01 \pm 0.01$ and $\alpha' = (0.14 \pm 0.03 \pm 0.03)\,\mathrm{GeV}^{-2}\,\mathrm{c}^2$. The two determined slope parameters α'_b and α' are compatible within errors.

Different theoretical approaches are compared to the data. The single pomeron model based on Regge theory does not describe the strong rise of $\sigma(W_{\gamma p})$ as a function of $W_{\gamma p}$. The two pomeron model is able to describe the $W_{\gamma p}$ dependence of the cross section $\sigma(W_{\gamma p})$ within the kinematic regime of HERA, but is not able to describe the combined results of HERA and of fixed target experiments at low values of $W_{\gamma p}$.

QCD predictions using different parameterisations of the gluon distribution in the proton are also compared to the measured cross section $\sigma(W_{\gamma p})$. The predictions show a strong dependence on the gluon distribution, since the gluon distribution enters the cross section quadratically. The comparison to the measured cross section $\sigma(W_{\gamma p})$ is therefore a sensitive test for the gluon distributions, which are determined in an indirect way from inclusive measurements. While some of these analyses result in gluon distributions consistent with the J/ψ measurements presented here, others can definitely be excluded.

Contents

Introduction **1**

1 Diffractive Photoproduction of J/ψ Mesons at HERA **5**

1.1 ep Scattering at HERA 5

1.2 Vector Meson Dominance Model and J/ψ Photoproduction 7

1.3 Weizsäcker-Williams-Approximation 9

1.4 Photoproduction of Vector Mesons 10

1.5 Hadro- and Photoproduction Data 11

1.6 Diffraction in Regge Theory 14

1.6.1 Hadron-Hadron Scattering in Regge Theory 15

1.6.2 Application to Photoproduction at HERA 19

1.6.3 Parameterisation of Donnachie and Landshoff 20

1.6.4 Proton-dissociative Vector Meson Production 23

1.7 Perturbative QCD 24

2 The H1 Detector at HERA **27**

2.1 The HERA Collider 27

2.2 The H1 Detector 29

2.2.1 Tracking System 31

2.2.1.1 Central Silicon Tracker 31

2.2.1.2 Backward Silicon Tracker 32

2.2.1.3 Central Tracking Chambers 33

2.2.1.4 Forward Tracking Chambers 33

2.2.1.5 Backward Drift Chamber 34

2.2.2 Calorimeters 34

2.2.2.1 Liquid Argon Calorimeter 34

2.2.2.2 Spaghetti Calorimeter 36

2.2.3 Muon System . . . 39
2.2.3.1 Central Muon Detector . . . 39
2.2.3.2 Forward Muon Detector . . . 39
2.2.4 Proton Remnant Tagger . . . 40
2.2.5 Time of Flight System . . . 40
2.2.6 Luminosity System . . . 41

3 J/ψ Event Topologies 43

4 Trigger System 49
4.1 Level 1 . . . 50
4.1.1 DC$r\phi$ Trigger Elements . . . 52
4.1.2 $z-$Vertex Trigger Elements . . . 52
4.1.3 LAr Trigger Elements . . . 53
4.1.4 SpaCal Trigger Elements . . . 54
4.1.5 Time-Of-Flight Trigger Elements . . . 55
4.1.6 Level 1 Subtriggers . . . 57
4.2 Level 2 . . . 59
4.2.1 Introduction to Neural Networks . . . 59
4.2.2 Hardware of the Level-2-Neural-Network-Trigger . . . 62
4.2.3 Feed Forward Neural Network for the Track-Cluster Sample . . 64
4.2.4 SpaCal-Back-To-Back Algorithm for the Cluster-Cluster Sample 64
4.3 Trigger Level 4 . . . 67
4.4 Trigger Level 5 . . . 69

5 Monte Carlo Simulation 71
5.1 Event Generators . . . 71
5.1.1 Vector Meson Event Generator `DiffVM` . . . 72
5.1.2 Lepton Pair Production Event Generator `LPair2` . . . 74
5.1.3 QED Compton Scattering Event Generator `COMPTON` . . . 75
5.1.4 Abbreviations . . . 76
5.2 Detector Simulation . . . 76

6 Reconstruction **77**

6.1 Trigger Calculation 77

6.2 BST Track Finding 78

6.2.1 BST Track Finding Algorithm 80

6.2.2 Improvement of the Measurement of the Polar Angle and the Vertex Position 81

6.2.3 Track Finding Efficiency and Data/MC Adjustment 83

6.2.3.1 Adjustment of the BST Detector Response 84

6.2.3.2 Adjustment of the BST Track Finding Efficiency as a Function of the Angles θ and ϕ in MC 87

6.2.3.3 Adjustment of the total BST Track Finding Efficiency as a Function of the `run number` in MC 88

6.2.3.4 Final adjusted Efficiencies for the different Running Periods 89

6.2.3.5 Coherent Loss 89

6.2.4 Comparison to the Standard BST Tracking 91

6.3 Reconstruction of Kinematic Variables 92

6.4 Alignment and Calibration 97

6.4.1 SpaCal Alignment 97

6.4.2 SpaCal Energy Calibration 97

6.4.3 Noise Simulation and Calibration for the Forward Detectors . . 98

6.4.4 z_{vtx} Reweighting 102

7 Selection of J/ψ Mesons in Photoproduction **103**

7.1 Run Selection 103

7.2 Event Selection 104

7.3 Kinematic Cuts 105

7.3.1 Basic Cuts 106

7.3.2 Angular Cuts 107

7.3.3 Energy Cuts 108

7.3.4 Miscellaneous Cuts 109

7.3.5 Mass Cut 111

7.3.6 BST Cut 111

7.4 Trigger Cuts 112

7.5 Forward Classification 115

7.6 Control Distributions 115

8 Analysis **118**

8.1 Luminosity Calculation 119

8.2 Binning and Photon Flux 121

8.2.1 $W_{\gamma p}$ Binning 121

8.2.2 p_t^2 Binning 122

8.2.3 Photon Flux 124

8.3 Signal Extraction 125

8.4 Efficiencies 127

8.5 Determination of the Number of proton-elastic Events 132

8.6 Unfolding of $p_t^2 \rightarrow |t|$ 133

8.7 Systematic Errors 137

9 Results **141**

9.1 Cross Section $\sigma(W_{\gamma p})$ 141

9.1.1 $W_{\gamma p}$ Dependence of $\sigma(W_{\gamma p})$ 143

9.1.2 Two Pomeron Fit 146

9.1.3 Shape Analysis of $\sigma(W_{\gamma p})$ 148

9.1.4 Comparison with QCD Predictions 152

9.2 Differential Cross Section $\frac{\mathrm{d}\sigma}{\mathrm{d}t}$ 152

9.2.1 t Dependence of $\frac{\mathrm{d}\sigma}{\mathrm{d}t}$ 154

9.2.2 Effective Pomeron Trajectory 156

9.2.2.1 Determination of the Slope of the Effective Pomeron Trajectory 157

9.2.2.2 Effective Pomeron Trajectory 158

9.3 Discussion 161

Summary **164**

A Signal Extraction **167**

Bibliography **176**

Danksagung **185**

Introduction

The search for the fundamental building blocks of matter and the investigation of their properties and of the interactions between them are the main tasks of elementary particle physics. Our present knowledge is reflected in the *standard model* of electro-weak and strong interactions. The fundamental building blocks of matter are two types of spin $\frac{1}{2}$ fermions[1]: *leptons* and *quarks*. Leptons are only sensitive to the electro-weak interaction, while quarks in addition also interact strongly. Leptons and quarks can be described as three families of doublets with increasing mass. In the lepton sector the pairs are electron and electron neutrino (e, ν_e), muon and muon neutrino (μ, ν_μ), tau and tau neutrino (τ, ν_τ). The three families of quarks are the up and down (u, d), the strange and charm (s, c) and the bottom and top quarks[2] (b, t).

Interactions are described in the framework of gauge theories, in which the three types of forces, electromagnetic, weak and strong are mediated by the exchange of integer spin *gauge bosons*. The exchange boson for the electromagnetic interaction is the photon (γ). The weak interaction is mediated by the exchange of the heavy gauge bosons (Z^0, W^+, W^-). The electromagnetic and weak interactions are united through their gauge groups into the electroweak theory. The gluons are exchanged in the strong interaction, which is described by *quantum chromo dynamics* QCD. Gravitation is not yet fully formulated as a quantum field theory and is therefore not included in the standard model. Also, gravitation is far too weak to have a noticeable influence on interactions of elementary particles.

The gauge bosons couple to a charge which is characteristic for the interaction. The electromagnetic interaction is associated with the electric charge, which is carried by the charged leptons e, μ and τ and all quarks. The weak charge is carried by all leptons and quarks. The colour charge $(c \in \{r = \text{red}, g = \text{green}, b = \text{blue}\})$ of the strong interaction is carried by quarks, not by leptons. Concerning the exchanged bosons, the photon does not carry the electric charge, while bosons of the weak interaction carry the weak charge and the gluons carry the colour charge as a $(c_1, \bar{c}_2)$ colour-anticolour pair.

Quarks are constituents of *hadrons*. Requiring colourless hadrons the quark-antiquark structure of *mesons* and the quark-quark-quark structure of *baryons* can be explained [1]. All stable matter is built from the lightest family: e, u, d.

[1] In this work natural units are used: $\hbar = c = 1$.

[2] Alternative names for bottom and top quarks are beauty and truth; truth has however become unfashionable.

Of special interest for this thesis are mesons with the quantum numbers of the photon[3] ($J^{PC} = 1^{--}$). Due to their spin-parity they transform like vectors and therefore are called *vector mesons* (ρ, ω, ϕ, J/ψ, Υ). The lightest $c\bar{c}$ vector meson is called J/ψ and has a mass $m_{J/\psi} = (3.09688 \pm 0.00004)\,\text{GeV}$. The electromagnetic decay $J/\psi \to e^+e^-$ has a significant branching ratio of about 5% and provides a clear experimental signature.

Scattering experiments are a crucial tool to investigate fundamental physics processes. Analysing the outgoing particles reveals the structure of the interaction. The possible spatial resolution is limited by the available energy in the scattering process. At the "Hadron-Elektron-Ring-Anlage" (HERA) [2] at the "Deutsches Elektronen-Synchroton" (DESY) [3] electrons[4] with an energy of 27.5 GeV are brought to collision with protons of an energy of 920 GeV. This results in a centre-of-mass energy of 318 GeV and therefore in a spatial resolution of less than 10^{-18} m, which is more than 3 orders of magnitude less than the charge radius of the proton $(0.845 \pm 0.05) \cdot 10^{-15}$ m [4]. This enables HERA to contribute significantly to the understanding of the structure of the proton and of the strong interaction.

The electron beam can be viewed as a source of high energy virtual photons, which interact with the proton. The four-momentum squared Q^2 of the photon is a measure for its virtuality. At $Q^2 \approx 0\,\text{GeV}^2$ the photon is quasi-real and the process is called *photoproduction*, while for non-vanishing Q^2 the process is called electroproduction.

Since vector mesons have the same quantum numbers as the photon, the photon can fluctuate into a vector meson, which then scatters off the proton. If in this scattering process only momentum and angular momentum are transferred, the process is called *diffractive*. In *elastic* scattering the proton stays intact (*proton-elastic*) and the vector meson production is called *exclusive*, since no other particles are produced. In *proton-dissociative* scattering the proton dissociates into a hadronic final state.

There are two different theoretical approaches to describe the exclusive vector meson photoproduction. On one hand there is a phenomenological ansatz, which is based on Regge theory [5]. In this ansatz the interaction is mediated at high energies by the exchange of a colourless object, which is called *pomeron*. On the other hand there are predictions from perturbative QCD (pQCD) [6, 7, 8, 9, 10] where a colourless system of gluons mediates the interaction.

Previous measurements at HERA show that the total photoproduction cross section for the light vector mesons ρ and ω are slowly rising with increasing photon-proton centre-of-mass energy $W_{\gamma p}$. This is quantitatively predicted by Regge theory [11, 12]. But the total cross section of the photoproduction of the heavier J/ψ vector meson rises much more steeply with increasing $W_{\gamma p}$ than predicted in Regge theory [13, 14]. The total cross sections for the light vector mesons ρ and ϕ also rise steeply at higher

[3] J^{PC}: $J = L + S$, L=angular momentum, S=spin, P=parity (space inversion), C=particle-antiparticle conjugation

[4] In different running periods HERA is using electrons or positrons. Since the physics process studied in this analysis does not depend on the charge of the lepton, the nomenclature electron is used for electron and positron.

values of Q^2 [15, 16][5]. These measurements suggest, that there is a transition from a (*"soft"*) region where Regge theory is valid to a (*"hard"*) region where pQCD may be applied. This transition is governed by two scales: the mass squared m_V^2 of the vector meson and the virtuality Q^2 of the exchanged photon.

In the pQCD picture the interaction of the J/ψ vector meson with the proton is mediated by the exchange of two gluons or, more generally, a gluon ladder. The strong rise of the proton structure function F_2 [17, 18] towards low values of the Bjorken variable[6] x_{B} can be interpreted as a dramatic increase of the gluon density within the proton towards low values of x_{B}. Low x_{B} is kinematically connected to high $W_{\gamma p}$. Therefore in pQCD the strong rise of the J/ψ cross section at high values of $W_{\gamma p}$ can be related to the strong rise of F_2 and the gluon density. Due to the exchange of two gluons, the cross section for exclusive vector meson photoproduction depends quadratically on the gluon density.

The behaviour of the J/ψ cross section led to an extension of the pomeron picture. Using J/ψ measurements at HERA an additional *"hard" pomeron* was phenomenologically introduced through a fit to the data [19]. Taking both pomerons — the old "soft" and the new "hard" pomeron — the steep rise of the total cross section of J/ψ photoproduction can be described. In the double-logarithmic presentation of the cross section vs. $W_{\gamma p}$ the two-pomeron model always predicts a "concave" shape, while pQCD predicts "convex" or "concave" shapes, depending on the gluon density used for the calculations.

Beyond the total cross section the analysis presented here also extracts differential cross sections to compare the different theoretical predictions. Diffractive high energy scattering processes show analogies to optical diffraction. In optical diffraction the width of the forward interference maximum is shrinking with increasing energy of the incoming light. Taking the four-momentum transfer squared t of the proton in analogy to the scattering angle in optical diffraction the $|t|$-dependence of the differential cross section $\frac{\mathrm{d}\sigma}{\mathrm{d}t}$ at small $|t|$ is investigated. Regge theory with the exchange of one pomeron predicts an increase of the slope of $\frac{\mathrm{d}\sigma}{\mathrm{d}t}$ with rising $W_{\gamma p}$ (*shrinkage*), while Regge theory including the hard pomeron predicts less shrinkage.

The aim of this analysis is to increase the precision of the measurement of the elastic photoproduction cross section $\sigma(W_{\gamma p})$ in the high $W_{\gamma p}$ regime and to extend the measurement up to almost the kinematic limit of HERA. This analysis provides first measurements of the differential cross section $\frac{\mathrm{d}\sigma}{\mathrm{d}t}$ in the high $W_{\gamma p}$ regime using H1 data. The new measurements in the range of $135\,\mathrm{GeV} < W_{\gamma p} < 305\,\mathrm{GeV}$ together with previous measurements at lower values of $W_{\gamma p}$ allow a comparison of the different theoretical predictions with the data over the full $W_{\gamma p}$ range accessible to H1 ($\approx 30\,\mathrm{GeV} < W_{\gamma p} < 305\,\mathrm{GeV}$).

For this thesis data are used which were taken with the H1 experiment in the years 1999 and 2000. Important special features of the H1 experiment, that make the analysis possible, are the *backward silicon tracker* (BST) and the *Level-2-Neural-Network-Trigger* (L2NN).

[5] The Q^2 dependence for ω production is not measured yet.

[6] x_{B} is the momentum fraction of the scattered parton in the proton.

In the kinematic region of $W_{\gamma p}$ important for this analysis one or both of the decay electrons of the J/ψ are detected in the backward region of the H1 detector. As the backward region is not covered by the central tracking chambers, the basic signature of a backward electron in the backward region is an energy *cluster*. Electrons in the central region are detected by *tracks* in the central tracking chambers. In this analysis two different event topologies are used: a *"track-cluster"* and a *"cluster-cluster"* sample, covering the high $W_{\gamma p}$ region.

Especially for the cluster-cluster sample the upgrade of the BST in 1998 is very important. Only by the additional track information a sufficiently precise measurement and electron identification are possible. The BST is the keystone in extending this analysis to the highest $W_{\gamma p}$, i.e. into the region up to the kinematic limit. It allows the association of an electron in the cluster-cluster sample with a track in the BST and thus the efficient rejection of background. In this kinematic region it is very important to reject background events even during data taking in order to obtain a sufficient number of J/ψ events. For this purpose H1 is using a four-level trigger system. For this analysis the Level-2-Neural-Network-Trigger is of special importance to keep high efficiency. For the track-cluster sample (high $W_{\gamma p}$ range) a feed-forward neural network is used since the middle of 1999. For the cluster-cluster sample (highest $W_{\gamma p}$) a special parallel algorithm is used for the online event selection.

This thesis is structured as follows: In chapter 1 the relevant theoretical models are described. An introduction to the HERA collider and the H1 experiment with special emphasis on parts important for this analysis is given in chapter 2. Event topologies are discussed in chapter 3. Since the trigger system and neural networks play a crucial role in this analysis, they are described in detail in chapter 4. Events from Monte-Carlo studies are important for the understanding of the background. Different MC methods which are used to estimate signal and background are discussed in chapter 5. The reconstruction of simulated and real data is described in chapter 6 which also contains the description of a track finding algorithm in the BST developed in this thesis. After the presentation of the selection and analysis of the data in chapter 7 and 8 the results are given in chapter 9.

Chapter 1

Diffractive Photoproduction of J/ψ Mesons at HERA

In this chapter first the kinematics of deep inelastic electron-proton scattering at HERA is defined. It is then applied to the exclusive photoproduction of the vector meson J/ψ. Theoretical models for the exclusive photoproduction of vector mesons are presented. This includes a review of relevant Regge phenomenology and the predictions from perturbative quantum chromo dynamics (QCD).

1.1 ep Scattering at HERA

At HERA electrons or positrons with an energy of $E_e = 27.5\,\text{GeV}$ collide with protons with an energy of $E_p = 920\,\text{GeV}$. In lowest order (Born approximation) ep-scattering is described by the exchange of a gauge boson ($\gamma^\star$, Z^0, W^+, W^-) between the electron and a parton of the proton. The exchange of the neutral bosons $\gamma^\star$ and Z^0 is called *neutral current* (NC) process and the exchange of charged bosons W^+ and W^- is called *charged current* (CC) process. The Feynman diagram for deep inelastic scattering (DIS) is shown in figure 1.1. This analysis concentrates on processes with photon exchange.

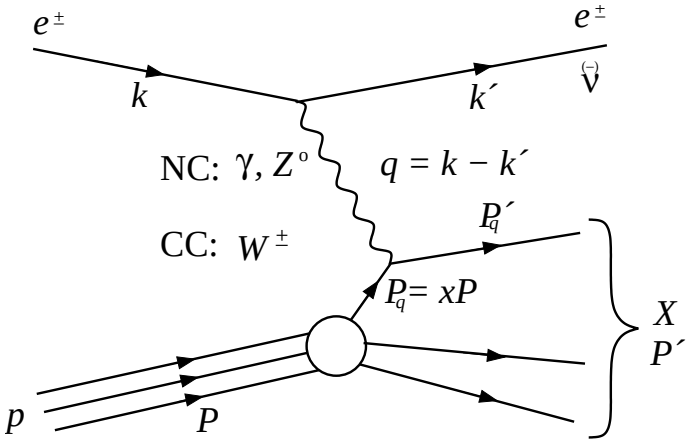

Figure 1.1: Feynman diagram of the deep inelastic electron quark scattering in lowest order.

The kinematic variables in figure 1.1 are the four-momenta of the incoming (k) and outgoing (k') electron, the incoming proton (P) and outgoing hadronic final state X (P') and of the exchanged photon ($q = k - k'$). In order to describe the kinematics the following Lorenz invariant variables are used:

- The centre-of-mass energy squared

$$s := (k + P)^2 = 4E_e E_p + m_e^2 + m_p^2 \approx 4E_e E_p \tag{1.1}$$

  is fixed by the energies of the electron and proton beams. The centre-of-mass energy is $\sqrt{s} \approx 318\,\mathrm{GeV}$.

- The four-momentum squared of the exchanged photon

$$Q^2 := -q^2 = -(k' - k)^2 \geq 0 \tag{1.2}$$

  represents the virtuality of the spacelike photon.

- In the rest system of the incoming proton the fraction of the electron energy which is transferred to the hadronic final state is given by

$$y := \frac{q \cdot P}{k \cdot P}\,. \tag{1.3}$$

- The energy in the photon proton centre-of-mass system

$$W_{\gamma p}{}^2 := (P + q)^2 = ys + m_p^2 - Q^2\,. \tag{1.4}$$

  For $Q^2 \approx 0$ this reduces to $W_{\gamma p}{}^2 \approx ys$.

- The fraction of the momentum of the scattered parton with respect to the proton momentum (Bjorken x_B):

$$x_\mathrm{B} := \frac{Q^2}{2P \cdot q}\,. \tag{1.5}$$

The kinematic variables are related as $Q^2 = s x_\mathrm{B} y$. If the centre of mass energy $\sqrt{s}$ is fixed, the kinematics is fully described by two out of the three variables x_B, y, Q^2.

The kinematic variables Q^2 and y can be determined by measuring e.g. the energy E'_e and polar angle θ_e of the outgoing scattered electron in the laboratory frame (H1 coordinate system, see section 2.2):

$$Q^2 = 4E_e\, E'_e\, \cos^2\frac{\theta_e}{2}\,, \tag{1.6}$$

$$y = 1 - \frac{E'_e}{E_e}\, \sin^2\frac{\theta_e}{2}\,. \tag{1.7}$$

This analysis concentrates on the region of $Q^2 \approx 0$. With equation 1.6 this corresponds to the region $\theta_e \approx 180°$ where the electron is almost not deflected by the collision. In

this kinematic regime the exchange of the weak gauge boson Z^0 is strongly suppressed with respect to photon exchange due to its large mass $m_{Z^0} = 91\,\text{GeV}$ and can be safely neglected.

The $Q^2 \approx 0$ regime is called photoproduction, which is explained in the following sections.

1.2 Vector Meson Dominance Model and J/ψ Photoproduction

The electron in figure 1.1 radiates a photon which interacts with the proton. Measurements [20] show, that the photon proton cross section at large centre-of-mass energies $\sqrt{s}$ does not fall as $\sqrt{s}$ which would be expected from pure QED cross sections.

This can be explained by the hadronic structure of the photon which is described in the vector meson dominance model (VDM) [21]. In this model the photon $|\gamma\rangle$ is composed of the electromagnetic field $|\gamma_{QED}\rangle$ and hadronic parts $|V\rangle$ with the quantum numbers of the photon ($J^{PC} = 1^{--}, Q = B = S = 0$), i.e. neutral vector mesons:[1]

$$|\gamma\rangle = N\,|\gamma_{QED}\rangle + \sum_V \frac{e}{\gamma_V}|V\rangle\,, \tag{1.8}$$

where N is a normalisation factor and $-e$ the charge of the electron. The coupling constant γ_V is determined by the mass m_V and the leptonic width Γ_V

$$\frac{\gamma_V^2}{4\pi} = \frac{\alpha_{em}^2 m_V}{3\Gamma_V}\,. \tag{1.9}$$

The connection between the total cross section $\sigma(\gamma p \to Vp)$ and the elastic cross section $\sigma(Vp \to Vp)$ of the vector meson production is then

$$\sigma(\gamma p \to Vp) = \frac{4\pi\alpha_{em}}{\gamma_V^2}\sigma(Vp \to Vp)\,. \tag{1.10}$$

Since pure QED cross sections fall with $1/s$, where s is the centre-of-mass energy squared, and hadron-hadron cross sections rise with s^ε at large s, where ε is a positive constant, the hadronic part in equation 1.8 dominates at high s.

The scattering process $\gamma p \to Vp$ can therefore be interpreted as a two step process: The photon fluctuates into a neutral vector meson (ρ^0, ω, ϕ, J/ψ, Υ) which scatters off the proton [21]. Real photons are transversely polarised. In the extension of the VDM towards virtual photons one has to take into account, that a longitudinal component is present in addition. The cross section for transversely polarised photons $\sigma_{\gamma p}^T$ depends on Q^2 [22]

[1] In this section generally V is used for a vector meson with four-momentum p_V and mass m_V.

$$\frac{\sigma^T_{\gamma p}(Q^2)}{\sigma^T_{\gamma p}(0)} = \left(\frac{m_V^2}{m_V^2 + Q^2}\right)^2 . \tag{1.11}$$

The transverse component is therefore suppressed with increasing Q^2 and the ratio of the cross sections from longitudinally and transversely polarised photons is predicted to be [22]

$$R(Q^2) = \frac{\sigma^L_{\gamma p}(Q^2)}{\sigma^T_{\gamma p}(Q^2)} = \xi \frac{Q^2}{m_V^2} , \tag{1.12}$$

where ξ is a constant.

The VDM model was conceived before heavy quarks were discovered. Extending it to charm quarks the basic picture of elastic J/ψ production at HERA is shown in figure 1.2.

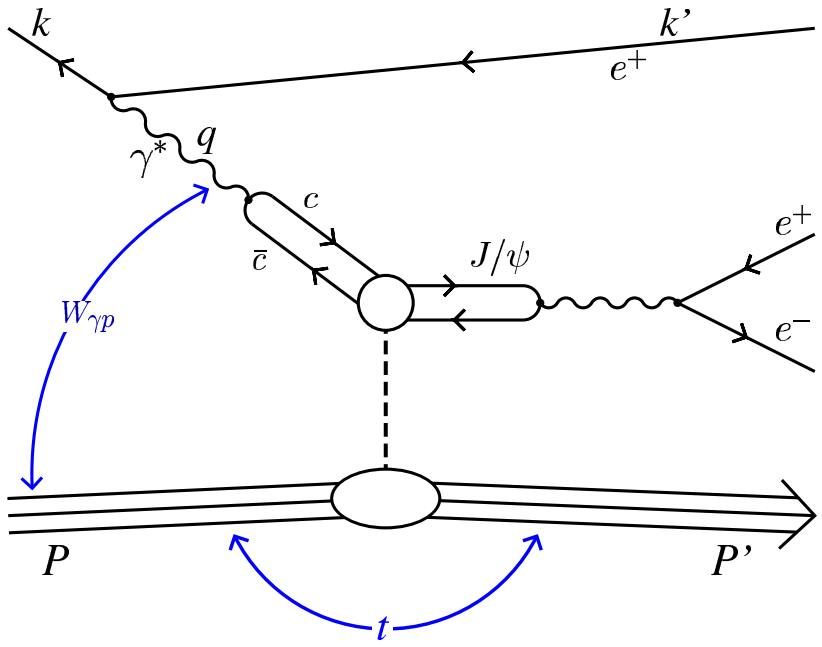

Figure 1.2: The electron or positron beam of HERA can be viewed as a source of virtual photons. These virtual photons form a J/ψ vector meson according to the vector meson dominance model. The J/ψ vector meson scatters off the proton. The J/ψ can be detected via the decay into an electron positron pair.

In addition to the kinematic variables of section 1.1 the following variables are defined:

- The four-momentum transfer squared at the proton vertex:

$$t := (P - P')^2 = (q - p_V)^2 \tag{1.13}$$
$$\approx -(\vec{p}_{tV})^2 \quad \text{for} \quad q^2 \approx 0 \tag{1.14}$$

  where $\vec{p}_{tV}$ is the transverse momentum of the vector meson.

- In the special scattering process $\gamma^\star p \to VX$, where X is a hadronic final state originating from the proton, the elasticity of the process is defined as

$$z := \frac{P \cdot p_V}{P \cdot q} \,. \tag{1.15}$$

The case $z = 1$ is called elastic photoproduction, because viewed in the proton rest frame the full photon energy is carried by the vector meson V.

1.3 Weizsäcker-Williams-Approximation

The measurable quantity at HERA is the cross section of electron-proton scattering σ_{ep}. This section describes the connection to the cross section of photon-proton scattering $\sigma_{\gamma p}$.

The probability of a beam electron to radiate a photon is called flux factor $\mathcal{F}_\gamma$. The measured electron-proton cross section can be separated into transversal and longitudinal components [23]:

$$\frac{\mathrm{d}^2\sigma_{ep}}{\mathrm{d}y\mathrm{d}Q^2} = \frac{\mathrm{d}^2\mathcal{F}_\gamma}{\mathrm{d}y\mathrm{d}Q^2}\,\sigma_{\gamma p} = \frac{\mathrm{d}^2\mathcal{F}_\gamma^T}{\mathrm{d}y\mathrm{d}Q^2}\,\sigma_{\gamma p}^T + \frac{\mathrm{d}^2\mathcal{F}_\gamma^L}{\mathrm{d}y\mathrm{d}Q^2}\,\sigma_{\gamma p}^L \,. \tag{1.16}$$

where $\mathcal{F}_\gamma^L$ and $\mathcal{F}_\gamma^T$ are the longitudinal and transversal components of $\mathcal{F}_\gamma$. Using an improved form of the Weizsäcker-Williams-approximation (WWA) [24, 25, 26] where terms of the order of m_e^2/Q^2 are included, the components for small values of Q^2 are given by [27, 28, 29]

$$\frac{\mathrm{d}^2\mathcal{F}_\gamma^T}{\mathrm{d}y\mathrm{d}Q^2} = \frac{\alpha_{em}}{2\pi y Q^2}\left(\underbrace{1+(1-y)^2}_{\text{WWA}} - 2(1-y)\frac{Q^2_{min}}{Q^2}\right) , \tag{1.17}$$

$$\frac{\mathrm{d}^2\mathcal{F}_\gamma^L}{\mathrm{d}y\mathrm{d}Q^2} = \frac{\alpha_{em}}{2\pi y Q^2}\,2(1-y) \tag{1.18}$$

where $Q^2_{min}(y) = m_e^2\frac{y^2}{1-y}$ is the kinematic smallest possible virtuality of the photon. This leads to a flux ratio of the longitudinally to transversely polarised incoming virtual photons

$$\varepsilon_{\mathcal{F}} = \frac{\frac{\mathrm{d}^2\mathcal{F}_\gamma^L}{\mathrm{d}y\mathrm{d}Q^2}}{\frac{\mathrm{d}^2\mathcal{F}_\gamma^T}{\mathrm{d}y\mathrm{d}Q^2}} \approx \frac{1-y}{1-y+y^2/2} \,. \tag{1.19}$$

With the VDM prediction for the ratio R (see equation 1.12) of the longitudinal and transversal cross sections one can write

$$\sigma_{\gamma p} = \sigma^T_{\gamma p} + \sigma^L_{\gamma p} = \sigma^T_{\gamma p} \cdot (1 + R)\,. \tag{1.20}$$

Combining equations 1.18, 1.19 and and 1.20 the following formula for the electron-proton cross section is obtained

$$\frac{\mathrm{d}^2\sigma_{ep}}{\mathrm{d}y\mathrm{d}Q^2} = \frac{\mathrm{d}^2\mathcal{F}^T_\gamma}{\mathrm{d}y\mathrm{d}Q^2}\,\sigma^T_{\gamma p}\,(1 + \varepsilon_\mathcal{F}\,R) = \frac{\mathrm{d}^2\mathcal{F}^T_\gamma}{\mathrm{d}y\mathrm{d}Q^2}\,\sigma_{\gamma p}\,\frac{1 + \varepsilon_\mathcal{F}\,R}{1 + R} \approx \frac{\mathrm{d}^2\mathcal{F}^T_\gamma}{\mathrm{d}y\mathrm{d}Q^2}\,\sigma_{\gamma p} \tag{1.21}$$

where in the kinematic region of the analysis $y \approx 0$ (see equation 1.7) and thus $\varepsilon_\mathcal{F} \approx 1$. Integration over y and Q^2 yields

$$\begin{aligned}\sigma_{ep}(y^{min}, y^{max}) &= \int_{y^{min}}^{y^{max}} \int_{Q^2_{min}(y)}^{Q^2_{max}} \frac{\mathrm{d}^2\mathcal{F}^T_\gamma}{\mathrm{d}y\mathrm{d}Q^2}\,\sigma_{\gamma p}\,\mathrm{d}Q^2\mathrm{d}y \\ &= \mathcal{F}_\gamma(y^{min}, y^{max}) \cdot \sigma_{\gamma p}(y_0, Q^2_0)\end{aligned} \tag{1.22}$$

and the photon-proton cross section $\sigma_{\gamma p}$ is connected with the electron-proton cross section σ_{ep} by the flux factor $\mathcal{F}_\gamma$ in the following way

$$\sigma_{\gamma p}(y_0, Q^2_0) = \frac{1}{\mathcal{F}_\gamma(y^{min}, y^{max})}\,\sigma_{ep}(y^{min}, y^{max}) \tag{1.23}$$

with

$$\mathcal{F}_\gamma(y^{min}, y^{max}) = \int_{y^{min}}^{y^{max}} \int_{Q^2_{min}(y)}^{Q^2_{max}} \frac{\mathrm{d}^2\mathcal{F}^T_\gamma}{\mathrm{d}y\mathrm{d}Q^2}\,\mathrm{d}Q^2\mathrm{d}y\,. \tag{1.24}$$

Since $\sigma_{\gamma p}$ is slowly varying in the region $\mathcal{I} := \{(y, Q^2) | y^{min} \le y \le y^{max}, Q^2_{min}(y) \le Q^2 \le Q^2_{max}\}$, values $(y_0, Q^2_0) \in \mathcal{I}$ can be found, so that equation 1.22 holds. Q^2_{max} is determined by the acceptance of the experiment. Below Q^2_{max} the scattered beam electron is not detected.

With equation 1.4 the interval $[y^{min}, y^{max}]$ is connected to the experimentally chosen interval $[W^{\min}_{\gamma p}, W^{\max}_{\gamma p}]$. The corresponding flux factor $\mathcal{F}_\gamma(W^{\min}_{\gamma p}, W^{\max}_{\gamma p})$ is obtained by numerical integration (equation 1.24).

1.4 Photoproduction of Vector Mesons

The electron beam at HERA can be viewed as a source of virtual photons (see figure 1.2). These photons are quasi-real in the photoproduction regime of $Q^2 \approx 0$.

Generalising, the basic picture of the process $\gamma^\star p \to Vp$ is shown in figure 1.3: the photon $\gamma^\star$ with virtuality $Q^2 \approx 0$ fluctuates into a quark-antiquark ($q\bar{q}$) pair, which

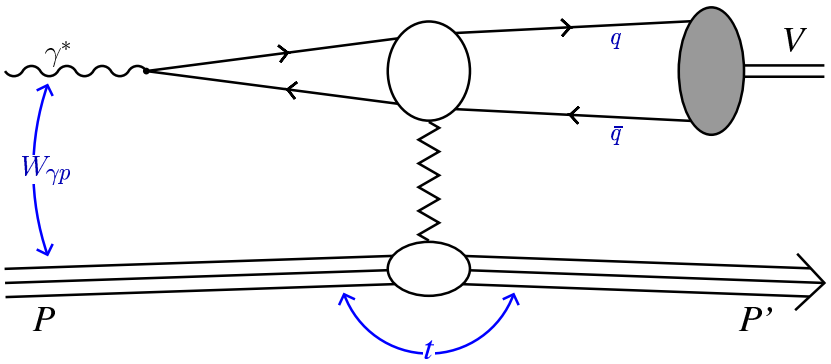

Figure 1.3: Basic picture of the elastic production of a vector meson V in $\gamma^\star p$ scattering. The $\gamma^\star p$ centre-of-mass energy is $W_{\gamma p}$ and the four-momentum transfer at the proton vertex is t.

then interacts elastically with the proton p. The details of the interaction remain unspecified here.

After the interaction with the proton the vector meson V with invariant mass m_V is formed, in first approximation by the $q\bar{q}$ pair. In the kinematic region of high centre-of-mass energy $W_{\gamma p}$ the time scales involved are the following: The typical lifetime $\tau_{\gamma^\star \to q\bar{q}}$ of the $\gamma^\star \to q\bar{q}$ fluctuation and the time $\tau_{q\bar{q}\to V}$ for the formation of the vector meson V are much longer than the duration τ_i of the interaction with the proton

$$\tau_{\gamma^\star \to q\bar{q}} >> \tau_i \,, \quad \tau_{q\bar{q}\to V} >> \tau_i \,. \tag{1.25}$$

Therefore the amplitude in this basic picture factorises into three parts: the fluctuation into $q\bar{q}$ denoted by $\psi^\gamma_{q\bar{q}}$, the interaction amplitude with the proton $A_{q\bar{q}+p}$ and the wave function of the vector meson $\psi^V_{q\bar{q}}$

$$A(\gamma^\star p \to Vp) = \psi^\gamma_{q\bar{q}} \otimes A_{q\bar{q}+p} \otimes \psi^V_{q\bar{q}} \,. \tag{1.26}$$

1.5 Hadro- and Photoproduction Data

The general features of hadro- and photoproduction data are discussed. They motivate the models described in the next sections.

The total cross sections for various incoming hadrons and photons are shown in figure 1.4. At low centre-of-mass energy $\sqrt{s}$ the formation of resonances is visible. Beyond these resonant effects the cross sections show a decrease at low values of $\sqrt{s}$ and a slow rise at higher values of $\sqrt{s}$. This slow rise seems to be independent of the type of the scattering hadrons. This universal behaviour indicates, that it is not a property of the scattering particles, but a property of "something" that is exchanged. Using specific assumptions for that "something" Regge theory was developed to describe this universal slow rise. Regge theory is explained in section 1.6.

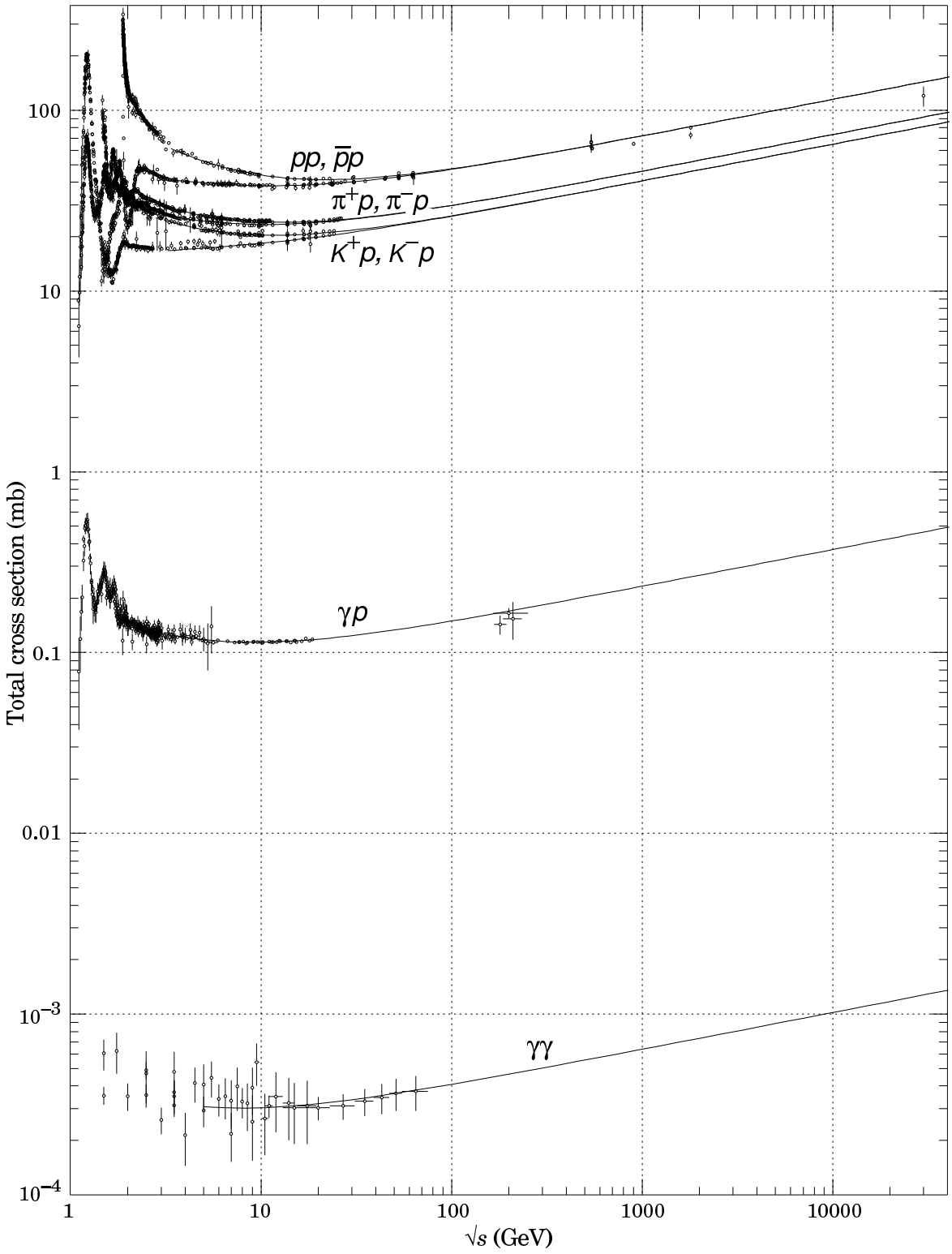

Figure 1.4: Summary of hadronic, γp, and $\gamma\gamma$ total cross sections as a function of the centre-of-mass energy $\sqrt{s}$ (from [20] p. 206).

The basic picture of photoproduction of vector mesons (see section 1.4) can be related to hadron-hadron scattering by the vector meson dominance model (see section 1.2). In figure 1.5 the total photoproduction cross section and several exclusive photoproduction cross sections are shown. The total photoproduction cross section and the exclusive photoproduction cross sections for the light vector mesons ρ, ω and ϕ show a similar slow rise with rising centre-of-mass energy $\sqrt{s}$ as observed for hadrons. However, the exclusive photoproduction cross sections for the heavy vector mesons J/ψ and $\psi(2s)$ show a much steeper rise. In order to describe this different behaviour previous models based on Regge theory had to be extended (see section 1.6.3) and an alternative theory (pQCD) was developed (see section 1.7).

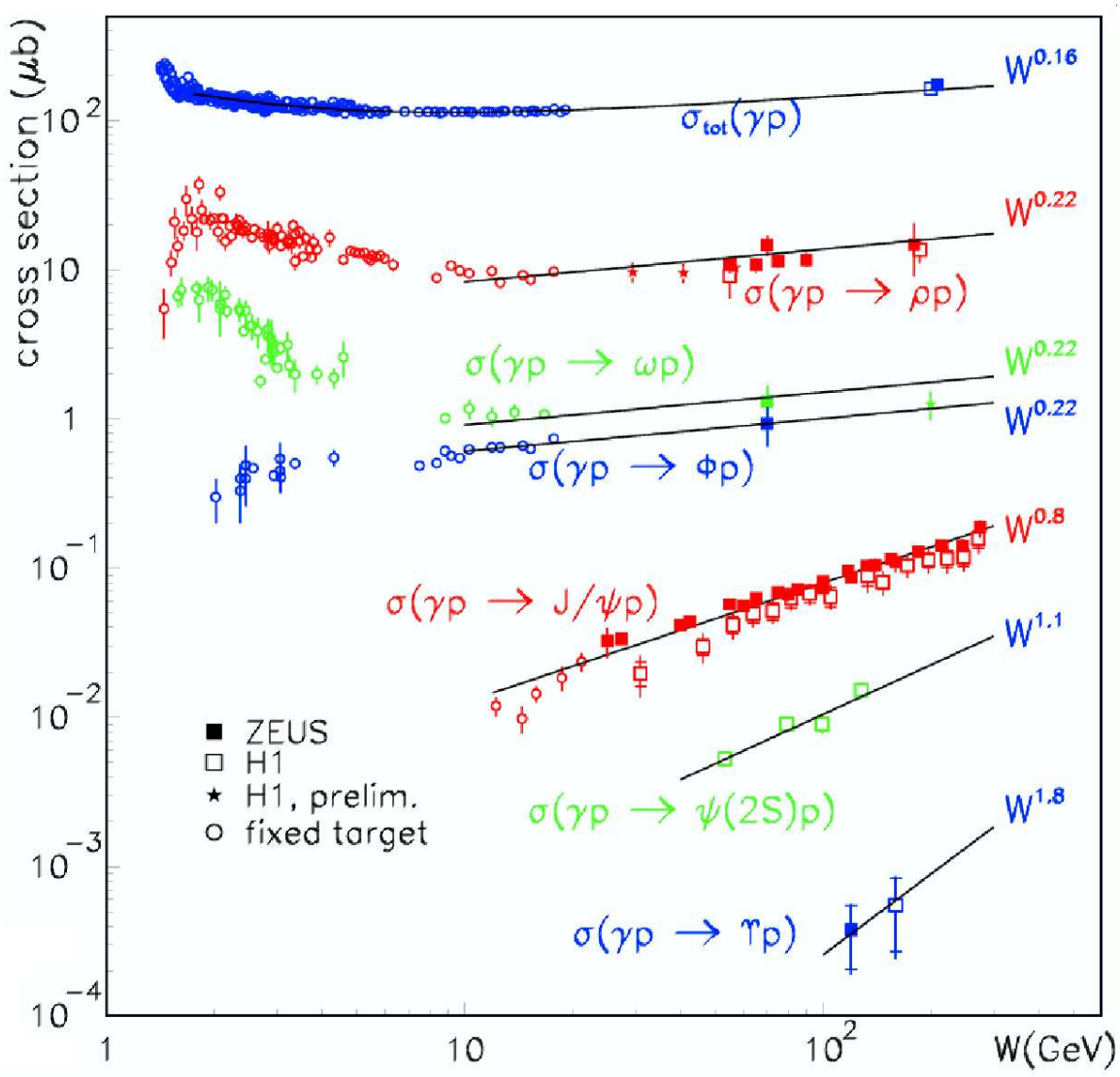

Figure 1.5: HERA total and exclusive photoproduction cross sections as a function of the photon proton centre-of-mass energy $W = W_{\gamma p}$. Fits to the data are shown. For the Υ cross section the $W_{\gamma p}$ dependence is not the result of a fit, but a prediction from pQCD is shown. (from [30]).

Both approaches, the one based on Regge theory and the other based on pQCD calculations, need experimental input concerning the shape of the differential cross section $\frac{d\sigma}{dt}$. In figure 1.6 the differential cross section $\frac{d\sigma}{dt}$ for elastic J/ψ photoproduction as a function of $|t|$ is shown for low $|t|$. Data suggest an exponential ansatz of the form e^{-bt}.

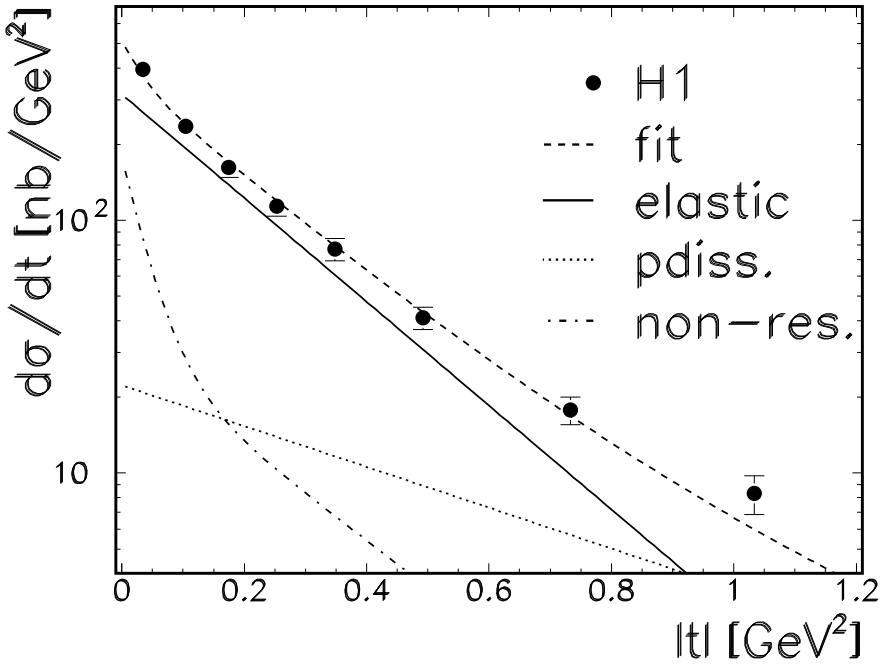

Figure 1.6: The differential cross section $\frac{d\sigma}{dt}$ for elastic J/ψ photoproduction as a function of $|t|$, integrated over the energy region $40\,\text{GeV} \leq W_{\gamma p} \leq 150\,\text{GeV}$, is shown (from [14]). Only statistical errors are shown. H1 data from 1996 and 1997 are used. The data (points) contain background from proton-dissociative J/ψ photoproduction (dotted line) and non resonant background (dashed dotted line). Together with an exponential slope e^{-bt} for the proton-elastic J/ψ photoproduction (solid line) a fit was performed. The result is $b = (4.73 \pm 0.25^{+0.30}_{-0.39})\,\text{GeV}^{-2}$ for $|t| \leq 1.2\,\text{GeV}^2$, where the first error is statistical and the second is systematic.

1.6 Diffraction in Regge Theory

Within Regge theory [31] total hadronic cross sections can be described over a wide range of centre-of-mass energies. The total cross sections of soft diffractive processes are also described, if in the scattering only momentum and angular momentum are exchanged. In Regge theory the exchanged particle left unspecified in figure 1.2 and figure 1.3 is called a *pomeron*.

In this section it is shown, that Regge theory with the exchange of one pomeron is universally applicable. The rise of the total photoproduction cross section and the rise of the exclusive photoproduction cross sections for the light vector mesons ρ, ω and ϕ (see section 1.5) can be described.

The strong rise of the exclusive photoproduction cross sections for the heavy vector mesons J/ψ and $\psi(2s)$ cannot be described by the exchange of one pomeron. The universal description by one pomeron breaks down and in this approach a second pomeron is necessary to describe J/ψ production. Since the large mass of the vector mesons provides a "hard" scale, this regime is called *hard*, while the regime of the light vector mesons is called *soft*. The second pomeron is called *hard* pomeron.

Referring to the similarity of hadron-hadron scattering and photon-hadron scattering first hadron-hadron scattering is discussed. The theoretical model is afterwards applied to photoproduction at HERA.

1.6.1 Hadron-Hadron Scattering in Regge Theory

For the general two-body scattering process $ab \to cd$ (figure 1.7) the Mandelstam variables can be defined[2]

$$\begin{aligned} s &:= (p_a + p_b)^2 \,, && (1.27)\\ t &:= (p_a - p_c)^2 = (p_b - p_d)^2 \,, && (1.28)\\ u &:= (p_a - p_d)^2 \,, && (1.29)\\ s + u + t &= m_a^2 + m_b^2 + m_c^2 + m_d^2 \,, && (1.30) \end{aligned}$$

where p_i and m_i ($i \in \{a, b, c, d\}$) are the four momenta and masses of the particles. s is the square of the centre-of-mass energy and t is the square of the four-momentum transfer, which particle b absorbs in the process. Because of equation 1.30 only two of the three variables s, t and u are independent. Usually s and t are used as independent variables.

By *crossing* and the assumption of CPT invariance[3] the scattering process $ab \to cd$ can be connected to the scattering process $b\bar{d} \to \bar{a}c$. For this process the square of the centre of mass energy is given by $t = (p_b - p_d)^2$. The different descriptions of the scattering process are denoted by the arrows in figure 1.7. The processes where s or t are the square of the centre of mass energy are called s-channel or t-channel processes respectively. The terminology s-channel exchange and t-channel exchange is explained in figure 1.7. The processes in s-channel and t-channel occupy different regions in the variables s and t. In the case of equal mass scattering[4] $m_0 = m_i$ ($i \in \{a, b, c, d\}$) — includes $m_i \approx 0$ — the physical region for the s-channel [1] is given by

$$s \geq 4m_0^2 \,, \quad t \leq 0 \,, \quad u \leq 0 \,. \qquad (1.31)$$

The t-channel exchange of a particle with mass m and the scattering amplitude A is governed by the following propagator

[2] The variables s and t are already defined in equation 1.1 and equation 1.14 respectively. The definitions are consistent with the definitions in this section.

[3] C: charge conjugation, P: parity inversion, T: time reversal

[4] For the general two body scattering refer to [31].

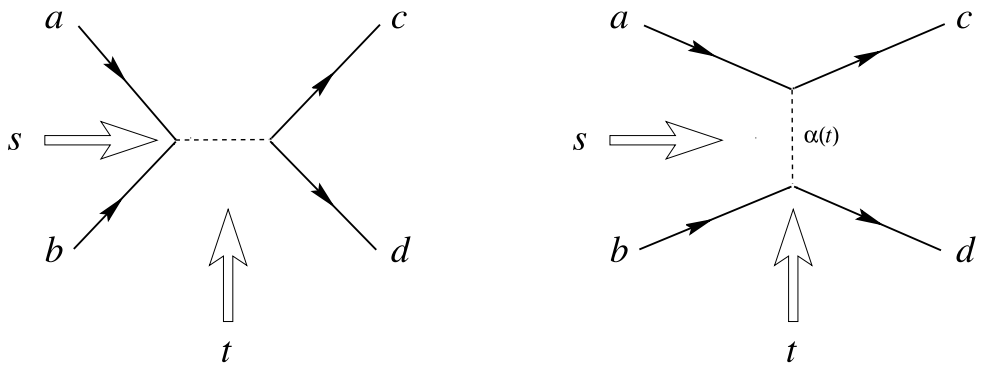

Figure 1.7: The scattering process $ab \to cd$ is mediated by the exchange of a virtual particle with four-momentum q. In case (a) it is $q^2 = (p_a + p_b)^2 = s \geq 0$. The virtual particle is time-like. A resonance in the s-channel is produced. In case (b) it is $q^2 = (p_a - p_c)^2 = t \leq 0$. The virtual particle is space-like. A particle (trajectory $\alpha(t)$ see equation 1.35) is exchanged in the t-channel.

$$A(s,t) \propto \frac{g^2}{t - m^2 \pm i\epsilon}\,, \tag{1.32}$$

where g is the coupling constant describing the strength of the interaction and $\epsilon > 0$ is small.

In Regge theory [32] the exchange of one particle is extended to the exchange of a set of particles with identical quantum numbers, but different angular momentum l and mass m_l. This set of particles is called *Regge trajectory* $\alpha(m_l^2) := l$. The scattering amplitude can be written as a sum of partial waves

$$A(s,t) = \frac{1}{16\pi} \sum_{l=0}^{\infty} (2l+1) A_l(t) P_l(\cos\theta_t)\,, \tag{1.33}$$

where θ_t is the scattering angle in the centre-of-mass system and P_l are the Legendre polynomials. The coefficients $A_l(t)$ are discussed in the following.

Requiring an analytic continuation of the scattering amplitude A into the complex plane of the angular momentum[5] $J = L + S$, the s-channel scattering by exchange of a virtual particle ($t < 0$) is connected to the production of a resonance in the t-channel ($t > 0$). Thus the scattering amplitude of an s-channel exchange can be described by poles in the t-channel, which are characterised by the virtuality $t = m_l^2$ and the spin $\alpha(m_l^2)$. Extending $\alpha(m_l^2)$ from discrete m_l^2 to continuous t, the coefficient $A_l(t)$ near a pole is

$$\lim_{\alpha(t)\to l} A_l(t) = \frac{\beta(t)}{\alpha(t) - l} \quad (l \in \mathbb{N})\,, \tag{1.34}$$

[5] L = angular momentum, S = spin

where the residuals $\beta(t)$ describe the strength of the coupling. In case of integer $\alpha(t)$ the pole is called a *Regge pole*, which can be identified with resonances/particles of mass $m^2 = t$. Only those Regge poles, which have the same quantum numbers as required for the scattering process, contribute to the scattering amplitude. Plotting $\alpha(t)$ versus $m^2 = t$ (see figure 1.8) suggests a linear ansatz for the *Regge trajectory*

$$\alpha(t) = \underbrace{1+\varepsilon}_{=:\alpha_0} + \alpha' t \,, \tag{1.35}$$

where α_0 is the *intercept* and α' the *slope* of the trajectory. $\varepsilon := \alpha_0 - 1$ is a conventional abbreviation. Extrapolating the trajectory to $t < 0$ the scattering in the s-channel can be described. The scattering amplitude is calculated by integration over all poles of the trajectory. In the region $t < 0$ and $s \to \infty$ the partial wave expansion leads to the scattering amplitude of one trajectory

$$A(s,t) \approx \beta(t) s^{\alpha(t)} \,. \tag{1.36}$$

The differential cross section for one trajectory is

$$\frac{\mathrm{d}\sigma}{\mathrm{d}t} \;=\; \frac{1}{16\pi s^2} \left|A(s,t)\right|^2 \;\propto\; s^{2(\alpha(t)-1)} \,. \tag{1.37}$$

In the following the elastic scattering process $ab \to ab$ is considered. Let $\beta_j(t)$ be the strength of the coupling of the Regge trajectory to the particle $j \in \{a, b\}$. Then the amplitude and differential cross section is obtained

$$A(s,t) \approx \beta_a(t)\beta_b(t) s^{\alpha(t)} \,, \tag{1.38}$$

$$\frac{\mathrm{d}\sigma}{\mathrm{d}t} = \frac{1}{16\pi s^2} \left|A(s,t)\right|^2 = \frac{1}{16\pi} \beta_a^2(t)\beta_b^2(t) s^{2(\alpha(t)-1)} \,. \tag{1.39}$$

Experimental data (e.g. figure 1.6) and the analogy to optical diffraction suggest the following exponential ansatz for small $|t|$:

$$\beta^2(t) = \beta_a^2 \beta_b^2 e^{-b_0|t|} \,. \tag{1.40}$$

This leads to the elastic differential cross section for the exchange of one trajectory

$$\frac{\mathrm{d}\sigma_{\mathrm{el}}^{ab}(s,t)}{\mathrm{d}t} \;=\; \frac{1}{16\pi} \beta_a^2 \beta_b^2 s^{2\varepsilon} e^{-(b_0 + 2\alpha' \ln \frac{s}{s_0})|t|} \;\propto\; s^{2\varepsilon} e^{-b(s)|t|} \,, \tag{1.41}$$

with

$$b(s) = b_0 + 2\alpha' \ln \frac{s}{s_0} \,. \tag{1.42}$$

Integration over t leads to the total elastic cross section

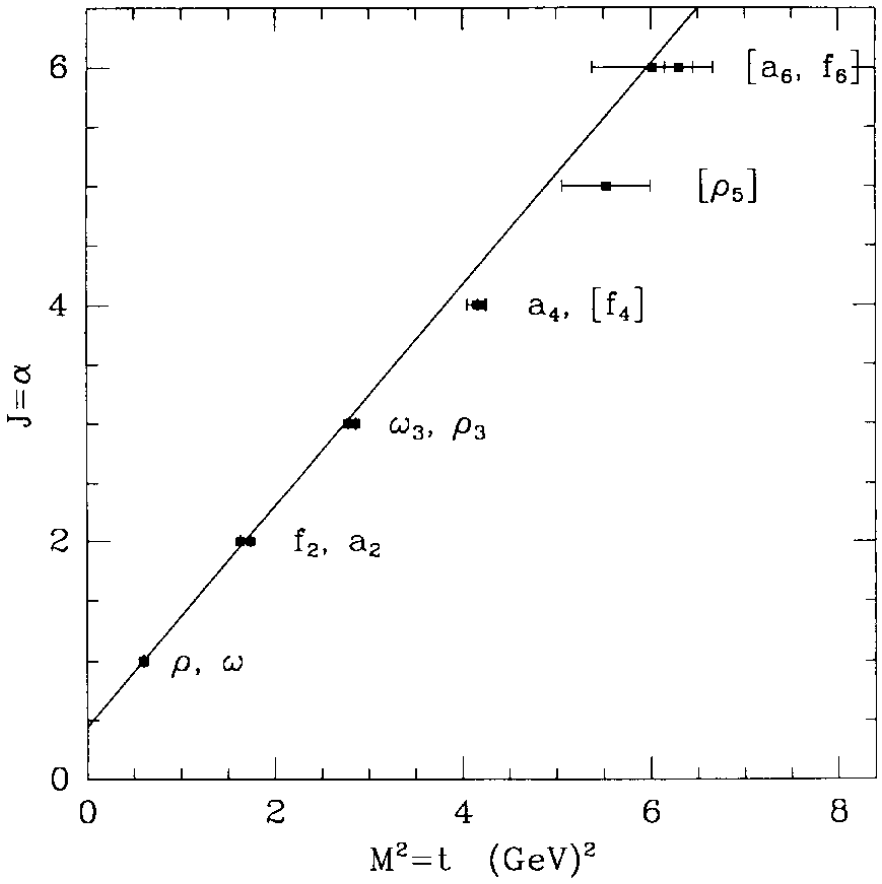

Figure 1.8: For the set of particles ρ, ω, f, a the total angular momentum (spin) is plotted versus the mass squared. This is called a Chew-Frautschi plot [33]. These particles belong to one Regge trajectory, which in section 1.6.3 is associated with reggeon exchange. The line is $\alpha(t) = 0.44 + 0.93 \cdot t$ (from [5]).

$$\sigma_{\mathrm{el}}^{ab}(s) \;=\; \frac{1}{16\pi}\beta_a^2\beta_b^2\frac{s^{2\varepsilon}}{b(s)} \;\propto\; \frac{1}{b(s)}s^{2\varepsilon}\,. \tag{1.43}$$

The total cross section for the exchange of one trajectory is obtained by the optical theorem from the imaginary part of the scattering amplitude at $t = 0$:

$$\sigma_{\mathrm{tot}} \;=\; \frac{1}{s}\Im(A(s,t=0)) \;=\; \frac{1}{16\pi}\beta_a\beta_b s^{\alpha_0-1} \;\propto\; s^{\varepsilon}\,. \tag{1.44}$$

Summarising, Regge theory gives the following predictions:

- The cross sections are proportional to a power of s.
  The intercept α_0 of a Regge trajectory causes the change of the cross section with s. For $\varepsilon > 0$ ($\varepsilon < 0$), i.e. $\alpha_0 > 1$ ($\alpha_0 < 1$), the cross section rises (falls) with increasing s.
- The shape of the differential cross section changes with s.
  The slope of the trajectory α' affects the differential cross section $\frac{\mathrm{d}\sigma}{\mathrm{d}t}$. α' causes the increase of the slope $b(s)$ of the differential cross section $\frac{\mathrm{d}\sigma}{\mathrm{d}t}$ with increasing s. Therefore the forward peak at small $|t|$ becomes narrower for rising s. This effect is called *shrinkage*.

The strong (exponential) drop of the elastic differential cross section $\frac{\mathrm{d}\sigma}{\mathrm{d}t}$ away from the forward direction is characteristic for optical diffraction. Because of this behaviour, the process is called *diffractive*.

Using the analogy to optical diffractive scattering from a black disk the data from pp-scattering can be used to estimate the radius of the proton to be $R_p \approx 1.3$ fm (see [34]), which is comparable to the proton charge radius $R_p = (0.845 \pm 0.05)$ fm [4].

1.6.2 Application to Photoproduction at HERA

In the VDM framework the photoproduction process $\gamma p \to J/\psi p$ is related to the elastic process $J/\psi p \to J/\psi p$. The centre-of-mass energy for this process is $W_{\gamma p}$. Replacing s by ${W_{\gamma p}}^2$ in equations 1.41 and 1.43 the following relations are obtained:

$$\frac{\mathrm{d}\sigma_{\mathrm{el}}^{J/\psi p}(W_{\gamma p},t)}{\mathrm{d}t} \;\propto\; e^{-b(W_{\gamma p})|t|}{W_{\gamma p}}^{4\varepsilon}\,, \tag{1.45}$$

$$\sigma_{\mathrm{el}}^{J/\psi p}(W_{\gamma p}) \;\propto\; \frac{1}{b(W_{\gamma p})}{W_{\gamma p}}^{4\varepsilon}\,, \tag{1.46}$$

$$b(W_{\gamma p}) \;=\; b_0 + 4\alpha' \ln\frac{W_{\gamma p}}{W_{\gamma p\,0}}\,. \tag{1.47}$$

Assuming $\alpha' = 0$ the slope $b(W_{\gamma p})$ becomes independent of $W_{\gamma p}$ and with $\delta := 4\varepsilon$ the following holds approximately

$$\sigma_{\mathrm{el}}^{J/\psi p}(W_{\gamma p}) \;\propto\; {W_{\gamma p}}^{\delta}\,. \tag{1.48}$$

1.6.3 Parameterisation of Donnachie and Landshoff

In section 1.6.1 the total cross section for only one Regge trajectory was given (see equation 1.44). Donnachie and Landshoff [5] assume two trajectories and performed a Regge fit with a sum of two powers for the total cross section

$$\sigma_{\text{tot}} = X s^{\varepsilon} + Y s^{-\eta} \,. \tag{1.49}$$

They used all data on hadronic final states available at that time like cross sections shown in figure 1.4. The result is[6]

$$\varepsilon = 0.0808, \quad \eta = 0.4525 \,. \tag{1.50}$$

The first term (ε-term) in equation 1.49 can be identified as arising from *pomeron* exchange and the second term (η-term) from *reggeon* exchange. The corresponding trajectories are

$$\alpha_{\mathbb{P}}(t) = \alpha^0_{\mathbb{P}} + \alpha'_{\mathbb{P}} \cdot t \quad \text{(pomeron)} \tag{1.51}$$

$$\alpha_{\mathbb{R}}(t) = \alpha^0_{\mathbb{R}} + \alpha'_{\mathbb{R}} \cdot t \quad \text{(reggeon)} \tag{1.52}$$

where the constants $\alpha^0_{\mathbb{P}}(\alpha'_{\mathbb{P}})$ and $\alpha^0_{\mathbb{R}}(\alpha'_{\mathbb{R}})$ are the intercept (slope) of the trajectories. The reggeon exchange can be identified with the exchange of the mesons ρ, ω, f, a (see figure 1.8). From the Chew-Frautschi plot in figure 1.8 the parameters for the Regge trajectory can be obtained:

$$\alpha^0_{\mathbb{R}} = 0.44, \quad \alpha'_{\mathbb{R}} = 0.93\,\text{GeV}^{-2}\,\text{c}^2 \,. \tag{1.53}$$

The contribution from reggeon exchange to the total cross section falls with rising centre-of-mass energy. At high centre-of-mass energies the reggeon exchange is strongly suppressed and can be neglected.

For the pomeron exchange the fit yields [5]

$$\alpha^0_{\mathbb{P}} = 1.08 \,, \quad \alpha'_{\mathbb{P}} = 0.25\,\text{GeV}^{-2}\,\text{c}^2 \,. \tag{1.54}$$

Regge theory thus produces an extremely simple and economical parameterisation of all total cross section data available at the time of [5] (see also figure 1.4).

The correct prediction of the slow rise of the total cross section, see figure 1.5, and the vector meson cross sections for the light vector mesons (ρ, ω, ϕ) in this new kinematic domain is a triumph for the pomeron exchange picture.

The measurement of the strongly rising cross section for the heavy vector mesons (J/ψ, $\psi(2s)$), see figure 1.5, however, does not easily fit into this picture.

[6] In this section values for most of the parameters of the two-pomeron fit, the soft and hard pomeron are presented without errors, since in [5, 19, 35, 36] no errors are provided.

In order to describe the steep rise of the cross section Donnachie and Landshoff introduced a second pomeron trajectory into equation 1.49, which they call "hard" pomeron exchange [19]. The previous pomeron is now called "soft" pomeron. Using HERA data the intercept of the hard pomeron is determined to be

$$\alpha^0_{\mathrm{I\!P}} = 1.418 \pm 0.05\,. \tag{1.55}$$

By fits [35] to the differential cross sections of the early elastic J/ψ photoproduction data the values $0\,\mathrm{GeV}^2$ and $0.2\,\mathrm{GeV}^2$ for the boundaries for the slope of the hard pomeron $\alpha'_{\mathrm{I\!P}}$ are obtained and the following value as a good choice for the slope of the hard pomeron is taken:

$$\alpha'_{\mathrm{I\!P}} = 0.1\,\mathrm{GeV}^{-2}\,\mathrm{c}^2\,. \tag{1.56}$$

Taking both pomerons into account the differential cross section is predicted to be $\frac{\mathrm{d}\sigma}{\mathrm{d}t} = |T(s,t)|^2$, where the amplitude $T(s,t)$ contains a sum over contributions of the hard ($i=0$) and the soft ($i=1$) pomeron [35, 36]:

$$T(s,t) = i \sum_{i=0}^{1} \beta_i(t)\, s^{\alpha_i(t)-1}\, \exp\left[-\frac{1}{2}\pi\,(\alpha_i(t)-1)\right]\,. \tag{1.57}$$

For the pomeron coupling functions $\beta_i(t)$ the following assumptions are made. The pomeron-γ-J/ψ coupling is independent of t and the coupling of the proton to the soft and hard pomeron is proportional to $F_1(t)$, the Dirac elastic form factor of the proton:

$$\beta_i(t) = \beta_{0i}\, F_1(t) \qquad (i \in \{0,1\})\,, \tag{1.58}$$

$$F_1(t) = \frac{4m^2 - 2.79t}{4m^2 - t}\,\frac{1}{(1 - t/0.71)^2}\,. \tag{1.59}$$

Integrating $\frac{\mathrm{d}\sigma}{\mathrm{d}t}$ over t a prediction for the total cross section for $\gamma p \to J/\psi p$ is obtained [37]. This two-pomeron fit to H1 data from [14] and fixed-target data yields [36]

$$\beta_{00} = 0.46 \quad \text{and} \quad \beta_{01} = 5.4\,. \tag{1.60}$$

In figure 1.9 a two-pomeron fit with the contributions of the soft and hard pomeron and their interference is shown. The two pomeron fit, adjusted to relative contributions of the two pomerons, is able to describe the data. The much larger intercept of the hard pomeron compared to the soft pomeron causes the steep rise of the cross section with rising $W_{\gamma p}$ (see equation 1.46).

Though neither pomeron has zero slope, the combined effect of the two pomerons shows almost no shrinkage.

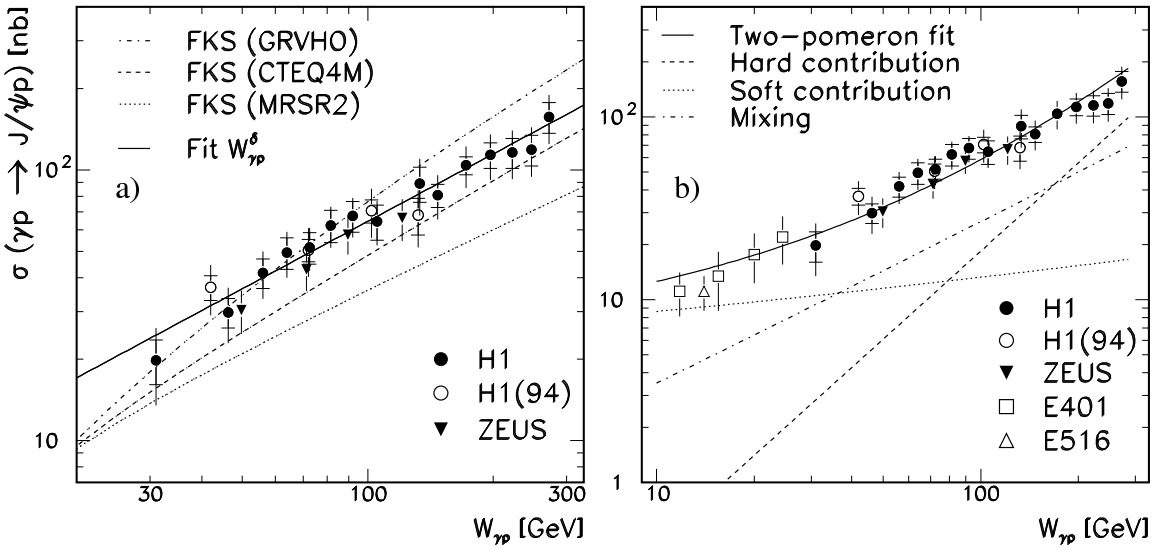

Figure 1.9: The total cross section $\sigma(\gamma p \to J/\psi p)$ versus $W_{\gamma p}$ from [14] and previous results are shown. Data up to the year 1997 were used. The inner and outer error bars show the statistical and total errors, repectively. In figure a) the full line is a fit of the form $\sigma_{\gamma p} \propto {W_{\gamma p}}^{\delta}$ with $\delta = 0.83 \pm 0.07$. The dashed lines are pQCD predictions by Frankfurt et al. [38] using various parameterisations of the gluon density in the proton. In figure b) also results from fixed target experiments are shown. The full line represents a fit of the two-pomeron model by Donnachie and Landshoff. The contributions of the soft and hard pomeron amplitudes were adjusted [19]. The contributions from the hard and soft pomeron and the interference are indicated by the dashed lines. For the two-pomeron model it is characteristic, that the fit has a "concave" shape in the double logarithmic presentation, while the shown QCD predictions in a) have a "convex" shape. New QCD predictions also show "concave" shapes (see figure 9.8).

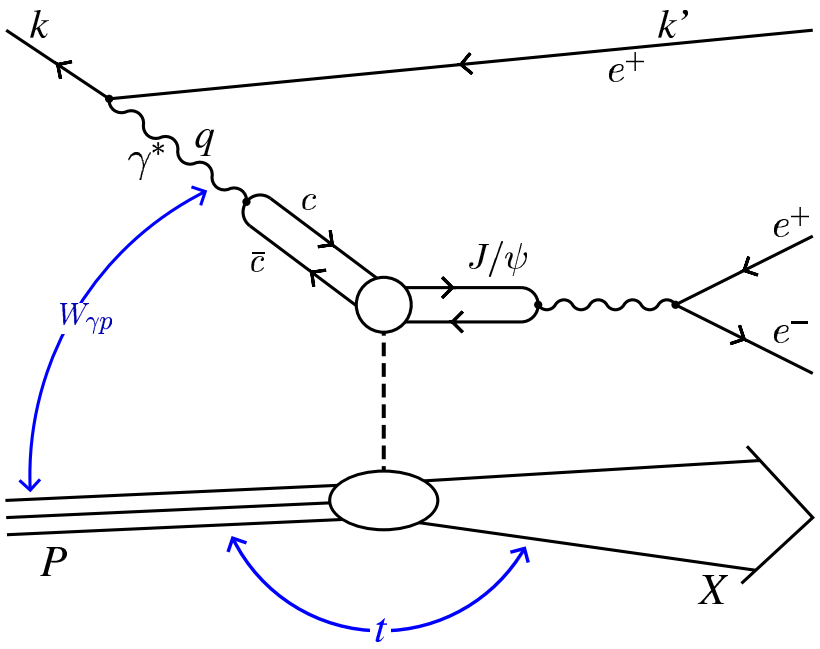

Figure 1.10: In proton-dissociative scattering the proton is excited and dissociates into hadrons. The hadronic system is called X.

1.6.4 Proton-dissociative Vector Meson Production

In proton-dissociative scattering the proton dissociates into hadrons. The hadronic system is called X and its mass is M_X (see figure 1.10). Especially systems with low M_X may not be detected. Therefore the proton-dissociative J/ψ production is a potential background to the proton-elastic J/ψ production. In order to determine this contamination a simulation of proton-dissociative J/ψ production will be used[7], for which the theoretical foundation is laid out here.

In the case of the diffractive scattering process $J/\psi\, p \to J/\psi\, X$, where the proton p dissociates into the hadronic state X, the exchange of one pomeron trajectory leads to the double differential cross section [39]

$$\begin{aligned}\frac{\mathrm{d}^2\sigma^{J/\psi p}_{\mathrm{pdiss}}}{\mathrm{d}t\,\mathrm{d}{M_X}^2} &\propto \frac{\beta_p(0)\beta^2_{J/\psi}(t)}{s^2}\cdot s^{2\varepsilon}\cdot\left(\frac{s}{{M_X}^2}\right)^{2\alpha_{\mathbb{P}}(t)}\cdot\left({M_X}^2\right)^{2\alpha_{\mathbb{P}}(0)} \\ &= \beta_p(0)\cdot\beta^2_{J/\psi}(t)\cdot s^{2\varepsilon}\cdot\frac{e^{-b_{\mathrm{pdiss}}(s)|t|}}{{M_X}^{2(1+\varepsilon)}}\,, \end{aligned} \tag{1.61}$$

where β_p and $\beta_{J/\psi}$ describe the couplings of the pomeron to the proton and the J/ψ meson and

$$b_{\mathrm{pdiss}}(s) = 2b_{\mathrm{pdiss},0} + 2\alpha'_{\mathbb{P}}\ln\frac{s}{{M_X}^2}\,. \tag{1.62}$$

[7] see chapter 5 and section 8.5

Applying this in analogy to section 1.6.2 to proton-dissociative J/ψ photoproduction at HERA with $s = {W_{\gamma p}}^2$ leads to:

$$\frac{\mathrm{d}^2\sigma^{J/\psi p}_{\mathrm{pdiss}}(W_{\gamma p}, t)}{\mathrm{d}t\,\mathrm{d}{M_X}^2} \propto e^{-b_{\mathrm{pdiss}}(W_{\gamma p})|t|}\,{W_{\gamma p}}^{4\varepsilon}\,\frac{1}{{M_X}^{2(1+\varepsilon)}}\,, \tag{1.63}$$

$$b_{\mathrm{pdiss}}(W_{\gamma p}) = b_{\mathrm{pdiss},0} + 4\alpha' \ln\frac{W_{\gamma p}}{M_X}\,. \tag{1.64}$$

- In first approximation the proton-dissociative cross section shows the same $W_{\gamma p}$ dependence as the proton-elastic cross section: $\propto {W_{\gamma p}}^{4\varepsilon}$.
- The proton-dissociative cross section has a similar t dependence as the proton-elastic cross section: $\propto e^{-b_{\mathrm{pdiss}}(W_{\gamma p})|t|}$, however $b_{\mathrm{pdiss}} \neq b_{\mathrm{el}}$.
- The $W_{\gamma p}$ dependence of the slope b_{pdiss} is the same logarithmic dependence as for the proton-elastic case, but the slope decreases logarithmically with increasing M_X.
- At fixed $W_{\gamma p}$ and t the cross section is $\propto \frac{1}{{M_X}^{2(1+\varepsilon)}} \approx \frac{1}{{M_X}^2}$.

1.7 Perturbative QCD

In perturbative QCD (pQCD) the reaction $\gamma^\star p \to Vp$ is viewed as a three step process (see figure 1.11):

- The virtual photon $\gamma^\star$ fluctuates into a $q\bar{q}$ pair.
- The $q\bar{q}$ pair scatters off the proton exchanging a colourless object. This object can be described to leading order in QCD by a colour singlet two-gluon system, more generally a gluon ladder. [8]
- The $q\bar{q}$ pair forms a vector meson.

Perturbative QCD is only applicable, if a sufficiently large scale is present. Experimental data from J/ψ production and the production of the light vector mesons ρ and ϕ [15, 16] suggest, that any of the following scales is sufficient to cause "hard" behaviour of the cross section:

- the photon virtuality $Q^2 >> \Lambda^2_{\mathrm{QCD}}$,
- the mass of the vector meson $m_V^2 >> \Lambda^2_{\mathrm{QCD}}$ or

[8] Meson exchange is already excluded because of high centre-of-mass energies, cf. reggeon exchange in section 1.6.3.

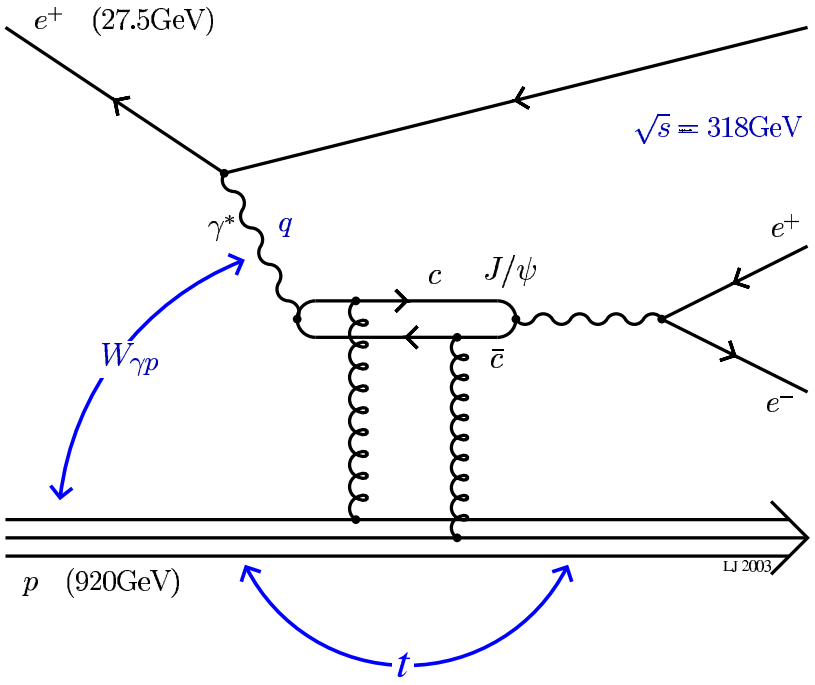

Figure 1.11: Feynman diagram of the J/ψ photoproduction in the pQCD picture.

- the four-momentum transfer squared at the proton vertex $t >> \Lambda^2_{\mathrm{QCD}}$.

Λ_{QCD} characterises the energy scale at which the strong coupling constant α_{s} becomes large. At large energy scale $>> \Lambda_{\mathrm{QCD}}$ the coupling between quarks and gluons is small, $\alpha_{\mathrm{s}} \to 0$ and perturbative methods can be applied.

The coupling of the two gluons to the $q\bar{q}$ fluctuation can then be treated reliably within pQCD. Since in this analysis the vector meson is produced in photoproduction ($Q^2 \approx 0$) and $|t| \leq 1\,\mathrm{GeV}^2$ the hard scale is provided by the mass of the vector meson $m^2_{J/\psi} \approx 10\,\mathrm{GeV}^2$.

The relevant calculations [8, 9, 10] were carried out in leading order of $\alpha_S \ln\left(Q^2/\Lambda^2_{\mathrm{QCD}}\right)$. The prediction for the forward differential cross section is

$$\left.\frac{\mathrm{d}\sigma^{\gamma^\star p}}{\mathrm{d}t}\right|_{t=0} = \frac{12\pi^3\Gamma_{ee}m_V^3}{\alpha_{em}(Q^2+4m_c^2)^4}\left|\alpha_S(\tilde{Q}^2)\left(1+\frac{i\pi}{2}\frac{\mathrm{d}}{\mathrm{d}\ln x}\right)x_{\mathrm{g}}\,g(x_{\mathrm{g}},\tilde{Q}^2)\right|^2\cdot\left(1+\varepsilon_{\mathcal{F}}\frac{Q^2}{m_V^2}\right)\mathcal{C}(Q^2) \tag{1.65}$$

where α_{em} and α_S are the electromagnetic and strong coupling constants. $g(x_{\mathrm{g}},\tilde{Q}^2)$ is the density of the gluons in the proton and m_c is the mass of the charm quark. $\varepsilon_{\mathcal{F}}$ is the flux ratio of the longitudinal to transversely polarised incoming virtual photons (see equation 1.19) which in the case of photoproduction ($y \approx 0$, see equation 1.7) is close to 1. $\mathcal{C}(Q^2)$ is determined from the vector meson wave function.

$$x_{\mathrm{g}} \approx \frac{Q^2+m_V^2}{{W_{\gamma p}}^2} \tag{1.66}$$

is the momentum fraction carried by the gluon. The coupling of the vector meson wave function to the photon is encoded in the electronic width Γ_{ee}. The effective scale is given by $\tilde{Q}^2 := (Q^2 + m_V^2)/4 \gg \Lambda_{\mathrm{QCD}}$.

In oder to predict the total elastic cross section from the forward elastic differential cross section, the t dependence has to be known. An exponential form $\exp(-b|t|)$ is assumed, with an experimentally measured slope parameter b [40, 41]. As pQCD neither predicts the exponential form nor its parameter, no statement about shrinkage can be made. The total elastic cross section is

$$\sigma^{\gamma^\star p} = \frac{1}{b} \frac{\mathrm{d}\sigma^{\gamma^\star p}}{\mathrm{d}t}\bigg|_{t=0} . \tag{1.67}$$

In the photoproduction regime at high $W_{\gamma p}$ equation 1.66 and 1.65 lead to

$$\sigma^{\gamma^\star p} \sim \Big(x_{\mathrm{g}}\, g(x_{\mathrm{g}}, \tilde{Q}^2)\Big)^2 \quad \text{with} \quad x_{\mathrm{g}} \propto \frac{1}{{W_{\gamma p}}^2} . \tag{1.68}$$

The steep rise of the cross section with rising $W_{\gamma p}$ can therefore be connected with the dramatic increase of the gluon density $g(x_{\mathrm{g}}, \tilde{Q}^2)$ towards small x_{g}, which was measured at HERA by the strong rise [17, 18] of the proton structure function F_2 towards low values of the Bjorken variable x_{B}. Figure 1.9 compares pQCD predictions with HERA data.

Chapter 2

The H1 Detector at HERA

The H1 detector is operated at the HERA facility at the German research centre DESY (Deutsches Elektronen-Synchroton) in Hamburg. In this chapter first an overview of the HERA collider is presented. Then the H1 detector is described with emphasis on the components, which are important for this analysis.

2.1 The HERA Collider

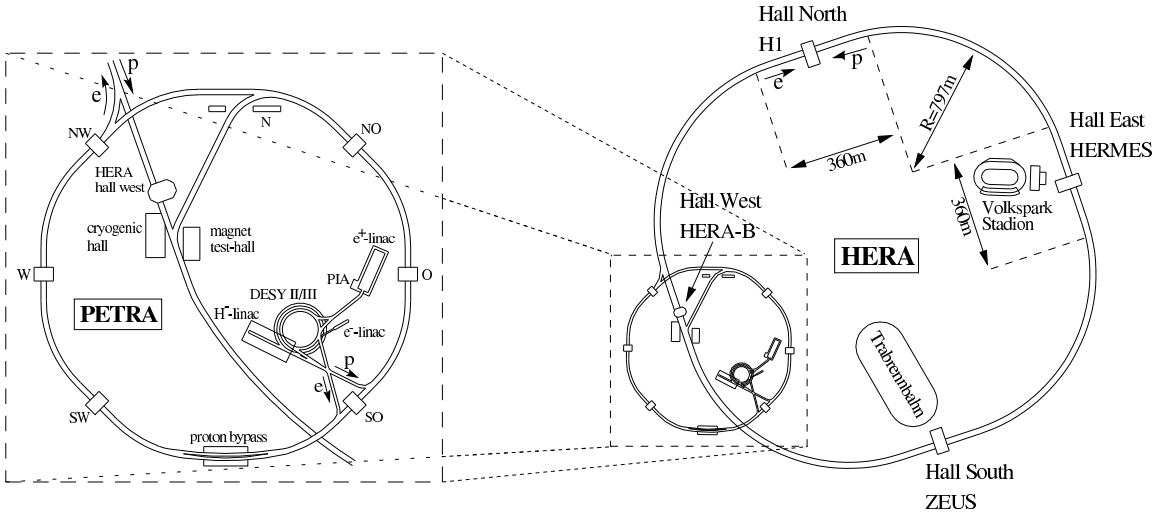

Figure 2.1: The electron proton storage ring facility HERA is shown on the right hand side. An enlarged view of the pre-accelerators is presented in the dashed box on the left hand side.

The HERA-collider ("Hadron-Elektron-Ring-Anlage") (see figure 2.1) consists of two storage rings with a circumference of 6.3 km for electrons[1] of 27.5 GeV and protons of 920 GeV [2]. At HERA there are four interaction regions for experiments: At H1

[1] The nomenclature electron is used for both electrons and positrons.

in hall north and ZEUS in hall south the electron and proton beams are brought to collision; HERA-B and HERMES are fixed target experiments. HERA-B uses only the halo of the proton beam and HERMES the electron beam.

The particles are accelerated to the collision energies in a multi step process. Pre-accelerators (LINAC, DESYIII, PETRA) bring the electrons and protons to energies of 12 GeV and 40 GeV, respectively. With these energies they are injected into the HERA storage rings where they are accelerated to their collision energies.

Beginning from the first acceleration in the linear accelerators (LINAC) the particles are packed in bunches. Proton and electron bunches consist of $2.1 \cdot 10^{13}$ protons and $0.8 \cdot 10^{13}$ electrons, respectively. PETRA ("Positron-Elektron-Tandem-Ring-Anlage") can hold up to 70 bunches. Three PETRA fills with protons and three PETRA fills with electrons are needed to fill 210 bunches in HERA. HERA has in total 220 bunch places. Taking the 220 bunch places and the circumference of 6336 m into account the resulting frequency of proton-electron bunch collisions (*bunch crossing*) is 10.4 MHz, which corresponds to a bunch crossing time (BC) of 96 ns [42, 43]. Bunch crossings where the corresponding other bunch position is not filled are called *pilot bunch* crossings. These are important for the study of background. The spatial size of the electron and proton bunches are: $\sigma_x^e \approx 280\ \mu$m, $\sigma_y^e \approx 60\ \mu$m, $\sigma_z^e \approx 1$ cm, $\sigma_x^p \approx 180\ \mu$m, $\sigma_y^p \approx 60\ \mu$m, $\sigma_z^p \approx 11$ cm. Typical beam currents are shown in figure 2.2. The design luminosity is $1.5 \cdot 10^{31}$ cm^{-2} s^{-1}.

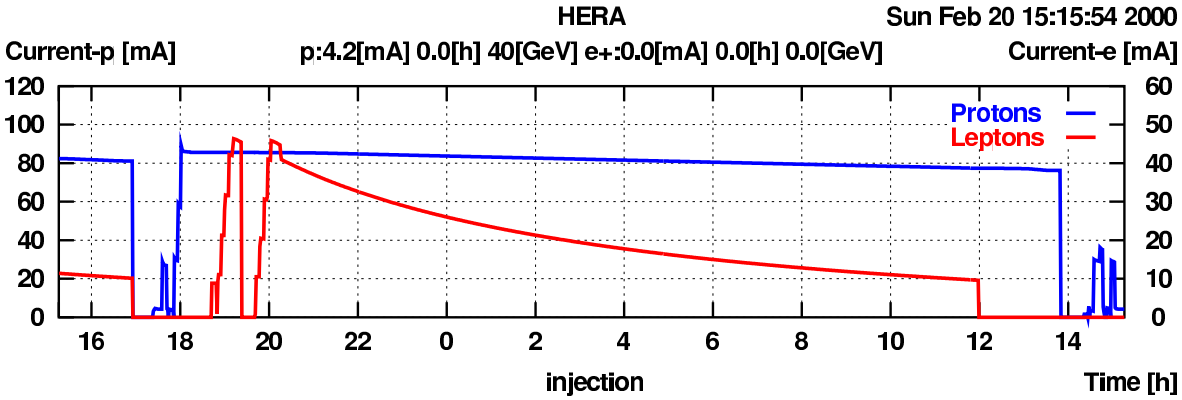

Figure 2.2: Typical electron and proton beam currents are shown. The strong decrease of the electron current during the fill is caused by synchrotron radiation.

While the electron beam energy is limited by the energy loss due to synchrotron radiation, the strength of the magnetic field of approximately 5 T of the superconducting magnets of the proton ring sets the limit for the proton beam energy. In machine studies it was demonstrated, that the superconducting coils for the proton beam can safely operate with a current 10% above design. In 1998 the proton beam energy was thus increased from the original value of 820 GeV to 920 GeV. This correspondingly increased the centre-of-mass energy from 300 GeV to 320 GeV.

A period of data taking with the same fill of electrons and protons is called a *luminosity fill* and lasts $\approx$ 12 hours (see figure 2.2). A time period of experimentally stable running

conditions is called a *run*. Runs can take from minutes to several hours, but are usually not longer than two hours.

2.2 The H1 Detector

The H1 detector [42, 43] is designed as a general purpose detector to study high energy interactions of electrons and protons at HERA.

The H1 experiment is arranged cylindrically symmetric around the beam axis (see figure 2.3). The origin of the H1 coordinate system is at the nominal interaction point. The z-axis is pointing in the direction of flight of the incoming protons and the y-axis is pointing vertically upwards. The definition of the polar angle θ and azimuthal angle ϕ is shown in figure 2.3. The positive (negative) z-direction are called *forward* (*backward*). The region around the interaction point is referred to as the *central* region.

Due to the imbalance of the energy of the beam electrons and beam protons the centre-of-mass system is boosted in positive z-direction with respect to the laboratory system. Therefore the H1 detector has different instrumentation in the forward/backward region.

Starting at the nominal interaction point and proceeding outwards the H1 detector is build up from following detector components. Detector components important for this analysis are highlighted in bold font:

- tracking system
  - central (CST) and **backward silicon tracker** (BST)
  - **central** and forward **tracking chambers**
  - **backward drift chamber**
- calorimetry
  - **Liquid-Argon (LAr) calorimeter**
  - **backward spaghetti calorimeter** (SpaCal)
- superconducting coil with uniform solenoidal magnetic field of 1.2 T
- muon system
  - central muon system included in the iron return yoke
  - **forward muon detector** in a toroidal magnetic field
- **proton remnant tagger** in the very forward region
- time of flight systems
- luminosity detectors.

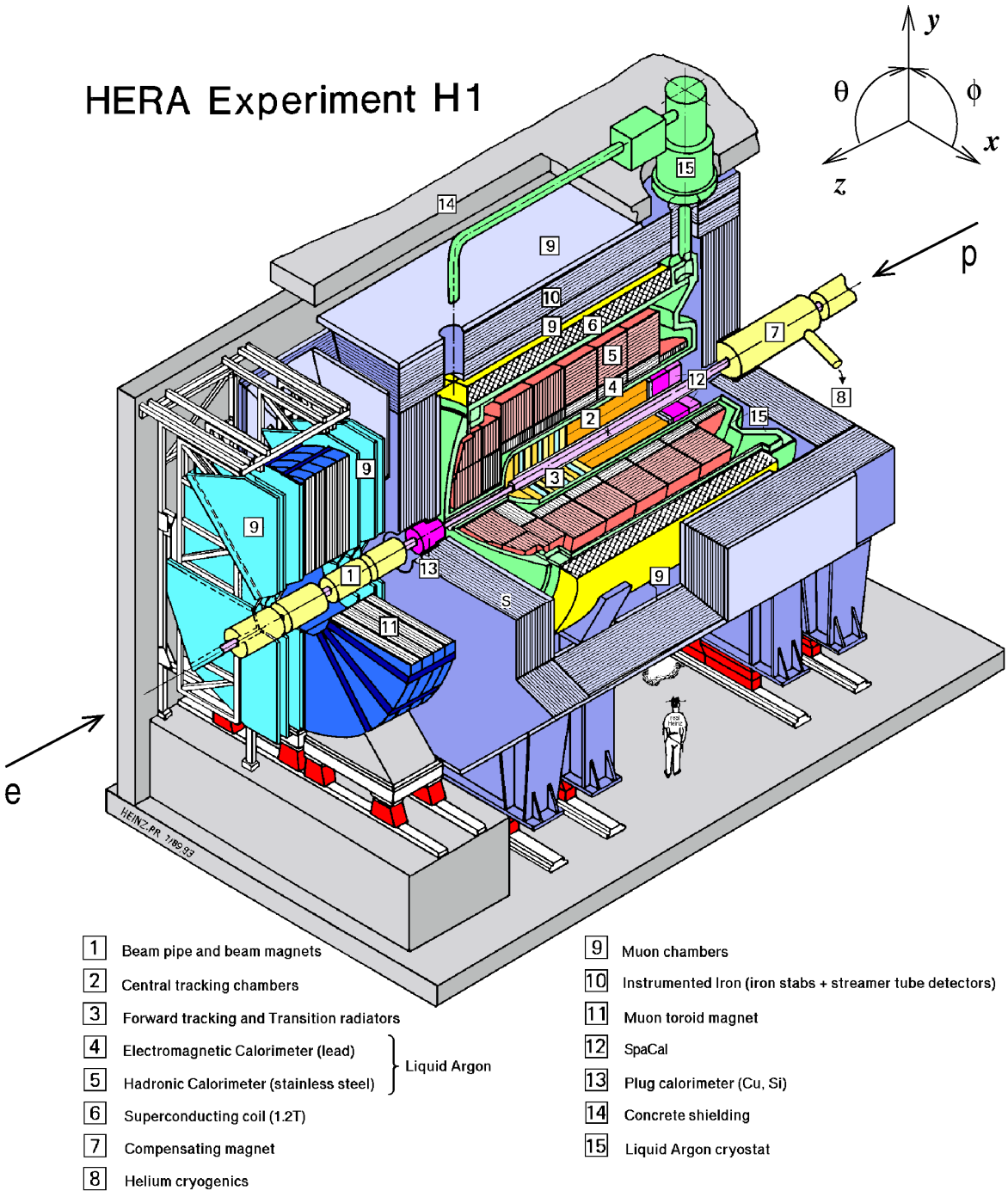

Figure 2.3: Schematic view of the H1 detector and the H1 coordinate system

In the following special emphasis is put on parts of the H1 detector which are essential for the analysis presented here. A detailed description of the H1 detector can be found in [42, 43].

2.2.1 Tracking System

Two technologies are used in the H1 tracking system. Close to the beam pipe silicon strip detectors are deployed. The large volume part of the system is realised as proportional chambers. An overview is given in figure 2.4.

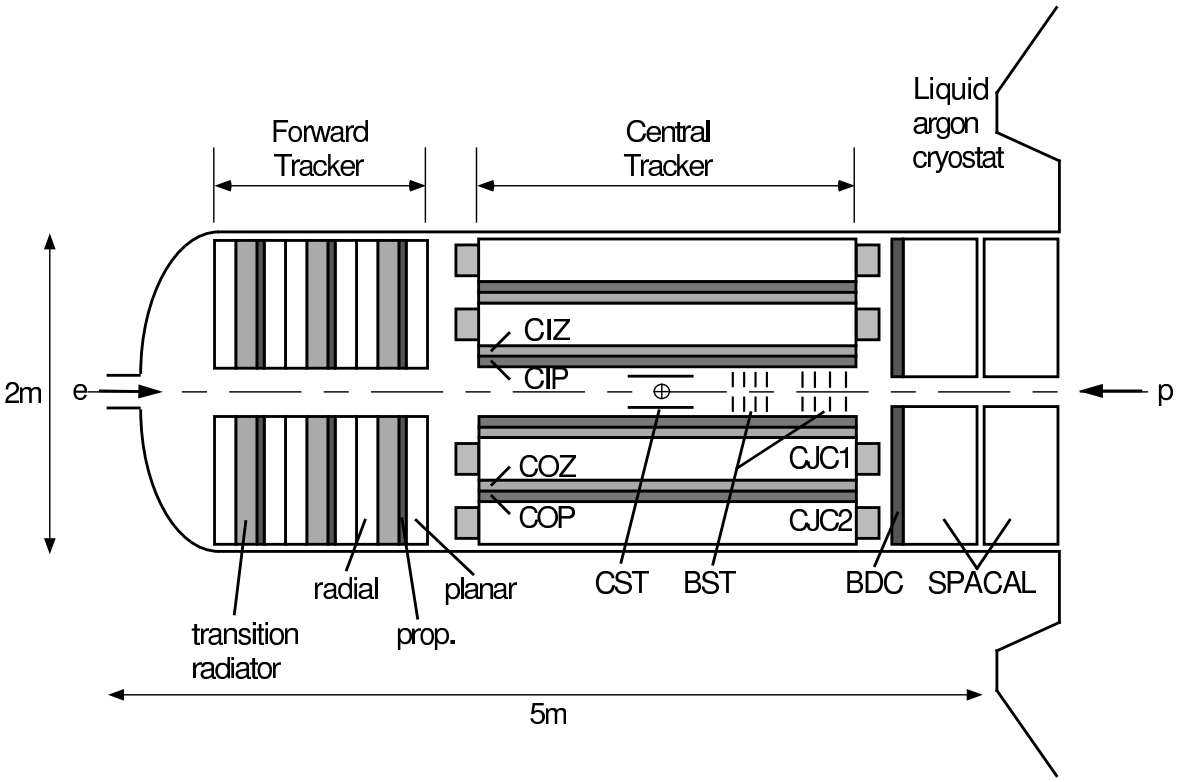

Figure 2.4: Side view of the H1 tracking system. For the abbreviations refer to the table.

CST	central silicon tracker	CIZ	central inner z-chamber
BST	backward silicon tracker	COZ	central outer z-chamber
CJC1	central jet chamber 1	CIP	central inner proportional chamber
CJC2	central jet chamber 2	COP	central outer proportional chamber
BDC	backward drift chamber	SpaCal	backward spaghetti calorimeter

2.2.1.1 Central Silicon Tracker

The central silicon tracker (CST) [44, 45] surrounds the beam pipe in the region around the nominal interaction point. It has an active length of 35.6 cm along the z-axis, which

corresponds to a covered range in the polar angle of $29° < \theta < 151°$. The silicon strip detectors are arranged at radii of 5.75 cm and 9.75 cm parallel to the z-axis. The main purpose of the CST is to measure secondary vertices. A resolution of 57 μm is achieved. Because of multiple scattering it is very important to keep the amount of material in front of the other detectors small. The CST adds only 1.4% of a radiation length.

2.2.1.2 Backward Silicon Tracker

The *backward silicon tracker* (BST) [46, 47] is located in the backward region of the H1 detector in front of the backward drift chamber BDC and the calorimeter SpaCal (see figure 2.4). It covers the range in polar angle of $165° < \theta < 175°$.

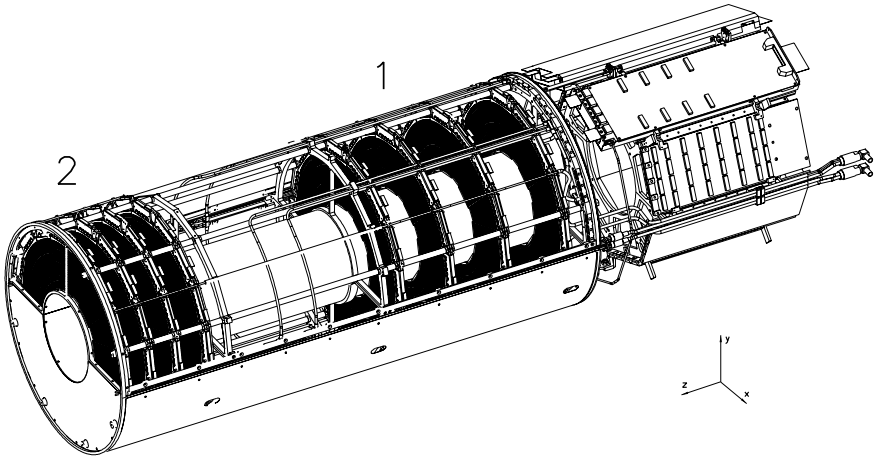

Figure 2.5: A schematic view of the BST II detector: The four planes at '1' are from BST I. The four planes at '2' are the four new planes of BST II (figure from [48]).

The BST consists of planes of silicon detectors which are arranged perpendicular to the beam axis (see figure 2.5). Originally the BST was installed in 1996 with four planes. This setup is called 'BST I'. In 1998 additional four planes were installed. The eight plane setup is called 'BST II'.

Each of the eight planes is divided in 16 segments in the azimuthal angle ϕ and each of these segments is planned to consist of three different types of detectors. They are a silicon pad detector and two kinds of silicon strip detectors, which have a different orientation of the strips. One orientation is parallel to the radial direction (ϕ-strip detector) and the other is perpendicular to the radial direction (r-strip detector).

The pad detectors are used for triggering, while the r-strip and ϕ-strip detectors are used for the measurement of the position in r and ϕ of the impact points of particles. In 1999/2000 only one sector was equipped with ϕ-strip detectors [48]. Therefore only the r-strip detectors are used in this analysis.

The r-strip detectors contain 1537 strips with radii from 5.24 cm to 12.16 cm. The pitch of the strips is 45 μm. Only every second strip is read out. The strips extend

in ϕ over $2\pi/16$ in order to gain a little overlap with the adjacent sectors. Therefore the sectors are staggered in z when mounted to a plane. With this overlap efficiency checks and alignment are possible.

The BST geometry was optimised in order to obtain a very good resolution in the polar angle θ and to provide the most efficient detection of the scattered electron. With a non-equidistant arrangement in z of the planes the largest possible plateau of the BST polar angle acceptance was reached [46, 49]. The z-positions in cm of the planes are -35.12, -38.46, -42.12, -46.02, -72.46, -79.29, -86.76, -94.92, where the first four positions are the positions of the additional planes of BST II. The BST adds ≈ 1.3 radiation length.

The BST detector is a keystone for this analysis. The rz-hit information allows reconstruction of tracks in the backward region with a resolution in the polar angle θ of $\sigma_\theta \approx 0.03°$. The BST tracks are used to determine vertex positions. In addition the existence of a track provides separation between electrons and photons.

2.2.1.3 Central Tracking Chambers

The central tracking chambers surround the nominal interaction point (see figure 2.4) and cover the range in polar angle $20° < \theta < 160°$. The central tracking chambers are a combination of the following chambers: the central jet chamber 1/2, the central inner/outer z-chamber, the central inner/outer proportional chamber.

The two *central jet chambers* CJC1 and CJC2 contain signal wires, which are parallel to the z-axis. These wires are arranged in rows, which are angled by 30° with respect to the radial direction. The CJC1 (CJC2) contains 30 (60) cells in ϕ (see figure 2.6). Through this arrangement of the rows the ionisation electrons of high energetic tracks drift almost perpendicular to these rows due to the magnetic field. In addition ambiguities are avoided. The CJC1 and CJC2 measure the projection of the tracks on the $r\phi$ (xy) plane with a spatial hit resolution in the $r\phi$ plane of $\sigma_{r\phi} = 170$ μm and a momentum resolution of $\sigma_p/p^2 < 0.01\,\mathrm{GeV}^{-1}$. Information about the z-position can be obtained by charge division with a resolution of about 2 cm.

The *inner* and *outer z-chambers* CIZ and COZ are thin drift chambers and surround the CJC1. The z-chambers consist of circular wires and improve the spatial resolution in z to $\sigma_z \approx 350$ μm.

The inner and outer multi wire *proportional chambers* (CIP, COP) are located at the inner side of CIZ and the outer side of COZ. The CIZ (COZ) consists of 60 (18) segments in the z-direction and of 16 sectors in ϕ. Both are mainly used for triggering purposes (see 4.1.2).

2.2.1.4 Forward Tracking Chambers

The forward tracking system covers the range of $5° < \theta < 25°$. It is build up from 3 super modules. Each of these contain a radial and a planar drift chamber, a proportional chamber (FPC) and a transition radiation tracker.

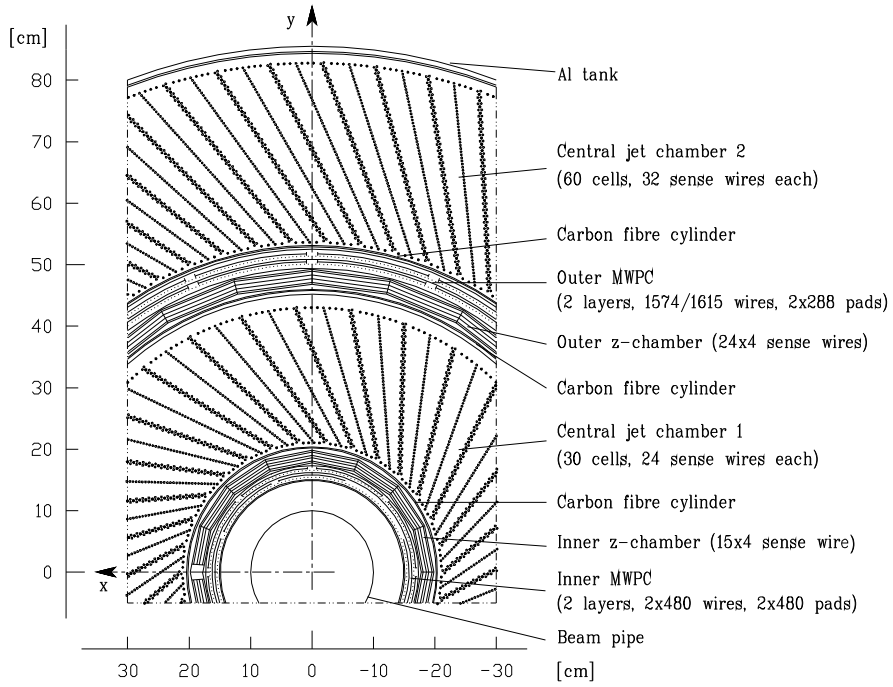

Figure 2.6: Radial view of the central tracking system

2.2.1.5 Backward Drift Chamber

The backward drift chamber (BDC) is located in front of the backward calorimeter SpaCal at $z \approx -142$ cm and covers the range in polar angle of $151° < \theta < 177.5°$ (see figure 2.4). The wires of the BDC are arranged in an octagonal form, which form four double-layers. These layers are rotated by 11.25° with respect to each other (see figure 2.7). The resolution of the track polar angle is $\sigma_\theta = 1.0$ mrad $\approx 0.06°$ with a systematic uncertainty of 0.5 mrad $\approx 0.03°$ [50].

2.2.2 Calorimeters

The H1 detector contains several calorimeters in order to determine the energy of final state particles. The two main calorimeters are the liquid argon calorimeter and the spaghetti calorimeter.

2.2.2.1 Liquid Argon Calorimeter

The liquid argon calorimeter (LAr) surrounds the central tracking system (see figure 2.8) and covers the central and forward region ($4° < \theta < 153°$). In order to have minimal dead material in front of the calorimeter, the LAr calorimeter directly follows the central tracking system, i.e. is placed inside of the superconducting solenoid coil.

The LAr calorimeter is segmented in an inner electromagnetic part and an outer hadronic part. In both parts liquid argon is used as active medium. Liquid argon

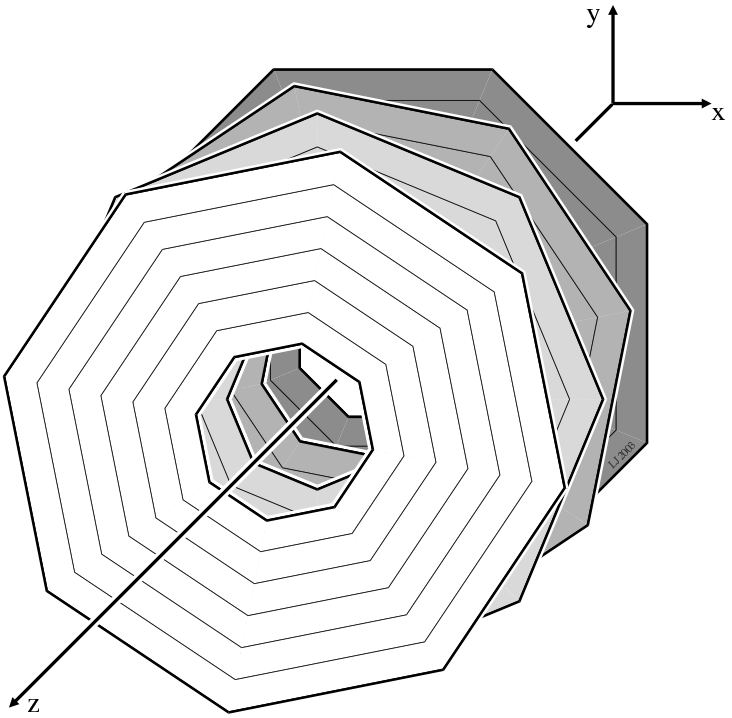

Figure 2.7: The schematic view of the BDC shows the octagonal form of the arrangement of the signal wires and the rotation of the four double-layers.

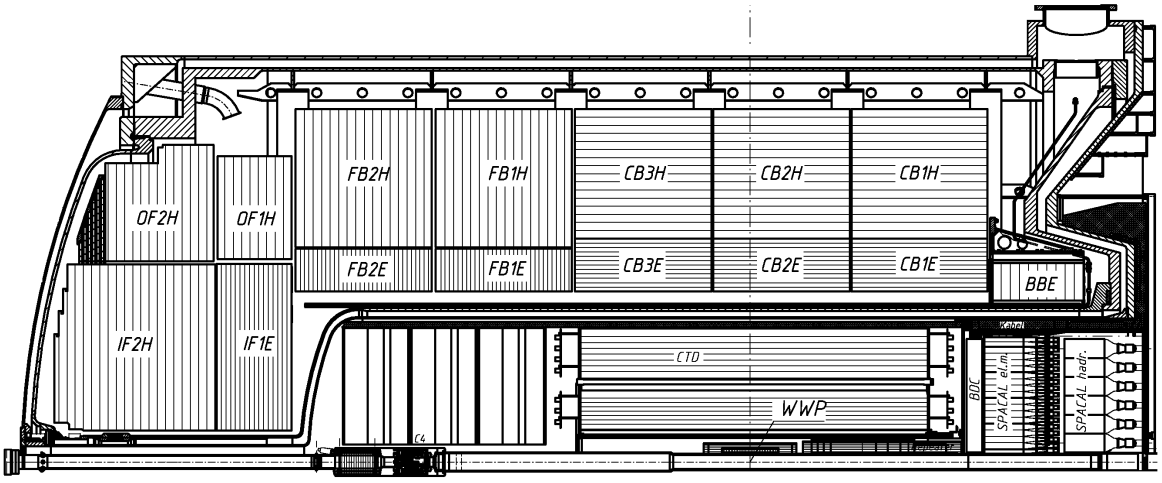

Figure 2.8: The side view of the LAr calorimeter surrounding the forward and central tracking system, the backward drift chamber and the backward calorimeter SpaCal are shown. The calorimeter is structured in an inner (electromagnetic) part (`E`) and an outer (hadronic) part (`H`). In addition there is a segmentations into barrels: inner forward (`IF`), outer forward (`OF`), central barrel (`CB`) and backard barrel electromagnetic (`BBE`).

has high Z nuclei and does not catch electrons from ionisation. In the electromagnetic part 2.3 mm thick lead plates are used as absorbing material, while the hadronic part contains 16 mm steal plates. Lead is chosen because of the high Z of its nuclei. Steal is used because of the mechanical stability. The electromagnetic part amounts to $\approx 20-30$ radiation lengths and the total depth of the calorimeter is $\approx 5-8$ interaction lengths.

The calorimeter is not compensating, i.e. pions with the same energy as electrons give a reduced energy response. The profiles of electromagnetic and hadronic showers have a different shape. The fine segmentation in the electromagnetic and hadronic part — the calorimeter has $\approx 6.5 \cdot 10^4$ channels — allows to distinguish the different showers by the shape and therefore to correct the different energy response. The LAr calorimeter provides a precise measurement of the energy of electrons, photons and hadronic jets. The energy resolution for electromagnetic showers is $\sigma_{\text{em}}(E)/E = 12\%/\sqrt{E/\,\text{GeV}} \oplus 1\%$ and $\sigma_{\text{had}} = 50\%/\sqrt{E_h/\,\text{GeV}} \oplus 2\%$ for hadronic showers[51, 52, 53].

2.2.2.2 Spaghetti Calorimeter

The spaghetti calorimeter (SpaCal) [54] is located in the backward region (see figure 2.4 and figure 2.9) at about $z \leq -150$ cm. The inner radius is 6.5 cm and the outer radius is 80 cm (figure 2.10). This corresponds to an angular acceptance in the polar angle of $153^\circ < \theta < 177.5^\circ$.

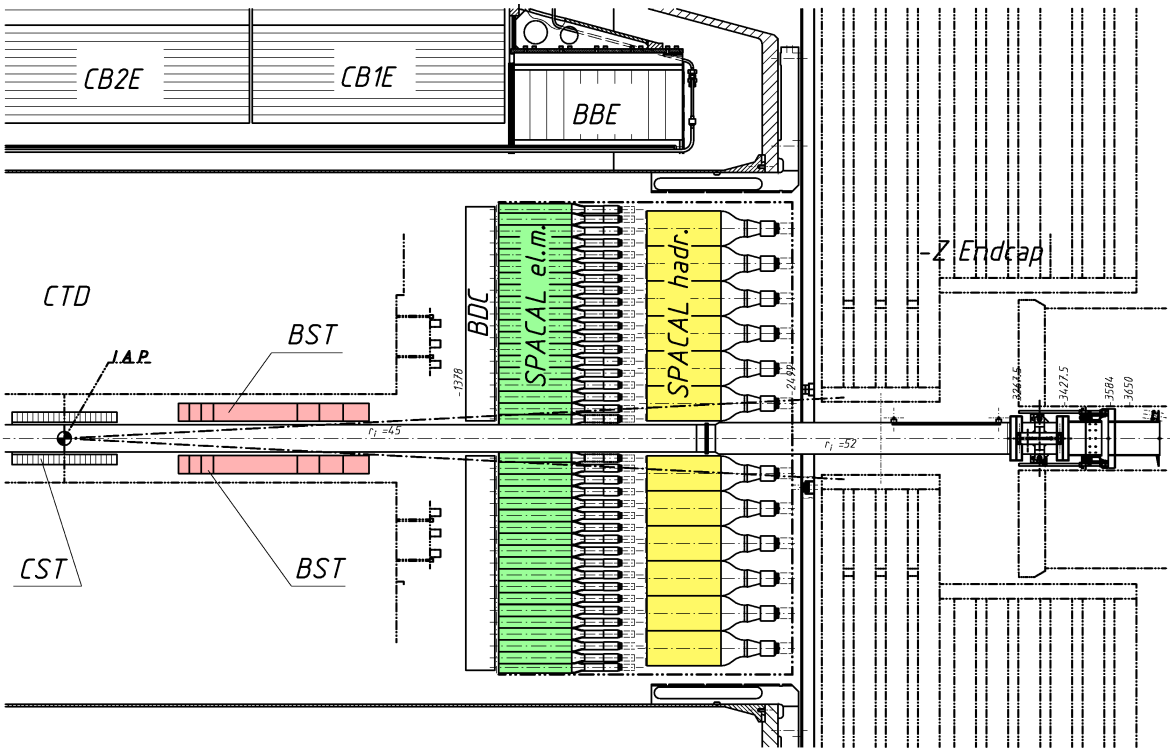

Figure 2.9: The backward region of the H1 detector: backward silicon tracker (BST), backward drift chamber (BDC), spaghetti calorimeter (SpaCal).

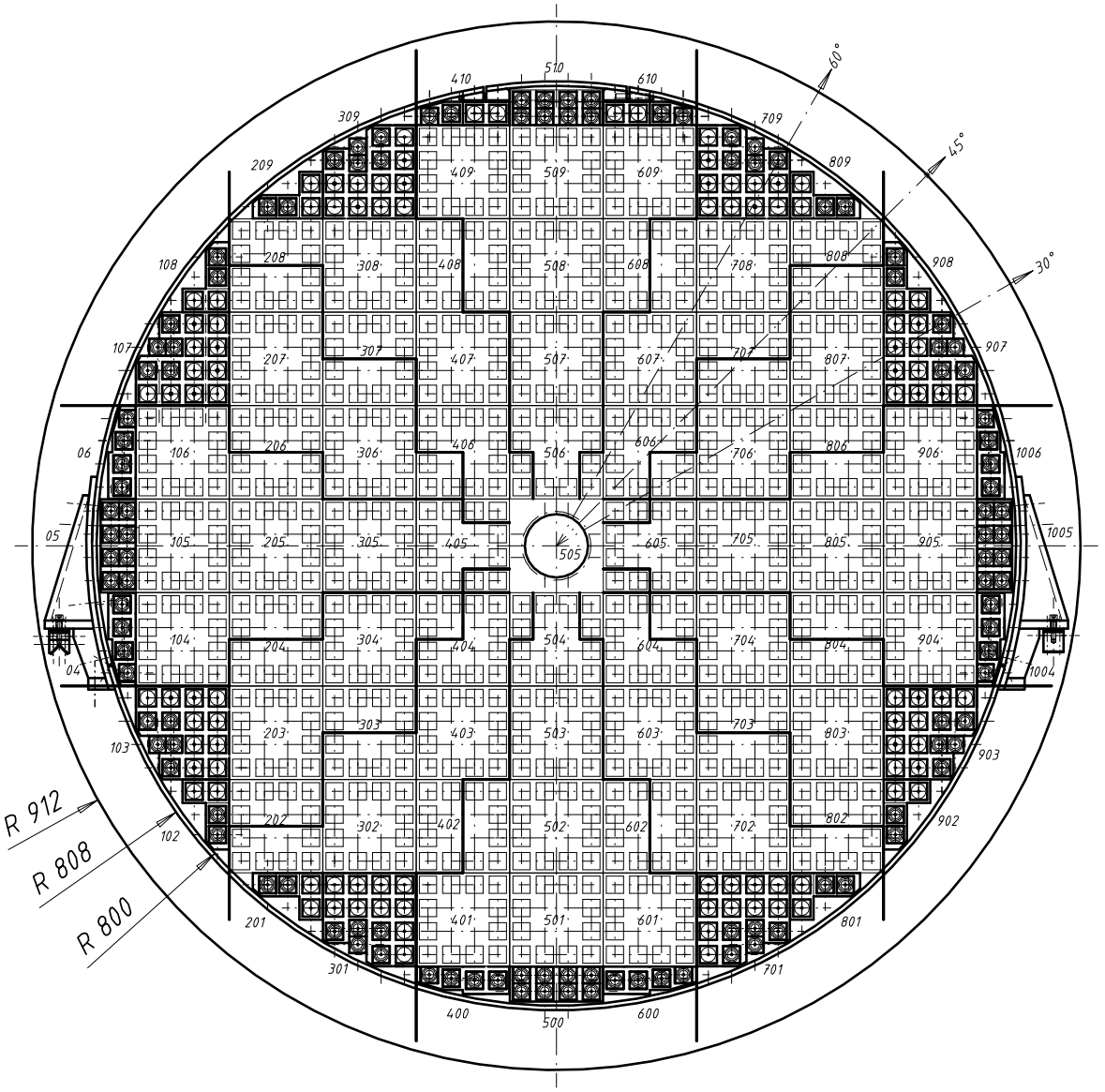

Figure 2.10: r-ϕ-view of the SpaCal

The SpaCal is separated in an electromagnetic part and a hadronic part. Both parts consist of grooved lead plates as absorber with grooves containing scintillating fibres. These spaghetti like fibres gave the calorimeter its name.

The scintillation light is guided by total reflection at both surfaces by the coating of the fibres. From the fibres the light goes to light mixers and then to photomultipliers. Since the energy measurement depends strongly on the photomultiplier gain, it its important to monitor any short-term fluctuations and long term drifts of the gain with a precision of a few per mil. This is done by the light-emitting diode (LED) monitoring system, which consists of LEDs connected by optical fibres to the light mixers and photodiodes. Each LED pulses several photomultipliers and its light output is controlled with a photodiode. Each photomultiplier is tested by two different LEDs. The shortest pulse length has a rise time and a decay time of 10 ns. The monitoring system operates usually at a rate of 1 Hz [54, 55].

The electromagnetic section is built up from cells with a cross section of 40.5×40.5 mm^2 in the xy-view matching the Molière radius of 25.5 mm. This allows good electron-pion separation and good position resolution. Taking the lateral dimensions of hadronic showers into account the cell cross section in the hadronic part is 119.3×119.0 mm^2.

The smallest mechanical unit of the electromagnetic section are 2-cell modules. These 2-cell modules are combined to square 16-cell modules, which are the main building blocks of the electromagnetic section. Due to the lead-fibre structure, the signal can depend on the orientation of the absorber plates. This effect is called *channeling* and causes the worsening of the energy resolution. The 2-cell modules are combined to 16-cell modules depending on the position of the 16-cell module so that different horizontal or vertical orientations of the lead plates are achieved. This minimises channelling.

Due to the round shape of the SpaCal it is not entirely built out of 16-cell modules. At the outer boarder the modules are reduced in size accordingly. The central module of the electromagnetic section around the beam pipe — the insert module — is also adapted in shape (figure 2.11). It contains 16 cells, where the four 8 mm thick cells surrounding the beam pipe, are called veto layer cells. With these veto layer cells energy leakage into the beam pipe can be determined. The outer radius of the veto layer cells is 65 mm and corresponds to $\theta \approx 177.5°$. A tantalum shielding protects the active detector elements from synchrotron radiation.

The electromagnetic and the hadronic part differ in the thickness of the lead plates and the diameter of the fibres. The electromagnetic section has 0.78 mm thick lead plates and fibres with a diameter of 0.5 mm. The hadronic part consist of 1.9 mm thick lead plates and fibres with a diameter of 1 mm. This causes different a lead-to-fibre ratios of 2.3 : 1 by volume for the electromagnetic part and of 3.1 : 1 for the hadronic part. The lead-to-fibre ratios are a compromise between improving the sampling term and a more compact calorimeter.

The 250 mm thick electromagnetic section corresponds to 28 radiation length. The energy leakage for 30 GeV electron showers is negligible. The hadronic part adds 1.02 interaction lengths to the 1.0 interactions length of the electromagnetic section.

The spatial resolution for electrons is $\sigma_{xy} = (4.4 \pm 0.4)\ \text{mm}/\sqrt{E/\,\text{GeV}} + (1.0 \pm 0.2)\ \text{mm}$,

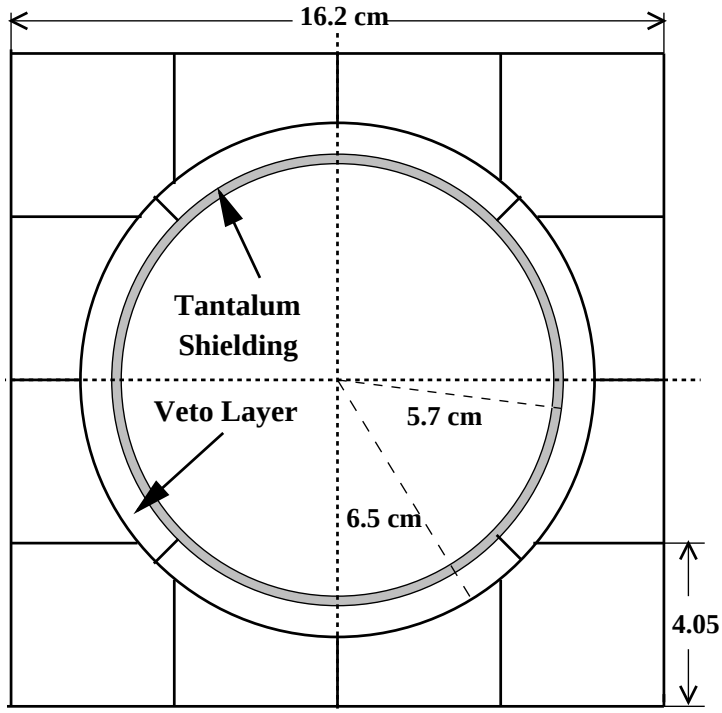

Figure 2.11: SpaCal: $r-\phi$-view of the insert module

which results in a resolution for the polar angle $\sigma_\theta \leq 2$ mrad $\approx 0.1°$.

Due to the small fibre diameter in the electromagnetic part a high sampling frequency is obtained, which gives an energy resolution of $\sigma_{\text{em}}(E)/E = 7\%/\sqrt{E(\,\text{GeV})} \oplus 1\%$. The energy resolution of the hadronic part is $\sigma_{\text{had}}(E)/E \approx 29\%/(E/\,\text{GeV})$ [56, 57]. The time resolution is (0.38 ± 0.03) ns.

2.2.3 Muon System

The H1 experiment contains two systems of muon detectors: the central muon detector and the forward muon detector.

2.2.3.1 Central Muon Detector

The *central muon detector* (CMD) is part of the instrumented iron yoke, which guides the magnetic field of the main solenoidal coil. It covers the polar angle $4° < \theta < 175°$ and is used to detect muons with $E_\mu > 1.2\,\text{GeV}$.

2.2.3.2 Forward Muon Detector

The *forward muon detector* (FMD) consists of a toroidal magnet and three double-layer drift chambers in front of and behind the magnet (see figure 2.12). The geometrical acceptance is $4° < \theta < 17°$.

Usually the FMD [58, 59, 60] is used for the measurement of high energetic muons ($p_\mu > 5\,\mathrm{GeV}$) in the forward region.

In this analysis the FMD is not used in order to detect muons, but to distinguish between proton-elastic and proton-dissociative events. The hadrons produced in a proton-dissociative event interact with the beam pipe and cause the production of secondary particles. These secondary particles are detected in the FMD. The sensitivity of the FMD to proton-dissociative events extends far beyond the geometrical acceptance to low polar angles $\theta \approx 0.15°$ [61]. Since the drift chambers behind the toroidal magnet are affected by synchrotron radiation, only the three drift chambers in front of the magnet are used in order to tag proton-dissociative events.

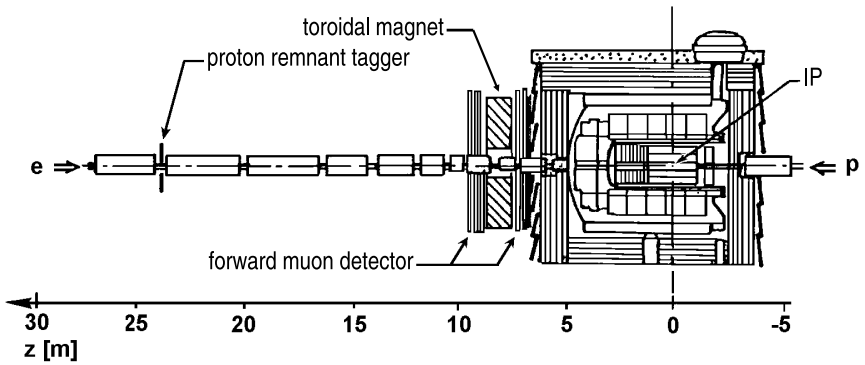

Figure 2.12: The positions of the forward muon detectors and the proton remnant tagger.

2.2.4 Proton Remnant Tagger

The proton-remnant-tagger (PRT) [62] is located at $z = 24$ m and consists of seven double-layer plastic scintillators (see figure 2.13), which are operated in coincidence. The PRT covers the polar angle $0.06° < \theta < 0.25°$ and is used to detect the products of proton-breakup or the scattered proton itself. In this analysis the PRT is used to distinguish between proton-elastic and proton-dissociative events.

2.2.5 Time of Flight System

The time of flight system consists of several scintillating detectors with high time resolution. In order to introduce the nomenclature, first the purpose of these detectors is described.

One big source of background events are events produced by the interaction of beam particles with e.g. residual gas in the beam pipe. If the interaction position is outside the nominal interaction region the produced particles can have the wrong direction of flight compared to particles coming from the nominal interaction region. To distinguish such particles, detectors with a time resolution of the order of 1 ns measuring the *time of flight* (ToF) are needed. The bunch crossing time defines a time slice for signal

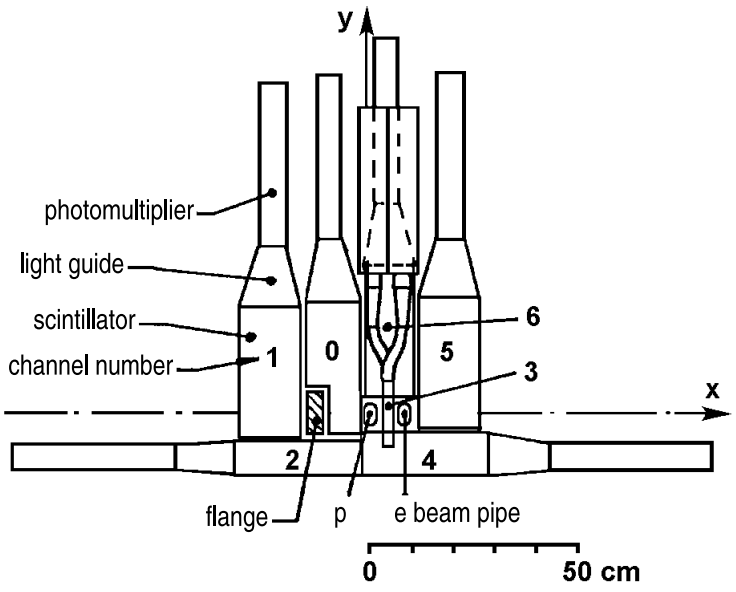

Figure 2.13: The figure shows a schematic xy-view of the proton-remnant-tagger (PRT). In the centre the two beam pipes for the proton and electron beams are marked. The seven double-layer scintillators are connected to photomultiplies with light guides. The numbers in the figure give the channel number of the read out. [62]

events. By checking this time slice with the ToF detectors additional background can be rejected.

The H1 experiment contains the following ToF scintillators:

- The *Forward-ToF* is located at $z = 700$ cm and consists of two layers of scintillators perpendicular to the beam with a size of 20×60 cm^2.
- The *Plug-ToF* is part of the plug calorimeter at $z = 530$ cm. The absorber plates are interleaved with eight layers of scintillators with size 15×15 cm^2.
- The *Forward Interaction Timer* (FIT) is located at $z = 270$ cm. The scintillator extends to $r = 25$ cm.
- The *inner veto wall* is located near the beam at $z = -650$ cm and extends over 100×90 cm^2. The *outer veto wall* is placed at $z = -810$ cm and has a size of 500×400 cm^2.
- The *VLQ-ToF* is part of the "Very Low Q^2" detector (VLQ) at $z = -320$ cm near the beam pipe. The VLQ-ToF consists of two layers of scintillators extending to $r = 16$ cm. The two layers are operated in coincidence [63].

In addition also the SpaCal provides ToF information.

2.2.6 Luminosity System

The *luminosity system* consist of two small calorimeters: the *electron tagger* and the *photon tagger*. The electron tagger is located at $z = -33.4$ m and the photon tagger is located at $z = -102.9$ m (see figure 2.14). The two calorimeters use TlCl and TlBr

crystals as scintillators. The electron tagger has a cross section of 154 mm × 154 mm in the xy-plane and the photon tagger of 100 mm × 100 mm.

The two calorimeters are operated in coincidence in order to detect the electrons and photons produced in the Bethe-Heitler process $ep \to ep\gamma$. This process is used as a reference to determine the luminosity, which depends on the actual beam conditions. The cross section of the Bethe-Heitler process is precisely calculable within quantum electro dynamics (QED). In addition the cross section is large enough to provide sufficient statistics. The luminosity system provides an online (offline) measurement of the relative luminosity with an accuracy of $\approx 5\%\ \mathrm{s}^{-1}$ ($\approx 2\%\ \mathrm{s}^{-1}$). The main background for the luminosity measurement arises from the residual gas in the beam pipe by the process $eA \to eA\gamma$. This background is expected to be 10% of the total $ep \to ep\gamma$ rate and is determined using data from electron pilot bunch events (see section 2.1). Further details of the determination of the luminosity at H1 can be found in [64].

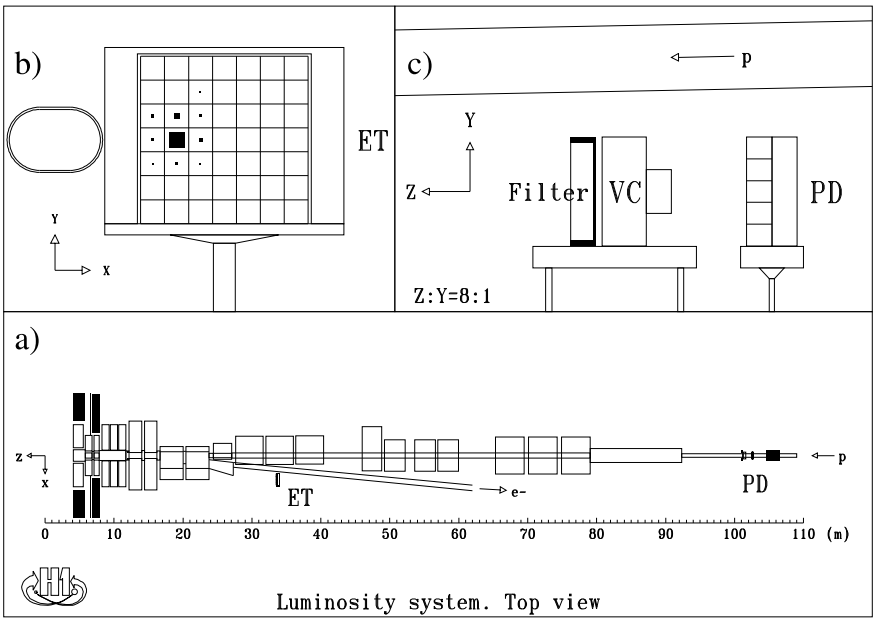

Figure 2.14: a) The position of the electron tagger (ET) and the photon tagger (photon detector = PD) with respect to the nominal interaction point (IP) is shown. b) A xy-view of the ET and the electron beam pipe is shown. c) The PD is protected from the high synchrotron radiation flux by a water Čerenkov veto counter (VC) and a lead filter (Filter). In the HERA tunnel the proton beam is separated from the electron beam. The proton ring is above the electron ring. The vertical distance between the beams at $z = -103$ m is visible in the picture.

Chapter 3

J/ψ Event Topologies

In this thesis the decay of the J/ψ to e^+e^- is used for the analysis.[1] According to the detector regions where the decay electrons are detected the events can be classified into three topologies (see figure 3.1):

- *track-track topology*: The two decay electrons enter the central part of the detector, where they are detected as tracks in the central tracking detector and corresponding energy depositions in the LAr calorimeter.
- *track-cluster topology*: One of the decay electrons enter the central part of the detector, where it is detected as a track in the central tracking detector with a corresponding energy deposition in the LAr calorimeter. The other decay electron enters the backward region, where it is detected as an energy deposition in the SpaCal and hits in the BST.
- *cluster-cluster topology*: Both decay electrons enter the backward region of the detector, where both are detected as an energy deposition in the SpaCal and hits in the BST.

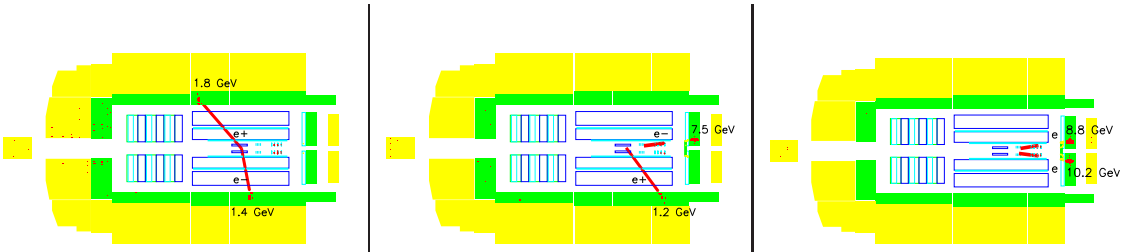

(a) (b) (c)

Figure 3.1: The three event topologies of the J/ψ decay to e^+e^- are shown: (a) track-track ($40\,\text{GeV} < W_{\gamma p} < 150\,\text{GeV}$), (b) track-cluster ($135\,\text{GeV} < W_{\gamma p} < 235\,\text{GeV}$) and (c) cluster-cluster ($205\,\text{GeV} < W_{\gamma p} < 305\,\text{GeV}$).

[1] J/ψ decays with hadrons in the final state are not used, because of a high contamination from background events. The J/ψ decay in a $\mu^+\mu^-$ pair is discussed later in this section.

The regions of the detector where the decay electrons will be registered depend on the boost of the J/ψ relative to the laboratory system. In the photoproduction regime the z-axis is a very good approximation for the direction of the boost. A direct handle for the boost is therefore the photon-proton centre-of-mass energy $W_{\gamma p}$. In figure 3.2 the $W_{\gamma p}$ distributions from simulation[2] for the three topologies are shown. The distributions demonstrate, that the track-track, track-cluster and cluster-cluster topologies cover the low, middle and high regions of the $W_{\gamma p}$ range, respectively.

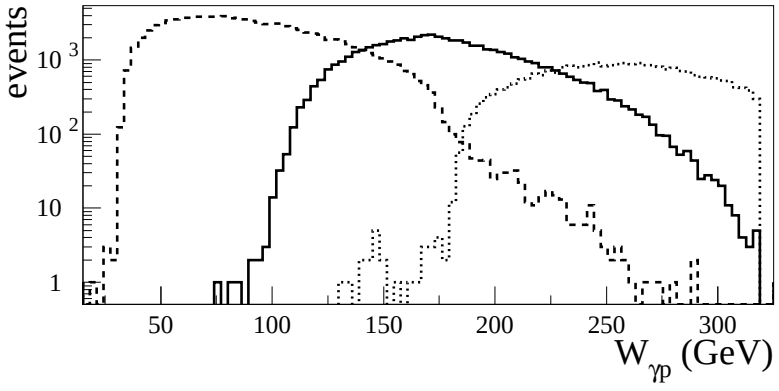

Figure 3.2: The $W_{\gamma p}$ distributions from simulation for the track-track (dashed line), track-cluster (solid line) and cluster-cluster topologies (dotted line) are shown.

This analysis concentrates on high photon-proton centre-of-mass energies $W_{\gamma p}$ where the data were previously limited in statistics. The high $W_{\gamma p}$ regime corresponds to to the track-cluster and cluster-cluster topologies. Detailed event displays for these topologies are shown in figure 3.3.

For track-cluster and cluster-cluster topologies at least one decay electron enters the backward region of the H1 detector. In this region the momentum of muons cannot be determined. Therefore the decays of J/ψ mesons into $\mu^+\mu^-$ pairs are not used in this analysis.

The experimental signature of the J/ψ events is the detection of their decay electrons. In order to give an impression of the properties of the decay electrons their angle and energy distributions from simulation are shown for the track-cluster and the cluster-cluster topologies in figure 3.4 and figure 3.5, respectively. These properties are taken into account in order to select the J/ψ events during data taking, which is the topic of the next chapter.

No detector information exists to unambiguously separate of the proton-elastic and low mass proton-dissociative J/ψ production. For both channels the proton or low mass proton-breakup leaves the detector either undetected or causes a detector signal in the following forward detectors: the inner forward region of the LAr calorimeter (see section 2.2.2.1), the FMD (see section 2.2.3.2) and the PRT (see section 2.2.4). Detector signals can also be caused by noise. Events with a signal in one of the forward detectors are called *fwd.-tagged*. The others are called *fwd.-untagged*. For the determination (see section 8.5) of the 'true' number of proton-elastic and proton-dissociative events, the fractions of proton-elastic and proton-dissociative events in the

[2] In this section results from the simulation of proton-elastic J/ψ photoproduction are shown. The subject of simulation is presented in chapter 5.

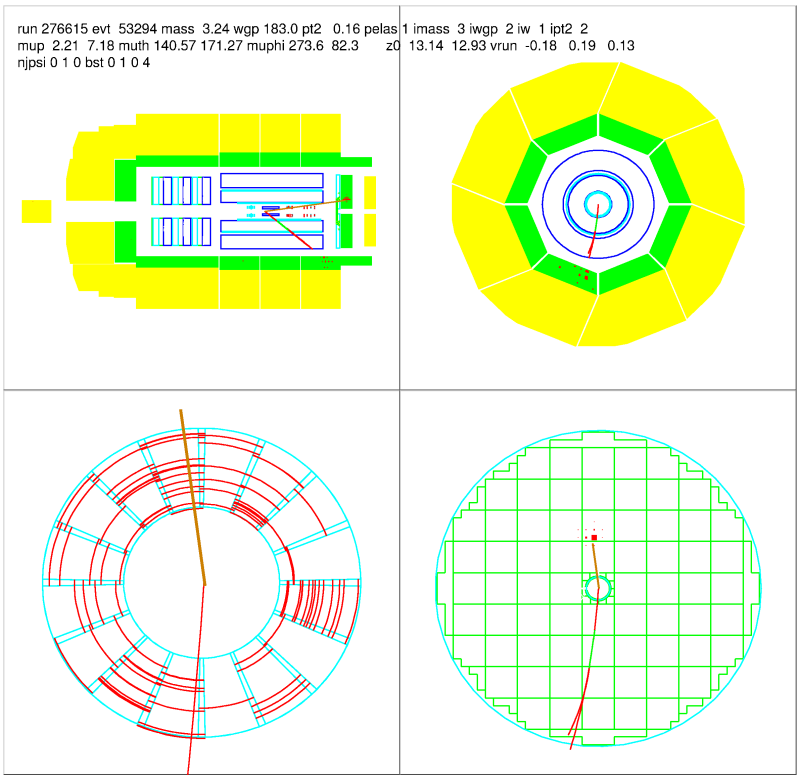

(a) J/ψ track-cluster event

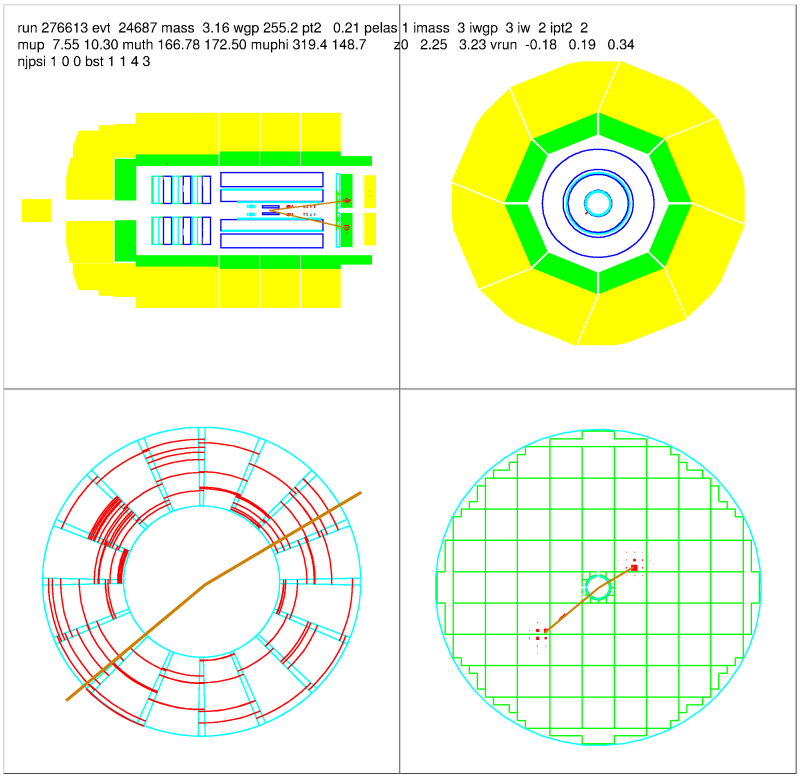

(b) J/ψ cluster-cluster event

Figure 3.3: Event displays of a J/ψ track-cluster event (a) and a J/ψ cluster-cluster event (b) from data of the year 2000 are shown. In the four subpictures a side-view and radial-view of the H1 detector, a zoomed radial view of the BST and a zoomed radial view of the SpaCal are presented. For the SpaCal clusters the BST tracks are shown in the side-view and the zoomed radial-views.

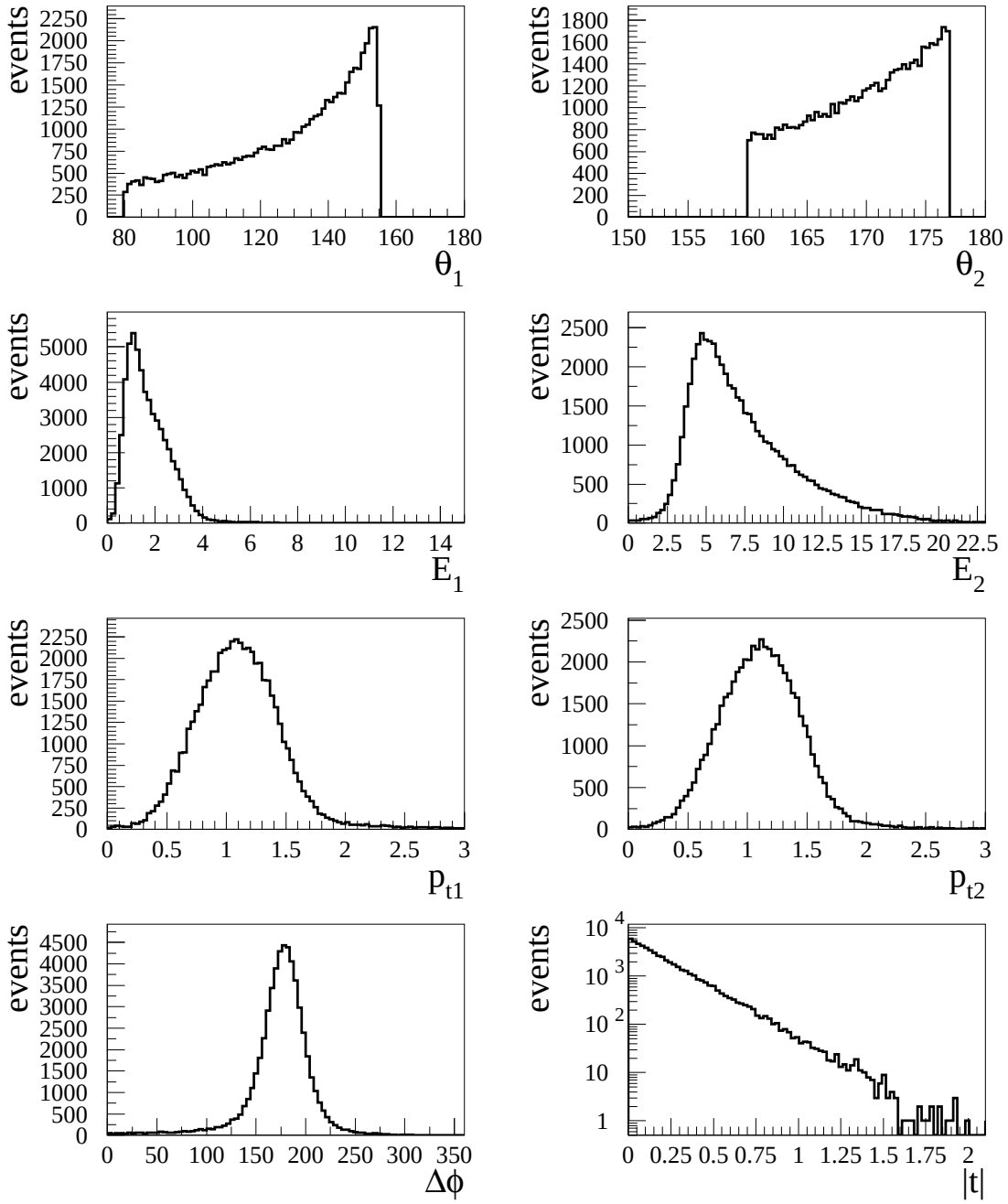

Figure 3.4: For the track-cluster topology the distributions of the polar angle θ, the energy E, the transverse momentum p_t and the difference $\Delta\phi$ of the azimuthal angles of the J/ψ decay electrons and the distribution of the kinematic variable t are shown. Events from the simulation of proton-elastic J/ψ photoproduction are used. The decay electrons are sorted by θ: the index 1 refers to the track-electron and the index 2 to the cluster-electron.

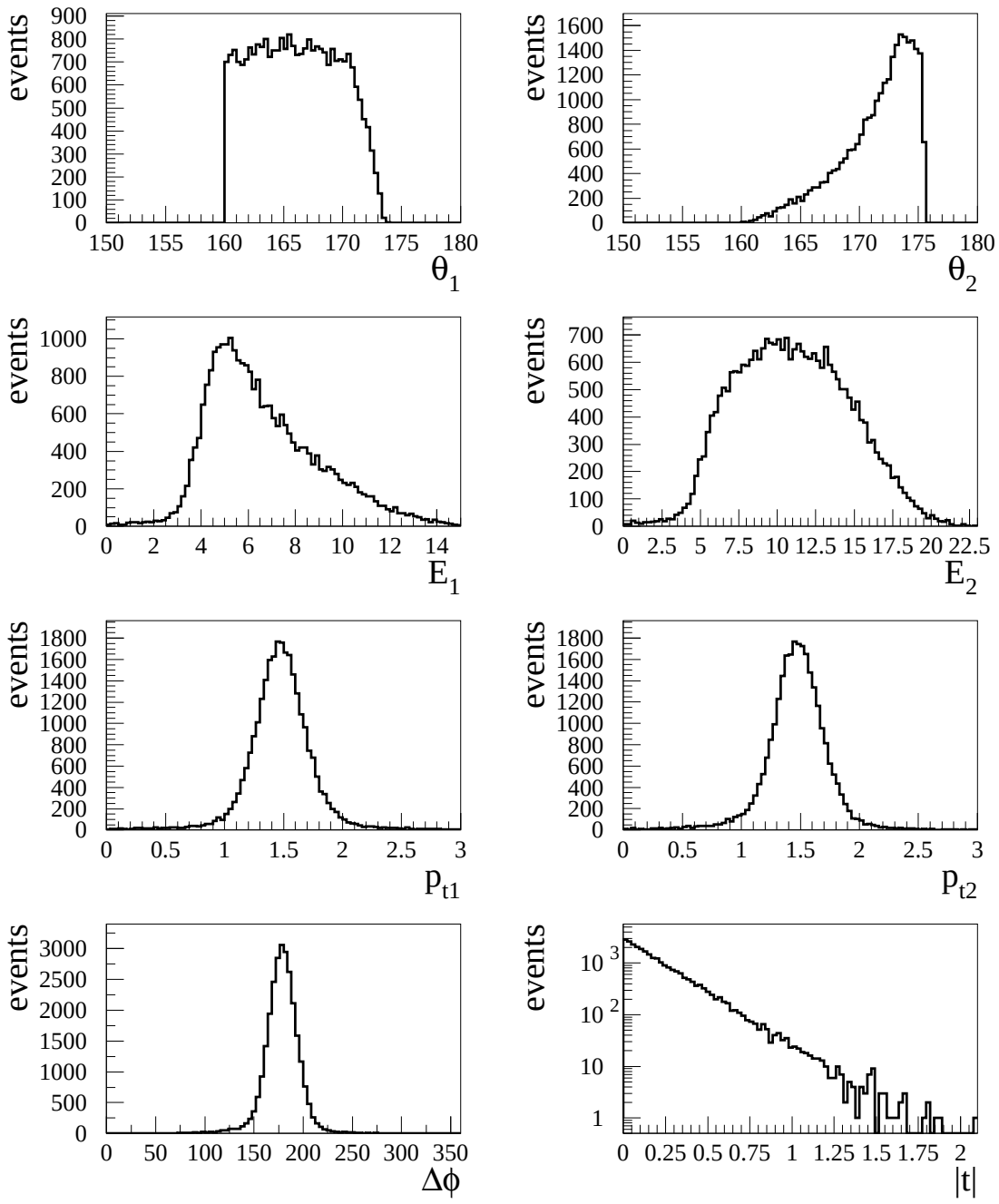

Figure 3.5: For the cluster-cluster topology the distributions of the polar angle θ, the energy E, the transverse momentum p_t and the difference $\Delta\phi$ of the azimuthal angles of the J/ψ decay electrons and the distribution of the kinematic variable t are shown. Events from the simulation of proton-elastic J/ψ photoproduction is used. The decay electrons are sorted by θ: the index 1 refers to the cluster-electron with lower θ and the index 2 to the cluster-electron with higher θ.

fwd.-untagged and fwd.-tagged samples are used. These fractions are determined by simulation (see section 6.4.3).

Chapter 4

Trigger System

The purpose of the trigger system is to select interesting events in a fast way during data taking and to start the complete read out of these selected events.

The read out rate is limited by the bandwidth available for the data transfer to mass storage devices. A full read out of the H1 experiment takes ≈ 1 ms. During this time the experiment is not sensitive, i.e. the read-out-time contributes to the dead-time of the experiment. Due to the limited transfer rate[1] and the aim for small dead-time the trigger system is needed.

The interesting events are *physics events*, i. e. those coming from ep-interactions[2]. At HERA the ep-interactions cause mainly photoproduction events, which have a cross section of several μb. This leads to a rate of about $20 - 30$ Hz at design luminosity. Events with e.g. high Q^2, where the beam electron is scattered to the LAr-calorimeter, have a rate of a few Hz.

Background events come from non ep-interactions. The rate of background events is $\approx$ 100 kHz and thus exceeds the rate of ep-interactions by several orders of magnitude. The main sources of background events are: beam-gas interactions, beam-wall-interactions, synchrotron radiation, cosmic radiation, which are described in the following: The dominant source of background events are collisions of the beam protons with atoms of the residual gas ($\approx 10^{-1}$ Pa) in the beam pipe (*beam-gas interactions*). Using the cross section of pp-scattering the rate of beam-gas interactions can be estimated to 100 kHz for a proton beam current of 100 mA. Protons from the halo of the proton beam interact with the beam pipe or parts of detectors (*beam-wall interactions*). They are topologically very similar to beam-gas interactions. The beams are adjusted with magnets. This causes *synchrotron radiation* emitted by the beam electrons[3]. Using collimators a large fraction of this background can be rejected. Muons from *cosmic*

[1] Using the read-out-time of $\approx$ 1 ms and the average size of a raw event of $\approx$ 110 kByte (see section 4.4) the data rate can be estimated to $\approx$ 107 MByte/ s. This is much larger than the possible transfer rate to mass storage of $\approx$ 10events/ s, which corresponds to $\approx$ 1.1 MByte/ s.

[2] Also some special events from non ep-intractions are interesting. E.g. muon events from cosmic radiation (a straight muon passing through the full detector) are used for the alignment of the detector and events from pilot-bunches (see section 2.1) are used for background studies.

[3] Synchrotron radiation of the beam protons is strongly suppressed by the large mass of the protons.

radiation hit the detector with a rate of ≈ 1 kHz. Using topological requirements, like a vertex near the nominal interaction point, these events can be efficiently rejected.

In order to cope with the high rate of background events compared to physics events H1 is using a 4 level trigger system (see figure figure 4.1): Level 1 and 2 are hardware trigger levels and level 3 and 4 are software trigger levels. In the years 1999 and 2000 the level 3 was not used.

Detector components (subdetectors) provide fast trigger information for each bunch crossing, i.e. every 96 ns. This information is stored in pipelines in order to provide a dead-time free level 1 trigger. With a latency of about 2.3 μs a level 1 trigger decision is derived.

After a positive L1 decision the read out of the detector is started and the level 2 trigger starts to build its decision. At this point the primary dead-time starts. No further level 1 triggers are accepted until the read out is completed or aborted by a fast clear signal due to a negative decision of the level 2 trigger. The level 2 trigger has to provide a decision after 20 μs in order to cope with a maximum rate of $1 - 2$ kHz from level 1 while keeping the dead time below 2%.

After a positive level 2 decision the full event information is sent to the trigger level 4. The trigger level 4 is a processor farm, where a full event reconstruction is performed and the final decision for permanent storage of the event is taken. The maximum input rate for level 4 is 100 Hz and the output rate is limited to about 10 Hz due to the bandwidth for writing on permanent storage.

In order to take the different conditions during a luminosity fill into account, different settings for the trigger system exist. These different settings are called *trigger phases*.

In the following sections the trigger levels are described in more detail.

4.1 Level 1

Most of the subdetectors provide fast trigger information for each bunch crossing. The resulting information packages are called *level-1-trigger-elements* (L1TE). There are 196 L1TEs. Due to the different technologies used in the different subdetectors, it takes different amounts of time for different subdetectors to create their L1TEs. For example the maximum drift time in the CJC is ≈ 1 μs and the maximum of the trigger signal of the LAr-calorimeter-trigger is reached after 1.4 μs [65]. In order to cope with the different limits due to physics and electronics the L1TE information is stored in pipelines, which can hold the information for up to 30 bunch crossings[4].

After the synchronisation of the L1TE information originating from one bunch crossing this information is used to form 128 *raw level-1-subtriggers* (raw L1ST) by logical combinations.

From the raw L1ST the *actual* L1ST are formed taking *prescale* counters into account, i.e. only for each n-th activated raw L1ST the actual L1ST is activated, where n is the

[4] Usually only 24 places are occupied.

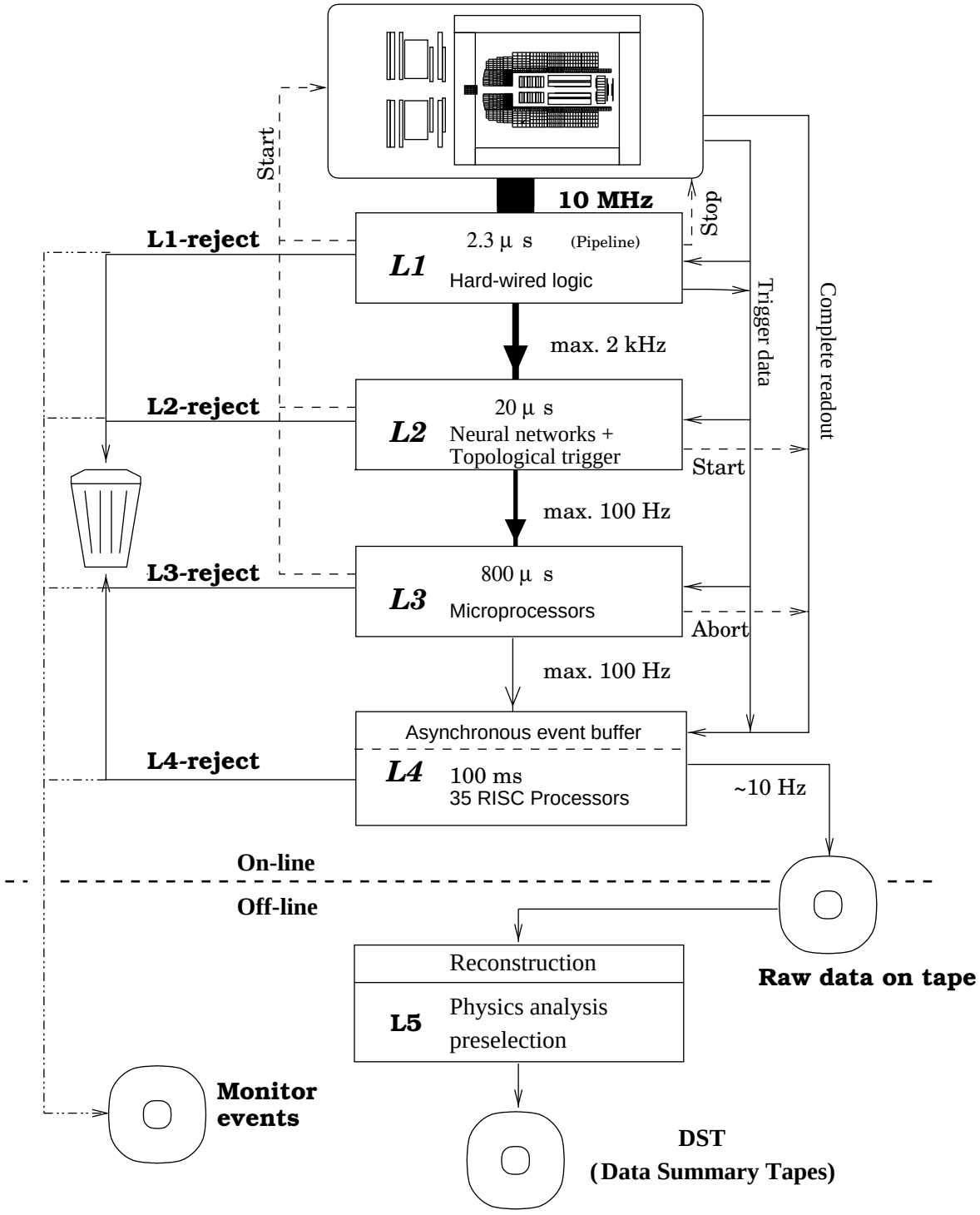

Figure 4.1: The trigger system and data taking system of the H1 detector: dashed lines show signals, solid and dashed-dotted lines show the flow of data. For the trigger levels the maximum input rates are given. The trigger level 3 was not used in the running periods 1999 and 2000. An overview of the trigger system is presented in the beginning of chapter 4. The detailed description of the different trigger levels is given in the sections 4.1 (L1), 4.2 (L2), 4.3 (L4) and 4.4 (L5).

prescale factor specific for each single L1ST. This is the simplest method to reduce the rate of a raw L1ST.

If one of the 128 actual L1ST fires, the level 1 trigger sends the signal `L1Keep`. The level 1 trigger decision is obtained after 2.3 μs (24 bunch crossings). Due to the usage of pipelines this time is just a latency but does not create dead-time.

The `L1Keep` signal causes that no further level 1 triggers are accepted. All L1TE information is sent to the level 2. Now the dead-time of the experiment starts.

In the following sections the trigger systems of the subdetectors (*subdetector triggers*) and trigger elements important for this analysis are described. Since the trigger level 2 uses the full information of the level 1 trigger as input, these quantities are also described at the level 1 trigger systems, which create them.

After the description of the trigger elements the subtriggers built up from them are explained.

4.1.1 DC$r\phi$ Trigger Elements

The central drift chambers CJC1 and CJC2 (see section 2.2.1.3) provide trigger information, which consists of fast information about track candidates in the $r\phi$ plane. The system is called *Drift Chamber $r\phi$-trigger* (DC$r\phi$-trigger).

The DC$r\phi$-trigger uses 10 out of the 56 wire layers of the CJC1 and CJC2 drift chambers. The signals are digitised and compared to 10^4 masks in order to identify track candidates. There are masks for tracks of positively and negatively charged particles with high ($p_t > 800\,\mathrm{MeV}$) and low ($400\,\mathrm{MeV} < p_t < 800\,\mathrm{MeV}$) transverse momentum. The masks are only activated, if the distance of closest approach (DCA) of the track to the z-axis is less than 2 cm. By this the background from beam-wall-events and synchrotron radiation is massively reduced.

The number of matching masks for each combination `high/pos`, `high/neg`, `low/pos` and `low/neg` is counted in 45 sectors in ϕ. With this information the DC$r\phi$-trigger builds several level 1 trigger elements. The trigger elements used in this analysis are listed in table 4.1.

4.1.2 $z-$Vertex Trigger Elements

The multi wire proportional chambers CIP, COP (see section 2.2.1.3) and FPC (see section 2.2.1.4) are used for a simple and fast validation of tracks on trigger level 1. Especially the impact points on the z-axis are estimated. Therefore the system is called the $z-$Vertex *trigger*.

CIP and COP have each 16 segments in ϕ and together 4 layers in r. If three or four segments in one ϕ-sector give signals, a *ray* is formed. All rays are extrapolated to the z-axis. The impact positions are filled into the $z-$vertex *histogram* (see figure 4.2), which has 16 bins and covers the central z-region of $|z| < 43.9$ cm. For forward track candidates also information from the FPC is used.

Trigger Information from the DC$r\phi$ Trigger		
	name	description
L1TE	DCRPh_Ta	al least one DC$r\phi$ mask activated
L1TE	DCRPh_Tc	al least $c = 3$ DC$r\phi$ masks activated
L1TE	DCRPh_THig	at least 1 mask for a track with $p_t > 800\,\mathrm{MeV}$ activated
L1TE	DCRPh_NL_many	at least 20 negative low momentum track candidates are found
L1TE	DCRPh_NH_many	at least 20 negative high momentum track candidates are found
L1TE	DCRPh_PL_many	at least 20 positive low momentum track candidates are found
L1TE	DCRPh_PH_many	at least 20 positive high momentum track candidates are found
L2 input	trtot	total number of masks activated

Table 4.1: Description of the L1 trigger elements of the DC$r\phi$ trigger and the input quantities for level 2 used in this analysis.

In addition a bitmap of the rays is created. This bitmap is called *bigray-bitmap* and has 16 segments in ϕ and 14 segments in θ.

The trigger elements used in this analysis are shown in table 4.2.

Trigger Information from the $z-$Vertex Trigger		
	name	description
L1TE	zVtx_T0	at least one ray
L1TE	zVtx_mul< 2	not more than 5 entries in the $z-$vertex histogram (zVtx_mul is an encoded number.)
L2 input	cpvmax	maximum entry in $z-$vertex histogram
L2 input	cpvsum	sum of entries in $z-$vertex histogram
L2 input	nbigbwd	number of rays in the most backward θ-bins 11, 12, 13 of the bigray-bitmap
L2 input	nbigray	total number of rays the bigray-bitmap

Table 4.2: Description of the L1 trigger elements of the $z-$vertex trigger and the input quantities for level 2 used in this analysis.

4.1.3 LAr Trigger Elements

The LAr calorimeter (see section 2.2.2.1) also provides trigger information. The LAr trigger is one of the most important subdetector triggers of the H1 experiment. This trigger is essential for triggering events with high Q^2 or missing transverse momentum. A detailed description of the powerful LAr trigger can be found in [65].

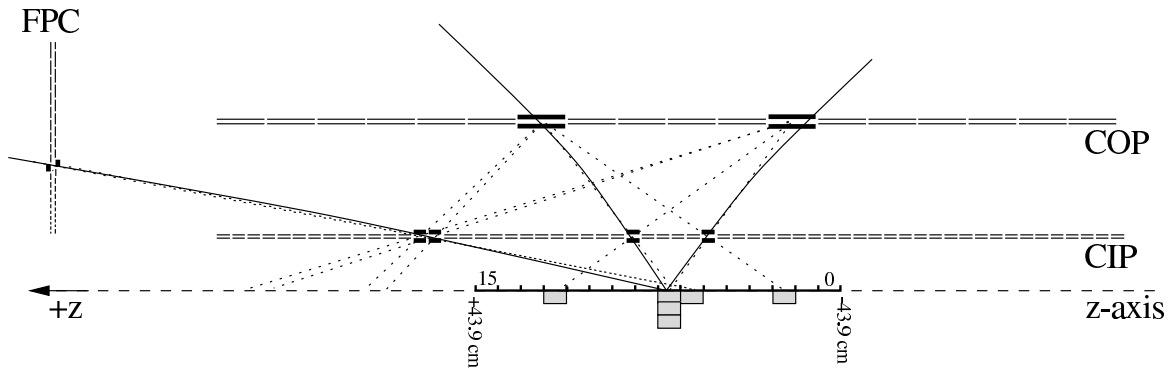

Figure 4.2: Signals of the CIP, COP and FPC are used to build rays. These rays are extrapolated to the z-axis. The impact points of the rays are filled into the $z-$vertex histogram.

The energy deposition of the electron track in track-cluster events is too small for an efficient use of LAr trigger elements. But some background events deposit sufficient energy in the inner forward part of the LAr calorimeter [66]. The LAr trigger element `larife` (see table 4.3) contains the energy in the inner forward part (see figure 2.8) and is used as input to trigger level 2 in order to suppress background events.

Trigger Information from the LAr Trigger		
	name	description
L2 input	`larife`	energy in the inner forward part of the LAr calorimeter

Table 4.3: Description of the input quantities for level 2 from the LAr trigger used in this analysis.

4.1.4 SpaCal Trigger Elements

The electromagnetic and hadronic cells of the SpaCal (see section 2.2.2.2) are used to provide trigger information for three different energy thresholds. The trigger information also includes a coarse position information.

The basic building blocks of the electromagnetic part of the SpaCal are 40.5×40.5 mm^2 cells. For the trigger 2×2 cells are grouped together, their analog signals are summed up and so called analog-sums are created. 2×2 analog-sums are again grouped to trigger modules. The trigger modules overlap. Each analog-sum is therefore part of four trigger modules (see figure 4.3). Due to the overlap each electromagnetic shower is fully contained in one trigger module [67].

If the SpaCal would be quadratic, there would be 20×20 trigger modules. Due to the circular shape of the SpaCal only 308 real trigger modules exist, the others are set to 0.

Comparing the signals of the trigger modules with three energy thresholds 0.5 GeV, 1.7 GeV and 5.2 GeV [68] the *SpaCal Intrinsic Electron Trigger* bits (SIET) are built.

Taking the 20×20 SIET bits and grouping them in groups of 4×4 the 5×5 *Local Intrinsic Electron Trigger* bits (LIET) are achieved (see figure 4.4). The grouping is done for all three energy thresholds separately. Performing a logical `or` on all LIET bits (with exception of the central LIET module surrounding the beam pipe) three global trigger elements for the different thresholds are derived.

The good time resolution of ≈ 0.4 ns is used to reject upstream beam-related background. These background events have a difference in their time-of-flight of ≈ 10 ns with respect to events originating from the nominal interaction point. With this method a part of the high rate beam-gas and beam-wall background caused by the proton beam can be rejected on trigger level 1.

The trigger elements used in this analysis are shown in table 4.4. From the hadronic SpaCal only time-of-flight trigger elements are used.

Trigger Information from the SpaCal Trigger		
	name	description
L1TE	`SPCLe_IET`> 1	global trigger element for the middle energy threshold
L1TE	`SPCLe_IET`> 2	global trigger element for the high energy threshold
L1TE	`SPCLe_IET_Cen_3`	the central LIET bit for the high energy threshold
L1TE	`SPCLh_AToF_E_1` `SPCLh_ToF_E_2`	energy deposition in the hadronic part of the SpaCal at a time, which does not correspond to an ep-interaction
L2 input	`spcent1`	number of SIET bits contributing to the central LIET bit for the low energy threshold
L2 input	`spcent3`	number of SIET bits contributing to the central LIET bit for the high energy threshold
L2 input	`spcll`i `spclh`j	bit packed information from the SIET bits for the medium threshold ($i \in \{0..31\} \setminus \{6\}$,$j \in \{0..31\} \setminus \{4, 6\}$)

Table 4.4: Description of the L1 trigger elements of the SpaCal trigger and the input quantities for level 2 used in this analysis.

4.1.5 Time-Of-Flight Trigger Elements

In this section the level 1 trigger elements, which are used as a veto against background events are collected. The trigger elements are built from information of the time-of-flight system (see section 2.2.5) and tag events where the detector response corresponds to the time window of a crossing of an electron-bunch with a proton-bunch or not. The ToF L1TEs used in this analysis are listed in table 4.5.

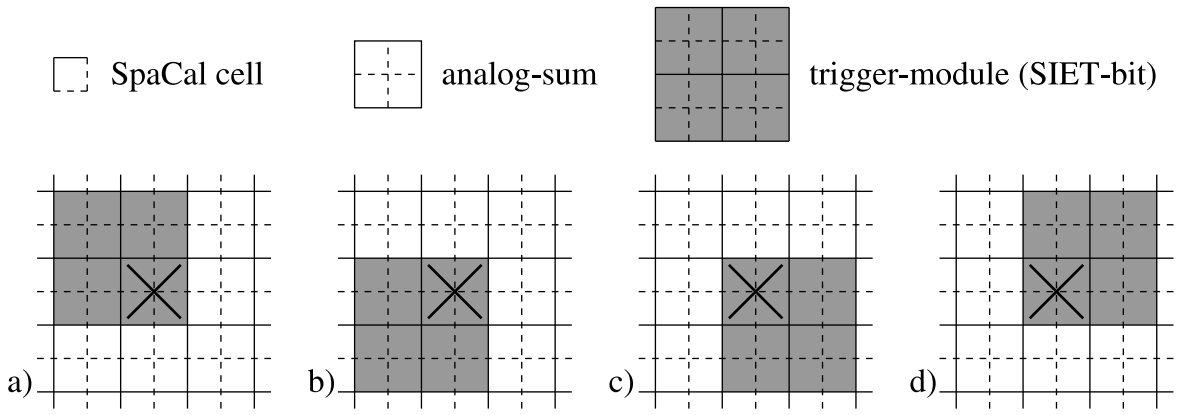

Figure 4.3: A schematic view of the SpaCal cells, the analog-sums and the trigger modules is shown. The small squares are the SpaCal cells (solid and dashed lines). 2×2 cells are grouped together (solid lines). Their analog signals are summed up and a so called analog-sum is created. Four of the analog-sums build a trigger modules (SIET bits) (shaded squares). The trigger modules overlap. Therefore one analog-sum (marked by $\times$) is taken into account for four trigger modules.

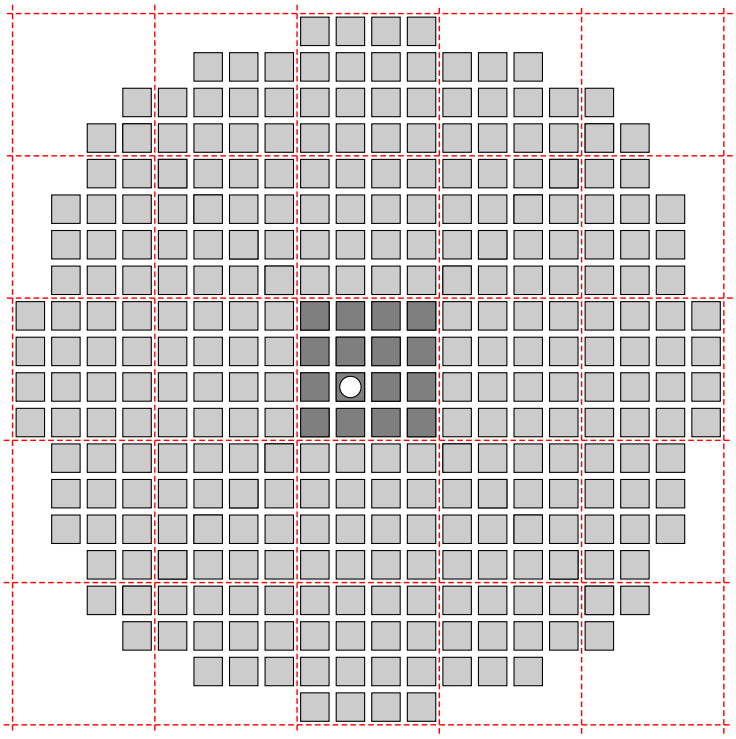

Figure 4.4: The segmentation of the SpaCal into SIET bits is shown. For simplicity the overlap of the trigger modules is not show. For each trigger module only the left lower analog-sum — the one marked by $\times$ in figure 4.3 d) — is drawn. This causes an asymmetry in the presentation. Therefore in the picture the beam pipe (marked by a circle) is slightly shifted from the centre. 4×4 SIET bits are combined to a LIET bit. This is indicated by the dashed lines. The central LIET bit is highlighted by the dark shaded squares. Due to the overlap of the trigger moduls also the 8 adjacent SIET bits contain information from the SpaCal insert module (see figure 2.11).

Trigger Information from ToF Triggers		
	name	description
L1TE	PToF_IA	PLUG ToF hit interaction time window
L1TE	FToF_IA	forward ToF hit in main proton time window
L1TE	FToF_BG	forward ToF hit in late satellite time window
L1TE	VETO_Inner_BG	inner veto wall proton related background timing
L1TE	VETO_Outer_BG	outer veto wall proton related background timing
L1TE	VLQToF_BG	VLQ ToF hit proton time window

Table 4.5: Description of the L1 trigger elements of the time-of-flight system used in this analysis.

4.1.6 Level 1 Subtriggers

Level 1 subtriggers (L1ST) are logical combinations of L1TEs (see previous sections). In this section the L1STs are described, which are used to select the track-cluster and cluster-cluster events. In order to take into account the different event topologies of the track-cluster and cluster-cluster samples (see section 3), different level 1 trigger elements are used and combined to subtriggers.

The signature of the track-cluster sample is a track in the central region of the detector and a cluster in the SpaCal. In order to select the track the L1TE DCRPh_Ta is required, which implies that at least one DC$r\phi$ mask is activated. In addition multi track events are suppressed by the L1TE zVtx_mul < 2, which is rejecting events with more than 5 entries in the $z-$vertex histogram. In order to select the cluster in the SpaCal a radius dependent energy criterion is used: In the central region the high threshold is required (L1TE SPCLe_IET_CEN_3) and for the non-central region the middle energy threshold is required (L1TE SPCLe_IET > 1). In order to suppress background events from non electron-proton bunch crossings additional veto L1TEs are used. The L1TEs are combined by logical operations to the L1ST S33 (see table 4.6).

For the track-cluster sample in addition the L1ST S61 is used as an independent monitor trigger for the trigger level 2. The track requirement for the S61 is the L1TE DCRPh_THig, which requires that at least 1 mask for a track with $p_t > 800\,\mathrm{MeV}$ is activated. The cluster is selected by the L1TEs SPCLe_IET > 2 and SPCLe_IET_Cen_3, which require an energy deposition in the SpaCal passing the high threshold. The formal definition of the L1ST S61 with the additional veto trigger elements can be found in table 4.6.

The signature of the cluster-cluster sample are two clusters in the SpaCal and an 'empty' central detector. The clusters in the SpaCal are selected by the L1TE SPCL_IET > 1. In order to have an 'empty' central detector a veto on more than 2 activated DC$r\phi$ masks is applied by the negated L1TE $\neg$DCRPh_Tc. Also here additional veto L1TEs are used. The created L1ST is called S40 (see table 4.6).

$$
\begin{array}{lcl}
\texttt{S33}_i & = & \texttt{S33}_C \wedge \texttt{S33}_{Vi} \quad (i \in \{0,1,2\}) \\
\\
\texttt{S33}_C & = & ((\texttt{SPCLe_IET} > 1) \vee \texttt{SPCLe_IET_CEN_3}) \wedge (\texttt{zVtx_mul} < 2) \wedge \texttt{DCRPh_Ta} \\
\\
\texttt{S33}_{V0} & = & \neg\texttt{SPCLh_AToF_E_1} \wedge \neg\texttt{SPCLh_ToF_E_2} \wedge \\
 & & \neg\texttt{VETO_inner_BG} \wedge \neg\texttt{VETO_Outer_BG} \wedge \neg\texttt{VLQToF_BG}) \wedge \\
 & & \neg(\texttt{DCRPh_NL_many} \wedge \texttt{DCRPh_NH_many} \wedge \texttt{DCRPh_PL_many} \wedge \texttt{DCRPh_PH_many}) \\
\texttt{S33}_{V1} & = & \texttt{S33}_{V0} \wedge (\texttt{FToF_IA} \vee \neg\texttt{FIT_BG}) \\
\texttt{S33}_{V2} & = & \texttt{S33}_{V0} \wedge ((\texttt{FToF_IA} \vee \texttt{FIT_IA}) \vee (\neg\texttt{FToF_BG} \wedge \neg\texttt{FIT_BG}))
\end{array}
$$

$$
\begin{array}{lcl}
\texttt{S40}_i & = & \texttt{S40}_C \wedge \texttt{S40}_{Vi} \quad (i \in \{0,1,2\}) \\
\\
\texttt{S40}_C & = & \texttt{SPCL_IET} > 1 \wedge \neg\texttt{DCRPh_Tc} \\
\\
\texttt{S40}_{V0} & = & (\texttt{zVtx_mul} < 7) \wedge \neg\texttt{SPCLh_AToF_E_1} \wedge \neg\texttt{VLQToF_BG} \wedge \\
 & & \neg\texttt{VETO_inner_BG} \wedge \neg\texttt{VETO_Outer_BG} \\
\texttt{S40}_{V1} & = & \texttt{S40}_{V0} \wedge (\texttt{FToF_IA} \vee \neg\texttt{FToF_BG}) \\
\texttt{S40}_{V2} & = & \texttt{S40}_{V0} \wedge ((\texttt{FToF_IA} \vee \texttt{FIT_IA}) \vee (\neg\texttt{FToF_BG} \wedge \neg\texttt{FIT_BG}))
\end{array}
$$

$$
\begin{array}{lcl}
\texttt{S61}_i & = & \texttt{S61}_C \wedge \texttt{S61}_{Vi} \quad (i \in \{0,1,2\}) \\
\\
\texttt{S61}_C & = & \texttt{DCRPh_THig} \wedge ((\texttt{SPCLe_IET} > 2) \vee \texttt{SPCLe_IET_Cen_3}) \\
\\
\texttt{S61}_{V0} & = & \neg\texttt{SPCLh_AToF_E_1} \wedge \neg\texttt{SPCLh_ToF_E_2} \wedge \\
 & & \neg\texttt{VETO_inner_BG} \wedge \neg\texttt{VETO_Outer_BG} \wedge \neg\texttt{VLQToF_BG}) \wedge \\
 & & \neg(\texttt{DCRPh_NL_many} \wedge \texttt{DCRPh_NH_many} \wedge \texttt{DCRPh_PL_many} \wedge \texttt{DCRPh_PH_many}) \\
\texttt{S61}_{V1} & = & \texttt{S61}_{V0} \wedge (\texttt{FToF_IA} \vee \neg\texttt{FIT_BG}) \\
\texttt{S61}_{V2} & = & \texttt{S61}_{V0} \wedge ((\texttt{FToF_IA} \vee \texttt{FIT_IA}) \vee (\neg\texttt{FToF_BG} \wedge \neg\texttt{FIT_BG}))
\end{array}
$$

Table 4.6: The definition of the level 1 subtriggers S33, S61 and S40 is shown. Each subtrigger is built up from a "core" part (C) and a set of veto conditions (V). The different veto conditions pay attention to the changing detector status in different run periods. This is indicated by the index i. A detailed list of the changes to the L1 subtriggers can be obtained from [69]. The trigger elements are described in the tables 4.1, 4.2, 4.4, 4.3 and 4.5. For an informal description of the subtriggers refer to the text.

4.2 Level 2

The input for the trigger level 2 (L2) is the information, which is used to build the level 1 trigger elements. The first possibility to have all this information available in one place is the trigger level 2. Here for the first time correlations between the various inputs can be exploited.

The level 2 trigger must built its decision within 20 μs. In order to cope with the time constraints, on the trigger level 2 inherent parallel machines are used. Two different systems are implemented: the Level-2-Topological-Trigger (L2TT) and the Level-2-Neural-Network-Trigger (L2NN). The L2TT exploits the correlations by conventional matrix operations and logical combinations. This analysis uses only the L2NN.

The L2NN uses a freely programmable parallel hardware, which is mainly used to evaluate feed-forward-neural-networks (FFNN). FFNN have been proven to be a very good technique in solving pattern recognition problems. In addition FFNN can be implemented easily on parallel hardware. An introduction into the subject of neural networks is given in section 4.2.1. Besides the FFNN also a special parallel algorithm is evaluated (see section 4.2.4). The hardware of the L2NN is described in section 4.2.2.

The algorithm and parameters of the two L2STs used in this analysis are presented in section 4.2.3 and section 4.2.4.

Each of the two level 2 trigger systems (L2NN, L2TT) creates 16 trigger decisions, the *level 2 trigger elements* (L2TE). The L2TE are combined with logical expressions to *raw level 2 subtriggers* (raw L2ST). While the transformation from the L2TE is just a copy procedure for the L2NN, the L2TT is using the logical combinations heavily. Taking possible prescale factors into account the *actual L2ST* are formed from the raw L2ST.

Each of the actual L2STs is used to validate a set of actual L1STs. Technically this is done by a logical vector matrix multiplication. Usually a L1ST with high efficiency for physics events has an intolerably high rate. Using the full trigger information the level 2 trigger therefore has the task to reduce the excess background rate in this subtrigger without reducing the efficiency for the chosen physics channel. L1ST, which are not associated with a L2ST of the L2NN or L2TT, are validated by an artificial L2ST, which fires for each event.

If one L1ST is validated by a L2ST, the signal `L2-keep` is sent, the detector read out is not aborted and the event is passed to the trigger level 4. If no L1ST is validated, a fast clear signal is sent and the trigger level 1 is activated again.

4.2.1 Introduction to Neural Networks

This section is a brief introduction to neural networks. A more detailed introduction can be found e.g. in [70].

A *neural network* is defined as a set of connected *neurons*. The mathematical definition of a neuron is a nonlinear function $f : \mathbb{R}^n \to \mathbb{R}$, which maps a high dimensional input to one dimension.

A biological neuron gets many inputs $x_i (i \in \{1, .., n\})$, which are weighted with the weights w_i and summed up. The result is compared with a threshold w_0:

$$f_w^l(x) := \sum_{i=1}^{n} w_i x_i - w_0 \quad (x \in \mathbb{R}^n \text{ and } w \in \mathbb{R}^{n+1}) . \tag{4.1}$$

Using a nonlinear function, called the *transfer function*, the "activation" $f_w \in]0, 1[$ is created. A conventional choice for the transfer function is the sigmoid function

$$\mathrm{s}(\xi) = \frac{1}{1 + \mathrm{e}^{-\xi}} \quad (\xi \in \mathbb{R}) , \tag{4.2}$$

which leads to

$$f_w(x) := \mathrm{s}(f_w^l(x)) \quad (x \in \mathbb{R}^n \text{ and } w \in \mathbb{R}^{n+1}) . \tag{4.3}$$

This definition of a neuron is called a *perceptron*. The space is divided by the plane into two regions: $\{x \in \mathbb{R}^n \,|\, f_w^l(x) > 0\}$ and $\{x \in \mathbb{R}^n \,|\, f_w^l(x) \leq 0\}$. Applying the sigmoid function s this separation is represented by the two regions: $\{x \in \mathbb{R}^n \,|\, f_w(x) > 0.5\}$ and $\{x \in \mathbb{R}^n \,|\, f_w(x) \leq 0.5\}$. The difference of $f_w(x)$ from 0.5 gives a handle on the distance of x to the separating plane.

Taking again nature as a paradigm a special choice for the connections between the neurons is made. All neurons are arranged in layers. The neurons of the first layer get $x \in \mathbb{R}^n$ as input. The outputs of the neurons of the first layer are passed to the neurons of the second layer as inputs (see figure 4.5). This procedure can be repeated until the outputs of the final layer are taken as the output of the neural network. Due to this arrangement information is processed forward through the layers. This network topology is called *feed forward neural network* (FFNN) or *multi layer perceptron* (MLP). A large part of the cortex of the human brain for example has this feed forward topology with 6 layers [70] and in total $3 \cdot 10^{10} - 10^{11}$ neurons [71].

Now the problem how to construct a neural network and to determine the weights is approached. Again nature gives a clue for solving this problem by looking at the following example. If a pupil should learn "vocables" $(x^j, o^j) \in \mathbb{R}^n \times \mathbb{R}^m (j \in \{1, ..\})$ this could be done under the supervision of a teacher. The teacher presents the pupil a "word" x^j and asks for the answer. If the answer is right, i.e. o^j, the teacher lauds the pupil. If the answer is false, the teacher corrects the pupil. By this *supervised training* procedure the pupil gets the "vocables" trained.

Transferring this to the neural networks, the multi layer neural network with n inputs and m outputs is represented by the function

$$N_w : \mathbb{R}^n \to \mathbb{R}^m . \tag{4.4}$$

where $w \in \mathbb{R}^p$ are the weights of all neurons in all layers. The dimension p depends on the number of layers and on the number of the neurons in the layers. The error function

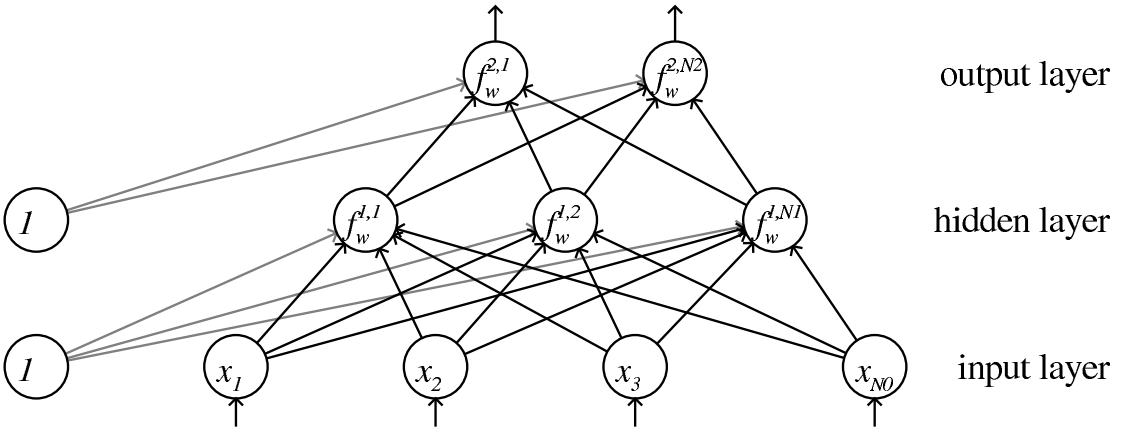

Figure 4.5: In a feed-forward-neural-network (FFNN) the neurons are arranged in layers. The output of the neurons in one layer is taken as input for the next layer. The FFFN shown contains three layers: the input layer with $N0$ neurons, the hidden layer with $N1$ neurons and the output layer with $N2$ neurons. Each neuron of the hidden and output layer performs an operation of the form f_w with different weights w for each neuron. The weights and the flow of information is represented by the arrows. The nodes with content 1 are added in order to be able to handle the thresholds for the neurons in a coherent picture.

$$E_w(x^j, o^j) := \left| N_w(x^j) - o^j \right|^2 \geq 0 \quad ((x^j, o^j) \in \mathbb{R}^n \times \mathbb{R}^m \text{ and } j \in \{1, ..\}) \tag{4.5}$$

describes the difference between the correct answer o^j and the network result $N_w(x^j)$. In order to "laud" or "correct" the neural network the weights w have to be adjusted. This is done by minimising the error function. The neural network N_w is built up from functions of the type f_w. Therefore N_w is differentiable. A usual gradient descent method

$$w \quad \rightarrow \quad w - \alpha \frac{\partial E_w(x^j, o^j)}{\partial w} \tag{4.6}$$

with a step size (*learning parameter*) α can be improved taking the layer structure of the neural network into account. Beginning with the last layer for each layer the derivatives $\partial E_w / \partial w$ are calculated. The error $N_w(x^j) - o^j$ is therefore backwards propagated through the network: *back propagation algorithm* (BPA) [72]. The training of a neural network can also be interpreted as a function approximation problem.

For the training of the neural network the data $(x^j, o^j) \in \mathbb{R}^n \times \mathbb{R}^m (j \in \{1, ..\})$ is separated into two parts: the training data and the test data. With the training data the neural network is trained as described above. With the independent test data the performance[5] of the network is controlled during the training. Also the very important feature of neural networks, the *generalisation*, the response to unknown inputs, is tested.

[5] One handle on the performance of a FFNN is the efficiency versus rejection plot (see figure 4.7)

According to the theorem from Kolmogorov (1957) (see [70]) each multi layer FFNN can be represented by a FFNN with only one hidden layer. While this is simplifying the network structure and usually also the training, it also increases the number of neurons in one layer, which has to be taken into account for a hardware implementation.

There are many methods to improve the performance of a neural network. The simplest is the variation of the training parameter α or the start weights w. Also the number of intermediate layers (hidden layers) and the number of the nodes contained in them (hidden nodes) can be varied. The number of hidden nodes determines the total number of weights, which are the free parameter in the training. As rule of thumb the number of free parameters should not exceed a tenth of the size of the training sample. With higher number of free parameters the network learns the training data "by heart", but the generalisation becomes worse. Since a high generalisation with a high number of correctly classified data is aimed for, the number of hidden nodes should be kept small.

Not all components of the input data x^j are necessarily important to derive the output o^j. The selection of the important components x_i^j is essential in order to achieve neural networks with a good performance. The reduction of the dimension of the input data also reduces the number of free parameters. This reduction can also be performed by special preprocessing of some input data. Further information about the supervised training of neural networks can be found in [34].

In contrast to the supervised learning methods for the two class problem, also unsupervised learning methods for one or multiple class problems exist. One application would be e.g. the encapsulation of background events [73]. Unsupervised learning methods have the advantage of evading possible bias in the selection of a specific physics class for training against the background. Unsupervised methods are not used in this analysis.

4.2.2 Hardware of the Level-2-Neural-Network-Trigger

All neural networks used in the L2NN trigger are feed-forward neural networks with one input layer, one hidden layer and one output layer. The output layer contains only one neuron. Therefore the challenge is not the neural network architecture, but the hardware implementation of the neural network and the input and preprocessing of detector data to usable input variables for the neural networks. In addition to FFNN also a special parallel algorithm is evaluated on L2NN.

In this section the hardware of the L2NN trigger is described. The description proceeds as the data stream goes from the level 1 system through the data preprocessing and the evaluation of the neural networks to the building of the level 2 trigger elements. A more detailed description of the hardware of the L2NN can be found in [74].

The trigger information of the various level 1 subsystems arrive in different formats (e.g. calorimetric energy sums, tracker vertex histograms, tracker rays (bits in the $\theta\phi$-plane), bit coded muon hit maps, etc.) on eight 10 MHz-buses with a width of 16 bits each: the L2-bus. The maximal amount of data per subsystem is 512 bits. This corresponds to a transmission time of 3.072 μs.

The input and preprocessing of the data is performed by data distribution boards (DDB), which listen to the L2-bus. In order to deal with the different formats of the data, each DDB is able to pick up a freely chooseable set of items from the L2-bus. On these items 8 bit $\mapsto$ 8 bit look-up tables (LUT) can be applied. LUTs for a bit counter, a single bit position finder and a dynamic range reduction table (overflow handler) are up to now implemented. After the LUT high and low bytes may be summed up. Any individual DDB can be initialised to perform a different preprocessing. Each DDB prepares at most 64 preprocessed 8 bit words, which are then sent directly to the local bus of the neural network boards via a specially developed so called mezzanine board in order to cope with the time constraint.

The networks are evaluated on the neural network boards featuring the 1064-CNAPS chips (20 MHz, 128 Mcps) by Adaptive Solutions [75]. This parallel-processor chip was commercially available. It is an array of 64 parallel fixed-point arithmetic processors. The processors are freely programmable in the single-instruction-multiple-data (SIMD) architecture. The CNAPS chip is able to perform fast matrix-vector multiplication and accumulation, which are the basic operations needed for the evaluation of FFNNs but also other parallel algorithms can be implemented. The neural network boards are usually equipped with only one 1064-CNAPS chip which leads to the upper limit on the size of the processable FFNN of $64 \times 64 \times 1$.

For synchronisation the neural network boards are driven with an external clock at 20.8 MHz (2 times the HERA clock frequency of 10.4 MHz). Performing the first matrix-vector multiplications already parallel to the input of network inputs, a $64 \times 64 \times 1$ FFNN is evaluated within 8 μs. The 8 bit network result is then sent back to the corresponding DDB from where it is sent to the central trigger logic.

The DDB and the corresponding neural network board is called a *trigger box* (L2TB). Each trigger box creates one level 2 trigger element of the L2NN trigger. In the years 1999 and 2000 the L2NN had 12 trigger boxes. Each trigger box is running a FFNN or a special parallel algorithm for dedicated physics reactions. This modular approach results in easy maintenance and update of the trigger. The FFNN and the parallel algorithm used in this analysis are described in the sections 4.2.3 and 4.2.4.

In order to load and monitor the L2NN trigger a Themis Sun Sparc two processor VME workstation is used. An additional card, the "spy" card, is listening also to the L2-bus and is collecting the raw detector data, the data preprocessed by the DDBs and the network results. Due to time constraints this cannot be performed for each event, but is done with a rate of ≈ 10 Hz. The collected raw detector information is taken as input for a bit-precise simulation of the L2NN trigger (see [76] and section 6.1). The simulated DDB-preprocessed data and the simulated network result are compared to the real data (*online-check*).

Easy and convenient requesting and checking of the monitoring results is provided by a CGI-based[6] interactive web-interface [77] which was developed as part of this work. This web-interface allows to control the running of the L2NN only requiring an usual web-browser. The information provided includes the system status of the Sun

[6] common gateway interface

workstation, the current and archived trigger rates, the current and archived control histograms and the results of the online-checks. In order to quickly — before the timeout of the web-server — retrieve the archived trigger rates and control histograms a specialised database system was developed.

4.2.3 Feed Forward Neural Network for the Track-Cluster Sample

Since July 1999 a FFNN is running on trigger box 8 (L2TB 8) of the L2NN in order to trigger J/ψ events of the track-cluster sample. The trigger box 8 is validating the high rate L1ST `S33` (see figure 4.6).

The FFNN has 8 input nodes, 6 hidden nodes and one output node. The 8 input quantities to the network contain information about the number of the track mask of the DC$r\phi$-trigger, the maximum and total content of the $z-$vertex histogram, the number of bigrays, and the energy in the LAr-calorimeter and the SpaCal:

`trtot`		(see table 4.1)
`cpvmax`,	`cpvsum`	(see table 4.2)
`nbigbwd`,	`nbigray`	(see table 4.2)
`larife`		(see table 4.3)
`spcent1`,	`spcent3`	(see table 4.4)

For the training of the neural network J/ψ events of the Track-Cluster sample of the year 1997 were used. These events were selected for an analysis contributing to [14]. During the development of this neural network the L1ST `S33` was created. In order to take the background situation of the new `S33` into account, background events had to be taken from the year 1999. The development of the `S33` and training of the neural network are described in [66]. The neural network is operated in the L2NN with a threshold value of the output node of 0.68, which corresponds to a *working point* at an efficiency of 94% and a rate reduction of a factor 16 (rejection of 93.8%). The efficiency versus rejection plot containing the working point is shown in figure 4.7.

4.2.4 SpaCal-Back-To-Back Algorithm for the Cluster-Cluster Sample

On trigger box 6 (L2TB 6) a special parallel algorithm, the SpaCal-Back-to-Back (SBaBa) [68], is running. This algorithm is designed to detect the back-to-back topology of the two clusters in the SpaCal of the decay electrons of the J/ψ in the cluster-cluster topology. The trigger box 6 is validating the high rate L1ST `S40` (see figure 4.6).

The SBaBa-algorithm uses the 20×20 SIET-bits of the medium threshold as input (see section 4.1.4). The information is transfered in the 61 bitpacked words `spcll`i and `spclh`j. The 400 trigger bits are mapped by a parallelised vector-matrix multiplication to 64 topological masks. These masks have a sector-like shape and the masks in the central region of the SpaCal are smaller than those in the outer part. A mask is

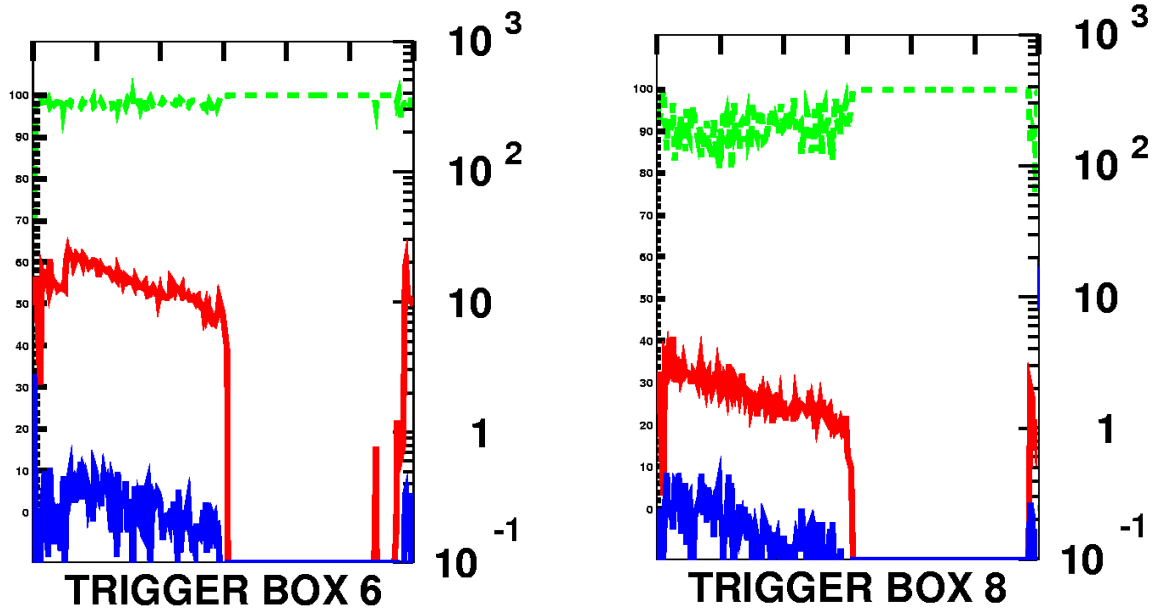

Figure 4.6: For the trigger box 6 (cluster-cluster sample) and the trigger box 8 (track-cluster sample) the input rate from level 1 (middle line) and the output rate of level 2 are shown (lower line) versus time. The corresponding scale is the logarithmic scale on the right side in Hz. From the input and output rates the rejection of the trigger boxes are calculated (upper line). The corresponding scale is the linear scale on the left side in percent. The figures show the rates for 24 hours (Feb. 20, 2000). The decreasing rate from level 1 shows the decreasing beam currents with time (see figure 2.2).

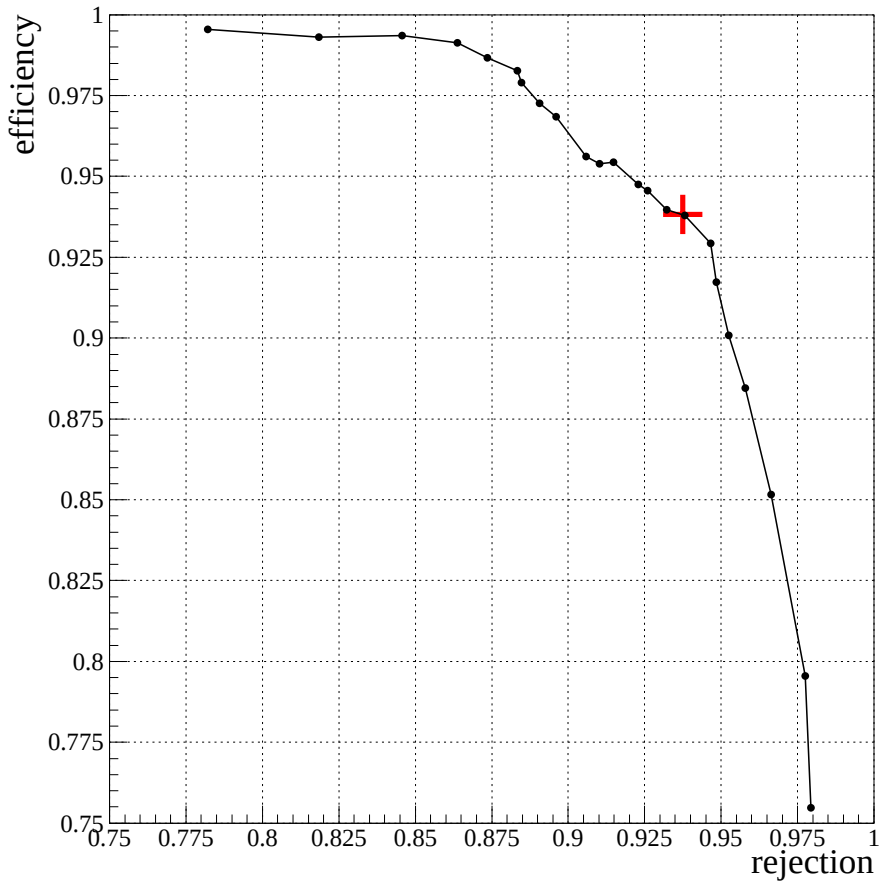

Figure 4.7: The efficiency versus the rejection of the FFNN for the track-cluster sample is shown. The *efficiency* is the fraction of signal events, which pass the network decision. The *rejection* is the the fraction of background events, which are classified as background. The different points result from a variation of the threshold value (*output cut*) of the neuron in the output layer. In order to obtain the values for efficiency and rejection the independent test sample (see section 4.2.1) was used. The data for the plot are taken from [66]. The working point of the network is chosen to be at an output cut of 0.68, which is marked by the cross. The efficiency versus rejection plot is a handle on the performance of the FFNN. The performance is better, if the curve is closer to the point (1,1).

activated, if one of the contained SIET-bit is set. Each of the mask is then associated with one processor node of the CNAPS-chip in order to allow fast parallel processing.

The next steps of the algorithm are explained using an example (see figure 4.8). An event with two back-to-back clusters in the SpaCal is considered. The SIET-bits of one cluster activate a mask A. The SBaBa-algorithm checks two conditions:

- Back-to-back condition: For the mask A a corresponding back-to-back zone is defined. It is then checked, if there is an activated mask in the back-to-back zone of mask A. In this example it is the mask B.
- Veto condition: Around the mask A a neutral zone is defined. It is checked, if a mask is activated, which does not belong to the neutral zone or the back-to-back zone. In this example there is no such mask.

A fulfilled back-to-back condition and failed corresponding veto condition is needed for a positive trigger decision of the SBaBa. The back-to-back condition and the veto condition are performed for all 64 masks, which is implemented as parallel scalar products.

The algorithm is designed to have an uniform efficiency up to a violation of the back-to-back condition of 30°. This directly affects the shape of the back-to-back and neutral zone.

In addition to the topological conditions the SIET-bits of the low threshold around the beam pipe are used as a veto. The total processing time on the CNAPS chip is 7.9 μs.

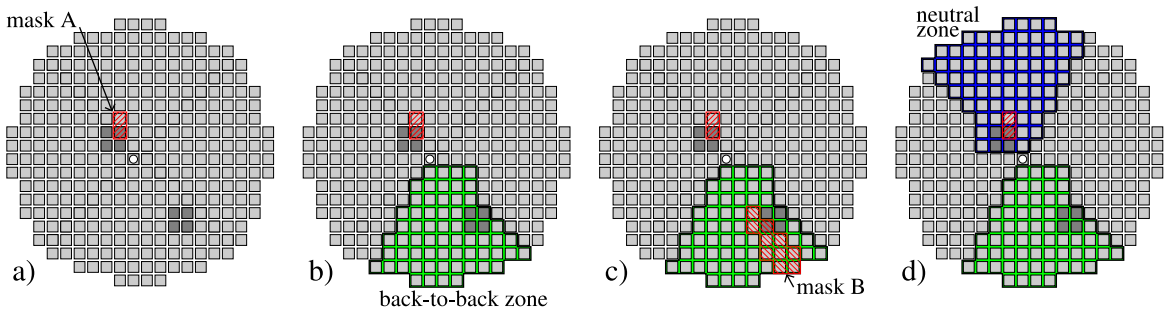

Figure 4.8: The "steps" of the SpaCal-Back-To-Back algorithm are shown: a) For the two clusters two SIET bits fire, shown in dark gray. The activated mask is shown as a dashed box. b) The corresponding back-to-back zone for the mask is highlighted. c) In the back-to-back zone an active mask is found. The back-to-back condition is fulfilled. d) The back-to-back zone and the neutral zone are highlighted. Outside of both zones no active mask is found. The veto condition is not fulfilled. The "steps" are calculated in parallel on the CNAPS chip.

4.3 Trigger Level 4

At the trigger level 4 the detector is fully read out and the detector data is fully available on trigger level. The information is stored in an event buffer with a capacity

of 30 events. After the information for one event is synchronised (event builder) a full event reconstruction is performed.

The strategy of the trigger level 4 is, that only events tagged by *finders* pass and are sent to permanent storage. A finder is a small software routine designed to select events of a special physics class. For monitoring purposes a small fraction of the rejected events is kept. Events not tagged by a finder get a high prescale, called *L4 weight*, of ≈ 100. According to the finders the events get a *classification bit*.

Regarding the different event topologies of the track-cluster and cluster-cluster events (see section 3) the finders `JPSPATC` and `JPSPAC`[7] are used in this analysis. The finders are described in the following in the order `JPSPAC`, `JPSPATC` in order to start with a simpler finder and to proceed to the more complicated one:

- `JPSPAC`: This finder selects events of the photoproduction J/ψ cluster-cluster topology. All electromagnetic clusters in the SpaCal have to fulfil the requirements on the energy and the radius of the cluster: $E > 3\,\mathrm{GeV}$ and $r_{\mathrm{cl}} < 5$ cm. An additional energy cut is applied on the energy E_{max} of the most energetic cluster in the SpaCal. The cut value depends on the distance R_{cl} of the cluster from the z-axis:

$$\begin{array}{rrll} E^{\mathrm{max}} > & 12\,\mathrm{GeV} & \text{for} & R_{\mathrm{cl}} < 15\ \mathrm{cm} \\ E^{\mathrm{max}} > & 7\,\mathrm{GeV} & \text{for} & R_{\mathrm{cl}} < 25\ \mathrm{cm} \\ E^{\mathrm{max}} > & 5\,\mathrm{GeV} & \text{for} & R_{\mathrm{cl}} \geq 25\ \mathrm{cm} \end{array}$$

- `JPSPATC`: The finder selects events of the photoproduction J/ψ and Υ track-cluster topology and the electroproduction J/ψ track-cluster topology, where the beam electron is scattered into the SpaCal. The algorithms for the both photoproduction finders are similar. For all clusters considered a minimal energy of 0.2 GeV and a maximal radius of 5 cm is required. For all tracks considered a maximal distance-of-closest- approach to the z-axis of 4 cm, a minimal track length of 10 cm, a minimal transverse momentum of 0.15 GeV and a maximal distance of the starting point of the track to the z-axis of 50 cm are required. There have to be 1 or 2 clusters in the SpaCal and 1 to 4 tracks in the central region. One of the tracks has to fulfil $\theta > \theta_i^{\mathrm{min}}$ and a corresponding cluster with the "back-to-back" condition $\phi_i^{\mathrm{min}} < |\phi_{\mathrm{track}} - \phi_{\mathrm{cluster}}| < \phi_i^{\mathrm{max}}$ has to exist ($i \in \{J/\psi, \Upsilon\}$). This cluster has to fulfil in addition an energy cut of the the following form

$$E_{\mathrm{cluster}} < \frac{s_i}{R - R_i^{\mathrm{offset}}} + E_i^{\mathrm{offset}}\,, \tag{4.7}$$

  where E_{cluster} is the cluster energy, R is the distance of the cluster from the z-axis and the parameters are listed below. In addition a cut on the energy of the highest energy cluster is applied $E_{\mathrm{cluster}}^{\mathrm{max}} < E_i^{\mathrm{max}}$ in order to reject events from DIS. For the Υ event selection an additional lower energy cut of the type

[7] The naming convention for the finders is not consistent. `JPSPAC` was the first finder for J/ψ events using SpaCal information. Later the finder `JPSPATC` for the track-cluster events was implemented.

equation 4.7 is applied. The parameters are marked by "<", ">" for the upper and lower energy cut. The parameters for the J/ψ and Υ sample are

$$
\begin{array}{lll}
s_{J/\psi} = 5\,\mathrm{GeV\ cm}\,, & R^{\mathrm{offset}}_{J/\psi} = 10\ \mathrm{cm}\,, & E^{\mathrm{offset}}_{J/\psi} = 2.5\,\mathrm{GeV}\,, \\
\theta^{\mathrm{min}}_{J/\psi} = 1.40\ \mathrm{rad} \approx 80^\circ\,, & \phi^{\mathrm{min}}_{J/\psi} = 1.64\ \mathrm{rad} \approx 94^\circ\,, & \phi^{\mathrm{max}}_{J/\psi} = 4.64\ \mathrm{rad} \approx 266^\circ\,, \\
E^{\mathrm{max}}_{J/\psi} = 20\,\mathrm{GeV}\,, & & \\
s^{<}_{\Upsilon} = 15\,\mathrm{GeV\ cm}\,, & R^{\mathrm{offset},<}_{\Upsilon} = 10\ \mathrm{cm}\,, & E^{\mathrm{offset},<}_{\Upsilon} = 4.5\,\mathrm{GeV}\,, \\
s^{>}_{\Upsilon} = -6\,\mathrm{GeV\ cm}\,, & R^{\mathrm{offset},>}_{\Upsilon} = 10\ \mathrm{cm}\,, & E^{\mathrm{offset},>}_{\Upsilon} = 24\,\mathrm{GeV}\,, \\
\theta^{\mathrm{min}}_{\Upsilon} = 0.35\ \mathrm{rad} \approx 20^\circ\,, & \phi^{\mathrm{min}}_{\Upsilon} = 2.64\ \mathrm{rad} \approx 151^\circ\,, & \phi^{\mathrm{max}}_{\Upsilon} = 3.64\ \mathrm{rad} \approx 209^\circ\,, \\
E^{\mathrm{max}}_{\Upsilon} = 10.1\,\mathrm{GeV}\,. & &
\end{array}
$$

For the electroproduction J/ψ track-cluster sample 1 to 4 tracks and 2 to 3 clusters are required. The energy E_1 of the cluster with highest energy has to fulfil $E_1 > 10\,\mathrm{GeV}$. The energy E_2 of the cluster with the second highest energy has to fulfil a position dependent cut of the form of equation 4.7 with the parameters

$$
s_{J/\psi,\mathrm{DIS}} = 10\,\mathrm{GeV\ cm}\,, \quad R^{\mathrm{offset}}_{J/\psi,\mathrm{DIS}} = 7\ \mathrm{cm}\,, \quad E^{\mathrm{offset}}_{J/\psi,\mathrm{DIS}} = 3\,\mathrm{GeV}\,.
$$

In addition to the event selection the full event information is used in order to perform an online check of the previous trigger levels and the detector read out. The read out of the detector components and the read out of the corresponding trigger systems are compared. For example the L1ST are recalculated and validated.

4.4 Trigger Level 5

The trigger level 5 is an offline trigger level and uses the *raw-data tapes* (RAWD) ($\approx$ 110 kByte/event) as input. On this trigger level the full event reconstruction is performed. Originally this trigger level was planned to also reject events. This became obsolete when the trigger level 4 was upgraded to perform a full event reconstruction.

The difference between the event reconstruction of the online trigger level 4 and the offline trigger level 5 is, that in the offline stage information can be used, which is only available after a run is finished. Such information are e.g. already improved alignment and calibration and better information about the beam position.

From the raw detector data the reconstruction builds e.g. tracks and clusters. This information and a subset of the information from the raw-data tapes are written to *physics output tapes* (POT) ($\approx$ 150 kByte/event). The information from POT is subjected to further selection and compression and is stored on *data summary tapes* (DST) ($\approx$ 14 kByte/event).

With this multi step process of data selection and compression the DST are achieved, which allow a convenient physics analysis. For checks of the detector read out, the trigger functionality and the performance of the event reconstruction in addition the more basic information from POT and RAWD is necessary.

After the data taking and the first physics analyses better alignment and calibration is achieved. Taking this into account a new event reconstruction is done using RAWD as input. The corresponding POT and DST are numbered with the reconstruction number: POT1, POT2, POT3, DST1, DST2, DST3.

Chapter 5

Monte Carlo Simulation

The simulation of a physics event is a two step process: the *generation* and the *detector-simulation*, which are described in this chapter. The reconstruction of simulated events and real data is described in the next chapter.

The *generation* step starts with the initial state particles — here electron and proton — and builds a set of final state particles with four-vector information according to the physics process being studied. A physics process can either be simulated from first principles or according to probability distributions. In either case a finite event sample is produced, which has to be large enough to represent the richness of the process. Technically this is done by throwing random numbers according to the probability distributions, which gave this technique the name *Monte Carlo method* (MC). The programs are called *event-generators* or *generators*.

In the *detector-simulation* step the final state particles are propagated through the H1 detector according to their four-vectors and the detector response is simulated.

The *reconstruction* step (see chapter 6) uses the simulated detector response in order to build physics objects like tracks and energy-clusters. The generated events which passed the detector-simulation and the reconstruction are called *MC events*.

The MC usage and the actual physics processes, which are simulated, are the topic of the following section.

5.1 Event Generators

In this analysis MC events are used in order to obtain

- the acceptance of the detector,
- the efficiency of subdetectors and triggers,
- the contamination from other physics processes (background).

For each of the purposes different event-generators are used. In order to obtain the acceptance and the efficiencies, simulated events from proton-elastic J/ψ photoproduction (*signal MC*) are used (see section 5.1.1).

The contamination from other physics processes has several sources. These processes show the same basic experimental signatures as the proton-elastic J/ψ photoproduction (*signal events*) (see chapter 3):

- detector signals from two electrons,
- detector signals from the forward detectors (fwd.-tagged/fwd.-untagged) and
- an empty detector otherwise.

The contaminating processes (see figure 5.1) are the proton-dissociative J/ψ photoproduction, the electron pair production and the QED compton scattering, which are described in the following.

In the *proton-dissociative J/ψ phototoproduction* (see figure 5.1 (b)) the proton is excited such, that it dissociates into hadrons X. This hadronic system leaves the detector either undetected through the beam pipe (fwd.-untagged) or is detected by the forward detectors (fwd.-tagged). The basic experimental signature is the same as for the signal events and contributes to background. The corresponding generator is described in section 5.1.1.

In *electron pair production* (see figure 5.1 (c) and (d)) both the beam electron and the beam proton radiate a photon and an electron pair is created. If the beam electron leaves the detector undetected through the beam pipe, these events also show the basic experimental signature of signal events and contribute to background. The electron pair production event generator for proton-elastic and proton-dissociative events is presented in section 5.1.2.

In *QED Compton scattering* (see figure 5.1 (e) and (f)) the beam electron radiates a photon. If the photon hits the detector in an area, where no photon-electron separation is possible, or the photon converts to an electron-positron pair of which only one is detected. The basic experimental signature is the same as for the signal events and these events contribute to the background. The QED Compton event generator is the topic of section 5.1.3. Proton-elastic and proton-dissociative events can be generated.

5.1.1 Vector Meson Event Generator `DiffVM`

The generator `DiffVM` [78, 79] simulates the diffractive production of vector mesons. It is based on the Vector Meson Dominance Model (see section 1.2) and Regge theory (see section 1.6). The generator is able to describe a variety of physics processes, i.e. the proton-elastic and proton-dissociative production of different vector mesons and their decay in different channels. In this analysis the production of J/ψ vector mesons with the decay into an e^+e^- pair is used.

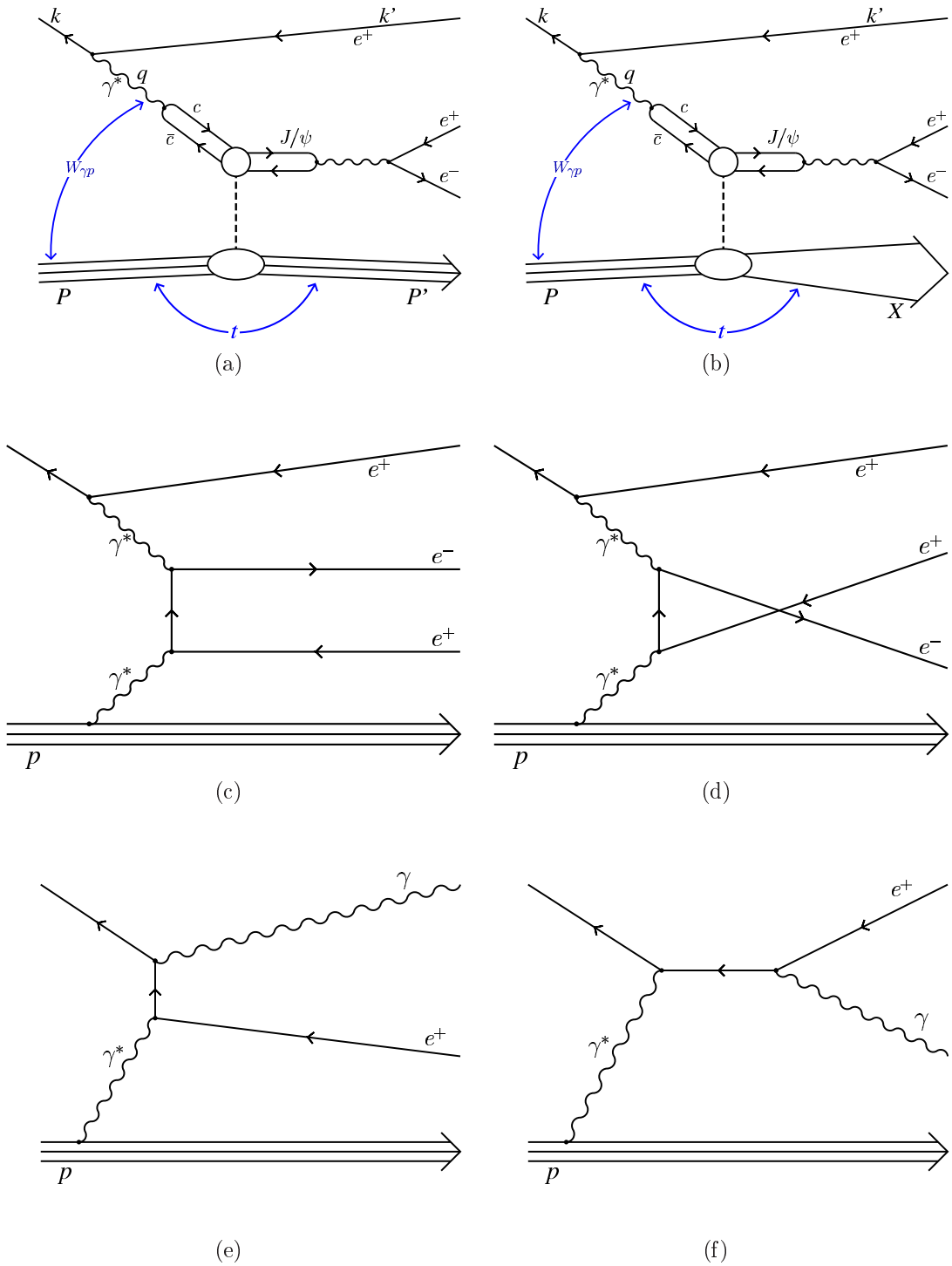

Figure 5.1: Feynman diagrams for the proton-elastic (a), the proton-dissociative J/ψ photoproduction (b), the electron pair production (c and d) and the QED Compton scattering (e and f) are shown. The processes (b) - (f) can exhibit the basic experimental signature of signal events (a).

The parametrisation of the Q^2 dependence of the cross section is based on equation 1.11 and equation 1.12. The exponent 2 in equation 1.11 is replaced by the parameter

$$n = 2.1 \tag{5.1}$$

and the proportionality sign of equation 1.12 is replaced by an equal sign.

The parametrisation of the $W_{\gamma p}$ and t dependence of the cross section is based on equation 1.45 for the proton-elastic case and on equation 1.61 for the proton-dissociative case. The parameters are set to the values

$$\begin{aligned} \varepsilon = \alpha^0 - 1 &= 0.175\,, & (5.2)\\ \alpha' &= 0.0\,, & (5.3)\\ b_{\text{pelas}} &= 4.8\,\text{GeV}^{-2}\,\text{c}^2\,, & (5.4)\\ b_{\text{pdiss}} &= 1.6\,\text{GeV}^{-2}\,\text{c}^2\,. & (5.5) \end{aligned}$$

In the case of proton-dissociative J/ψ production the `DiffVM` generator includes the following parametrisation of the cross section with the mass of the hadronic system M_X [78] (see also equation 1.63)

$$\frac{\mathrm{d}\sigma^{J/\psi p}_{\text{pdiss}}}{\mathrm{d}{M_X}^2} \propto \frac{f({M_X}^2)}{{M_X}^{2(1+\varepsilon_M)}}\,, \tag{5.6}$$

where the parameter ε_M can be chosen independently from ε and is set to

$$\varepsilon_M := 0.0808\,. \tag{5.7}$$

For small $M_X < 3.6\,\text{GeV/c}^2$ the dissociated proton is assumed to be one of the resonances $N(1440)$, $N(1520)$, $N(1680)$ or $N(1700)$, which decay isotropically in their rest system. A fit to data from proton-deuterium scattering in this mass regime yields the function $f({M_X}^2)$ [39]. For larger masses $M_X \geq 3.6\,\text{GeV/c}^2$ the function is set to $f({M_X}^2) = 1$ and the fragmentation of the dissociated proton is treated according to the Lund-String-Model using the `JETSET` program [80].

5.1.2 Lepton Pair Production Event Generator `LPair2`

The electron pair production process $e^+p \to e^+p\,e^+e^-$ contributes to the background for the elastic J/ψ photoproduction. The lowest order Feynman graphs are shown in figure 5.2. The main contribution to the background results from the Bethe-Heitler process [81] (see figure 5.2 (a) and (b)), where both the beam electron and beam proton radiate a photon which scatter and produce an electron-positron pair.

The generator LPair2 [82] simulates the Bethe-Heitler process. The interference between the beam positron and the positron of the electron pair is included.

In the Cabibbo-Parisi process (see figure 5.2 (c) and (d)) a photon is exchanged between the beam electron and the beam proton. The beam electron radiates another photon which converts to an electron-positron pair. In [83, 84] it is shown, that additional contributions due to the Cabibbo-Parisi process or further processes containing the radiation of a photon from the proton or the exchange of Z^0 do not give significant additional contribution and can be neglected.

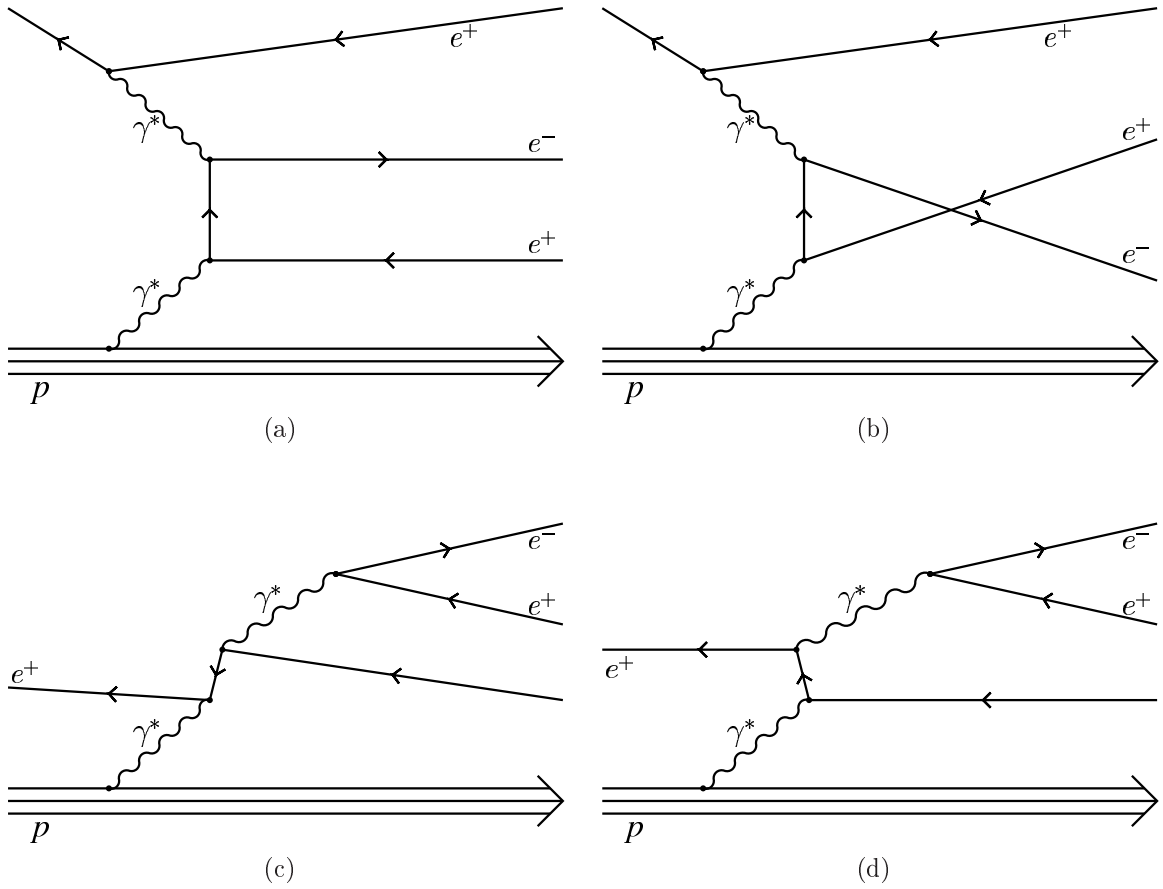

Figure 5.2: The lowest order Feynman graphs which contribute to the electron pair production are shown. The graphs (a) and (b) are called Bethe-Heitler process and the graphs (c) and (d) are called Cabibbo-Parisi process.

5.1.3 QED Compton Scattering Event Generator COMPTON

In the QED Compton process $e^+p \to e^+\gamma p$ the beam-electron interacts with the beam-proton by the exchange of a virtual photon and the beam-electron radiates a real photon (see figure 5.1 (e) and (f)).

The simulation of the QED Compton process is done by the COMPTON generator [85, 86]. [87] implemented the generation of the hadronic final state, i.e. proton breakup.

The elastic, resonance and continuum inelastic QED Compton events are generated simultaneously. For the production of the hadronic final state with low hadronic mass $M_X < 5\,\mathrm{GeV}/\,\mathrm{c}^2$ the EPSOFT2 package is used. EPSOFT2 is based on EPSOFT [88], which is a generator for soft diffractive and non-diffractive photoproduction collisions. For high hadronic mass $M_X > 5\,\mathrm{GeV}/\,\mathrm{c}^2$, where the quark parton model is valid, the fragmentation is done by PYTHIA and JETSET [89].

5.1.4 Abbreviations

In the legend of figures the following abbreviations for the different MC samples are used:

DVM pel.	:	proton-elastic	`DiffVM`
DVM pdi.	:	proton-dissociative	`DiffVM`
LPR pel.	:	proton-elastic	`LPair2`
LPR pdi.	:	proton-dissociative	`LPair2`
COM pel.+pdi.	:	proton-elastic and proton-dissociative	`COMPTON`

5.2 Detector Simulation

The output of the different generator programs for each event is a set of particles in the final state with four-vector information. In the detector simulation these particles are propagated through a virtual detector and the interactions of the particles with the detector components are simulated. For this purpose the `GEANT` program package [90, 91] is used. It also applies MC methods. From the simulated interactions and the resulting ionisations and energy depositions the detector response is calculated. This is done in the `H1SIM` program package [92], which includes the `GEANT` program package and handles the simulation of the full H1 detector. The result of the detector simulation is detector response information, which has the same format as real data. The detector response information is taken as input for the reconstruction (see chapter 6).

Chapter 6

Reconstruction

The result of the detector read out and of the MC simulation is detector response information, which is caused by localised energy depositions or ionisations. Based on this information the reconstruction builds high level physics objects like tracks or energy clusters. The detector response information for real data and for simulated MC events has the same format and is processed with the `H1REC` [93] program package. For simulated MC events the standard reconstruction includes also the calculation of the trigger decision.

The description of the reconstruction concentrates on the following topics essential for this analysis: the trigger calculation, especially the level 2 neural network trigger (see section 6.1), the special BST track finding (see section 6.2), the reconstruction of kinematic variables (see section 6.3) and the treatment of the forward detectors (see section 6.4.3). The standard reconstruction is described in [93].

6.1 Trigger Calculation

The trigger calculation is part of the `H1REC` [93] and `H1TRIG` program packages. The calculation of the trigger decision for simulated MC events is the basis for the determination of the level 1 trigger efficiencies and for the check and determination of the level 2 trigger efficiencies (see section 8.4).

In order to cross check the calculation of the level 1 subtriggers `S33` and `S40` for the track-cluster and cluster-cluster sample (see section 4.1.6) the distribution of the level 1 trigger elements for simulated MC events are compared to data. Figure 6.1 shows good agreement of simulation with data.

The calculation of the level 2 neural network trigger (L2NN) (see section 4.2) is performed by the program package `NETSIM` [76], which is a part of `H1TRIG`. The calculation of the L2NN takes the calculated output of the level 1 subdetector triggers as input. `NETSIM` performs a bit-precise simulation of the L2NN. It simulates the preprocessing of the input data by the DDB (see section 4.2.2) and the calculation of the neural networks or other algorithms on the CNAPS chips.

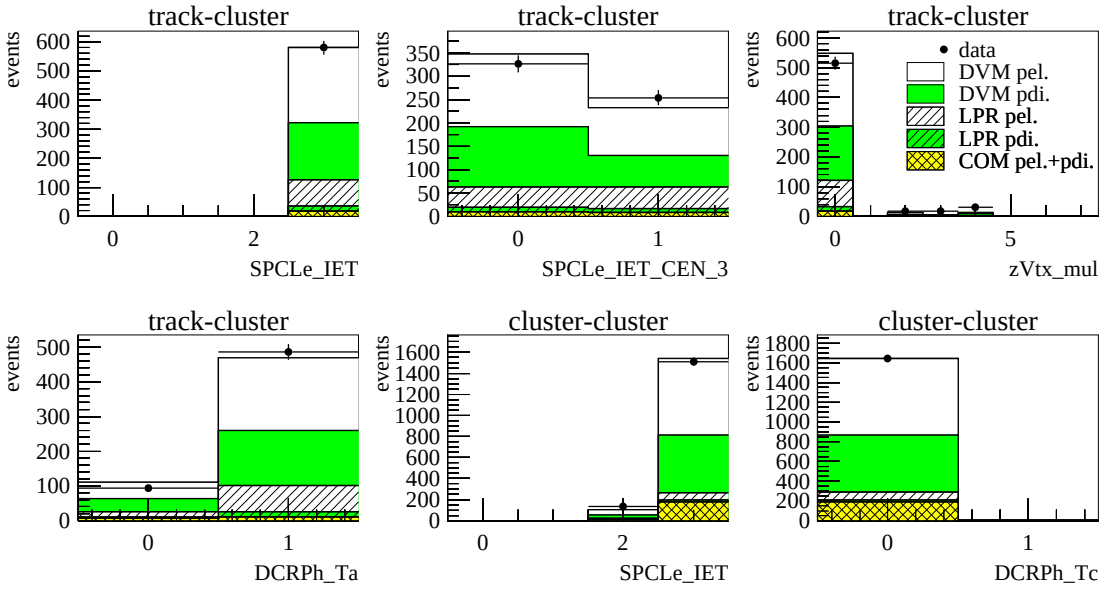

Figure 6.1: The distribution of the level 1 trigger elements of the L1ST `S33` and `S40` are compared for data and MC events. The trigger elements are described in section 4.1 and the abbreviations in the legend are described in section 5.1.4.

In figure 6.2 and figure 6.3 the distributions of the input quantities and the trigger results for the L2TE of the track-cluster and cluster-cluster samples are shown for data and MC events. The distributions agree well. Thus the simulation can be used to determine the trigger efficiency from MC.

Further applications of the simulation of the L2NN are the monitoring of the L2NN system and the training of new networks. Monitoring of the operation of the L2NN hardware is performed by comparing the trigger information delivered by the hardware to the calculated result. This comparison is done online in regular intervals on the Sun-workstation of the L2NN. It is planed to implement `NETSIM` into the trigger level 4 in order to increase the online-monitoring capabilities. As an offline application `NETSIM` monitors, whether consistent data is written to tape. `NETSIM` computes also the network inputs from already taken data. This information is used for the training and testing of new networks.

6.2 BST Track Finding

In the cluster-cluster sample both J/ψ decay electrons are detected in the SpaCal and no central tracks exist. Therefore no event vertex information is available, which would lead to a precise measurement of the polar angle θ of the decay electrons. In order to determine the event vertex for cluster-cluster events the use of other tracking detectors is discussed.

The backward drift chamber BDC (see section 2.2.1.5) has limited spatial extension in

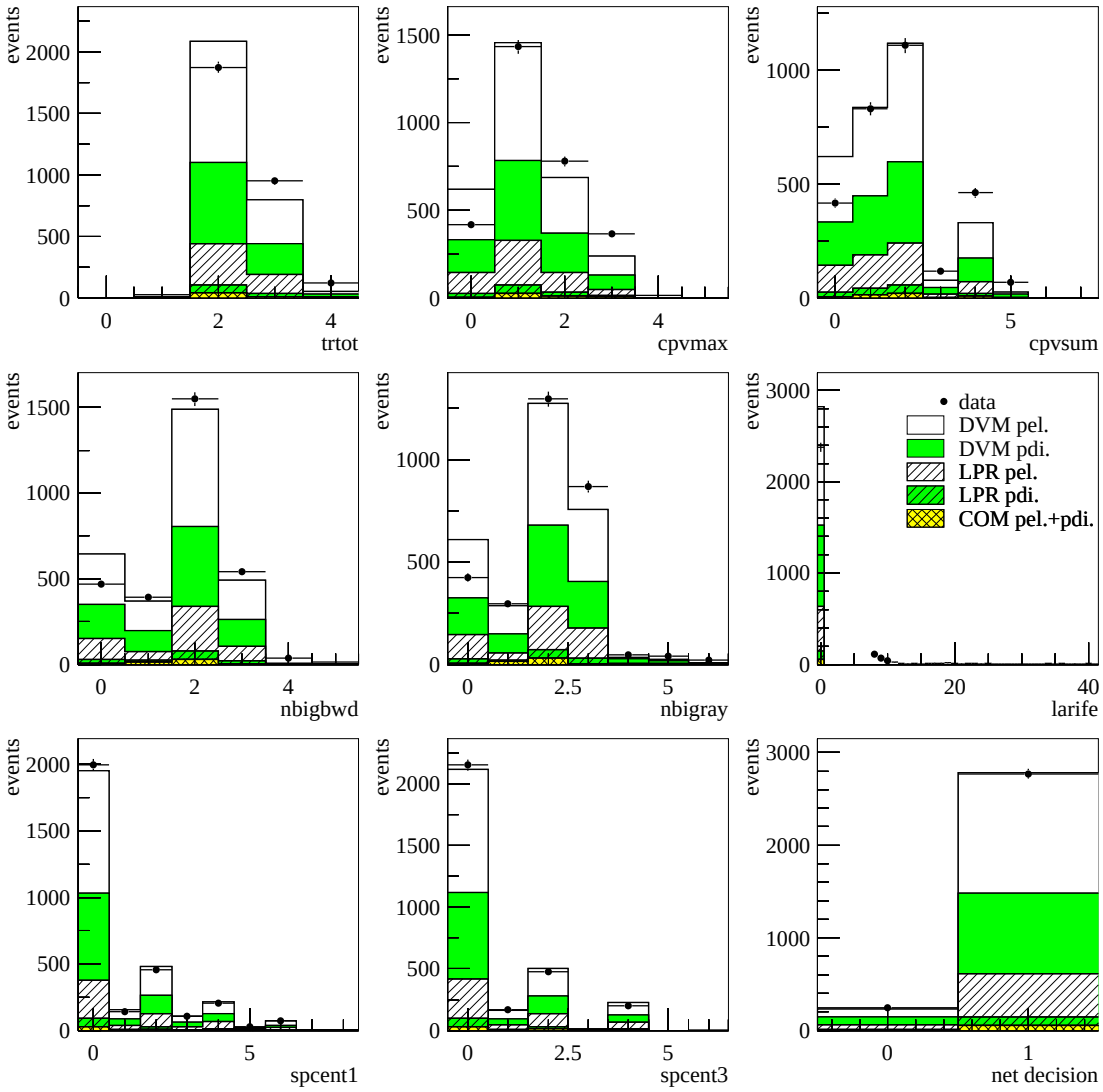

Figure 6.2: For the track-cluster neural network the distributions of the input quantities and the network decision are shown. The network is described in section 4.2.3. There references to detailed descriptions of the input quantities are given.

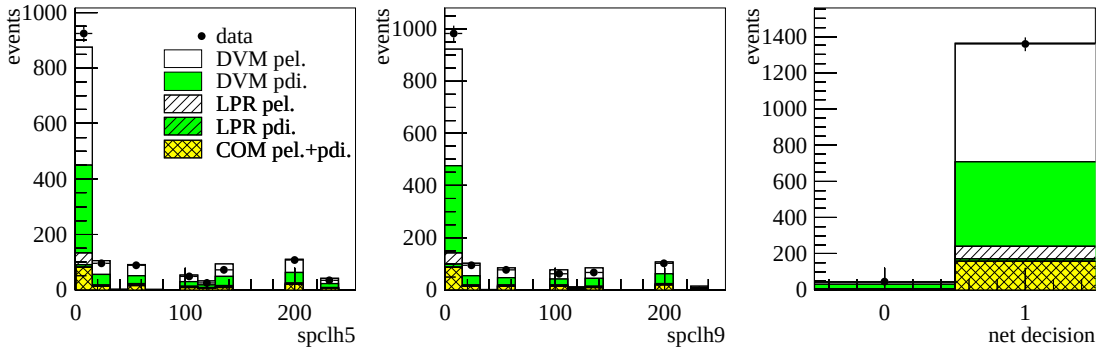

Figure 6.3: For the SBaBa algorithm (see section 4.2.4) the distribution of a subset of the 61 input quantities (see section 4.1.4) and the trigger decision are shown.

z-direction. This results in an insufficient resolution in the polar angle θ of the standalone BDC tracking. Therefore the BDC cannot be used for the vertex determination. However, the BDC is used to improve the measurement of the spatial position of the SpaCal clusters.

The precise hit information of the backward silicon tracker BST (see section 2.2.1.2) enables us to perform a track-fit in the very backward region with sufficient resolution. Therefore an algorithm for the reconstruction of tracks based on BST hit information was developed in this analysis in order to reconstruct an event vertex.

In the following sections the algorithm of the BST track finding is described.

6.2.1 BST Track Finding Algorithm

In this analysis independent tracking in the BST is not attempted. Instead a track finding procedure for a given SpaCal cluster with polar angle θ_c and azimuthal angle ϕ_c is implemented. The track finding algorithm is performed for each J/ψ decay electron cluster.

The BST-II detector provides hit information from the r-strip detectors (section 2.2.1.2) for the 8 planes in z-direction with 16 segments in ϕ. The event display in figure 3.3 shows r-strip hits in the xy-view. The 8 planes in z-direction are overlaid.

First step of the algorithm is to obtain a set of (r, z)[1] pairs being candidates to belonging to the track for the given cluster.

The BST hits are selected by the ϕ-position of the centre of their segment ϕ_{seg}: $|\phi_{\text{seg}} - \phi_c| < 2\pi/16$. This takes the 16 segments in ϕ of the BST into account.

For the selected BST hits the r-position is determined. Based on the r-strip number and the azimuthal angle ϕ_c of the cluster the r-position of the hit is determined. Using ϕ_c the shape of the r-strips is taken into account (see figure 3.3). In this procedure

[1] $r = \sqrt{x^2 + y^2}$

the internal and external alignment[2] of the BST is applied. The r-position is further corrected for the xy-beam position and for the beam tilt. This results in a set of (r, z) pairs for the hits which are distributed over the 8 planes in the z-direction.

The next step is the selection of hits, which are used for the track finding.

Tracks starting from the region of the nominal vertex cause usually hits in at most 5 neighbouring planes [94]. Therefore all 5-hit, 4-hit, 3-hit and 2-hit combinations in 5 neighbouring planes are used as candidates for the track finding. The technical implementation of the selection of hit combinations is shown in figure 6.4. This procedure ensures, that tracks with higher number of hits are preferred to those with lower number of hits. The procedure yields high precision and high efficiency.

For each of the hit combinations a straight line fit (linear regression) is performed taking into account also the r-position of the SpaCal cluster.

In the fit the following errors on the radial position of the hits and the cluster are used: $\sigma_r^{\mathrm{BST}} = 12\ \mu$m and $\sigma_r^{\mathrm{SpaCal}} = 0.559$ cm. The value for $\sigma_r^{\mathrm{SpaCal}}$ is obtained by "stand-alone" BST tracking, i.e. the r-position of the SpaCal cluster is not taken into account for the fit. The impact position of the track in the SpaCal and the position of the SpaCal cluster are compared. The value of σ_r^{BST} is determined requiring a flat distribution of the fit probability. For further description refer to figure 6.5.

If the probability of a track fit exceeds 1% the corresponding track is taken and the track finding is stopped. For the tracks with 2 BST hits the following criteria are required in addition: The distance of the impact point of the track to the SpaCal cluster is less than 1 cm; the distance of the $z-$vertex of the track to the run-vertex is less than 35 cm; the polar angle θ of the track is less than 178°.

The resulting track is used for the measurement of the polar angle θ. The reconstruction of the event vertex depends on the number of tracks. In the case of one track the vertex position is obtained combining the track information and information of the xy-beam position. In the case of two BST tracks the vertex position for each track is determined and for the event vertex the average is taken.

6.2.2 Improvement of the Measurement of the Polar Angle and the Vertex Position

Without BST track finding the best choice for the vertex position is the average vertex position in a run $z_{\mathrm{vtx}}^{\mathrm{run}}$. Using this vertex information the following resolutions for the vertex position z_{vtx} and the polar angle θ are obtained from MC simulation:

$$\sigma(z_{\mathrm{vtx}}) = (10.5 \pm 0.3)\ \mathrm{cm}\,, \quad \sigma(\theta) = (0.52 \pm 0.02)^\circ \quad \text{(no BST track finding)}.$$

[2]For the determination of the r-position of hits a routine of the official BST reconstruction code `BSTREC` is used. `BSTREC` is part of `H1REC`.

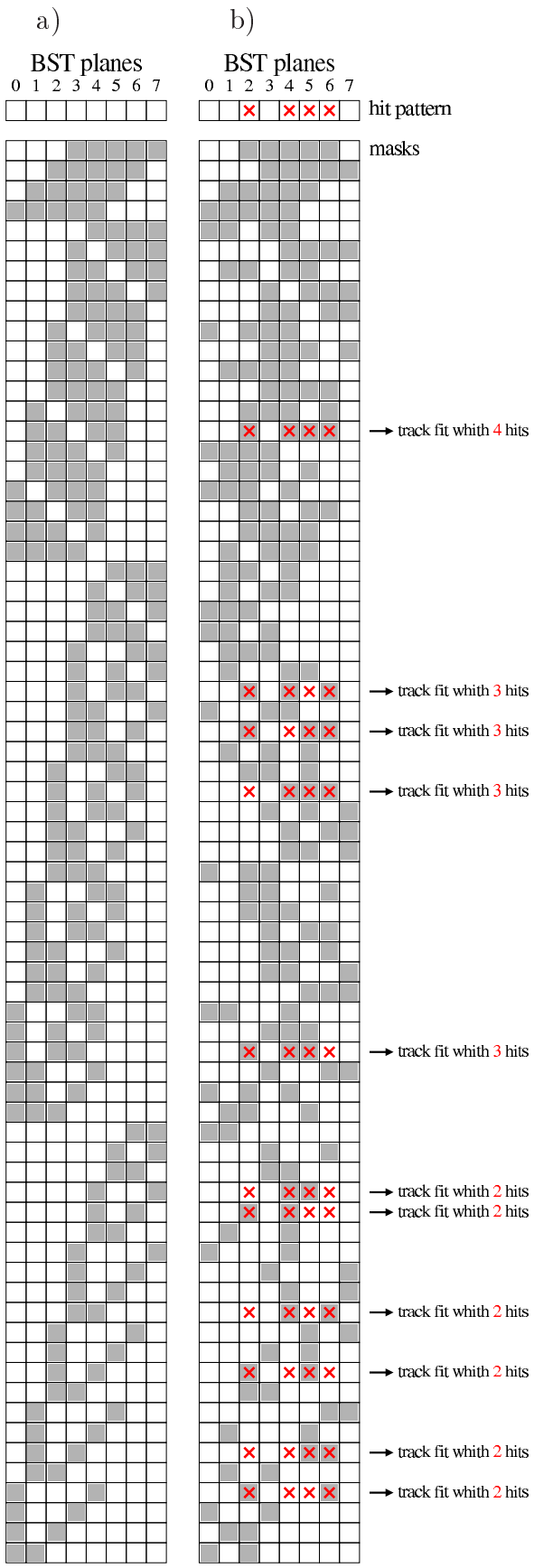

Figure 6.4: The selection of hit combinations for the track fit is shown.
a) A look-up-table with hit-selection-masks is used. The 8 columns represent the 8 planes of the BST-II. The lines contain all possible combinations of 5, 4, 3 and 2 hits on the eight planes. The combinations are sorted by the number of hits. A plane with a possible hit is shaded. Each line represents a hit-selection-mask.
b) The ordering of the hit-selection-mask with equal number of hits is randomised in order to minimise a possible bias due to the ordering of the masks. For an actual event the hits on the BST planes are taken and stored in a hit-pattern. In the hit-pattern all planes are marked (×), which contain one ore more hits. The hit-pattern is compared to the hit-selection-masks in the look-up-table starting from the top. If all selected planes of a hit-selection-mask contain a mark of the hit-pattern, a set of planes is found, which contain hits being candidates for the track fit. The hit information is presented to the track fit procedure. If there are more than one hit per plane, a loop over the multiple hits is performed.
This selection procedure ensures, that hit combinations with higher hit number are presented to the track fitting before those with lower hit number.

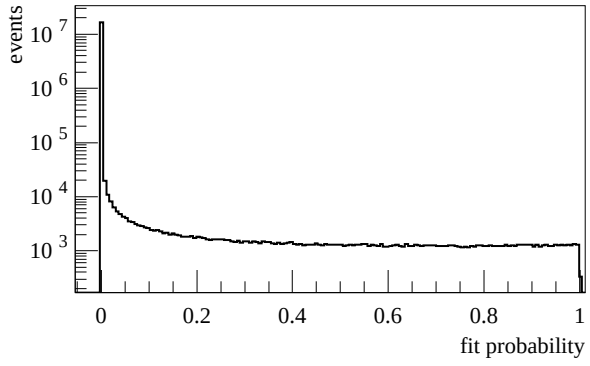

Figure 6.5: The fit probability of BST tracks fitted to 3 hits is shown for data. Beyond a probability of 0.2 the distribution for data is flat, which is expected, if the errors taken into account for the fit are well understood. For gaussian errors the probability distribution is flat over the full range. The strong rise to very low probabilities is due to noise hits.

With the track information from the BST track finding the vertex resolution with one BST track improves to:[3]

$$\sigma(z_{\mathrm{vtx}}) = (0.27 \pm 0.01)\ \mathrm{cm}\,, \quad \sigma(\theta) = (0.026 \pm 0.01)^\circ \quad \text{(with BST track finding)}.$$

The $z_{\mathrm{vtx}}^{\mathrm{BST}}$ measurement based on BST tracks is compared to the $z_{\mathrm{vtx}}^{\mathrm{CTD}}$ vertex position for track-cluster events. $z_{\mathrm{vtx}}^{\mathrm{CTD}}$ is determined from the central track and has a resolution of $\sigma(z_{\mathrm{vtx}}^{\mathrm{CTD}}) = (0.18 \pm 0.04)$ cm. Using data the following resolution for the comparison of the central track and the BST track is obtained

$$\sigma(z_{\mathrm{vtx}}^{\mathrm{BST}} - z_{\mathrm{vtx}}^{\mathrm{CTD}}) = (0.49 \pm 0.02)\ \mathrm{cm}$$

which is larger than the quadratic sum of the single resolutions. In addition to the gaussian errors systematic effects like the relative alignment of the central tracking detectors and the BST or the xy position of the beam have to be taken into account. Avoiding these systematic effects the $z_{\mathrm{vtx},1}^{\mathrm{BST}}$, $z_{\mathrm{vtx},2}^{\mathrm{BST}}$ positions of two BST tracks are compared using a subset of the cluster-cluster sample where both clusters are in the acceptance of the BST:

$$\sigma(z_{\mathrm{vtx},2}^{\mathrm{BST}} - z_{\mathrm{vtx},1}^{\mathrm{BST}}) = (0.55 \pm 0.03)\ \mathrm{cm}.$$

This value is consistent with the resolution obtained from the comparison to the central track.

6.2.3 Track Finding Efficiency and Data/MC Adjustment

The efficiency of the BST track finding is studied for data and MC[4] with special track-cluster samples, where the cluster is in the acceptance of the BST. This sample is suited

[3] The effect of the improved measurement on the invariant mass of the two decay electrons of the J/ψ is later shown in figure 7.4. For this plot the reconstruction of the invariant mass and the event selection are necessary, which are described in the following sections.

[4] In this section MC refers to proton-elastic `DiffVM`.

for the determination of the track finding efficiency, since it can be assumed, that the cluster is caused by a charged particle, i.e. electron or positron. [5]

The track finding efficiency in the data is not described by MC (see figure 6.6 a)). The adjustment of data and MC is a multiple step process and is described in the following sections.

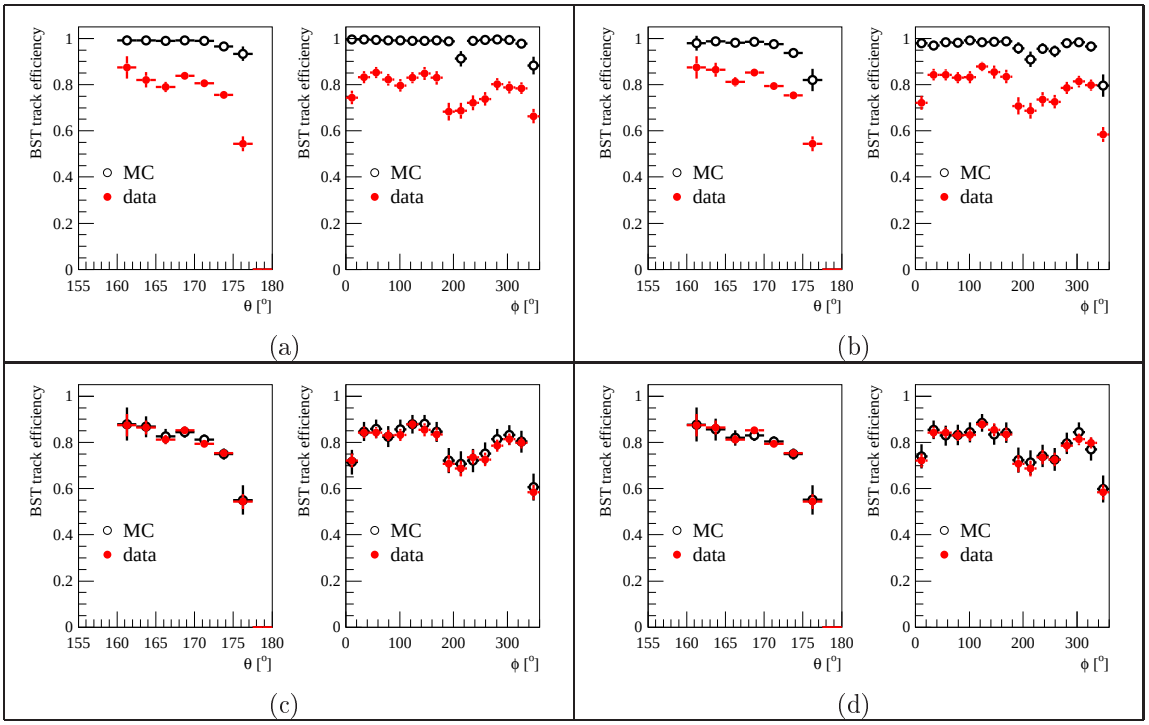

Figure 6.6: The BST track finding efficiency for data and MC is shown as a function of the polar angle θ and the azimuthal angle ϕ for the running period 2000 e^+. The four sets of plots correspond to different levels of data and MC adjustment: a) no adjustment; b) after the adjustment of the BST detector response; c) after the adjustment of the efficiency as function of ϕ and θ; d) after the adjustment of the total efficiency as a function of the `run number`.

6.2.3.1 Adjustment of the BST Detector Response

In order to improve the description of the BST track finding efficiency by MC the basic detector response of the BST is studied as a first step. The basic detector response for the track finding is the BST hit information. Each of the 8 BST-planes contains 16 sectors of detector plates, which contain 640 r-strips (see section 2.2.1.2). The number of hits per strip is shown in figure 6.7 and figure 6.8 for data and MC events. The differences between data and MC can be classified as follows:

[5] For the track-cluster sample the background is originating from the QED-Compton process and the electron-pair-production process. The rejection of QED-Compton background events is described in section 7.3.4. The contribution of the QED-Compton background can be neglected here (see the control distributions in figure 7.6). The remaining background is caused by the electron-pair-production process. Where both J/ψ decay electron candidates are due to charged particles, i.e. electron and positron.

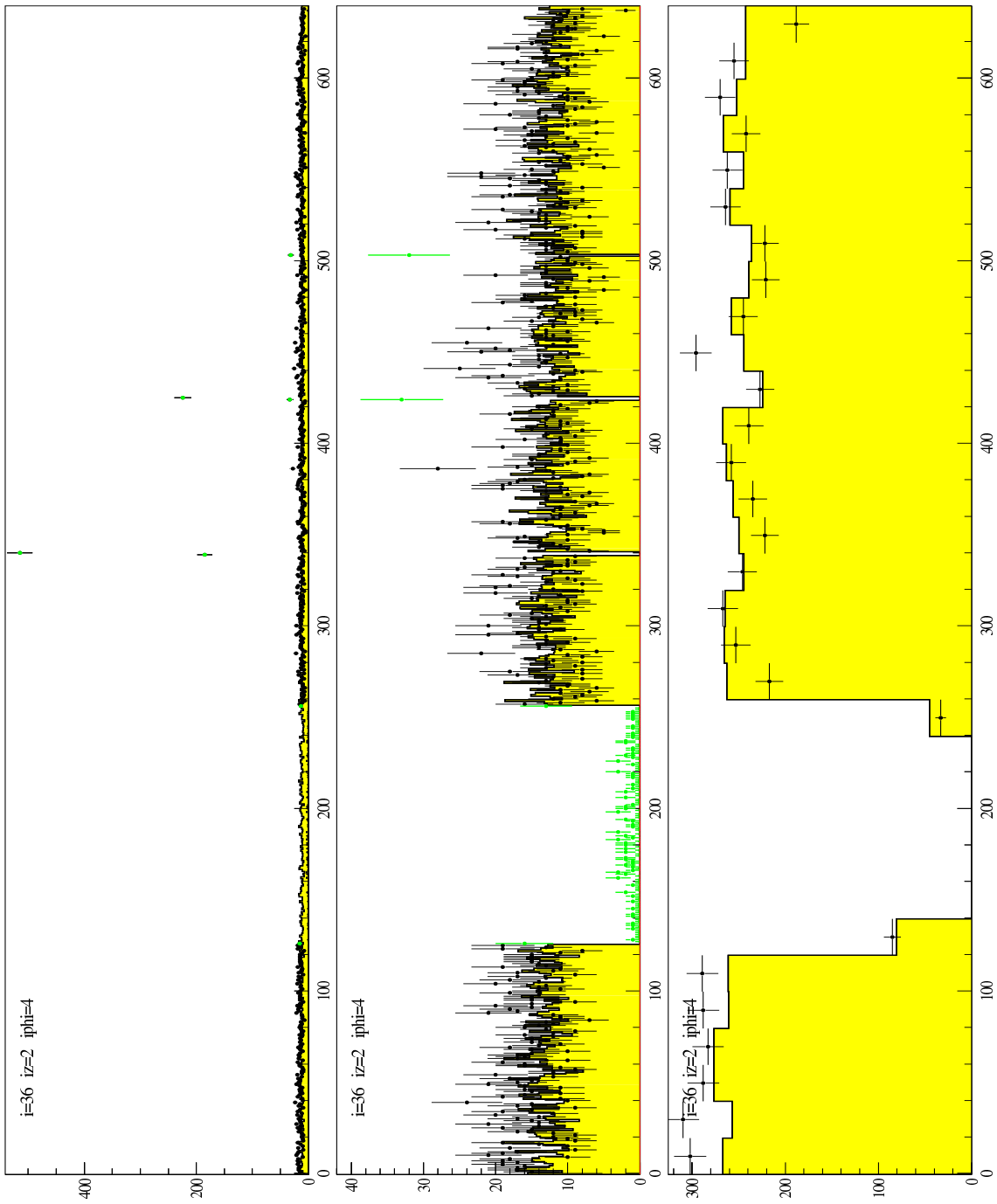

Figure 6.7: The number of hits per strip (strip number 0 to 639) are shown for the ϕ-sector 4 on z-plane 2 for the running period 2000 e^+. The dots represent data and the shaded histogram MC. The upper figure contains uncorrected data and MC. Here the 'run-away' noisy strips are clearly visible. The inefficient region in the data is also not described by MC. In the middle figure corrected data and MC are shown: The 'run-away' noisy strips and the inefficient region are cut out. The cut-out data points are drawn in grey. In the lower figure corrected data and MC are compared in a wider binning and agree well.

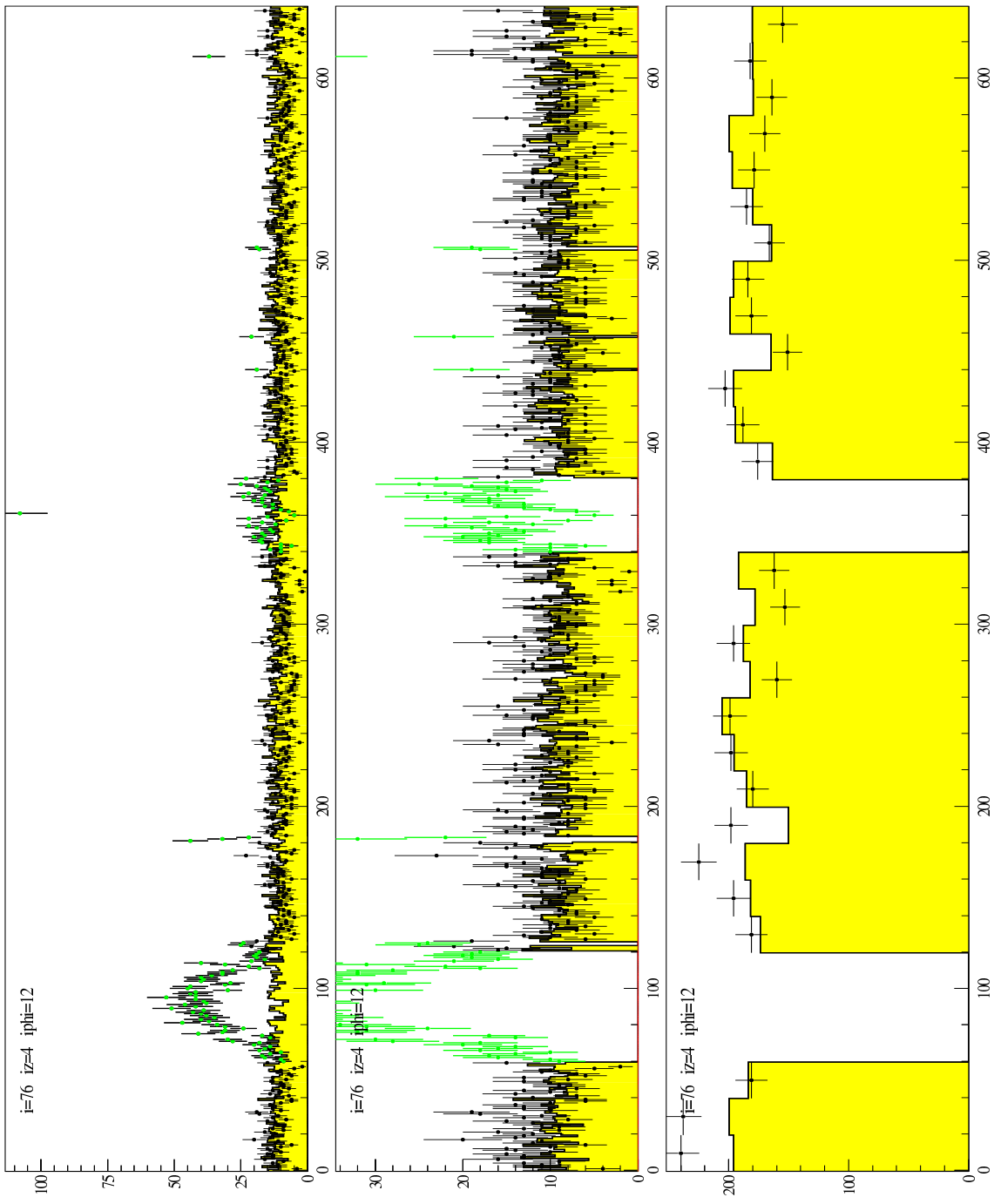

Figure 6.8: The number of hits per strip (strip number 0 to 639) are shown for the ϕ-sector 12 on z-plane 4 for the running period 2000 e^+. Noisy regions in the data are clearly visible. For further description refer to the description of figure 6.7.

- *'run-away' noisy strip*, i.e. a single strip with very high number of hits compared to the average hit number of the surrounding strips;
- *noisy region*, i.e. a region of neighbouring strips with a higher number of hits as the average of the surrounding hits or of the detector plate;
- *inefficient region*, i.e. a region of strips with low operation efficiency;
- *dead region*, i.e. a region of non operational strips;
- *dead sector*, i.e. a full sector is not operational.

For the search for the 'run-away' noisy strips a two step process is used: In a region of ± 50 strips around each strip the mean μ and standard deviation σ of the number of hits is calculated. If the central strip has more than $\mu + 3 \cdot \sigma$ hits, this strip is classified as 'run-away' noisy strip and is removed. Then a global mean and standard deviation criterion is applied to classify further strips as 'run-away' noisy strips. The dead regions are also detected as part of this automatic procedure. The noisy regions and dead sectors are selected by 'hand'.

For all of the above classes the problematic strips and regions are cut out from data and MC. The number of corrections for the different running periods is listed in table 6.1.

run period	dead sectors	'run-away' noisy strips and dead regions	noisy and ineff. regions
1999 e^-	39	1750	37
1999 e^+	8	1953	40
2000 e^+	8	1606	77

Table 6.1: The number of corrections for BST stips applied to data and MC are listed for the running periods 1999 e^-, 1999 e^+ and 2000 e^+. In 1999 e^- the first two z-planes were not operational at all, which results in the high number of dead sectors.

The BST track finding efficiency after the correction of the BST detector response is shown in figure 6.6 b). This correction improves the shape of the track finding efficiency as a function of the polar angle θ and azimuthal angle ϕ, but further corrections are necessary.

6.2.3.2 Adjustment of the BST Track Finding Efficiency as a Function of the Angles θ and ϕ in MC

The efficiency of the track finding in MC is adjusted to the efficiency determined from the data. The procedure is described in the following.

The statistics in the data sample is not sufficient for a two dimensional (θ, ϕ) correction of the track finding efficiency. Therefore the efficiency in MC is adjusted in two steps. First the efficiency is adjusted to data as a function of the azimuthal angle ϕ and then as a function of the polar angle θ. The adjustment as a function of ϕ is the main effect, while the adjustment as a function of θ is only a small correction of up to $\approx 2\%$.

In the run range 269000 to 272000 in the running period 2000 e^+ the BST had readout problems [95]. This results in a significantly lower efficiency[6] for the BST track finding in the region $180° < \phi < 360°$. An investigation of the number of hits per BST pad as a function of the run number was showing no obvious effects. Therefore the BST track finding efficiency as a function of the angle ϕ and θ is corrected separately for the following run ranges in 2000 e^+: a) `run number` $<$ 269000, b) 269000 $<$ `run number` $<$ 272000 and c) 272000 $<$ `run number`.

For the three run ranges the efficiency of the BST track finding is shown for data and the corrected efficiency for MC in figure 6.9. The corresponding plot for the full running period 2000 e^+ is shown in figure 6.6 c).

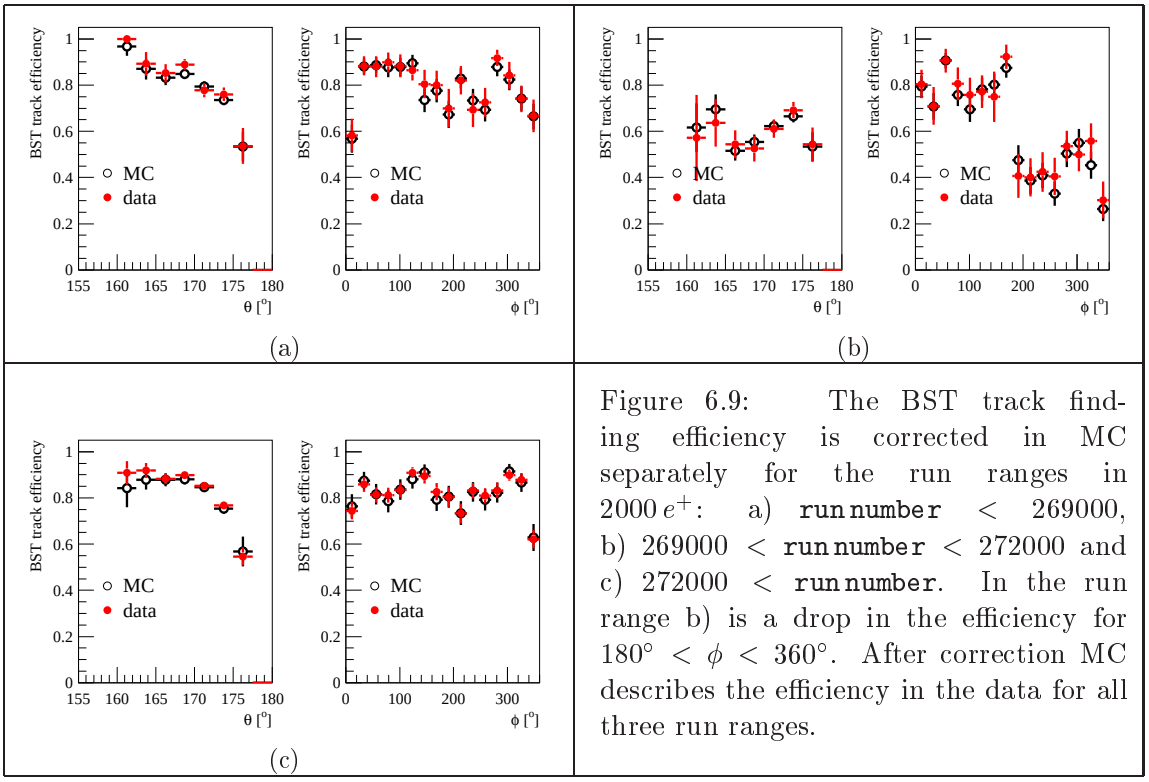

Figure 6.9: The BST track finding efficiency is corrected in MC separately for the run ranges in 2000 e^+: a) `run number` $<$ 269000, b) 269000 $<$ `run number` $<$ 272000 and c) 272000 $<$ `run number`. In the run range b) is a drop in the efficiency for $180° < \phi < 360°$. After correction MC describes the efficiency in the data for all three run ranges.

The MC adjustment is shown in detail for the running period 2000 e^+. For the running periods 1999 e^- and 1999 e^+ the same procedures are applied. For these running periods only the final adjustment is presented in section 6.2.3.4.

6.2.3.3 Adjustment of the total BST Track Finding Efficiency as a Function of the `run number` in MC

In figure 6.10 the total efficiency of the BST track finding is shown as a function of the `run number` for the running periods 1999 e^+ and 2000 e^+.[7]

[6] This is also visible in the event yield (see figure 8.2).

[7] The running period 1999 e^- is not used in this analysis, as explained in section 6.2.3.4.

The run range 290000 to 272000 in 2000 e^+ with lower efficiency is already well corrected, by splitting up 2000 e^+ in three regions. The run dependent correction is a small adjustment. The final adjusted BST track finding efficiency is shown in figure 6.6 d).

The running period 1999 e^+ has not sufficient statistics to allow corrections like the previous sections in smaller ranges. Therefore the run dependent correction for the running period 1999 e^+ is larger.

6.2.3.4 Final adjusted Efficiencies for the different Running Periods

The final corrected efficiencies of the BST track finding for the different running periods are shown in figure 6.11.

In the running period 1999e^- the first two z-planes were not operational at all. This causes the low track finding efficiency for the low values of the polar angle θ (see figure 6.11 a)). In this running period the BST was generally not working well. This results in a low efficiency. Although the corrected efficiencies in data and MC agree well, the running period 1999 e^- is excluded due to the small statistics and the unstable detector situation. [8]

The BST track finding efficiency applies to a single track. For cluster-cluster events with two BST tracks the corrections are applied independently for each track. Here, the effect of the track finding efficiency applies squared. In the case of the small efficiency in the running period 1999 e^- the squared efficiency is 'vanishing'.

For the running periods 1999 e^+ and 2000 e^+ and the combined run range 1999 e^+ + 2000 e^+ the final corrected BST track finding efficiencies in data and MC agree well. The larger errors for the running period 1999 e^+ are caused by the smaller statistics.

6.2.3.5 Coherent Loss

A special kind of inefficiency of the BST are the so called *coherent losses*, which are caused by several reasons due to the detector structure and the readout mechanism. The conversion of the analog detector signals to digital signals depends on the gain of the preamplifiers and on the offset of the FADC's[9]. Due to the quadrant-wise readout structure an overflow results in a 'hot' quadrant with more than 500 hits and an underflow results in a 'silent' quadrant with no hits. In the online hit finding procedure all hits of a 'hot' quadrant are rejected. For both cases — 'hot' and 'silent' quadrants — the online hit finding procedure fails. In addition also problems in the pipeline counters and in the data acquisition add to coherent losses [96, 49]. The effect of coherent losses is studied in detail in [49] and amounts to $\approx 4\%$.

Due to the method of adjusting MC to the data, the effect of coherent losses is already covered. A systematic error of 3% is applied[96].

[8] The low efficiency of the BST track finding in the running period 1999 e^- is also visible in the event yield as a function of the run number (see figure 8.2).

[9] Fast Analog Digital Converter

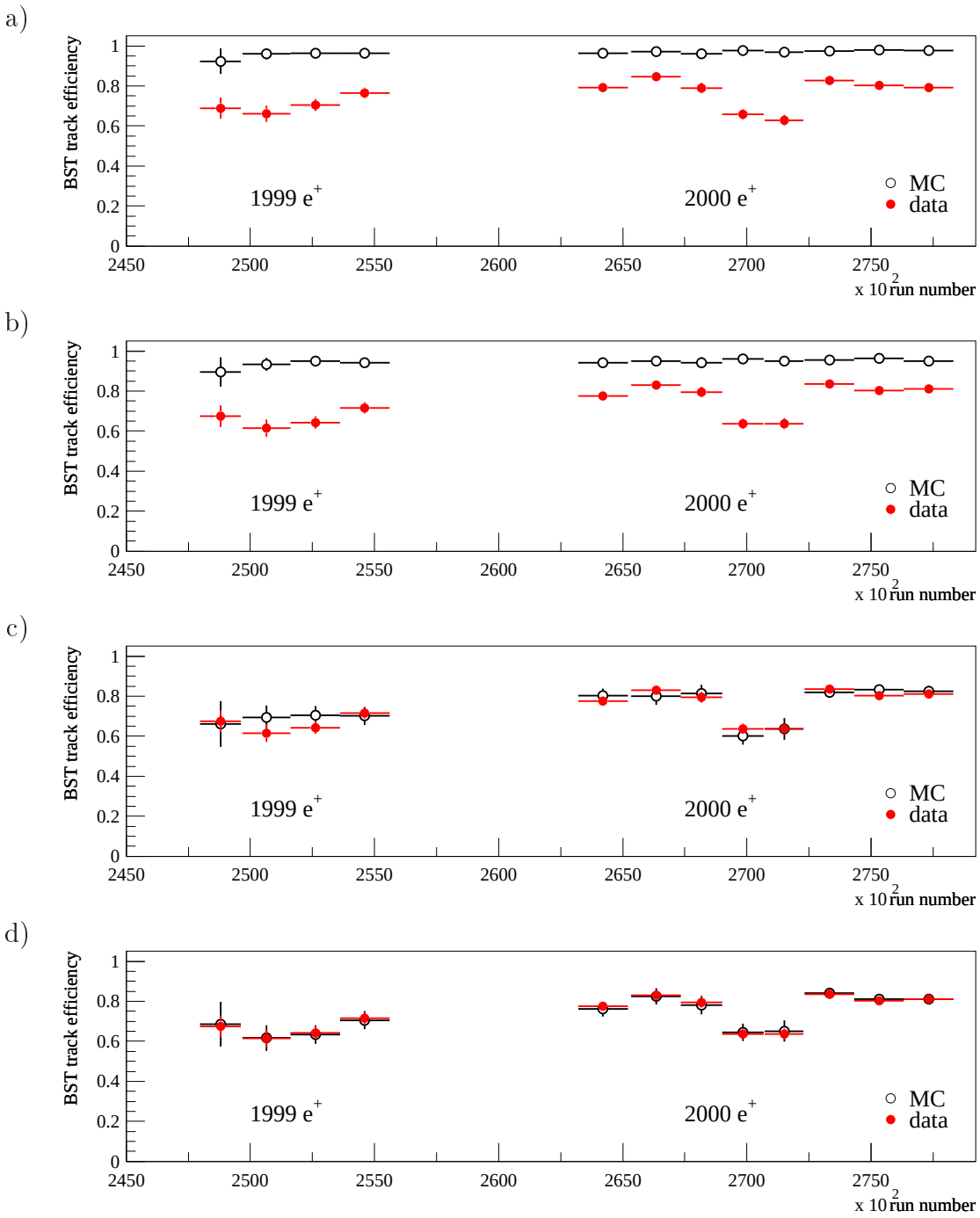

Figure 6.10: The total BST track finding efficiency for data and MC is shown as a function of the `runnumber` for the running periods 1999 e^+ and 2000 e^+. The four plots correspond to different levels of data and MC adjustment: a) no adjustment; b) after the adjustment of the BST detector response; c) after the adjustment of the efficiency as function of ϕ and θ; d) after the adjustment of the total efficiency as a function of the `runnumber`. The run range from 269000 to 272000 in the running period 2000 e^+ with lower efficiency is described in section 6.2.3.2.

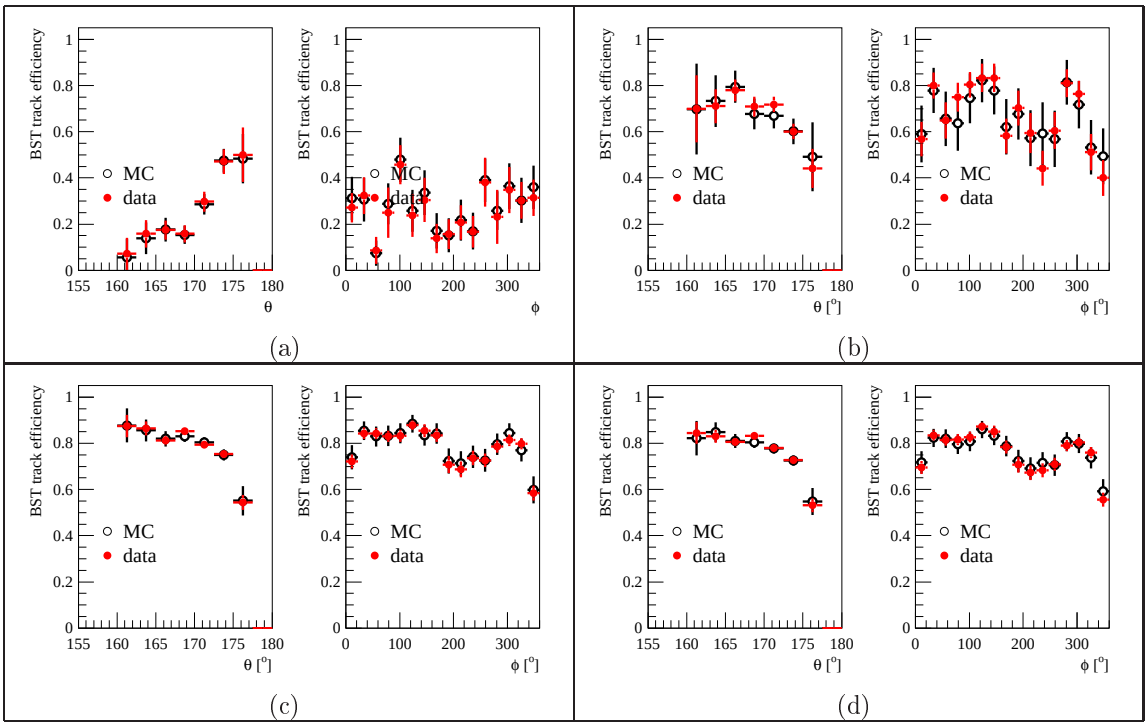

Figure 6.11: The BST track finding efficiency for data and MC is shown as a function of the polar angle θ and the azimuthal angle ϕ for the following running periods: a) 1999 e^-, b) 1999 e^+, c) 2000 e^+, d) 1999 e^+ + 2000 e^+.

6.2.4 Comparison to the Standard BST Tracking

No tracking for the BST-II was available at the beginning of this analysis. Therefore the BST track finding described above was developed. Now also a tracking developed by the BST group [49] exists. This *standard BST tracking* is based on a sagitta criterion of hits in three neighbouring planes for the pattern matching of tracks.

For the comparison of the two algorithms standard BST tracks are taken into account, which are in a wide[10] window around the SpaCal cluster: $\Delta\theta < 1°$ and $\Delta\phi < 360°/16$.

The efficiency for a standard BST track in this wide window is 0.72 ± 0.01, if a track of the BST track finding exist. The efficiency for a track of the BST track finding is 0.95 ± 0.01, if a standard BST track exists. The BST track finding of this analysis has a $\approx 1.3 - 1.4$ times higher efficiency than the standard BST tracking. This is especially important, since the efficiency enters quadratically in the cluster-cluster sample with both clusters in BST acceptance.

[10] The θ-range is wide, compared to the resolution in θ presented in section 6.3.

6.3 Reconstruction of Kinematic Variables

For this analysis the following kinematic variables are needed: [11]

- $m_{e^+e^-}$ the invariant mass of the two decay electrons of the J/ψ vector meson,
- p_t^2 the transverse momentum squared of the J/ψ vector meson,
- t the four-momentum transfer squared at the proton vertex (see equation 1.14) and
- $W_{\gamma p}$ the γp centre-of-mass energy (see equation 1.4).

The reconstruction of the kinematic variables is based on angular and energy information of the reconstructed physics objects tracks and clusters.

In photoproduction the scattered beam electron is not detected. Therefore no information about the beam electron can be obtained. Also no kinematic information about the scattered beam proton is available. From the possible detector response of the forward detectors no kinematic information is obtained. This leaves the two decay electrons of the J/ψ vector meson as only source of information for the kinematic variables.

For the clusters in the SpaCal the charge of the particle cannot be directly obtained, because the track curvature of the corresponding track cannot be measured. For the track-cluster sample the charge of the cluster-particle is chosen opposite to the charge of the track-particle and the effect of the magnetic field is taken into account (see figure 6.12). In the cluster-cluster sample only for few J/ψ decay electron candidates with low azimuthal angle θ a charge information from the central tracking detector is available. In the case of charge information the charge of the other J/ψ decay electron candidate is chosen to be opposite. If no charge information is available, both J/ψ decay electron candidates get no charge assigned. This results in a triple peak structure in the resolution plot for azimuthal angle ϕ_1 for electron 1 and in a wide peak for the resolution in azimuthal angle ϕ_2 for electron 2 (see figure 6.13).

The invariant mass $m_{e^+e^-}$ of the J/ψ decay electron system is calculated by the angles and energies of the decay electron candidates

$$\begin{aligned} {m_{e^+e^-}}^2 &= (p_{e^+} + p_{e^-})^2 \\ &= 4E_{e^+}E_{e^-}\sin^2(\xi/2)\ , \end{aligned} \tag{6.1}$$

where p_{e^+} and p_{e^-} are the four-momenta and E_{e^+} and E_{e^-} the energies of the J/ψ decay electron candidates in the laboratory system. ξ is the opening angle between the J/ψ decay electron candidates in the laboratory system. For the track-cluster and cluster-cluster sample the energy resolution of the J/ψ decay electron candidates and the resolution of the invariant mass are shown in figure 6.12 and figure 6.13.[12]

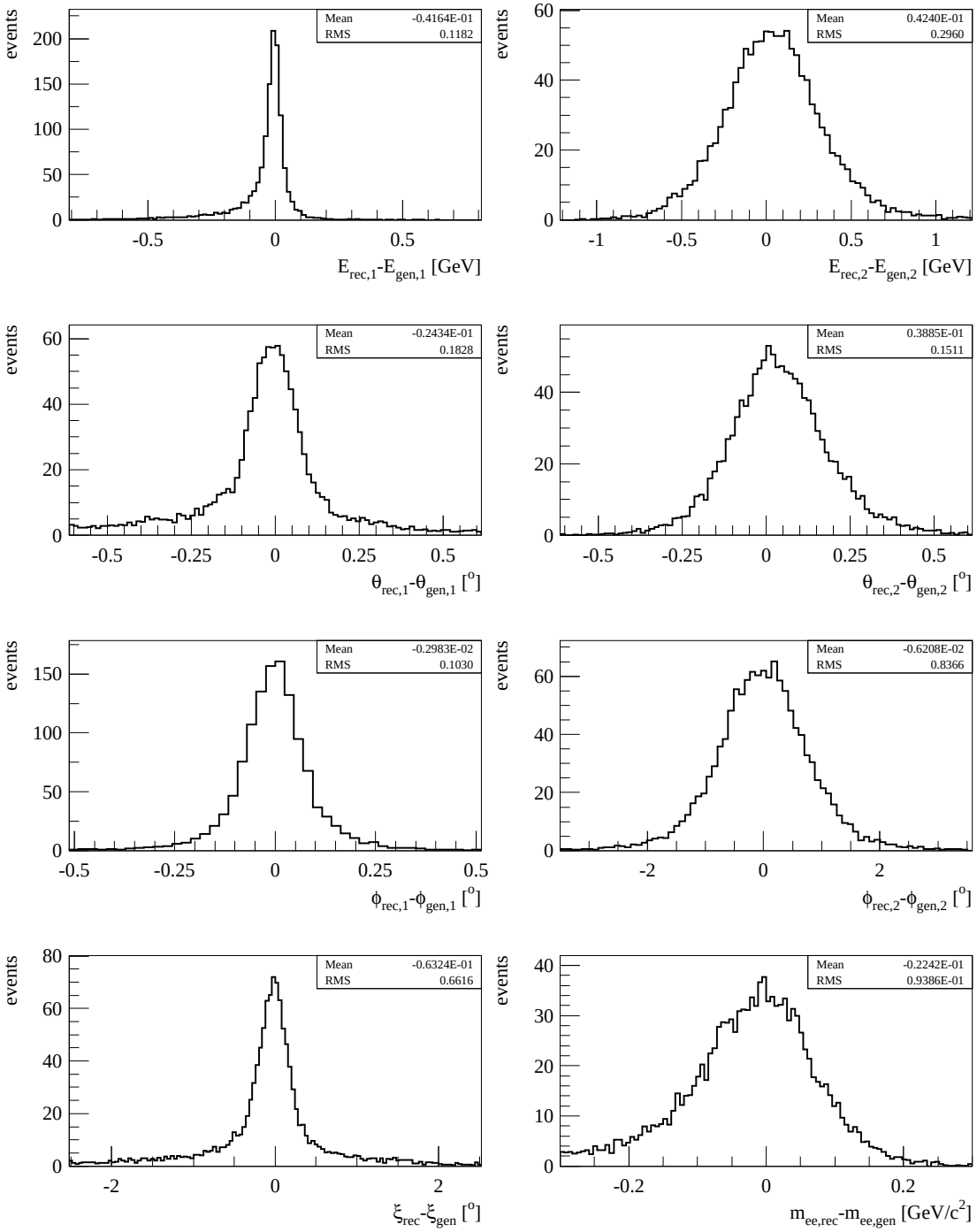

Figure 6.12: Track-cluster: The difference between reconstructed and generated values for the energy and angle of the decay electrons and the opening angle ξ and the invariant mass $m_{e^+e^-}$ are shown.

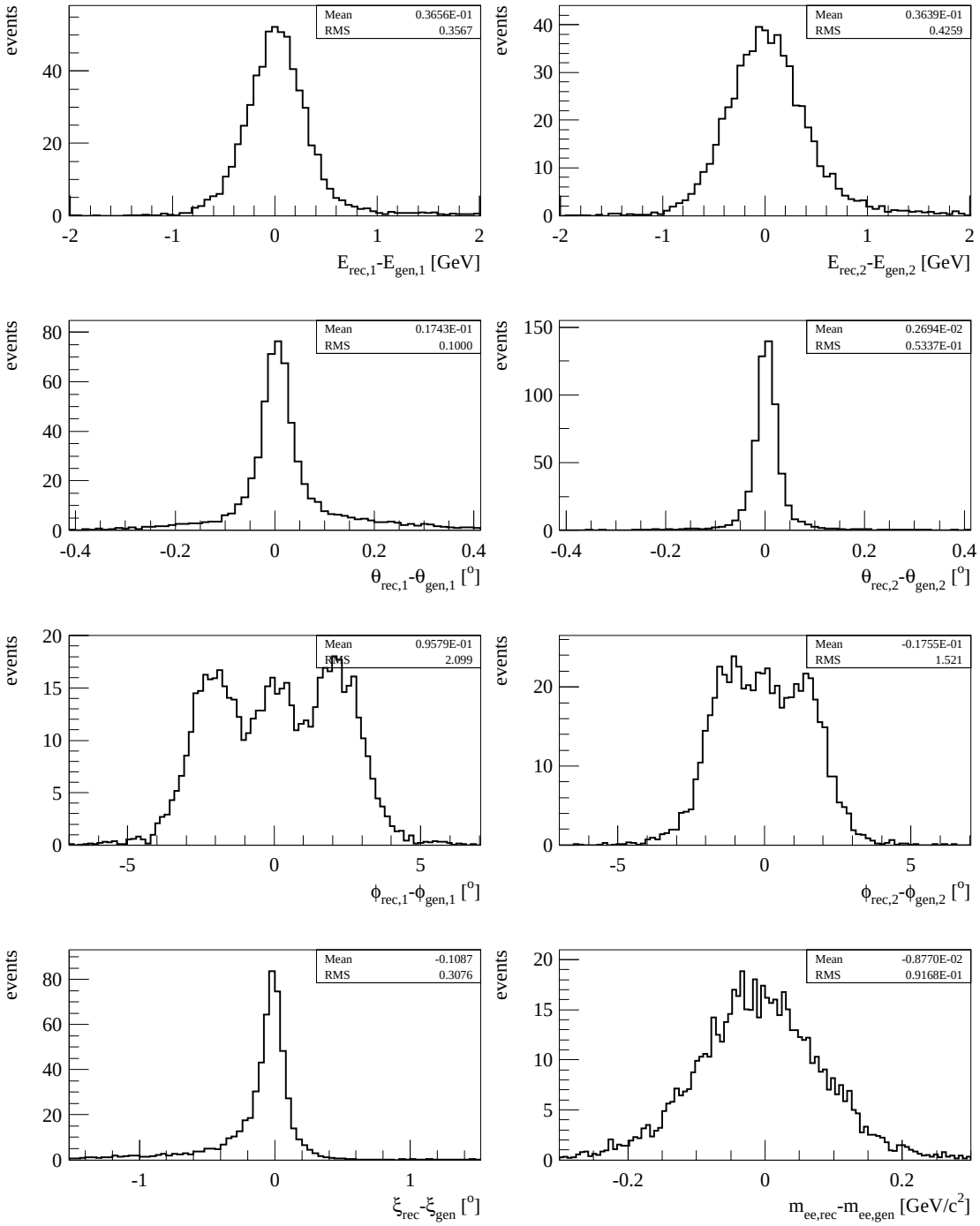

Figure 6.13: Cluster-cluster: The difference between reconstructed and generated values for the energy and angle of the decay electrons and the opening angle ξ and the invariant mass $m_{e^+e^-}$ are shown. In the distributions of the azimuthal angle $\phi_{\mathrm{rec},1/2} - \phi_{\mathrm{gen},1/2}$ the effect of the unknown charge is visible. For some electrons with low azimuthal angle θ a charge information is avaliable. This results in the triple peak structure of the $\phi_{\mathrm{rec},1} - \phi_{\mathrm{gen},1}$ distribution and the wide distribution of $\phi_{\mathrm{rec},2} - \phi_{\mathrm{gen},2}$.

For the reconstruction of the kinematic variable t the approximation $|t| \approx p_t^2$ (see equation 1.14) cannot be directly used. Though the approximation is very well fulfilled in the photoproduction case, the detector effects limit the resolution on the measured p_t^2. In figure 6.14 the reconstructed p_t^2 is compared to the generated p_t^2 and generated $|t|$. The main effect is the limited resolution in the reconstruction of p_t^2.

An unfolding method is applied in order to improve the measurement by treating the migration due to the limited resolution in p_t^2. The unfolding method uses the $(p_{t\,\mathrm{rec}}^2, |t|_{\mathrm{gen}})$ information from the simulation. In section 8.2 the binning in p_t^2 is introduced. The handling of migration and the unfolding procedure is presented in section 8.6.

For general DIS events without information about the scattered beam electron (NC) or the scattered neutrino (CC), the *hadron method* or *Jaquet-Blondel method* [97] is used to calculate y_{JB}, where only information from the hadronic final state is used. Applied to the photoproduction of J/ψ vector mesons the hadronic final state consists of the J/ψ, respectively its decay electrons. The hadron method calculates for the hadronic final state the variable

$$\Sigma = \sum_i \left(E_i - p_{z,i}\right) , \tag{6.2}$$

where the summation takes all particles of the hadronic final state — here the J/ψ decay electrons — into account and E_i is the energy and p_i the momentum of particle i. Using the variable Σ the kinematic variable y_{JB} is obtained by the hadron method

$$y_{\mathrm{JB}} = \frac{\Sigma}{2E_e} , \tag{6.3}$$

where E_e is the energy of the incident electron beam. With equation 1.4 the γp centre-of-mass energy is obtained

$${W_{\gamma p}}^2 \approx y_{\mathrm{JB}}\, s + m_p^2 , \tag{6.4}$$

where m_p is the mass of the proton. The resolution for y_{JB} and $W_{\gamma p}$ is shown in figure 6.14 for the track-cluster and cluster-cluster sample. In section 8.2 the binning in $W_{\gamma p}$ is introduced. It is shown, that the migration is small and no unfolding procedure is necessary.

[11] The invariant mass $m_{e^+e^-}$ is used in section 8.3 for the signal extraction. The kinematic variables p_t^2, t and $W_{\gamma p}$ are used in section 8.2 and section 8.6 for the binning of the cross section measurement.

[12] The effect of the BST tracking on the distribution of the reconstructed invariant mass is shown in figure 7.4. For the understanding of this plot the event selection is necessary, which is described in chapter 7. Mass signals in bins of the kinematic variables $W_{\gamma p}$ and p_t^2 are used for the signal extraction and are presented in section 8.3 and appendix A.

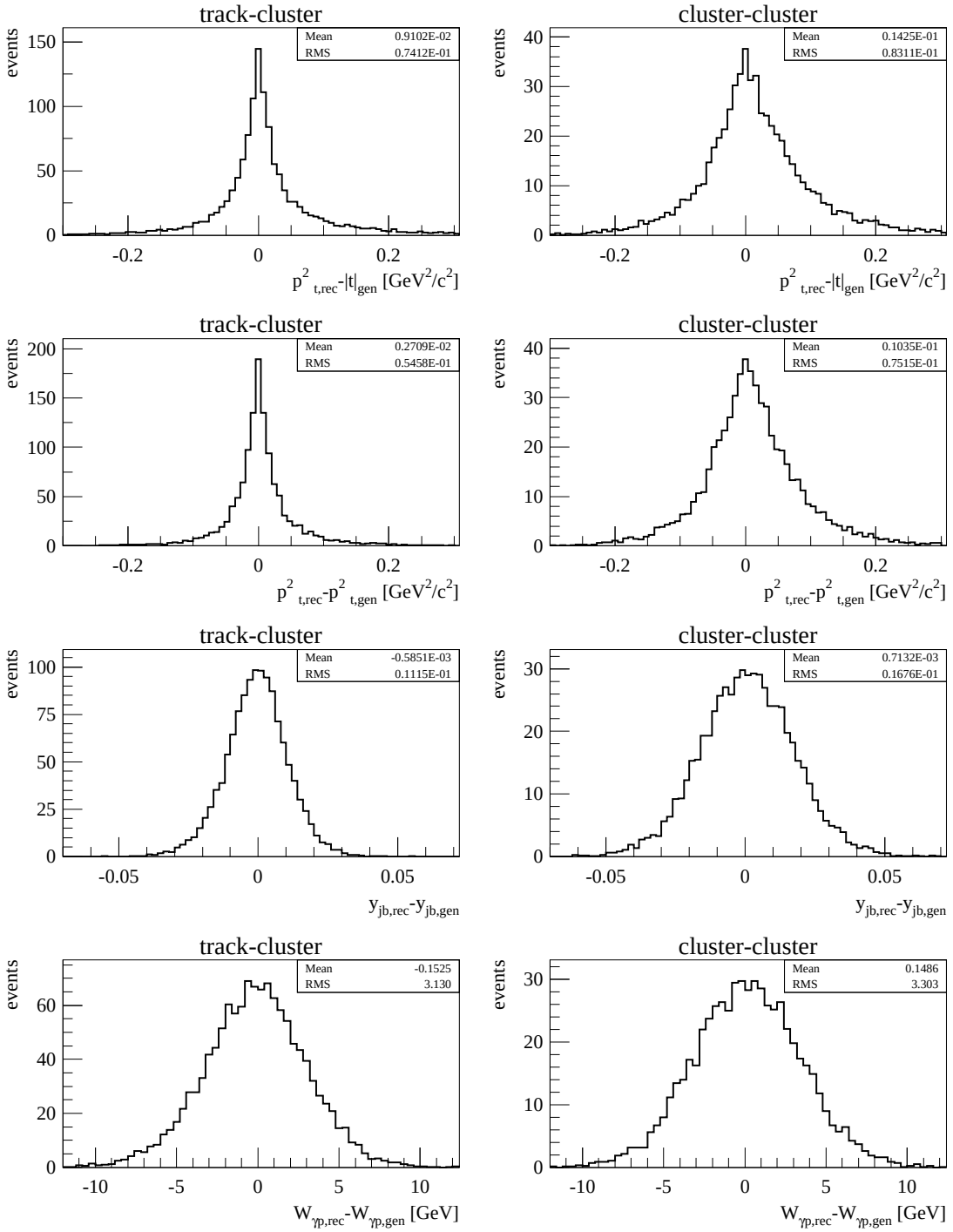

Figure 6.14: The reconstructed and generated values for the variables p_t^2, $|t|$, y_{JB} and $W_{\gamma p}$ are compared for the track-cluster and cluster-cluster sample.

6.4 Alignment and Calibration

In this section special alignment and calibration of detector components are described. The SpaCal calorimeter is aligned using the BST track finding. A calibration for the energy measurement of the clusters in the SpaCal is applied. The alignment and calibration of the SpaCal is done for both, data and MC. The description of the forward detector response is adjusted in MC to data.

The distribution of the vertex position z_{vtx} is adjusted in MC to data.

6.4.1 SpaCal Alignment

BST track finding is used to improve the relative alignment between the BST and the SpaCal. For this purpose the r-position of the SpaCal cluster is not taken into account for the tracking. The resulting track is extrapolated to the SpaCal. The alignment parameters for data and MC in table 6.2 are obtained.

	run period	Δx	Δy
data	1999 e^-	-0.10 ± 0.02 cm	-0.18 ± 0.02 cm
data	1999 e^+	-0.09 ± 0.01 cm	-0.20 ± 0.01 cm
data	2000 e^+	-0.06 ± 0.02 cm	-0.19 ± 0.01 cm
MC	all	-0.22 ± 0.02 cm	-0.05 ± 0.01 cm

Table 6.2: The SpaCal is shifted by the alignment parameters Δx and Δy in order to improve the relative alignment betweeen the BST and the SpaCal.

6.4.2 SpaCal Energy Calibration

The standard energy calibration of the SpaCal calorimeter uses the position of the kinematic peak of the scattered beam electron at $\approx 27.5\,\text{GeV}$. This method leads to a good calibration for high energies but not for low energies. In this analysis energies down to $\approx 4\,\text{GeV}$ are used. Therefore an additional calibration is needed.

The calibration for low energies was developed in [87, 98] using elastic QED Compton events with the aim to provide a calibration down to energies 4 GeV. First MC is calibrated in such a way, that it describes data. Then an additional "absolute" calibration is applied on both data and MC. The distribution of the energy calibration factors for data and MC are shown in figure 6.15.

For the calibration QED Compton events from the running period 1997 are used. Since the SpaCal detector is unchanged from 1997 to 2000, this calibration is applied in this analysis. The quality of the calibration is checked by comparing the position of the mass peak to the value of the the J/ψ mass $m_{J/\psi} = (3.09688 \pm 0.00004)\,\text{GeV}$. In figure 6.16 this comparison is done for data and MC. The calibration provides better agreement of the mass peak position with the J/ψ mass.

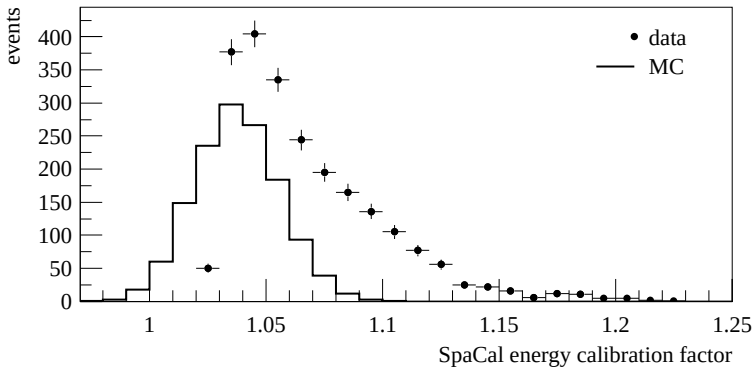

Figure 6.15: The distribution of the SpaCal energy calibration factor is shown for data and MC.

6.4.3 Noise Simulation and Calibration for the Forward Detectors

The experimental handle for the separation of the proton-elastic and proton-dissociative events are the signals of the forward detectors (see also section 3):

- E_{LAr10} the energy in the forward LAr calorimeter (see section 2.2.2.1) for the polar angle range $\theta < 10°$,
- N_{FMD} the hits in the forward muon detector (FMD) (see section 2.2.3.2) and
- N_{PRT} the hits in the proton remnant tagger (PRT) (see section 2.2.4).

If one of the following cuts is fulfilled, the event is classified as fwd.-tagged, otherwise it is classified as fwd.-untagged:

- $E_{\mathrm{LAr10}} > 0.75\,\mathrm{GeV}$,
- $N_{\mathrm{FMD}} > 1$ in the layers 1, 2 and 3 of the FMD,
- $N_{\mathrm{PRT}} > 0$ for the channels 1, 2 and 3 of the PRT.

The determination of the number of proton-elastic and proton-dissociative events from the number of fwd.-untagged and fwd.-tagged events relies on the MC simulation.[13] In [84] the treatment of the forward detectors and the methods to improve the simulation in MC is described in detail. For the running periods $1999e^+$ and $2000e^+$ the MC adjustment is developed in [99]. The energy calibration of the forward LAr calorimeter is improved and the noise in the FMD and PRT are adjusted.

The description of the response of the forward detectors of data by MC simulation is checked with a set of MC, which contains proton-elastic and proton-dissociative contributions from `DiffVM`, `LPair2` and `COMPTON` MC events (see figure 6.17 and 6.18).

[13] The determination of the number of proton-elastic and proton-dissociative produced events is described in section 8.5.

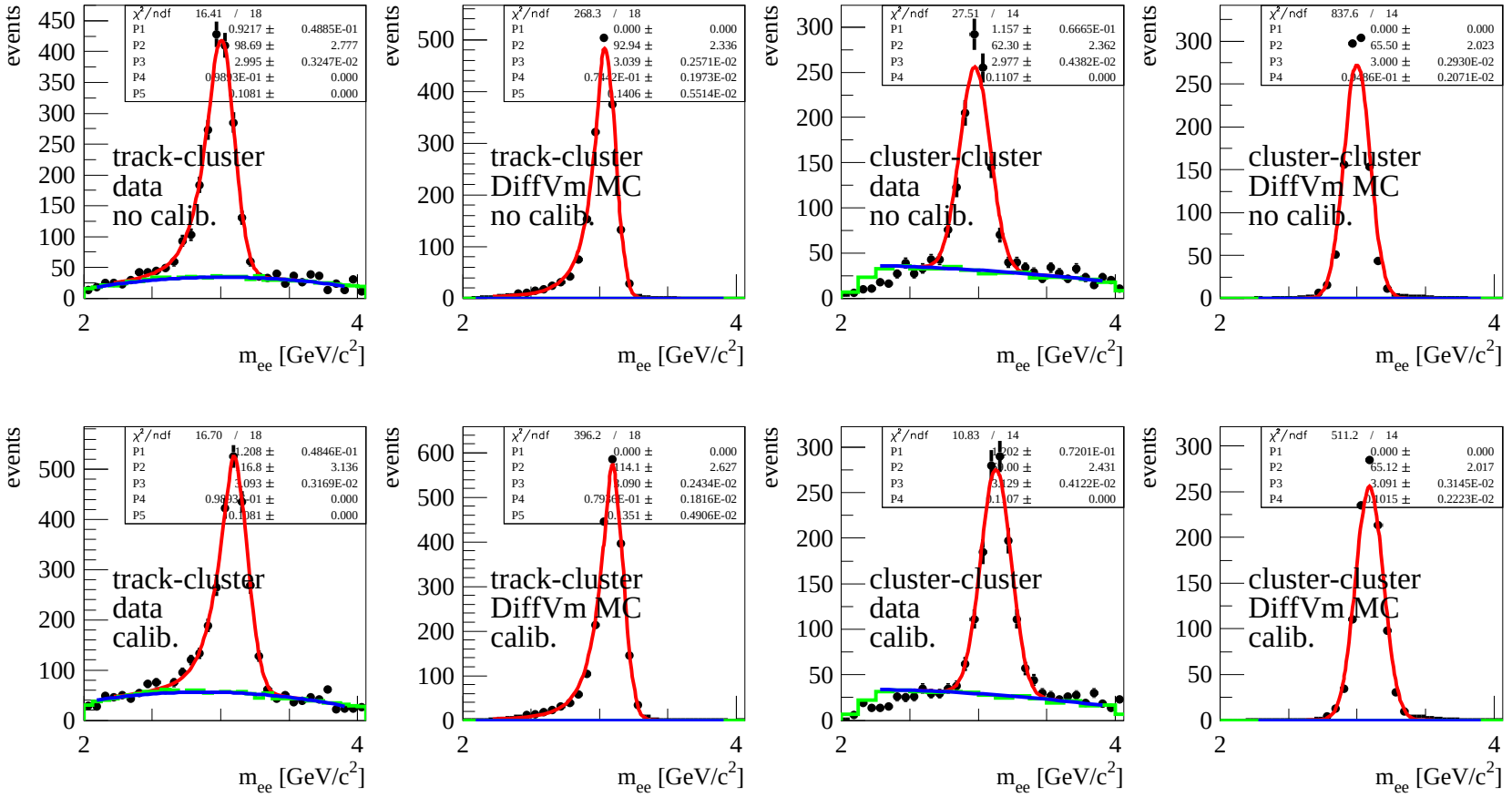

Figure 6.16: The J/ψ mass peak for data and MC for the track-cluster and cluster-cluster sample are shown. For the plots in the first line standard SpaCal calibration is applied, i.e. no additional calibration ("no calib."). For the plots in the second line the calibration described in the text is applied. The calibration shifts in data and MC the peak position to the mass of the J/ψ: $m_{J/\psi} = (3.09688 \pm 0.00004)\,\mathrm{GeV}$. The fit parameter `P3` represents the peak position. For the event selection refer to chapter 7. The fit procedure is described in detail in section 8.3.

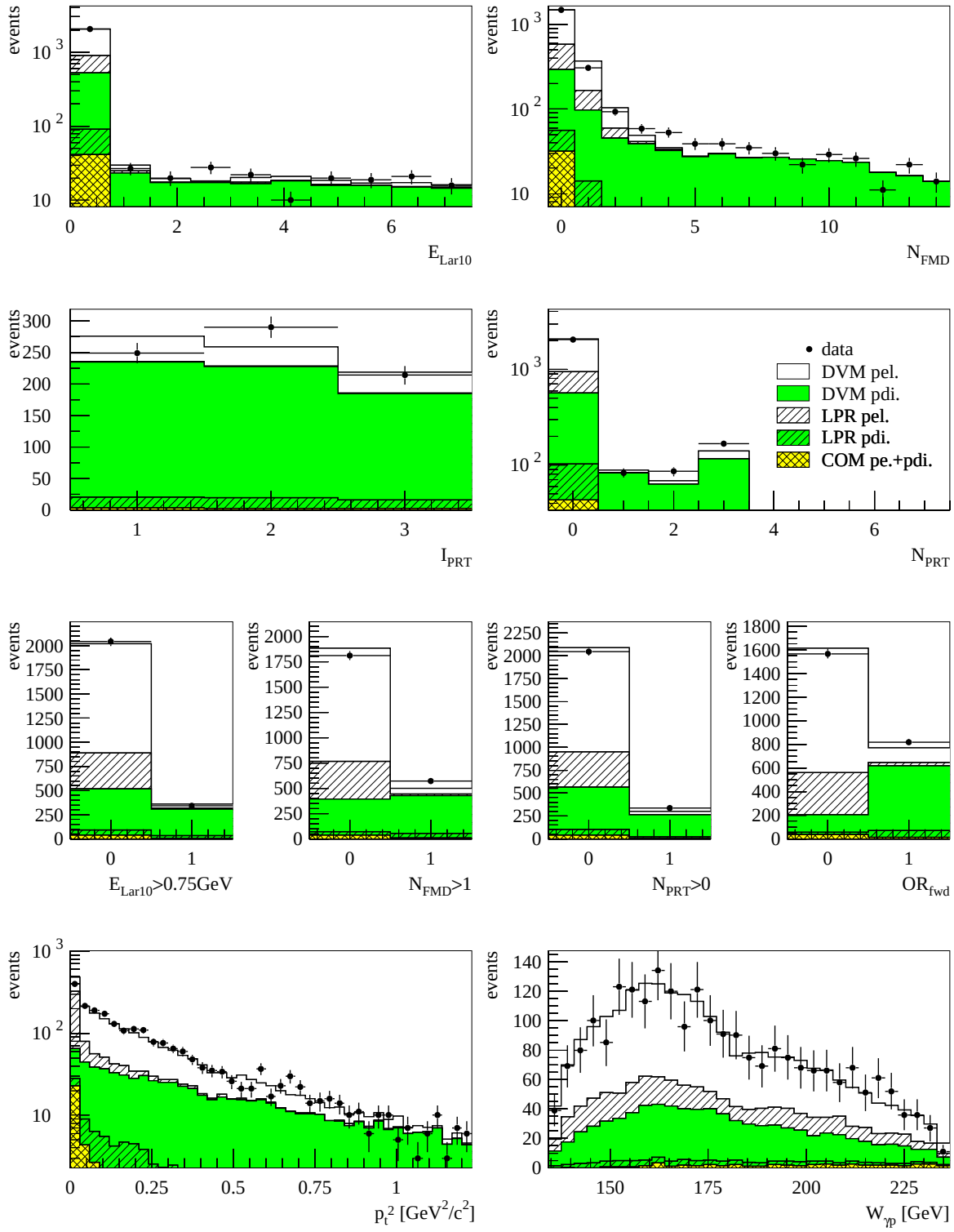

Figure 6.17: Track-cluster: The detector response of the forward detectors, the results of the cuts on the forward detectors, the logical $\mathrm{OR}_{\mathrm{fwd}}$ of these cuts and the distribution of the kinematic variables p_t^2 and $W_{\gamma p}$ are shown. Data is compared to a set of MC, which contains proton-elastic and proton-dissociative contributions from `DiffVM`, `LPair2` and `COMPTON` MC events.

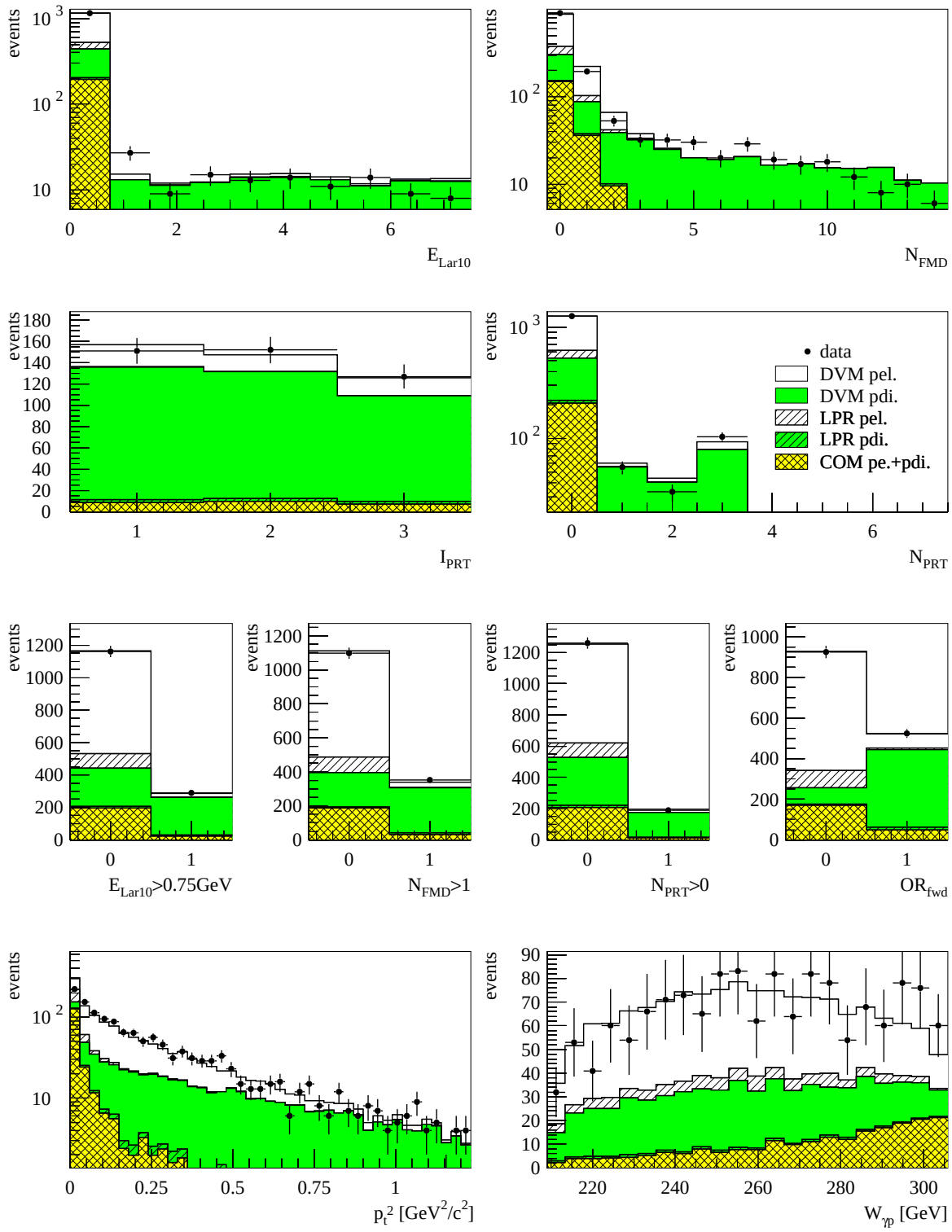

Figure 6.18: Cluster-cluster: The detector response of the forward detectors, the results of the cuts on the forward detectors, the logical $\mathrm{OR}_{\mathrm{fwd}}$ of these cuts and the distribution of the kinematic variables p_t^2 and $W_{\gamma p}$ are shown. Data is compared to a set of MC, which contains proton-elastic and proton-dissociative contributions from `DiffVM`, `LPair2` and `COMPTON` MC events.

	track-cluster		cluster-cluster	
	$\langle z_{\text{vtx}} \rangle$ [cm]	$\sigma_{z_{\text{vtx}}}$ [cm]	$\langle z_{\text{vtx}} \rangle$ [cm]	$\sigma_{z_{\text{vtx}}}$ [cm]
data	3.6 ± 0.2	11.2 ± 0.2	2.7 ± 0.3	11.7 ± 0.2
uncorrected MC	2.2 ± 0.2	10.7 ± 0.2	0.9 ± 0.3	10.9 ± 0.2
corrected MC	3.4 ± 0.2	11.0 ± 0.2	2.2 ± 0.3	$11.1 \pm .02$

Table 6.3: Gaussian fits are applied to the distributions of the z_{vtx} position of data, uncorrected and corrected MC. The mean value $\langle z_{\text{vtx}} \rangle$ and the width $\sigma_{z_{\text{vtx}}}$ are listed.

6.4.4 z_{vtx} Reweighting

The distribution of the vertex position z_{vtx} differ in data and MC. Gaussian fits are applied to the distributions and the MC events are reweighted accordingly. In table 6.3 the values of the mean value $\langle z_{\text{vtx}} \rangle$ and the width $\sigma_{z_{\text{vtx}}}$ are listed for data, uncorrected and corrected MC for both the track-cluster and the cluster-cluster sample.

Chapter 7

Selection of J/ψ Mesons in Photoproduction

In this chapter the selection of J/ψ vector mesons in photoproduction is described.

First the run and event selection, i.e. cuts[1] which ensure a well operating detector, are described. Then the kinematic selection and the trigger selection are presented. Both take into account the topology of the J/ψ events for the selection. While the kinematic selection is applied on analysis level the trigger selection is applied during data taking.

7.1 Run Selection

In this section cuts are presented, which ensure a well operating detector system, i.e. a minimum set of operational subdetectors, trigger components and readout systems. This set depends on the analysed physics process. For the selection of track-cluster and cluster-cluster events the following detector components are necessary either for a measurement or a veto for/against e.g. tracks: central tracking system (see section 2.2.1.3), LAr calorimeter (see section 2.2.2.1), SpaCal (see section 2.2.2.2), PRT (see section 2.2.4), FMD (see section 2.2.3.2) and BST (see section 2.2.1.2) (only cluster-cluster).

The status of detector components is recorded for each *run*, i.e. a time period of experimentally stable running (see section 2.1). In order to ensure a well operating detector system cuts on the following information are performed:

- the *run quality*,
- the *readout status*,
- the *trigger phase*,
- the *status of the level 1 subtrigger* and

[1] Selection criteria are called *cuts*.

- *unstable runs.*

Depending on the overall detector performance, background situation or problems with the readout runs are classified as "good", "medium" or "poor" (*run quality*). This classification takes the main detector components (central tracking chambers, LAr calorimeter, SpaCal etc.) into account. In this analysis a run quality of "good" is required for the event selection.

According to the requirements of the specialised physics analysis checks on the *readout status* of detector components are done. The readout of the detector is divided into several branches, the so called *TAXI branches*[2], for different subdetector systems. The status of the branches is stored bit-encoded for each run. In this analysis the following branches are required to be in readout: LAr calorimeter trigger, LAr calorimeter ADC[3] and SpaCal, central drift chambers CJC1 and CJC2, multi wire proportional chambers (CIP, COP), silicon detectors (e.g. BST) (only for cluster-cluster).

The trigger phase (see section 4) is set according to the beam condition and the background situation during a luminosity fill (see section 2.1). Especially in the beginning of a luminosity fill — trigger phase 1 — the tracking detectors cannot be switched on, due to the severe background situation. Therefore this analysis uses only runs with trigger phase 2 to 4.

The status of a level 1 subtrigger is stored in the so called *L1ST-enable-flag*. It contains the information, if the corresponding L1ST is operational. For the track-cluster selection the operation of the subtrigger `S33` has to be enabled; for the cluster-cluster selection the operation of the subtrigger `S40`. At this stage it is checked only, that the L1ST is operational, not the trigger decision.

In addition to the previous selection criteria some *unstable runs* are rejected due to unstable performance of different detector components: PRT or FMD has high noise; FMD is not operational; L2NN is not working; CJC1, CJC2 have a broken wire in 1999; the L2 neural network for the track-cluster topology is not installed in some ranges of year 1999; trigger level 4 is in transparent mode; trigger level 2 and 4 are in transparent mode; trigger level 4 is not working.

7.2 Event Selection

In addition to the detector status, which is recorded for each run, the information about the detector status for shorter timeslices is available. During data taking every ≈ 10 s the status of hardware components is checked and written to a database. This information is accessible for each single event (*event wise status information*).

H1 uses the so called *high-voltage-bit system*, which creates the high-voltage bits (*HV-bits*), and the *slow control system*, which creates the *BBL3-bits*. A failure of the corresponding hardware system is represented by a bit set. The recorded information is

[2]The name TAXI branch comes from the name of the read out hardware: `VME-TAXI`[100].
[3]analog digital converter

differently delayed for the individual status bits, since it takes time from seconds to a minute for the high voltage system and the slow control system to build the detector status information. Even though the information is delayed, the event wise detector information is used to select events, as recommended and discussed in [101].

According to the detector requirements for this analysis (see section 7.1) the following status bits are used:

HV-bits: CJC1, CJC2, CIP, COP (only track-cluster), BST (only cluster-cluster), SpaCal, luminosity system

BBL3-bits: CJC1+CJC2, SpaCal and the low and high voltage status of CIP+COP, LAr calorimeter ADC and luminosity system.

The COP has negligible geometrical acceptance for cluster-cluster events (see figure 2.4) and is therefore only required for the track-cluster sample.

The event wise detector status informations enables to use those runs, in which some detector components are not operational for a short time. The fraction of the run useful for physics analysis is determined and the luminosity for the run is corrected accordingly.[4]

7.3 Kinematic Cuts

In this section the selection criteria are described, which select events according to the J/ψ topology. In order to be able to treat data and MC events in the same way the following procedure is applied.

The selection of the events from real data is done in a two step process. The first step uses DST (see section 4.4) as input and performs a 'soft' selection, which is called *preselection*. Only for those events, which fulfil the preselection, information is written in the `Ntuple`-format to `HBOOK` files.

The selection of MC events uses generated-simulated-reconstructed events as input. Here the information is written in the `Ntuple`-format for all events. This is necessary for the calculation of efficiencies. The preselection decision is added to the `Ntuple`.

Data and MC events are subjected to the same selection starting from the `Ntuple`. The selection is separated into the following groups of cuts, which are described in the following sections:[5]

- **basic cuts**: preselection (see section 7.3.1),
- **angular cuts**: cuts on the angle of the J/ψ decay electron candidates (see section 7.3.2),

[4] The caluclation of the luminosity takes also other effects into account and is the topic of section 8.1.
[5] The ordering of the cut groups is based on the determination of the efficiencies in section 8.4.

- **energy cuts**: cuts on the energy and transverse momentum of the J/ψ decay electron candidates (see section 7.3.3),
- **miscellaneous cuts** (see section 7.3.4),
- **mass cut**: window cut on the invariant mass of the J/ψ decay electron candidates (see section 7.3.5),
- **BST cut**: BST track requirement for the cluster-cluster sample (see section 7.3.6),
- **trigger cuts**: cut on trigger level 1, 2 and 4 (see section 7.3.4)
- **forward classification** (see section 7.5).

7.3.1 Basic Cuts

The basic cuts are the selection criteria applied in the preselection. Although most of the cuts are applied on analysis level in stronger version, the preselection cuts have to be treated separately — as explained in section 7.3 — because of the efficiency determination (see section 8.4).

The preselection cuts use properties of central tracks, energy clusters in the LAr calorimeter and the SpaCal. According to the nomenclature 'track-cluster' and 'cluster-cluster' sample, in the following 'track' refers always to a track in the central tracking system and 'cluster' refers to an energy deposition in the SpaCal. Tracks resulting from the BST track finding are explicitely called 'BST-tracks' and energy depositions in the LAr calorimeter are called LAr-clusters.

The track selection is based on [102]. There, small track segments are combined and double counting of track candidates is avoided. The following cuts are applied on the track candidates:

$$\begin{aligned}
\theta^{\text{track}} &> 20^\circ\,, \\
\theta^{\text{track}} &< 160^\circ\,, \\
p^{\text{track}} &> 0.6\,\text{GeV/c}\,, \\
p_t^{\text{track}} &> 0.15\,\text{GeV/c}\,, \\
\texttt{DCA}^{\text{track}} &< 2.0\ \text{cm}\,, \\
r_{\text{start}}^{\text{track}} &< 50.0\ \text{cm}\,, \\
l^{\text{track}} &> 10.0\ \text{cm} \quad \text{for } \theta^{\text{track}} < 150^\circ\,, \\
l^{\text{track}} &> 5.0\ \text{cm} \quad \text{for } \theta^{\text{track}} > 150^\circ\,, \\
\texttt{elqual} &\geq \text{poor}\,,
\end{aligned} \tag{7.1}$$

where θ^{track}, p^{track}, p_t^{track} are the polar angle, the momentum and the transverse momentum of the track candidate. $\texttt{DCA}^{\text{track}}$ is the distance of closest approach of the track to the beam axis and $r_{\text{start}}^{\text{track}}$ is the distance of the starting point of the track to the

beam axis in the xy-plane. The different cut values for the track length l^{track} take the geometry of the tracking chambers at large polar angle θ into account (see figure 2.4).

The quantity `elqual` is a handle for the particle identification of the track candidate as originating from an electron. The energy deposition of hadrons, e.g. pions, in the LAr calorimeter (see section 2.2.2.1) is less than the energy deposition of electrons with the same energy (non compensating calorimeter). The hadronic and electromagnetic shower also differ in shape. In order to determine `elqual` the track candidate is prolonged to the LAr calorimeter. On basis of calorimeter cells the energy in the electromagnetic part and the hadronic part, the weighted distance of the calorimeter cell to the track, the weighted shower depth and the ratio of the energy deposition in the calorimeter to the track momentum is calculated. The evaluation of the shower shape is necessary due to the low energy deposition in the calorimeter. Taking the contributions into account, the quality criterion `elqual` is created. For a detailed description refer to [68]. For the event selection the low criterion '`elqual` $\geq$ poor' is used.

For the track-cluster selection exactly one track fulfilling the conditions in equation 7.1 is required. For the cluster-cluster selection no track candidate passing the criteria in equation 7.1 is allowed.

The conditions for the cluster candidates in the SpaCal are different for the track-cluster (TC) and cluster-cluster (CC) selection:

$$\begin{array}{lll} \text{TC}: & E^{\text{cluster}} > 3.0\,\text{GeV}\,, & \theta^{\text{cluster}} > 150^\circ \\ \text{CC}: & E^{\text{cluster}} > 3.5\,\text{GeV}\,, & \max\{E^{\text{cluster}}\} > 5.0\,\text{GeV} \\ \text{TC and CC}: & r^{\text{cluster}} < 4\ \text{cm}\,, & E^{\text{cluster}}_{\text{had}} < 0.5\,\text{GeV} \end{array} \tag{7.2}$$

E^{cluster}, θ^{cluster}, r^{cluster} are the energy, the polar angle and the radius ('size') of the clusters. $E^{\text{cluster}}_{\text{had}}$ is the energy in the hadronic SpaCal behind a cluster in the electromagnetic SpaCal. For the description of the cuts on r^{cluster} and $E^{\text{cluster}}_{\text{had}}$ refer to section 7.3.4. The values for the energy cuts are motivated by figure 3.4 and figure 3.5.

For the track-cluster selection one cluster and for the cluster-cluster selection two clusters have to fulfil the conditions in equation 7.2. In addition to these clusters additional 4 clusters are allowed, which are used in section 7.3.4.

An opening angle $\Delta\phi > 50^\circ$ in the xy-plane between the two decay electron candidates is required.

7.3.2 Angular Cuts

The decay electron candidates are sorted by the polar angle θ. For the track-cluster sample the index 1 refers to the 'track' and the index 2 to the 'cluster'. The following cuts on the polar angle of the decay electrons are applied for the track-cluster (TC) and the cluster-cluster (CC) sample:

$$\begin{array}{rclcl} 80^\circ & < & \theta_1^{\text{TC}} & < & 155^\circ\,, \\ 160^\circ & < & \theta_2^{\text{TC}} & < & 177^\circ\,, \end{array} \qquad \begin{array}{rclcl} 160^\circ & < & \theta_1^{\text{CC}} & < & 174.0^\circ\,, \\ 160^\circ & < & \theta_2^{\text{CC}} & < & 175.5^\circ\,. \end{array}$$

The polar angle ranges are basically determined by the the acceptance of the corresponding detector components: the central tracking chambers $20° < \theta < 160°$ (see section 2.2.1.3), the LAr calorimeter $4° < \theta < 153°$ (see section 2.2.2.1) and the SpaCal $153° < \theta < 177.5°$ (see section 2.2.2.2).

The lower limit of 80° for the polar angle θ_1^{TC} of the track in the track-cluster selection is determined by the L4 finder `JPSPATC` (see section 4.3). The lower limit of 160° for the polar angle θ_2^{TC} for the cluster in the track-cluster selection is a remnant of the preselection. Its purpose is a clear classification as 'track' and 'cluster' for the track-cluster sample.

For the other limits refer to the distribution of the polar angle of the J/ψ decay electron candidates in figure 7.6 and figure 7.7 for both samples, track-cluster and cluster-cluster. There all cuts described in this chapter are applied with exception of the cut on the corresponding polar angle and the forward classification (see section 7.5). It is visible, that the other cuts — mainly the energy cuts — work as implicit θ-cuts. The explicit θ cuts are therefore very soft cuts. They are applied with view on the determination of the geometrical acceptance in section 8.2.1.

The cut $\theta_1^{\mathrm{CC}} < 174°$ ensures for the cluster-cluster sample, that at least one SpaCal cluster is in the geometric acceptance of the L1 trigger element `SPCLe_IET` > 1 (see section 4.1.4).

An additional implicit $\theta\phi$-cut is applied. Events with one cluster in the xy-regions of inefficient SpaCal trigger cells are not selected for the analysis. The xy-regions vary with the `run number` [103].

7.3.3 Energy Cuts

The following cuts on the momentum p_1, the energy E_1 and E_2 and the transverse momentum $p_{t,1}$ and $p_{t,2}$ of the J/ψ decay electron candidates are applied for track-cluster (TC) and cluster-cluster (CC) selection:

$$
\begin{array}{rr}
p_1^{\mathrm{TC}} > 0.8\,\mathrm{GeV/c}\,, & E_1^{\mathrm{CC}} > 4.2\,\mathrm{GeV}\,, \\
E_2^{\mathrm{TC}} > 4.2\,\mathrm{GeV}\,, & E_2^{\mathrm{CC}} > 4.2\,\mathrm{GeV}\,, \\
E_2^{\mathrm{TC}} > 6.0\,\mathrm{GeV}\ (\text{in SpaCal-box})\,, & \max\left\{E_1^{\mathrm{CC}}, E_2^{\mathrm{CC}}\right\} > 6.0\,\mathrm{GeV}\,, \\
p_{t,1}^{\mathrm{TC}} > 0.7\,\mathrm{GeV/c}\,, & p_{t,1}^{\mathrm{CC}} > 1.0\,\mathrm{GeV/c}\,, \\
p_{t,2}^{\mathrm{TC}} > 0.7\,\mathrm{GeV/c}\,, & p_{t,2}^{\mathrm{CC}} > 1.0\,\mathrm{GeV/c}\,.
\end{array}
$$

The energy and momentum distributions are shown in figure 7.6 and figure 7.7. There, all cuts with exception of the cut on the corresponding quantity and the forward classification (see section 7.5) are applied. The trigger selection leads to implicit energy cuts. The distributions show, that the above cuts are soft. They are applied, in order to determine the combined acceptance of the angular and energy cuts in section 8.2.1.

The cut '$E_2^{\mathrm{TC}} > 6.0\,\mathrm{GeV}$ (in SpaCal-box)' is necessary, because the L1 subtrigger `S33` (see section 4.1.6) contains the trigger element `SPCLe_IET_CEN_3` (see section 4.1.4). This trigger element is built from SpaCal trigger information from the central region:

-24.5 cm $< x <$ 16.6 cm, -17.2 cm $< y <$ 24.5 cm. This region defines the 'SpaCal-box'. In figure 7.1 the efficiency of the trigger element `SPCLe_IET_CEN_3` as a function of the energy is shown. At the energy of 6 GeV the trigger element reaches 50% efficiency. Therefore the cut '$E_2^{\mathrm{TC}} > 6.0\,\mathrm{GeV}$ (in SpaCal-box)' is applied for the track-cluster selection.

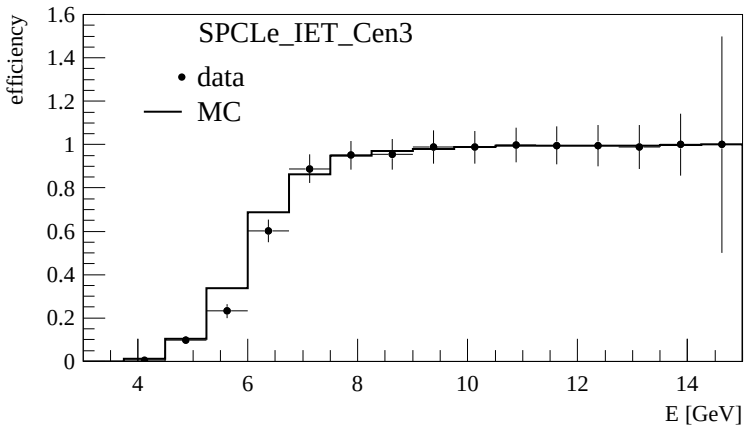

Figure 7.1: The efficiency of the trigger element `SPCLe_IET_CEN_3` as a function of the energy is shown for data and MC. The spatial range is restricted to the central region of the SpaCal: -24.5 cm $< x <$ 16.6 cm, -17.2 cm $< y <$ 24.5 cm.

The following cut on the reconstructed squared transverse momentum p_t^2 of the J/ψ is applied to data and MC events: [6]

$$\begin{aligned} p_t^2 &< 1.2\,\mathrm{GeV}^2/\,\mathrm{c}^2 \quad \text{for fwd.-untagged events,} \\ p_t^2 &< 5.0\,\mathrm{GeV}^2/\,\mathrm{c}^2 \quad \text{for fwd.-tagged events.} \end{aligned}$$

Using this cut the proton-elastic and proton-dissociative cross sections of the J/ψ photoproduction are equal and the MC contributions can be mixed taking the same number of generated events for each sample [84, 104, 105].

7.3.4 Miscellaneous Cuts

The following selection criteria are applied for the track-cluster (TC) and the cluster-cluster (CC) selection:

$$\begin{array}{lllll} \text{TC and CC :} & r^{\mathrm{cluster}} & < & 3.5\ \mathrm{cm}\,, \\ \text{TC and CC :} & |z_{\mathrm{vtx}} - z_{\mathrm{vtx}}^{\mathrm{run}}| & < & 40\ \mathrm{cm}\,, \\ \text{TC :} & \texttt{jpesclus} & < & 0.06\,, \\ \text{CC :} & \texttt{jpesclus} & < & 0.04\,. \end{array}$$

The lateral size of clusters r^{cluster} in the electromagnetic SpaCal is a good handle for the separation of hadronic and electromagnetic shower. This is possible due to the fine segmentation of the electromagnetic SpaCal and the Molière radius of 25.5 mm

[6] For the nomenclature 'fwd.-untagged' and 'fwd.-tagged' refer to section 3, section 6.4.3 or section 7.5.

(see section 2.2.2.2). In [106] it is shown, that the requirement of $r^{\text{cluster}} < 3.5$ cm and $E_{\text{had}}^{\text{cluster}} < 0.2\,\text{GeV}$ yields an electron identification efficiency of $(99 \pm 1)\%$ and a pion misidentification of $< 2\%$. $E_{\text{had}}^{\text{cluster}}$ is the energy in the hadronic SpaCal in a circle with 17.5 cm radius behind the electromagnetic cluster. [107] suggest, not to use the information from the hadronic SpaCal for this analysis, since at these low energies the value is strongly influenced by noise, which is not simulated in MC. In order to avoid a systematic bias due to noise in the hadronic SpaCal no additional cut on the hadronic energy in the SpaCal is applied (see the preselection in section 7.3.1). In addition it is checked, that the cut on $E_{\text{had}}^{\text{cluster}} < 0.2\,\text{GeV}$ would reject only less than 0.4% of the events in the data.

The cut on the z_{vtx} position uses the reconstructed vertex position from the central-track for the track-cluster sample and from the BST-track(s) for the cluster-cluster sample. This cut is important for the satellite bunch correction in the luminosity calculation (see section 8.1). $z_{\text{vtx}}^{\text{run}}$ is the average vertex position z_{vtx} in a run.

`jpesclus` is the ratio of the energy in the SpaCal outside of the energy depositions of the J/ψ decay electron candidates. The cut on `jpesclus` ensures an empty SpaCal besides the main clusters, which is the expected signature of events in photoproduction. The preselection in section 7.3.1 allows additional SpaCal clusters. The energy of these additional clusters is summed up and divided by E_2 for the track-cluster and E_1+E_2 for the cluster-cluster sample. The minimal energy of each additional cluster is 200 MeV. The noise in the electromagnetic SpaCal is $\approx 3\,\text{MeV/cell}$. On average $15-25$ cells contribute to a cluster, which results in noise for a cluster of $\sqrt{15-25} \times 3\,\text{MeV} \approx 12-15\,\text{MeV}$ [108]. Therefore pure noise does not contribute to the sum. The distributions of `jpesclus` are shown in figure 7.2 for the track-cluster and cluster-cluster sample.

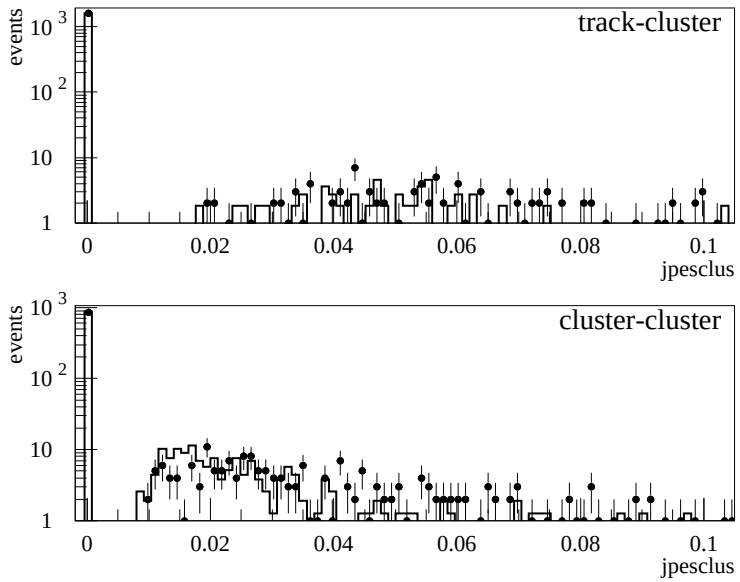

Figure 7.2: The energy fraction `jpesclus` is shown for the the track-cluster and cluster-cluster sample for data (dots) and MC events (solid line).

Usually a cut on y_{JB} is applied in order to reject QED-Compton events[68, 109]. In the case of QED-Compton events $ep \to e\gamma p$ the scattered beam electron and a photon are detected in the detector and give a topology similar to J/ψ decays. Due to energy

and momentum conservation it is therefore $y_{\mathrm{JB}} \approx 1$. y_{JB} is connected to the γp centre of mass energy $W_{\gamma p}$ by equation 6.4: ${W_{\gamma p}}^2 \approx y_{\mathrm{JB}}\, s + m_p^2$. An usual value for the cut on y_{JB} is 0.81. In section 8.2 the binning in $W_{\gamma p}$ is presented for the track-cluster and the cluster-cluster sample. The binning in $W_{\gamma p}$ for the track-cluster sample is implicitly an even stronger cut on y_{JB}. The upper limit $W_{\gamma p} \leq 235\,\mathrm{GeV}$ corresponds to $y_{\mathrm{JB}} \leq 0.54$. Due to the $W_{\gamma p}$ range for the cluster-cluster sample, the y_{JB} cut cannot be applied. Therefore no explicit cut on y_{JB} is applied for the track-cluster and cluster-cluster selection.

7.3.5 Mass Cut

For the calculation of efficiencies the following cut on the invariant mass $m_{e^+e^-}$ of the J/ψ decay electron candidates is applied for the track-cluster (TC) and the cluster-cluster (CC) selection:

$$\begin{aligned} \mathrm{TC}: &\quad 2.6\,\mathrm{GeV/c^2} < m_{e^+e^-} < 3.4\,\mathrm{GeV/c^2} \\ \mathrm{CC}: &\quad 2.8\,\mathrm{GeV/c^2} < m_{e^+e^-} < 3.4\,\mathrm{GeV/c^2} \end{aligned}$$

These mass windows are also used in section 8.3 as intervals for the integration in the signal extraction. The asymmetric mass window for the track-cluster cut around the nominal J/ψ mass $m_{J/\psi} \approx 3.1\,\mathrm{GeV/c^2}$ is a consequence of the radiative tail in the distribution of the invariant mass towards lower masses (see section 8.3).

7.3.6 BST Cut

The BST cut is based on the tracks resulting from the BST track finding (see section 6.2). The main purpose of the BST tracks is the reconstruction of a vertex, if no information from a central track is available. With the vertex position the measurement of the polar angle θ in the backward region is improved. If a vertex information is already avaliable, the additional improvement by the precise θ measurement is a small effect. While the improvement on the resolution is negligible for the track-cluster sample, it is essential for the cluster-cluster sample. Taking this and the efficiency of the BST track finding into account (see figure 6.11), no BST track is required for the track-cluster selection, since the central-track already provides the vertex information.

For the cluster-cluster sample the BST track finding is essential, since no central track exists and only the BST track provides vertex information. Therefore at least one BST track is required for the cluster-cluster selection. If the second cluster is also in the geometrical acceptance of the BST, a second BST track is required, in order to suppress background events originating from the QED-Compton process, where one cluster is caused by a photon.

The geometrical acceptance of the BST is determined from the data. For each plane and each ϕ-segment the minimum and maximum radius of hits is determined. By this method inefficient regions at the inner or outer edges of the segments are taken into account. Based on this information, the z-position of the vertex z_{vtx} and the

polar angle θ of a particle candidate the number of BST planes n^{planes} is determined which would be hit. Taking into account in addition the resolution of z_{vtx} and θ, the minimum $n^{\text{planes}}_{\text{min}}$ and maximum number $n^{\text{planes}}_{\text{max}}$ of BST planes is determined which a particle candidate would cross. In figure 7.3 the values of n^{planes}, $n^{\text{planes}}_{\text{min}}$ and $n^{\text{planes}}_{\text{max}}$ are shown as functions of the polar angle θ for different values of the vertex position z_{vtx}.

A cluster is in the geometrical acceptance of the BST, if $n^{\text{planes}}_{\text{min}} \geq 3$.

In figure 7.4 the distribution of the reconstructed invariant mass $m_{e^+e^-}$ of the J/ψ decay electron candidates is shown for the cluster-cluster sample: without BST cut, with BST cut and in addition with improved polar angular measurement. The figure shows, that the usage of the BST information is essential in the cluster-cluster selection.

7.4 Trigger Cuts

The triggers for the track-cluster and the cluster-cluster selection are described in chapter 4. The motivation for the choice of the particular chain of level 1 subtrigger (see section 4.1.6), level 2 subtrigger (see section 4.2.3 and section 4.2.4) and L4 finder (see section 4.3) for each of the two topologies is also given in chapter 4:

sample	L1ST	L2ST	L4 finder
track-cluster	`S33`	L2TB 8	`JPSPATC`
cluster-cluster	`S40`	L2TB 6	`JPSPAC`

The activation of the corresponding L1ST and L2ST and L4 finder are required for the selection of data and MC events.

The trigger chain is determined by the choice of the L1ST. In order to study other L1ST candidates all cuts described in this chapter are applied with exception of the trigger cuts. All activated L1STs are shown in figure 7.5. In order to study whether also other L1ST are suitable for triggering J/ψ events, the activated L1ST are shown, where the subtrigger `S33` for the track-cluster sample and the `S40` for the cluster-cluster sample are not activated respectively. Figure 7.5 shows, that the other L1ST deliver not enough statistics to be included in the analysis. The independent L1 subtriggers `S61` is used to crosscheck the efficiency of the L2NN for the track-cluster selection. No independent L1 subtrigger exists for the the cluster-cluster selection, since all high statistics L1 subtrigger in figure 7.5 are also validated by L2 subtriggers.

A possibility to increase the statistics would be, to take several L1ST (*L1ST cocktail*) for the selection of one sample. This complicates the calculation of the luminosity. In section 8.1 the calculation of the luminosity is described, where the prescale factor of one L1ST is taken into account. For a L1ST cocktail the relative prescale factors of all L1ST in the cocktail have to be taken into account. The individual prescale factors are adjusted automatically in order to take the different beam conditions into account. Therefore the relative prescale factors for the L1ST cocktail can change from run to run. Comparing the additional systematics and the low statistics of the other L1ST, the possibility of a L1ST cocktail is discarded. Therefore only one L1ST is chosen for each sample.

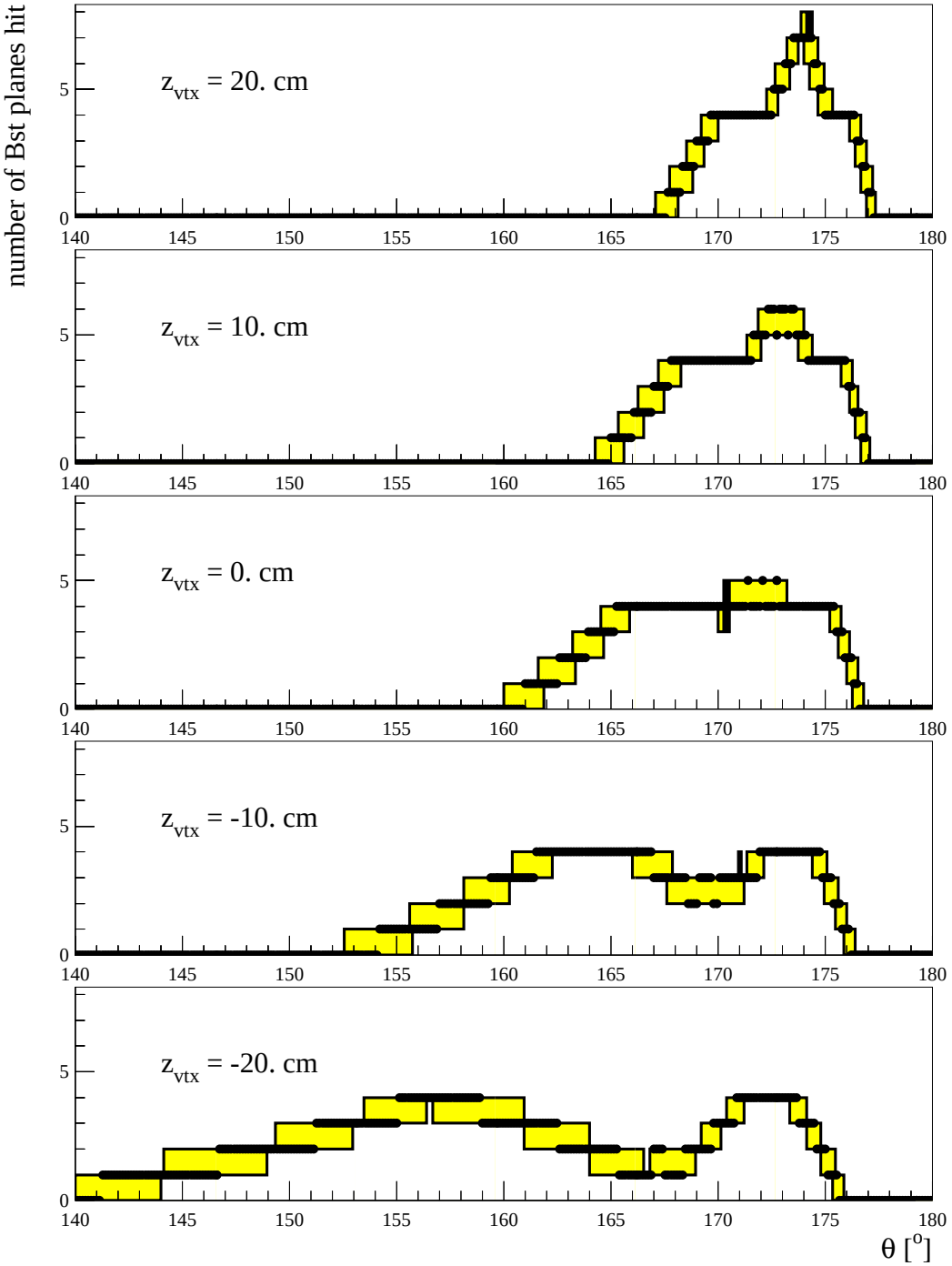

Figure 7.3: The points show the number n^{planes} of BST planes a track with a given polar angle θ and vertex position z_{vtx} would cross at azimuthal angle $\phi = 0°$. The variation of the polar angle θ and the vertex position z_{vtx} by the measurement resolution gives the shaded band of the minimum $n^{\text{planes}}_{\text{min}}$ and maximum number $n^{\text{planes}}_{\text{max}}$ of BST planes a track would hit. This information is used to determine the geometrical acceptance of the BST.

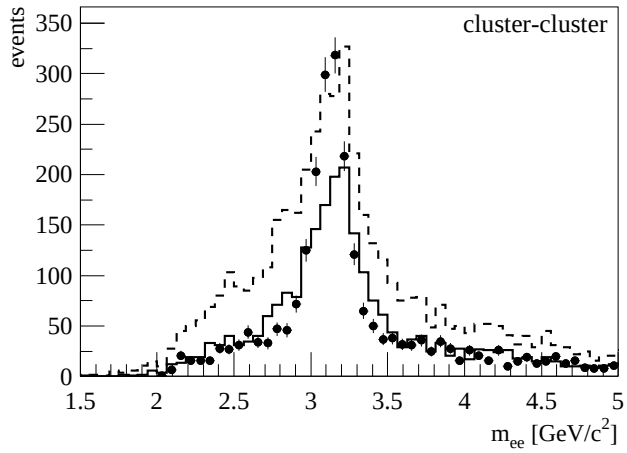

Figure 7.4: The distribution of the reconstructed invariant mass $m_{e^+e^-}$ of the J/ψ decay electron candidates is shown for the cluster-cluster sample. The dashed and solid line show the distributions without and with application of the BST cut. Taking the improved measurement of the polar angle into account the distribution represented by the points is reached.

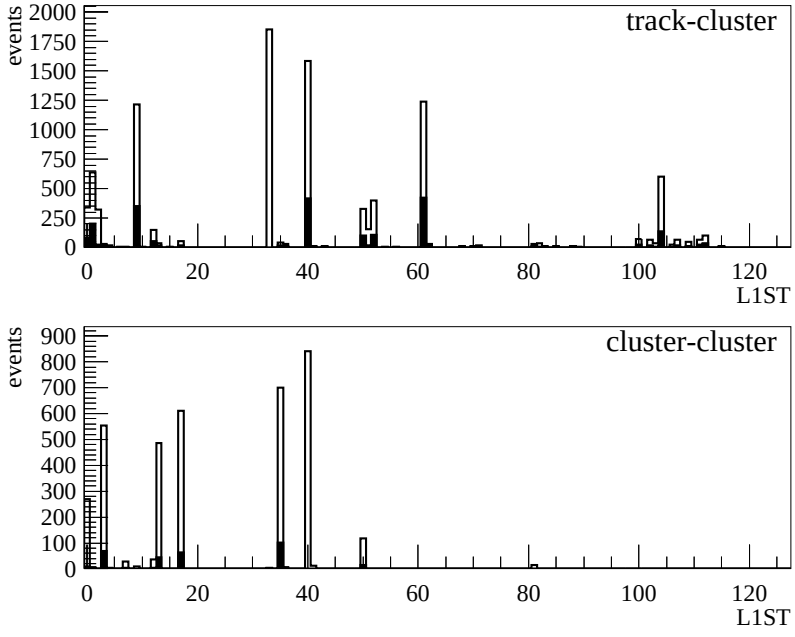

Figure 7.5: The activated L1ST for the track-cluster and cluster-cluster sample are shown. All cuts of this chapter with exception of the trigger selection are applied (solid line). The filled histograms show the activated L1ST in the case when `S33` and `S40` are not activated for the track-cluster and cluster-cluster sample respectively.

7.5 Forward Classification

The information of the forward detectors — the forward part of the LAr Calorimeter (see section 2.2.2.1), the forward muon detector FMD (see section 2.2.3.2) and the proton remnant tagger PRT (see section 2.2.4) — is used for the classification of events as fwd.-tagged and fwd.-untagged (see section 3 for the nomenclature). The classification criteria are already defined in section 6.4.3. An event is called fwd.-tagged if one of the following cuts is fulfilled:

- $E_{\mathrm{LAr10}} > 0.75\,\mathrm{GeV}$,
- $N_{\mathrm{FMD}} > 1$ in the layers 1, 2 and 3 of the FMD,
- $N_{\mathrm{PRT}} > 0$ for the channels 1, 2 and 3 of the PRT,

where E_{LAr10} is the energy in the forward LAr calorimeter for the polar angle range $\theta < 10°$, N_{FMD} is the number of hits in the FMD and N_{PRT} is the number of hits in the PRT.

The classification in fwd.-tagged or fwd.-untagged is used for the determination of the number of proton-elastic or proton-dissociative events (see section 8.5).

7.6 Control Distributions

In figure 7.6 and figure 7.7 the distribution of the the energy $E_{1/2}$, the transverse momentum $p_{t,1/2}$, the polar angle $\theta_{1/2}$, the azimuthal angle $\phi_{1/2}$, the z_{vtx} position and the kinematic variables $W_{\gamma p}$ and p_t^2 are shown for the combined data of the running periods 1999 e^+ and 2000 e^+. The two plots for the kinematic variable p_t^2 contain the same data, but have a different scale on the abscissa.

For the track-cluster selection the index 1 refers to the track, the index 2 to the cluster. For the cluster-cluster selection the index 1 refers to the decay electron candidate with lower polar angle θ.

The distributions of data are compared with the sum of proton-elastic and proton-dissociative MC distributions of the generators `DiffVM` (see section 5.1.1), `LPair2` (see section 5.1.2) and `COMPTON` (see section 5.1.3). For the distributions all cuts described in chapter 7 are applied except the cut on the plotted quantity and the forward classification (see section 7.5). The data distributions are well described almost everywhere.

Two wires of the CJC2 in the region of the azimuthal angle $\phi \approx 0°$ broke at run 263235 and 265173 respectively. This affects the distribution ϕ_1 of the track-cluster sample, which shows a drop in the number of events at around $\phi_1 \approx 0°$. The distribution of the azimuthal angle ϕ_2 of the cluster shows the expected lower statistics at $\phi_2 \approx 180°$. The effect of the broken wires is well described by MC.

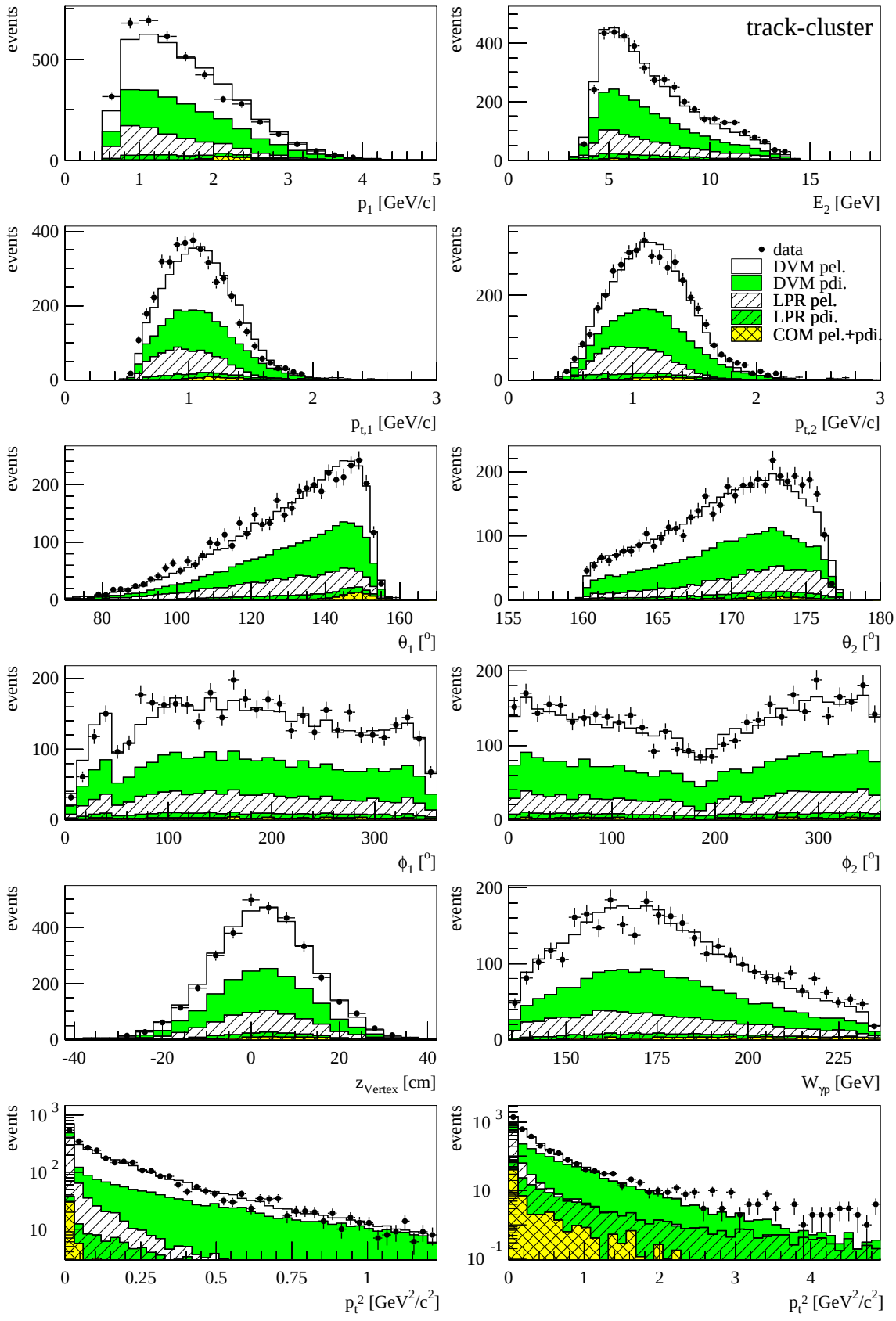

Figure 7.6: Track-Cluster: For the description of the distributions refer to section 7.6.

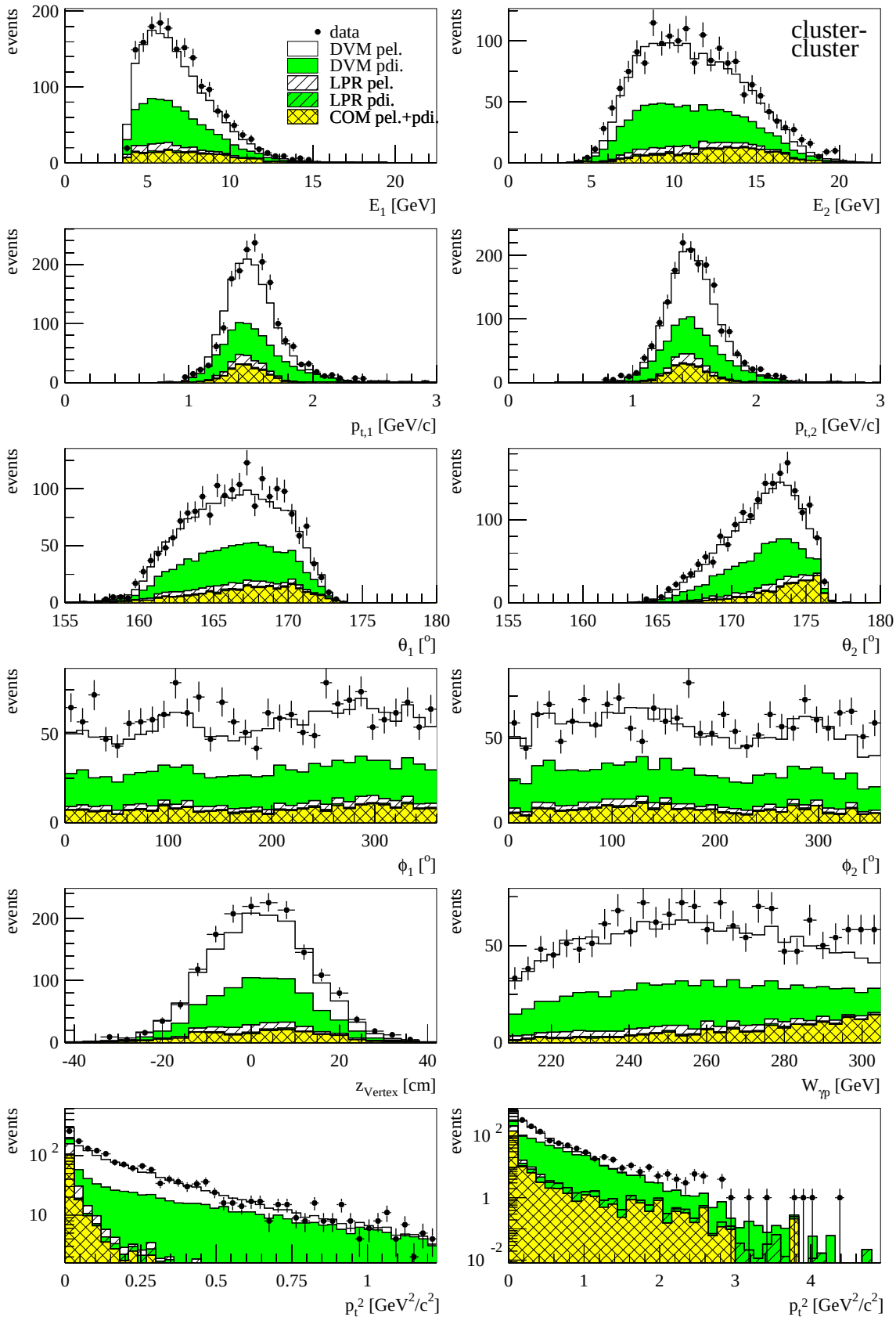

Figure 7.7: Cluster-Cluster: For the description of the distributions refer to section 7.6.

Chapter 8

Analysis

In this chapter the basis for the calculation of cross sections is presented. The formula for the calculation of the elastic photoproduction cross section $\sigma_{\gamma p \to J/\psi p}$ is

$$\sigma_{\gamma p \to J/\psi p} = \frac{N_{\text{notag}} \cdot (1 - f_{\psi(2S)}) \cdot f_{\text{ed}}}{\mathcal{F}_\gamma \cdot \varepsilon_{\text{tot}} \cdot \mathcal{B} \cdot \mathcal{L}} \,, \tag{8.1}$$

where N_{notag} is the number of fwd.-untagged signal events for the corresponding channel in a region of phase space, $\mathcal{B} = (5.93 \pm 0.10)\%$ [110] is the branching ratio for $J/\psi \to e^+e^-$, $\mathcal{L}$ the integrated luminosity, ε_{tot} the total efficiency and $\mathcal{F}_\gamma$ is the photon flux factor connecting the γp cross section with the ep cross section (see equation 1.24). f_{ed} is the correction factor for the proton elastic photoproduction and $f_{\psi(2S)}$ is the correction factor for the contamination from $\psi(2S)$ decays.

The calculation of the integrated luminosity $\mathcal{L}$ is described in section 8.1.

The elastic photoproduction cross section[1] $\sigma(W_{\gamma p})$ is calculated for different regions of phase space, in this case for intervals in $W_{\gamma p}$. These intervals are also called *bins*. The differential cross section $\frac{\mathrm{d}\sigma}{\mathrm{d}t}$ will be given in bins of $|t| \approx p_t^2$. The choice of binning is presented in section 8.2.

At HERA the e^+p cross section $\sigma_{e^+p \to J/\psi e^+p}$ is measured. In order to obtain the photoproduction cross section $\sigma_{\gamma p \to J/\psi p}$ equation 1.23 is used which connects the two cross sections by the photon flux factor $\mathcal{F}_\gamma$ (see section 1.3):

$$\sigma_{\gamma p \to J/\psi p} = \frac{1}{\mathcal{F}_\gamma} \sigma_{e^+p \to J/\psi e^+p} \,. \tag{8.2}$$

The photon flux factor $\mathcal{F}_\gamma$ is calculated by numerical integration of equation 1.24 for the corresponding $W_{\gamma p}$ ranges of the different binnings (see section 8.2.3).

The total efficiency ε_{tot} includes effects from detector acceptance and the selection criteria from chapter 7 including the kinematic and the trigger selection. The determination of the efficiencies is described in section 8.4.

[1] The shorthand notations $\sigma(W_{\gamma p})$ and $\frac{\mathrm{d}\sigma}{\mathrm{d}t}$ are used for the total and differential elastic J/ψ photoproduction cross secions.

The signal extraction and the background subtraction are explained in section 8.3. The number of proton-elastic events is obtained by applying the correction factor f_{ed}. Its determination is described in section 8.5.

The J/ψ signal contains also events originating from $\psi(2S)$ decays to J/ψ and neutral particles. The contamination amounts to $f_{\psi(2S)} = 0.040 \pm 0.005$ [99]. This contamination is reduced to $f^{\mathrm{TC}}_{\psi(2S)} = 0.012 \pm 0.005$ and $f^{\mathrm{CC}}_{\psi(2S)} = 0.005 \pm 0.005$ by the cut `jpesclus` (see section 7.3.4) for the track-cluster and the cluster-cluster samples respectively [111].

For the calculation of the differential cross section $\frac{\mathrm{d}\sigma}{\mathrm{d}t}$ an unfolding of the number of events in bins of p_t^2 to the number of events in bins of $|t|$ is necessary. The unfolding method is described in section 8.6.

In section 8.7 the determination of the systematic errors is presented.

8.1 Luminosity Calculation

For each run an integrated luminosity is measured by the luminosity system (see section 2.2.6). The following corrections are applied: satellite bunch correction, HV-bit correction and L1ST-prescale correction.

The HERA proton beam has a complicated longitudinal structure. This is the consequence of the methods used for the acceleration. In addition to the main bunches (see section 2.1) several neighbouring bunches — so called *satellite bunches* — exist. Events originating from collisions of the proton satellite bunches with bunches of the electron beam contribute to the measurement of the luminosity. Events from such collisions are 'out of time' and therefore lead to additional peaks in the distribution of the vertex position z_{vtx} besides the main interaction region. The largest effect on the luminosity calculation have the 'late satellite bunches', which lead to an additional peak in the z_{vtx} distribution at +72 cm. On the other hand, for the selection of J/ψ events the cut $|z_{\mathrm{vtx}}| < 40$ cm (see section 7.3.4) is applied. This cut is taken into account in the calculation of the integrated luminosity (so called *satellite bunch correction*). This correction is typically $5 - 10\%$ with an uncertainty of $0.6 - 1\%$ [112, 113].

In addition the integrated luminosity is corrected according to the requirements of the individual physics analysis. Each physics analysis needs a special set of detector components to be operational. The fraction of a run in which these detectors are operational is obtained from the event wise detector status information (see section 7.2). The integrated luminosity is corrected accordingly (*HV-bit correction*).

The prescale factors (see section 4.1) of the corresponding L1ST are also taken into account for the luminosity calculation (*L1ST-prescale correction*). The integrated luminosity is corrected for each run. The amount of data, taken with different prescale factors of the L1ST `S33` and S40, is shown in figure figure 8.1. The continuous, integer distribution of the prescale factors is a feature of the autoprescale mechanism, which adjusts the prescale factors according to the maximum rate of the subtrigger. The average prescale factors for the different running periods are listed in table 8.1.

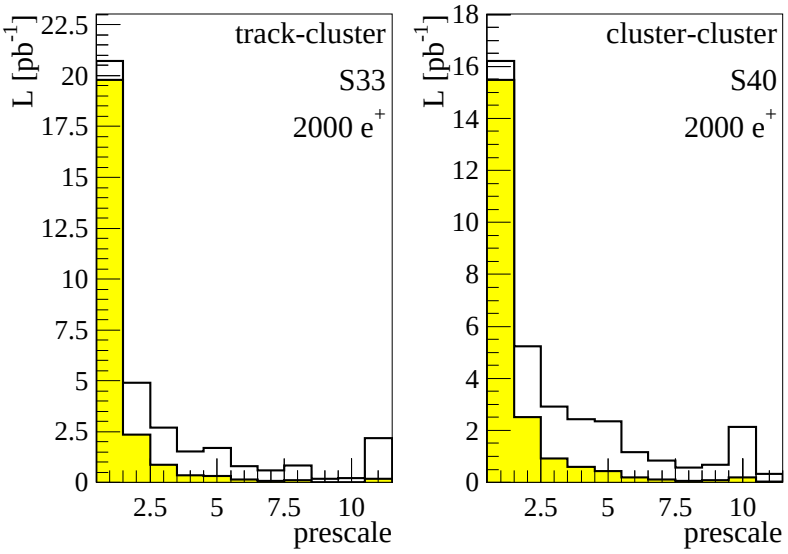

Figure 8.1: The amount of data, taken with different prescale factors of the L1ST `S33` and S40 for the track-cluster and the cluster-cluster selection, is shown for the running period 2000 e^+. The entries in the histograms are weighted by the integrated luminosity of the runs (solid line) and by the final corrected integrated luminosity (shaded histogram).

The final corrected integrated luminosity is summed up for all runs passing the run selection described in section 7.1. In table 8.1 the value and error of the corrected integrated luminosity for the L1ST `S33` and `S40` for the different running periods are listed.

The number of selected events per 1 pb^{-1} for the track-cluster and cluster-cluster sample is shown in figure 8.2. The low event yield for the running period 1999 e^- is caused by the low BST track finding efficiency (see figure 6.11). The running period 1999 e^- is therefore excluded from this analysis. The second half of the running period 1999 e^+ (`run number` $>$ 256000) is excluded from the analysis due to broken wires in each the CJC1 and the CJC2. The drop in the event yield for the cluster-cluster selection in the run range 269000 $\leq$ `run number` $\leq$ 272000 is caused by BST read-out problems [95], which result in a reduced BST track finding efficiency (see figure 6.9).

			track-cluster	cluster-cluster
1999 e^+	$\langle$pr$\rangle$		1.20	1.16
	$\mathcal{L}$	[pb^{-1}]	5.89	6.10
	$\delta\mathcal{L}$	[%]	1.10	
	$\delta\mathcal{L}_{\text{sat}}$	[%]	1.00	
	$\delta\mathcal{L}_{\text{tot}}$	[%]	1.50	
2000 e^+	$\langle$pr$\rangle$		1.54	1.80
	$\mathcal{L}$	[pb^{-1}]	24.37	20.80
	$\delta\mathcal{L}$	[%]	1.30	
	$\delta\mathcal{L}_{\text{sat}}$	[%]	0.60	
	$\delta\mathcal{L}_{\text{tot}}$	[%]	1.45	
total	$\langle$pr$\rangle$		1.47	1.65
	$\mathcal{L}$	[pb^{-1}]	30.26	26.90
	$\delta\mathcal{L}_{\text{tot}}$	[%]	1.50	

Table 8.1: The average prescale factors $\langle$pr$\rangle$ and the corrected integrated luminosity $\mathcal{L}$ for the track-cluster and cluster-cluster sample for the different run periods are shown. The relative error of the luminosity measurement $\delta\mathcal{L}$, the relative error of the satellite bunch correction $\delta\mathcal{L}_{\text{sat}}$ and the total relative error $\delta\mathcal{L}_{\text{tot}}$ are taken from [113].

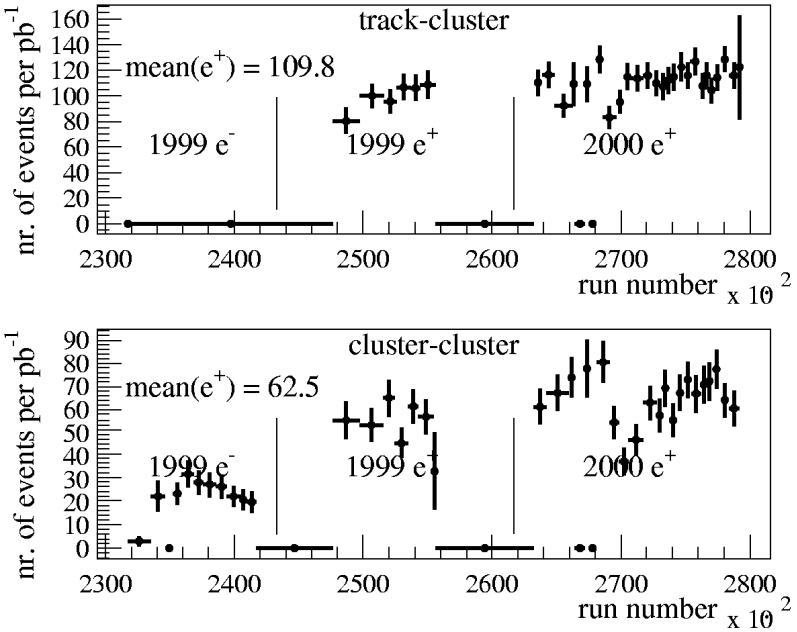

Figure 8.2: The number of selected events per 1 pb^{-1} for the track-cluster and cluster-cluster sample and the mean values for the running periods 1999 e^+ and 2000 e^+ are shown. All cuts of chapter 7 are taken into account with the exception of the forward selection. Background is not subtracted.

8.2 Binning and Photon Flux

The measurement of the cross sections $\sigma(W_{\gamma p})$ and $\frac{\mathrm{d}\sigma}{\mathrm{d}t}$ is performed in intervals of the phase space. The choice of these intervals, the so called *binning*, is described in the following sections 8.2.1 and 8.2.2.

The photon flux $\mathcal{F}_\gamma$ depends on the $W_{\gamma p}$ interval. The calculation is described in section 8.2.3.

8.2.1 $W_{\gamma p}$ Binning

The cross section $\sigma(W_{\gamma p})$ is measured in bins of $W_{\gamma p}$, the so called $W_{\gamma p}$ *binning*. The overall $W_{\gamma p}$ ranges for the track-cluster and cluster-cluster samples are determined by the acceptance. In the chosen $W_{\gamma p}$ range the acceptance is $\geq 30\%$ (see figure 8.3). The $W_{\gamma p}$ bins are chosen to have similar statistics in the bins within the sample. This choice of binning leads to a statistically stable signal extraction (see section 8.3).

The definition of the bins used for the cross section calculation is listed in table 8.2. As abscissa for the cross section measurements the mean value $\langle W_{\gamma p} \rangle$ of the $W_{\gamma p}$ bins is used. $\langle W_{\gamma p} \rangle$ is determined as the centre of gravity by MC.

The resolution of $W_{\gamma p}$ within the bins ranges from 2.9 GeV to 3.4 GeV which is much smaller than the width of the bins. The migration of events from bin to bin is studied using purity and stability. The quantities purity and stability are defined for each bin in the following way:

$$\begin{aligned} \text{purity} &= N_{\text{gen+rec}}/N_{\text{rec}}\,, \\ \text{stability} &= N_{\text{gen+rec}}/N_{\text{gen}}\,, \end{aligned} \tag{8.3}$$

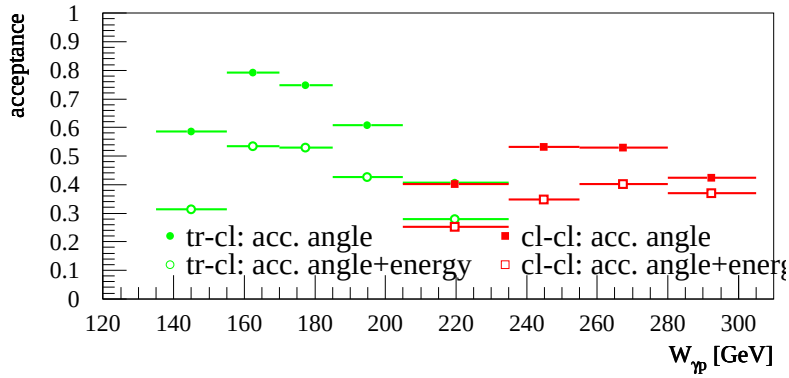

Figure 8.3: The acceptance as a function of $W_{\gamma p}$ is shown for the track-cluster and cluster-cluster sample. The angular cuts (see section 7.3.2) alone or together with the energy cuts (see section 7.3.3) are applied on generated values of J/ψ decay electrons.

	track-cluster					cluster-cluster			
min. $W_{\gamma p}$ [GeV]	135.0	155.0	170.0	185.0	205.0	205.0	235.0	255.0	280.0
max. $W_{\gamma p}$ [GeV]	155.0	170.0	185.0	205.0	235.0	235.0	255.0	280.0	305.0
$\langle W_{\gamma p} \rangle$ [GeV]	144.9	162.5	177.3	194.8	219.6	219.6	244.8	267.2	292.3
$\mathcal{F}_\gamma / 10^{-2}$	0.885	0.545	0.464	0.517	0.607	0.607	0.320	0.329	0.267

Table 8.2: For the $W_{\gamma p}$ binning the bin boundaries, the mean value $\langle W_{\gamma p} \rangle$ and the photon flux $\mathcal{F}_\gamma$ are shown for the track-cluster and cluster-cluster sample.

where N_{gen} is the number of events generated in the bin, N_{rec} the number of events reconstructed in the bin. $N_{\text{gen+rec}}$ is the number of events which are generated and reconstructed in this bin. The numbers N_{gen}, N_{rec}, $N_{\text{gen+rec}}$ are determined with a signal MC sample which passed all selection criteria.

The purity and stability for the $W_{\gamma p}$ binning are shown in figure 8.4. The high values for both, purity and stability, indicate low migration between the bins.

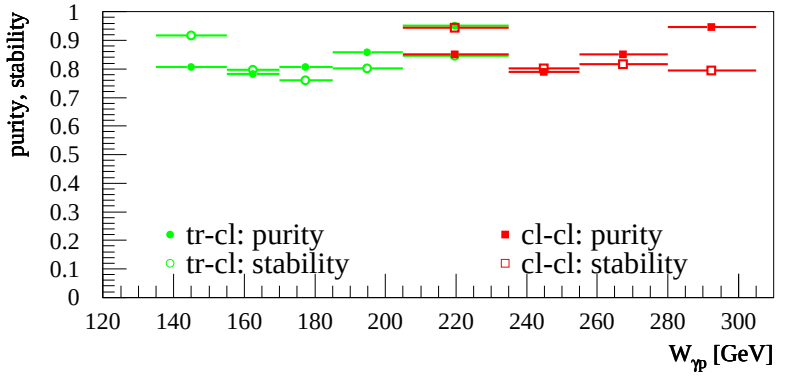

Figure 8.4: The purity and stability for the $W_{\gamma p}$ binning are shown for the track-cluster and cluster-cluster sample.

8.2.2 p_t^2 Binning

For the measurement of the differential cross section $\frac{d\sigma}{dt}$ two binnings are necessary: a binning in p_t^2 and a binning in $|t|$.

The kinematic variable $|t|$ is experimentally not accessible (see section 6.3). Therefore the approximation $|t| \approx p_t^2$ is used for the event counting. The number of events is determined in bins of $W_{\gamma p}$ and p_t^2.

Due to limited statistics the differential cross section $\frac{\mathrm{d}\sigma}{\mathrm{d}t}$ is measured for the track-cluster and cluster-cluster sample in one bin of $W_{\gamma p}$ for each sample. These two $W_{\gamma p}$ bins are the total $W_{\gamma p}$ ranges of the track-cluster and cluster-cluster samples respectively.

The overall range in p_t^2 is limited by the p_t^2 cut for the fwd.-untagged event selection (see section 7.3.3). A non-equidistant binning in p_t^2 is chosen taking into account the exponential distribution of data in the bins. The actual bin boundaries are adjusted to the values in [99] in order to be able to combine the results from both analyses. Because of lower statistics the highest three p_t^2 bins are each a combination of two bins from [99]. The bin boundaries are listed in table 8.3.

	track-cluster					cluster-cluster				
min. $W_{\gamma p}$ [GeV]	135.0					205.0				
max. $W_{\gamma p}$ [GeV]	235.0					305.0				
$\langle W_{\gamma p} \rangle$ [GeV]	180.6					250.7				
min. p_t^2 [GeV^2/c^2]	0.000	0.070	0.140	0.300	0.600	0.000	0.070	0.140	0.300	0.600
max. p_t^2 [GeV^2/c^2]	0.070	0.140	0.300	0.600	1.200	0.070	0.140	0.300	0.600	1.200
$\langle p_t^2 \rangle$ [GeV^2/c^2]	0.033	0.103	0.211	0.420	0.798	0.033	0.103	0.211	0.420	0.791
$\mathcal{F}_\gamma / 10^{-2}$	3.016					1.522				

Table 8.3: For the p_t^2 binning the bin boundaries, the mean value $\langle p_t^2 \rangle$ for the bins and the photon flux $\mathcal{F}_\gamma$ are shown for the track-cluster and cluster-cluster sample.

The mean value $\langle p_t^2 \rangle$ for a p_t^2 bin or $|t|$ bin is determined by generated MC events. Because of the exponential behaviour of the differential cross section and the wide bins this value is not suited as abscissa for the differential cross section measurement. As discussed in [114] the correct position t_{pos} in the bin $[t_{\mathrm{min}}, t_{\mathrm{max}}]$ is

$$\frac{\mathrm{d}\sigma}{\mathrm{d}t}(t_{\mathrm{pos}}) = \frac{1}{t_{\mathrm{max}} - t_{\mathrm{min}}} \int_{t_{\mathrm{min}}}^{t_{\mathrm{max}}} \frac{\mathrm{d}\sigma}{\mathrm{d}t}(t)\,\mathrm{d}t\,. \tag{8.4}$$

With the assumption $\frac{\mathrm{d}\sigma}{\mathrm{d}t}(t) \propto \mathrm{e}^{-b\cdot|t|}$ this leads to

$$t_{\mathrm{pos}} = t_{\mathrm{min}} + \frac{1}{b}\left\{\ln(b\cdot(t_{\mathrm{max}} - t_{\mathrm{min}})) - \ln(1 - \mathrm{e}^{-b\cdot(t_{\mathrm{max}} - t_{\mathrm{min}})})\right\}\,, \tag{8.5}$$

where the slope parameter b is determined in an exponential fit to $\frac{\mathrm{d}\sigma}{\mathrm{d}t}$ (see section 9.2.1). Therefore the determination of the positions t_{pos} in the bins and the slope parameter b is done in an iterative procedure.[2]The convergence is tested.

The calculation of the differential cross section $\frac{\mathrm{d}\sigma}{\mathrm{d}t}$ needs the number of events in bins of $|t|$. The number of events in bins of $|t|$ is determined from the number of events in bins of p_t^2 by an unfolding method (see section 8.6). The same bin boundaries for the

[2]The results of t_{pos} and b for the track-cluster and cluster-cluster samples are listed in table 9.4.

$|t|$ binning are used as for the p_t^2 binning (see table 8.3). The choice of the binning both in p_t^2 and in $|t|$ is referred to as the p_t^2 *binning*.

In order to study the approximation $|t| \approx p_t^2$ (see section 6.3) the following method for the calculation of purity and stability is used. On the generator level the bin is determined by the quantity $|t|$ and on reconstruction level by the quantity p_t^2.

The low values for purity and stability (see figure 8.5) indicate large migration[3] between the bins. Therefore the unfolding method of the number of events in bins of p_t^2 to the number of events in bins of $|t|$ is necessary. The unfolding method is described in section 8.6.

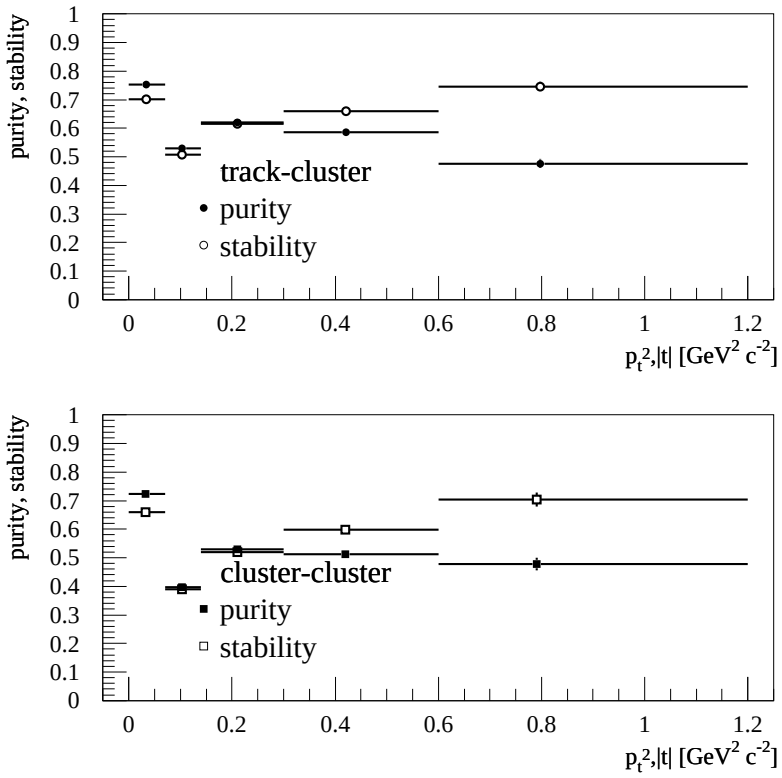

Figure 8.5: The purity and stability for the p_t^2 binning are shown for the track-cluster and cluster-cluster sample.

8.2.3 Photon Flux

The photon flux $\mathcal{F}_\gamma$ is needed for the measurement of the photoproduction cross section $\sigma_{\gamma p \to J/\psi p}$ (equation 8.2). $\mathcal{F}_\gamma$ depends on the $W_{\gamma p}$ interval. For the corresponding $W_{\gamma p}$ intervals in the $W_{\gamma p}$ binning and the p_t^2 binning the photon flux $\mathcal{F}_\gamma$ is calculated by numerical integration of equation 1.24.

The $W_{\gamma p}$ intervals are transformed to y intervals using equation 1.4. The upper limit of the integration is[4] $Q^2_{\max} := 1\,\mathrm{GeV}^2/\,\mathrm{c}^2$.

[3] The migration is shown in figure 8.9.

[4] The choice of $Q^2_{\max} := 1\,\mathrm{GeV}^2/\,\mathrm{c}^2$ is the standard value for photoproduction analyses in H1. For $Q^2 \leq 1\,\mathrm{GeV}^2/\,\mathrm{c}^2$ the scattered beam electron is usually not detected. This choice of $Q^2_{\max}$ is also used as a cut on generator level in order to select the photoproduction topology in the J/ψ simulation.

The photon flux $\mathcal{F}_\gamma$ as a function of $W_{\gamma p}$ is shown in figure 8.6. The values of $\mathcal{F}_\gamma$ for the $W_{\gamma p}$ binning and p_t^2 binning are shown in table 8.2 and table 8.3.

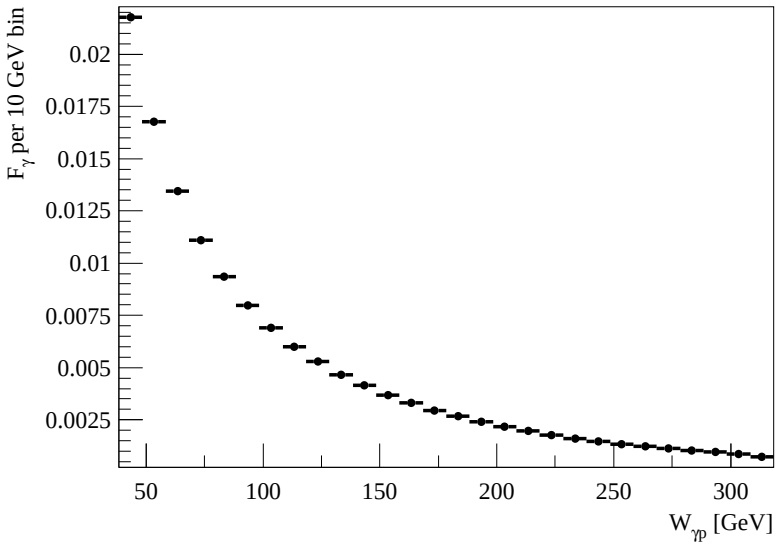

Figure 8.6: The photon flux as a function of $W_{\gamma p}$ is shown. The numerical integration is done for intervals in $W_{\gamma p}$, which are indicated by the horizontal lines.

8.3 Signal Extraction

In the signal extraction procedure the number of signal events is determined for a given bin. The method applied in this analysis starts with the distribution of the invariant mass $m_{e^+e^-}$ of the J/ψ decay electron candidates. All selection criteria from chapter 7 are applied.

In figure 8.7 the distribution of the invariant mass $m_{e^+e^-}$ is shown for the track-cluster and cluster-cluster samples. In both samples the J/ψ events give a clear peak at $\approx 3.1\,\text{GeV}$.

In the track-cluster sample the distribution has a *radiative tail* towards lower mass values. This tail is caused by events where the track-electron has radiated a photon. The momentum measurement of the track by the central tracking detectors does not take into account the radiated photon. Therefore the measured track momentum is lower than the momentum of the original electron. This results in a lower reconstructed invariant mass $m_{e^+e^-}$.

The peak for the cluster-cluster sample is symmetric, since the energy depositions of the radiated photons in the SpaCal belong to the same cluster as for the originating decay electron. This is due to the fact that the radiated photons are emitted collinear to the decay electrons and at large polar angle θ the track curvature due to the solenoidal magnetic field is small.

The distribution of the invariant mass $m_{e^+e^-}$ is contaminated by background events. The prominent processes are the electron pair production and QED Compton scattering (see section 5.1). The relative contribution of the two processes changes with $W_{\gamma p}$. At

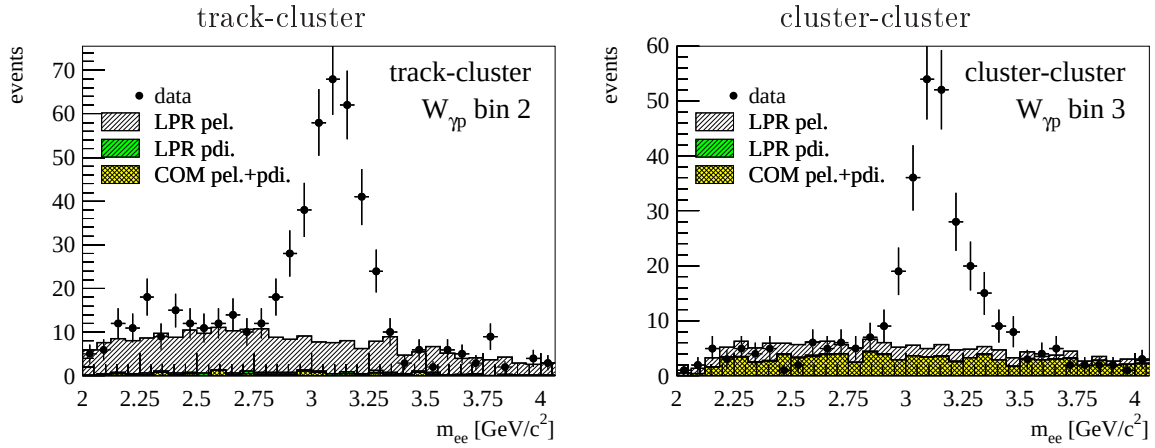

Figure 8.7: The distribution of the invariant mass $m_{e^+e^-}$ of the J/ψ decay electrons is shown for the second $W_{\gamma p}$ bin of the track-cluster and the third $W_{\gamma p}$ bin of the cluster-cluster sample. The contribution from the electron pair production and QED Compton process are shown.

small values of $W_{\gamma p}$ the main contribution comes from the electron pair production. While at large $W_{\gamma p}$ the QED Compton scattering is dominating (see figure 8.7).

In order to handle the changing background contribution in the different bins the following method is applied. For each bin the shape of the background is determined by a fit of a polynomial of second order to the MC background prediction. The MC background prediction contains events from electron pair production and QED Compton process. No forward classification (see section 7.5) is applied. The result is a polynomial function describing the background shape. For further steps all parameters of the background polynomial are fixed with exception of the normalisation (parameter P_1).

The next step of the signal extraction is a fit to the $m_{e^+e^-}$ distribution in the data. The fit function is a sum of an asymmetric peak function describing the signal and the polynomial function from the previous step for the background. The peak function is

$$f_{\text{peak}}(\zeta) = P_2 \cdot \frac{1}{\sqrt{2\pi} \cdot f_{\text{sigma}}(\zeta)} \cdot \exp\left\{ -\frac{1}{2} \cdot \left(\frac{\zeta - P_3}{f_{\text{sigma}}(\zeta)} \right)^2 \right\}$$

$$f_{\text{sigma}}(\zeta) = P_4 + P_5 \cdot (|\zeta - P_3| - (\zeta - P_3)),$$

where ζ is the argument in GeV for the invariant mass $m_{e^+e^-}$ and the parameters

P_2: normalisation of the peak function
P_3: peak position
P_4: width of the peak
P_5: asymmetry of the peak.

During the fitting procedure the normalisation P_2 and the peak position P_3 are free parameters. In order to take into account the different shape of the peaks for the track-cluster and cluster-cluster samples the parameters P_4 and P_5 are set to fixed values

determined from data. The width of the peak P_4 is fixed to the values 0.0989 and 0.1107 for the track-cluster and cluster-cluster sample respectively. The asymmetry of the peak P_5 is set to 0.1081 for the track-cluster sample. For the cluster-cluster sample the asymmetry is set to $P_5 := 0$.

The total number of events, the number of signal and background events are then calculated by integration of the corresponding fit functions from the previous step. As limits for the integration the mass window from section 7.3.5 is used. This takes the asymmetry due to the radiative tail into account. The statistical error of the number of signal and background events are determined from the errors of the fit parameters.

Figure 8.8 shows examples for the peak and background fit for one bin of the track-cluster and cluster-cluster samples for the fwd.-untagged selection. Appendix A contains the full set of figures of the fits used for the signal extraction for the different binnings, the different event samples and the different fwd. classification. The extracted number of events are listed in table 8.4 and table 8.5.

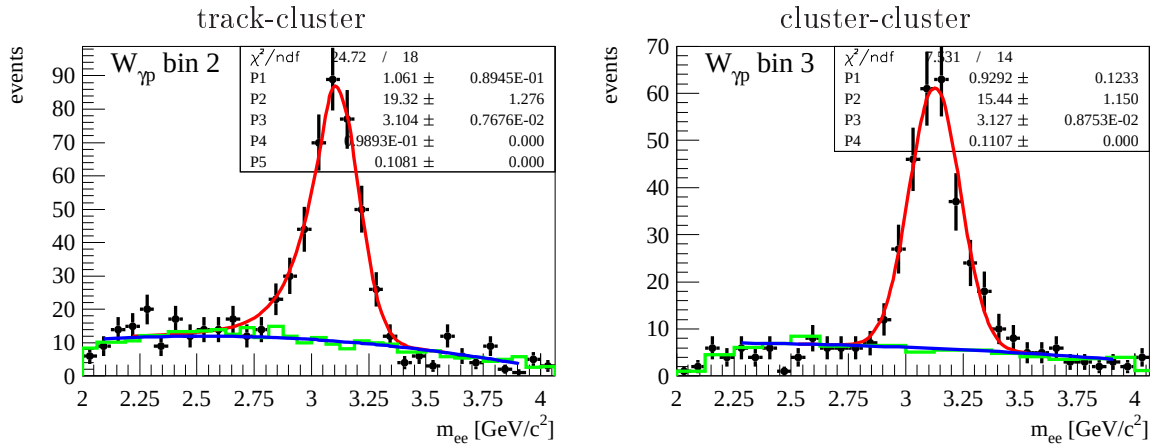

Figure 8.8: The distribution of the invariant mass $m_{e^+e^-}$ of the J/ψ decay electrons is shown for the second $W_{\gamma p}$ bin of the track-cluster and the third $W_{\gamma p}$ bin of the cluster-cluster sample (points). The peak and background fit functions are shown. The background histogram contains MC events from electron pair production and the QED Compton process. The normalisation of the background fit function is applied to the background histogram.

In order to study the systematic uncertainty due to the peak function the peak fit is repeated on the MC mass distributions. The difference between the integral and the number of events is in all bins less than 0.8%.

8.4 Efficiencies

The total efficiencies $\varepsilon_{\text{tot}}^{\text{TC}}$ and $\varepsilon_{\text{tot}}^{\text{CC}}$ of the selection of J/ψ photoproduction events for the track-cluster and the cluster-cluster samples respectively are the following combination of single efficiencies

	track-cluster					cluster-cluster			
min. $W_{\gamma p}$ [GeV]	135.0	155.0	170.0	185.0	205.0	205.0	235.0	255.0	280.0
max. $W_{\gamma p}$ [GeV]	155.0	170.0	185.0	205.0	235.0	235.0	255.0	280.0	305.0
$N^{\mathrm{tot}}_{\mathrm{notag}}$	436.0 ±23.6	478.6 ±25.3	464.2 ±26.0	412.5 ±24.2	377.2 ±24.4	259.3 ±17.6	251.9 ±17.0	301.4 ±19.7	266.4 ±19.8
$N^{\mathrm{bg}}_{\mathrm{notag}}$	117.4 ±10.1	137.5 ±11.6	123.7 ±12.0	102.9 ±11.2	101.3 ±11.9	42.7 ±6.0	30.8 ±5.2	56.5 ±7.5	90.1 ±9.5
N_{notag}	318.6 ±21.4	341.2 ±22.5	340.5 ±23.1	309.6 ±21.4	275.9 ±21.3	216.6 ±16.6	221.0 ±16.2	244.9 ±18.2	176.4 ±17.4
$N^{\mathrm{tot}}_{\mathrm{tag}}$	220.6 ±17.2	257.9 ±18.5	254.2 ±17.8	262.3 ±18.9	198.3 ±17.5	147.4 ±13.0	147.8 ±12.9	188.4 ±15.1	140.5 ±14.0
$N^{\mathrm{bg}}_{\mathrm{tag}}$	51.4 ±7.1	52.5 ±7.5	35.8 ±6.5	65.1 ±8.7	52.2 ±8.5	12.1 ±3.4	12.5 ±3.5	33.1 ±5.5	39.2 ±6.2
N_{tag}	169.2 ±15.7	205.5 ±16.9	218.4 ±16.5	197.2 ±16.8	146.1 ±15.3	135.3 ±12.5	135.3 ±12.4	155.3 ±14.1	101.3 ±12.5

Table 8.4: For the $W_{\gamma p}$ binning the total number of events ($N^{\mathrm{tot}}_{\mathrm{notag}}$, $N^{\mathrm{tot}}_{\mathrm{tag}}$), the number of signal (N_{notag}, N_{tag}) and background events ($N^{\mathrm{bg}}_{\mathrm{notag}}$, $N^{\mathrm{bg}}_{\mathrm{tag}}$) are listed. The forward classification is applied.

	track-cluster					cluster-cluster				
min. $W_{\gamma p}$ [GeV]	135.0					205.0				
max. $W_{\gamma p}$ [GeV]	235.0					305.0				
min. p_t^2 [GeV^2/c^2]	0.000	0.070	0.140	0.300	0.600	0.000	0.070	0.140	0.300	0.600
max. p_t^2 [GeV^2/c^2]	0.070	0.140	0.300	0.600	1.200	0.070	0.140	0.300	0.600	1.200
$N^{\mathrm{tot}}_{\mathrm{notag}}$	812.2 ±34.5	403.7 ±23.4	520.0 ±26.6	308.9 ±20.9	125.0 ±13.6	404.2 ±23.4	203.0 ±15.9	263.9 ±17.9	149.9 ±14.1	62.0 ±8.9
$N^{\mathrm{bg}}_{\mathrm{notag}}$	334.2 ±18.1	70.6 ±9.6	92.3 ±11.0	71.4 ±9.4	31.4 ±6.3	126.9 ±10.5	30.6 ±5.6	23.4 ±5.4	25.3 ±5.5	14.6 ±3.7
N_{notag}	478.1 ±29.4	333.1 ±21.4	427.7 ±24.2	237.5 ±18.7	93.6 ±12.0	277.4 ±20.9	172.4 ±14.9	240.5 ±17.0	124.6 ±13.0	47.4 ±8.1
$N^{\mathrm{tot}}_{\mathrm{tag}}$	170.4 ±15.8	138.1 ±13.7	201.2 ±16.9	219.8 ±17.2	222.9 ±17.3	78.7 ±9.7	68.0 ±9.1	101.6 ±11.4	128.0 ±13.3	131.1 ±13.1
$N^{\mathrm{bg}}_{\mathrm{tag}}$	61.0 ±7.9	31.1 ±6.0	54.2 ±8.1	50.9 ±7.6	36.8 ±7.0	14.9 ±3.6	11.9 ±3.3	18.6 ±4.4	27.3 ±5.5	23.9 ±5.1
N_{tag}	109.5 ±13.6	107.0 ±12.3	147.0 ±14.9	168.9 ±15.5	186.1 ±15.8	63.8 ±9.1	56.1 ±8.5	83.1 ±10.5	100.7 ±12.1	107.2 ±12.1

Table 8.5: For the p_t^2 binning the total number of events ($N^{\mathrm{tot}}_{\mathrm{notag}}$, $N^{\mathrm{tot}}_{\mathrm{tag}}$), the number of signal (N_{notag}, N_{tag}) and background events ($N^{\mathrm{bg}}_{\mathrm{notag}}$, $N^{\mathrm{bg}}_{\mathrm{tag}}$) are listed. The forward classification is applied.

efficiency	selection criterion	reference
ε_{sel}	$= \varepsilon_{\text{basic}} \cdot \varepsilon_{\text{run}} \cdot \varepsilon_{\text{angle}} \cdot \varepsilon_{\text{energy}} \cdot \varepsilon_{\text{misc}} \cdot \varepsilon_{\text{mass}}$	equation 8.8
$\varepsilon_{\text{basic}}$	basic cuts	section 7.3.1
$\varepsilon_{\text{angle}}$	angular cuts	section 7.3.2
$\varepsilon_{\text{energy}}$	energy cuts	section 7.3.3
$\varepsilon_{\text{misc}}$	miscellaneous cuts	section 7.3.4
$\varepsilon_{\text{mass}}$	mass window	section 7.3.5
ε_{BST}	BST selection (only cluster-cluster)	section 7.3.6
$\varepsilon_{\text{trig1}}$	trigger level 1	section 7.4
$\varepsilon_{\text{trig2}}$	trigger level 2	section 7.4
$\varepsilon_{\text{trig4}}$	trigger level 4	section 7.4

Table 8.6: The single efficiencies which correspond to different selection criteria are listed.

$$\varepsilon_{\text{tot}}^{\text{TC}} = \varepsilon_{\text{sel}} \cdot \varepsilon_{\text{trig1}} \cdot \varepsilon_{\text{trig2}} \cdot \varepsilon_{\text{trig4}} , \tag{8.6}$$

$$\varepsilon_{\text{tot}}^{\text{CC}} = \varepsilon_{\text{sel}} \cdot \varepsilon_{\text{BST}} \cdot \varepsilon_{\text{trig1}} \cdot \varepsilon_{\text{trig2}} \cdot \varepsilon_{\text{trig4}} , \tag{8.7}$$

$$\varepsilon_{\text{sel}} = \varepsilon_{\text{basic}} \cdot \varepsilon_{\text{angle}} \cdot \varepsilon_{\text{energy}} \cdot \varepsilon_{\text{misc}} \cdot \varepsilon_{\text{mass}} . \tag{8.8}$$

The description of the single efficiencies are given in table 8.6.

In chapter 6 and section 7.6 it is shown, that the data are well described by the MC simulation. Therefore MC is used as the standard method to obtain the efficiencies.

The selection efficiency ε_{sel} is strongly influenced by the acceptance. Therefore the values given in table 8.7 show the same behaviour as the acceptance in figure 8.3.

The BST selection is only applied for the cluster-cluster sample. The efficiency of the BST track finding is adjusted in MC to describe the efficiency for single BST tracks in data (see section 6.2.3). The efficiency ε_{BST} contains further effects of the BST selection (see section 7.3.6), which includes the geometrical acceptance of the BST and an additional second BST track.

For the level 1 subtriggers `S33` and `S40` no other level 1 subtriggers with sufficient rate exist, which consist of an independent set of level 1 trigger elements. Therefore the efficiency of the trigger level 1 cannot be obtained from data and MC simulation is the only possibility to determine the efficiency.

The efficiency of the trigger level 2 for the track-cluster sample is determined from data using independent L1ST `S61` (see section 4.1.6) which is not subjected to further rejection on trigger level 2. For the first bin in the $W_{\gamma p}$ binning the independent L1ST `S61` delivers insufficient statistics and therefore the level 2 trigger efficiency is determined from MC for this bin. For the cluster-cluster sample no independent L1ST exists (see section 7.4) and therefore the efficiency of the trigger level 2 is determined using MC.

The trigger level 4 cut is applied after all other cuts which are stronger. Therefore the efficiency $\varepsilon_{\text{trig4}}$ is always 1.

The values for the single efficiencies and the total efficiency ε_{tot} are listed in table 8.7 and table 8.8 for the $W_{\gamma p}$ binning and the p_t^2 binning respectively. For the measurement of the differential cross section $\frac{\mathrm{d}\sigma}{\mathrm{d}t}$ the total efficiency $\varepsilon_{\text{tot},|t|}$ in bins of $|t|$ is necessary. The uncorrected efficiency $\varepsilon^{\text{uncorr}}_{\text{tot},|t|}$ is determined from MC. The efficiency of the level 2 trigger in bins of $|t|$ cannot be obtained from data, since $|t|$ is experimentally not accessible. In order to use the efficiency of the level 2 trigger determined from data, the following correction is applied for the track-cluster sample

$$\varepsilon_{\text{tot},|t|} = \varepsilon^{\text{uncorr}}_{\text{tot},|t|} \cdot \frac{\varepsilon^{\text{data}}_{\text{trig2},p_t^2}}{\varepsilon^{\text{MC}}_{\text{trig2},p_t^2}},$$

where $\varepsilon^{\text{data}}_{\text{trig2},p_t^2}$ and $\varepsilon^{\text{MC}}_{\text{trig2},p_t^2}$ are the corresponding efficiencies of the level 2 trigger in bins of p_t^2 determined from data and MC.

The total efficiency ε_{tot} does not contain the forward classification. The forward classification is taken into account in the factor f_{ed}, which is derived in the next section.

	track-cluster					cluster-cluster			
min. $W_{\gamma p}$ [GeV]	135.0	155.0	170.0	185.0	205.0	205.0	235.0	255.0	280.0
max. $W_{\gamma p}$ [GeV]	155.0	170.0	185.0	205.0	235.0	235.0	255.0	280.0	305.0
$\varepsilon_{\text{basic}}$	0.515 ±0.003	0.691 ±0.004	0.779 ±0.004	0.691 ±0.004	0.513 ±0.003	0.295 ±0.003	0.444 ±0.005	0.525 ±0.004	0.518 ±0.005
$\varepsilon_{\text{angle}}$	0.917 ±0.003	0.966 ±0.002	0.856 ±0.003	0.773 ±0.004	0.695 ±0.004	0.994 ±0.001	0.994 ±0.001	0.922 ±0.003	0.778 ±0.005
$\varepsilon_{\text{energy}}$	0.609 ±0.005	0.766 ±0.004	0.822 ±0.004	0.818 ±0.004	0.786 ±0.005	0.894 ±0.004	0.912 ±0.004	0.930 ±0.003	0.974 ±0.002
$\varepsilon_{\text{misc}}$	0.933 ±0.003	0.917 ±0.003	0.920 ±0.003	0.927 ±0.003	0.924 ±0.003	0.900 ±0.004	0.908 ±0.004	0.916 ±0.004	0.914 ±0.004
$\varepsilon_{\text{mass}}$	0.959 ±0.003	0.955 ±0.002	0.956 ±0.002	0.968 ±0.002	0.971 ±0.002	0.928 ±0.004	0.940 ±0.004	0.952 ±0.003	0.957 ±0.003
ε_{sel}	0.258 ±0.003	0.447 ±0.004	0.483 ±0.004	0.392 ±0.004	0.252 ±0.003	0.219 ±0.003	0.344 ±0.004	0.393 ±0.004	0.343 ±0.004
ε_{BST}	− − −	− − −	− − −	− − −	− − −	0.739 ±0.006	0.723 ±0.007	0.669 ±0.007	0.608 ±0.008
$\varepsilon_{\text{trig1}}$	0.873 ±0.004	0.837 ±0.004	0.783 ±0.005	0.743 ±0.005	0.706 ±0.006	1.000 ±0.000	1.000 ±0.000	1.000 ±0.000	1.000 ±0.000
$\varepsilon_{\text{trig2}}$	0.975 ±0.002	0.884 ±0.029	0.933 ±0.013	0.889 ±0.013	0.837 ±0.016	0.996 ±0.001	0.993 ±0.002	0.982 ±0.002	0.971 ±0.003
$\varepsilon_{\text{trig4}}$	1.000 ±0.000	1.000 ±0.000	1.000 ±0.000	1.000 ±0.000	1.000 ±0.000	1.000 ±0.000	1.000 ±0.000	1.000 ±0.000	1.000 ±0.000
ε_{tot}	0.219 ±0.003	0.331 ±0.034	0.353 ±0.015	0.259 ±0.014	0.149 ±0.014	0.161 ±0.003	0.247 ±0.004	0.258 ±0.004	0.203 ±0.004

Table 8.7: The efficiencies of the selection criteria for the track-cluster and cluster-cluster selection are listed in the $W_{\gamma p}$ binning. The selection criteria are applied in the same ordering as in the table. $\varepsilon_{\text{trig4}} = 1$, since all the previous cuts are already strong enough.

	track-cluster					cluster-cluster				
min. $W_{\gamma p}$ [GeV]	135.0					205.0				
max. $W_{\gamma p}$ [GeV]	235.0					305.0				
min. p_t^2 [GeV^2/ c^2]	0.000	0.070	0.140	0.300	0.600	0.000	0.070	0.140	0.300	0.600
max. p_t^2[GeV^2/ c^2]	0.070	0.140	0.300	0.600	1.200	0.070	0.140	0.300	0.600	1.200
$\varepsilon_{\text{basic}}$	0.618 ±0.003	0.614 ±0.004	0.620 ±0.003	0.604 ±0.004	0.631 ±0.006	0.433 ±0.004	0.438 ±0.005	0.425 ±0.004	0.407 ±0.005	0.381 ±0.008
$\varepsilon_{\text{angle}}$	0.855 ±0.003	0.852 ±0.003	0.851 ±0.003	0.832 ±0.004	0.795 ±0.006	0.914 ±0.003	0.917 ±0.004	0.923 ±0.003	0.936 ±0.004	0.937 ±0.006
$\varepsilon_{\text{energy}}$	0.822 ±0.003	0.785 ±0.004	0.759 ±0.004	0.716 ±0.005	0.630 ±0.008	0.943 ±0.003	0.944 ±0.003	0.933 ±0.003	0.907 ±0.004	0.878 ±0.009
$\varepsilon_{\text{misc}}$	0.944 ±0.002	0.940 ±0.003	0.931 ±0.003	0.902 ±0.004	0.826 ±0.008	0.926 ±0.003	0.920 ±0.004	0.907 ±0.004	0.901 ±0.005	0.840 ±0.010
$\varepsilon_{\text{mass}}$	0.979 ±0.001	0.970 ±0.002	0.958 ±0.002	0.941 ±0.003	0.921 ±0.006	0.946 ±0.003	0.949 ±0.004	0.945 ±0.003	0.937 ±0.004	0.938 ±0.007
ε_{sel}	0.401 ±0.003	0.375 ±0.004	0.358 ±0.003	0.305 ±0.003	0.241 ±0.005	0.327 ±0.004	0.332 ±0.004	0.314 ±0.004	0.292 ±0.004	0.248 ±0.007
ε_{BST}	− − −	− − −	− − −	− − −	− − −	0.682 ±0.007	0.697 ±0.008	0.691 ±0.007	0.680 ±0.008	0.665 ±0.015
$\varepsilon_{\text{trig1}}$	0.798 ±0.004	0.795 ±0.005	0.791 ±0.004	0.767 ±0.006	0.794 ±0.010	1.000 ±0.000	1.000 ±0.000	1.000 ±0.000	1.000 ±0.000	0.999 ±0.001
$\varepsilon_{\text{trig2}}$	0.908 ±0.013	0.911 ±0.018	0.922 ±0.014	0.849 ±0.022	0.867 ±0.026	0.996 ±0.001	0.993 ±0.002	0.986 ±0.002	0.973 ±0.003	0.955 ±0.008
$\varepsilon_{\text{trig4}}$	1.000 ±0.000	1.000 ±0.000	1.000 ±0.000	1.000 ±0.000	0.999 ±0.001	1.000 ±0.000	1.000 ±0.000	1.000 ±0.000	1.000 ±0.000	0.998 ±0.002
$\varepsilon_{\text{tot},p_t^2}$	0.291 ±0.015	0.271 ±0.019	0.261 ±0.015	0.199 ±0.026	0.166 ±0.029	0.222 ±0.003	0.230 ±0.004	0.214 ±0.003	0.193 ±0.004	0.158 ±0.006
$\varepsilon_{\text{tot},\lvert t\rvert}$	0.281 ±0.014	0.267 ±0.019	0.251 ±0.015	0.198 ±0.026	0.167 ±0.030	0.226 ±0.003	0.225 ±0.004	0.210 ±0.003	0.186 ±0.004	0.149 ±0.006

Table 8.8: The efficiencies of the selection criteria for the track-cluster and cluster-cluster selection are listed in the p_t^2 binning. The selection criteria are applied in the same ordering as in the table. $\varepsilon_{\text{trig4}} = 1$, since all the previous cuts are already strong enough.

8.5 Determination of the Number of proton-elastic Events

The aim of this analysis is measurement of the proton-elastic J/ψ photoproduction. After application of all selection criteria from chapter 7 the sample contains events from proton-elastic and low mass proton-dissociative J/ψ photoproduction.

The information of the forward detectors is used to classify events as fwd.-untagged and fwd.-tagged as described in section 7.5. According to the MC the fwd.-untagged sampe is dominated by proton-elastic events. The fwd. classification gives the possibility to determine the number of events produced in the proton-elastic process. For this purpose MC events from proton-elastic and proton-dissociative J/ψ photoproduction are used. Two methods are described in the following.

The first method is the so called *MC method*. It relies on the mixture of proton-elastic and proton-dissociative events in the MC sample. In [84, 104, 105] it is shown, that the proton-elastic and proton-dissociative MC contributions can be mixed taking the same number of generated events for each sample, if the different p_t^2 cut (see section 7.3.3) for the fwd.-untagged and fwd.-tagged events is applied.

The total number of fwd.-untagged events N_{notag} is the sum of proton-elastic fwd.-untagged events $N_{\mathrm{notag}}^{\mathrm{pelas}}$ and proton-dissociative fwd.-untagged events $N_{\mathrm{notag}}^{\mathrm{pdiss}}$. With the ratio $\varepsilon_{\mathrm{pelas}\to\mathrm{notag}} := N_{\mathrm{notag}}^{\mathrm{pelas}}/N^{\mathrm{pelas}}$ of the proton-elastic fwd.-untagged events to the total number of proton-elastic events the following expression for the total number of proton-elastic events is obtained:

$$\begin{aligned} N^{\mathrm{pelas}} &= \frac{N^{\mathrm{pelas}}}{N_{\mathrm{notag}}^{\mathrm{pelas}}} \cdot N_{\mathrm{notag}}^{\mathrm{pelas}} = \frac{1}{\varepsilon_{\mathrm{pelas}\to\mathrm{notag}}} \cdot N_{\mathrm{notag}}^{\mathrm{pelas}} \\ &= \frac{1}{\varepsilon_{\mathrm{pelas}\to\mathrm{notag}}} \cdot \frac{N_{\mathrm{notag}}^{\mathrm{pelas}}}{N_{\mathrm{notag}}} \cdot N_{\mathrm{notag}} \\ &= \underbrace{\frac{1}{\varepsilon_{\mathrm{pelas}\to\mathrm{notag}}} \cdot \frac{N_{\mathrm{notag}}^{\mathrm{pelas}}}{N_{\mathrm{notag}}^{\mathrm{pelas}} + N_{\mathrm{notag}}^{\mathrm{pdiss}}}}_{=:f_{\mathrm{ed}}^{\mathrm{MC}}:=f_{\mathrm{ed}}} \cdot N_{\mathrm{notag}} \end{aligned}$$

The factor $f_{\mathrm{ed}}^{\mathrm{MC}}$ is determined from MC. Applying it to data the number of proton-elastic produced events is determined from the number of fwd.-untagged events:

$$N^{\mathrm{pelas}}\Big|_{\mathrm{data}} = f_{\mathrm{ed}}^{\mathrm{MC}} \cdot N_{\mathrm{notag}}\Big|_{\mathrm{data}} .$$

The drawback of the MC method is, that it relies on the mixture of proton-elastic and proton-dissociative produced MC being correct. The *matrix unfolding method* overcomes this drawback.

In the matrix unfolding method the following four efficiencies of the classification as fwd.-untagged and fwd.-tagged are determined from proton-elastic and proton-dissociative J/ψ photoproduction MC: $\varepsilon_{\mathrm{pelas}\to\mathrm{notag}}$, $\varepsilon_{\mathrm{pelas}\to\mathrm{tag}}$, $\varepsilon_{\mathrm{pdiss}\to\mathrm{notag}}$, $\varepsilon_{\mathrm{pdiss}\to\mathrm{tag}}$.

These efficiencies connect the number of proton-elastic N^{pelas} and proton-dissociative N^{pdiss} events with the number of fwd.-untagged N_{notag} and fwd.-tagged N_{tag} events by the following equation:

$$\begin{pmatrix} N_{\mathrm{notag}} \\ N_{\mathrm{tag}} \end{pmatrix} = \begin{pmatrix} \varepsilon_{\mathrm{pelas}\to\mathrm{notag}} & \varepsilon_{\mathrm{pdiss}\to\mathrm{notag}} \\ \varepsilon_{\mathrm{pelas}\to\mathrm{tag}} & \varepsilon_{\mathrm{pdiss}\to\mathrm{tag}} \end{pmatrix} \cdot \begin{pmatrix} N^{\mathrm{pelas}} \\ N^{\mathrm{pdiss}} \end{pmatrix} . \tag{8.9}$$

Matrix inversion leads to

$$N^{\mathrm{pelas}} = \underbrace{\frac{1}{\varepsilon_{\mathrm{pelas}\to\mathrm{notag}}} \frac{1}{1 - \frac{\varepsilon_{\mathrm{pdiss}\to\mathrm{notag}}\,\varepsilon_{\mathrm{pelas}\to\mathrm{tag}}}{\varepsilon_{\mathrm{pelas}\to\mathrm{notag}}\,\varepsilon_{\mathrm{pdiss}\to\mathrm{tag}}}} \left(1 - \frac{\varepsilon_{\mathrm{pdiss}\to\mathrm{notag}}}{\varepsilon_{\mathrm{pdiss}\to\mathrm{tag}}} \frac{N_{\mathrm{tag}}}{N_{\mathrm{notag}}}\right)}_{=: f_{\mathrm{ed}}^{\mathrm{matr}}} \cdot N_{\mathrm{notag}} \,. \tag{8.10}$$

The factor $f_{\mathrm{ed}}^{\mathrm{matr}}$ has components derived from MC — the efficiencies — and the components measured in data — the number of fwd.-untagged N_{notag} and fwd.-tagged N_{tag} events.

The drawback of the matrix unfolding method are the numerical instabilities due to the matrix inversion and the fluctuations due to the measured number of events N_{notag} and N_{tag}.

The values for $f_{\mathrm{ed}}^{\mathrm{MC}}$ and $f_{\mathrm{ed}}^{\mathrm{matr}}$ are listed in table 8.9 and table 8.10 for the $W_{\gamma p}$ binning and the p_t^2 binning respectively. The two methods agree within the statistical error of the number of events N_{notag}. The MC method is numerically more stable and therefore used for the cross section calculation ($f_{\mathrm{ed}} := f_{\mathrm{ed}}^{\mathrm{MC}}$). The matrix unfolding method is used to estimate the systematic uncertainty of the determination of the number of proton-elastic events.

8.6 Unfolding of $p_t^2 \to |t|$

For the measurement of the differential cross section $\frac{\mathrm{d}\sigma}{\mathrm{d}t}$ the number of proton-elastic events in bins of $|t|$ is necessary. Experimentally the kinematic variable $|t|$ is directly not accessible. Using the approximation $|t| \approx p_t^2$ (see equation 1.14) the number of proton-elastic events in bins of p_t^2 is determined. The approximation is not precise enough due to detector effects and there is significant migration between the bins (see section 6.3 and section 8.2.2). In order to determine the number of events in bins of $|t|$ from the number of events in bins of p_t^2 an unfolding method is used.

In figure 8.9 the *migration* or *unfolding matrices* $M_{\mathrm{MC}}(|t| \to p_t^2)$ for the track-cluster and cluster-cluster samples are shown. The 5×5 matrices correspond to the ($5\,|t|$ bins) $\times$ ($5\,p_t^2$ bins) and are filled with the generated $|t|$ and reconstructed p_t^2 values of MC

	track-cluster					cluster-cluster			
min. $W_{\gamma p}$ [GeV]	135.0	155.0	170.0	185.0	205.0	205.0	235.0	255.0	280.0
max. $W_{\gamma p}$ [GeV]	155.0	170.0	185.0	205.0	235.0	235.0	255.0	280.0	305.0
N_{notag}	318.6 ±21.4	341.2 ±22.5	340.5 ±23.1	309.6 ±21.4	275.9 ±21.3	216.6 ±16.6	221.0 ±16.2	244.9 ±18.2	176.4 ±17.4
N_{tag}	169.2 ±15.7	205.5 ±16.9	218.4 ±16.5	197.2 ±16.8	146.1 ±15.3	135.3 ±12.5	135.3 ±12.4	155.3 ±14.1	101.3 ±12.5
$\varepsilon_{\mathrm{pelas}\to\mathrm{notag}}$	0.913 ±0.004	0.898 ±0.004	0.903 ±0.004	0.899 ±0.005	0.905 ±0.005	0.906 ±0.005	0.895 ±0.006	0.902 ±0.005	0.888 ±0.007
$\varepsilon_{\mathrm{pelas}\to\mathrm{tag}}$	0.087 ±0.004	0.102 ±0.004	0.097 ±0.004	0.101 ±0.005	0.095 ±0.005	0.094 ±0.005	0.105 ±0.006	0.098 ±0.005	0.112 ±0.007
$\varepsilon_{\mathrm{pdiss}\to\mathrm{notag}}$	0.204 ±0.007	0.196 ±0.006	0.184 ±0.006	0.184 ±0.007	0.188 ±0.008	0.175 ±0.008	0.161 ±0.008	0.172 ±0.007	0.186 ±0.009
$\varepsilon_{\mathrm{pdiss}\to\mathrm{tag}}$	0.796 ±0.007	0.804 ±0.006	0.816 ±0.006	0.816 ±0.007	0.812 ±0.008	0.825 ±0.008	0.839 ±0.008	0.828 ±0.007	0.814 ±0.009
$f_{\mathrm{ed}}^{\mathrm{MC}}$	0.962 ±0.007	0.967 ±0.007	0.952 ±0.007	0.954 ±0.008	0.947 ±0.009	0.965 ±0.008	0.981 ±0.009	0.963 ±0.008	0.954 ±0.011
$f_{\mathrm{ed}}^{\mathrm{matr}}$	0.969 ±0.018	0.978 ±0.019	0.969 ±0.018	0.975 ±0.019	0.993 ±0.019	0.978 ±0.019	1.009 ±0.018	0.983 ±0.020	1.005 ±0.025
N^{pelas}	306.5 ±20.7	329.8 ±21.9	324.2 ±22.1	295.4 ±20.6	261.3 ±20.3	209.1 ±16.1	216.9 ±16.0	236.0 ±17.7	168.3 ±16.7

Table 8.9: The number of events N_{notag} and N_{tag}, the efficiencies for the matrix unfolding method and the factors $f_{\mathrm{ed}}^{\mathrm{MC}}$ and $f_{\mathrm{ed}}^{\mathrm{matr}}$ for the $W_{\gamma p}$ binning are shown. The number of events N^{pelas} is calculated with the MC method.

	track-cluster					cluster-cluster				
min. $W_{\gamma p}$ [GeV]	135.0					205.0				
max. $W_{\gamma p}$ [GeV]	235.0					305.0				
min. p_t^2 [GeV^2/ c^2]	0.000	0.070	0.140	0.300	0.600	0.000	0.070	0.140	0.300	0.600
max. p_t^2 [GeV^2/ c^2]	0.070	0.140	0.300	0.600	1.200	0.070	0.140	0.300	0.600	1.200
N_{notag}	478.1 ±29.4	333.1 ±21.4	427.7 ±24.2	237.5 ±18.7	93.6 ±12.0	277.4 ±20.9	172.4 ±14.9	240.5 ±17.0	124.6 ±13.0	47.4 ±8.1
N_{tag}	109.5 ±13.6	107.0 ±12.3	147.0 ±14.9	168.9 ±15.5	186.1 ±15.8	63.8 ±9.1	56.1 ±8.5	83.1 ±10.5	100.7 ±12.1	107.2 ±12.1
$\varepsilon_{\mathrm{pelas}\to\mathrm{notag}}$	0.929 ±0.003	0.932 ±0.004	0.915 ±0.004	0.852 ±0.006	0.786 ±0.011	0.929 ±0.004	0.925 ±0.005	0.905 ±0.005	0.854 ±0.008	0.772 ±0.017
$\varepsilon_{\mathrm{pelas}\to\mathrm{tag}}$	0.071 ±0.003	0.068 ±0.004	0.085 ±0.004	0.148 ±0.006	0.214 ±0.011	0.071 ±0.004	0.075 ±0.005	0.095 ±0.005	0.146 ±0.008	0.228 ±0.017
$\varepsilon_{\mathrm{pdiss}\to\mathrm{notag}}$	0.238 ±0.009	0.231 ±0.010	0.220 ±0.007	0.211 ±0.006	0.188 ±0.006	0.221 ±0.012	0.219 ±0.013	0.200 ±0.009	0.174 ±0.008	0.163 ±0.008
$\varepsilon_{\mathrm{pdiss}\to\mathrm{tag}}$	0.762 ±0.009	0.769 ±0.010	0.780 ±0.007	0.789 ±0.006	0.812 ±0.006	0.779 ±0.012	0.781 ±0.013	0.800 ±0.009	0.826 ±0.008	0.837 ±0.008
$f_{\mathrm{ed}}^{\mathrm{MC}}$	0.995 ±0.005	0.978 ±0.006	0.968 ±0.006	0.930 ±0.010	0.756 ±0.019	0.995 ±0.007	0.989 ±0.008	0.978 ±0.008	0.957 ±0.013	0.746 ±0.027
$f_{\mathrm{ed}}^{\mathrm{matr}}$	1.024 ±0.012	0.991 ±0.014	1.013 ±0.014	0.994 ±0.029	0.723 ±0.104	1.028 ±0.013	1.004 ±0.019	1.037 ±0.015	1.003 ±0.038	0.748 ±0.150
$N_{p_t^2}^{\mathrm{pelas}}$	475.6 ±29.3	325.6 ±21.0	413.8 ±23.5	220.9 ±17.6	70.8 ±9.2	275.9 ±20.8	170.5 ±14.8	235.3 ±16.8	119.3 ±12.6	35.3 ±6.2

Table 8.10: The number of events N_{notag} and N_{tag}, the efficiencies for the matrix unfolding method and the factors $f_{\mathrm{ed}}^{\mathrm{MC}}$ and $f_{\mathrm{ed}}^{\mathrm{matr}}$ for the p_t^2 binning are shown. The number of events $N_{p_t^2}^{\mathrm{pelas}}$ is calculated with the MC method.

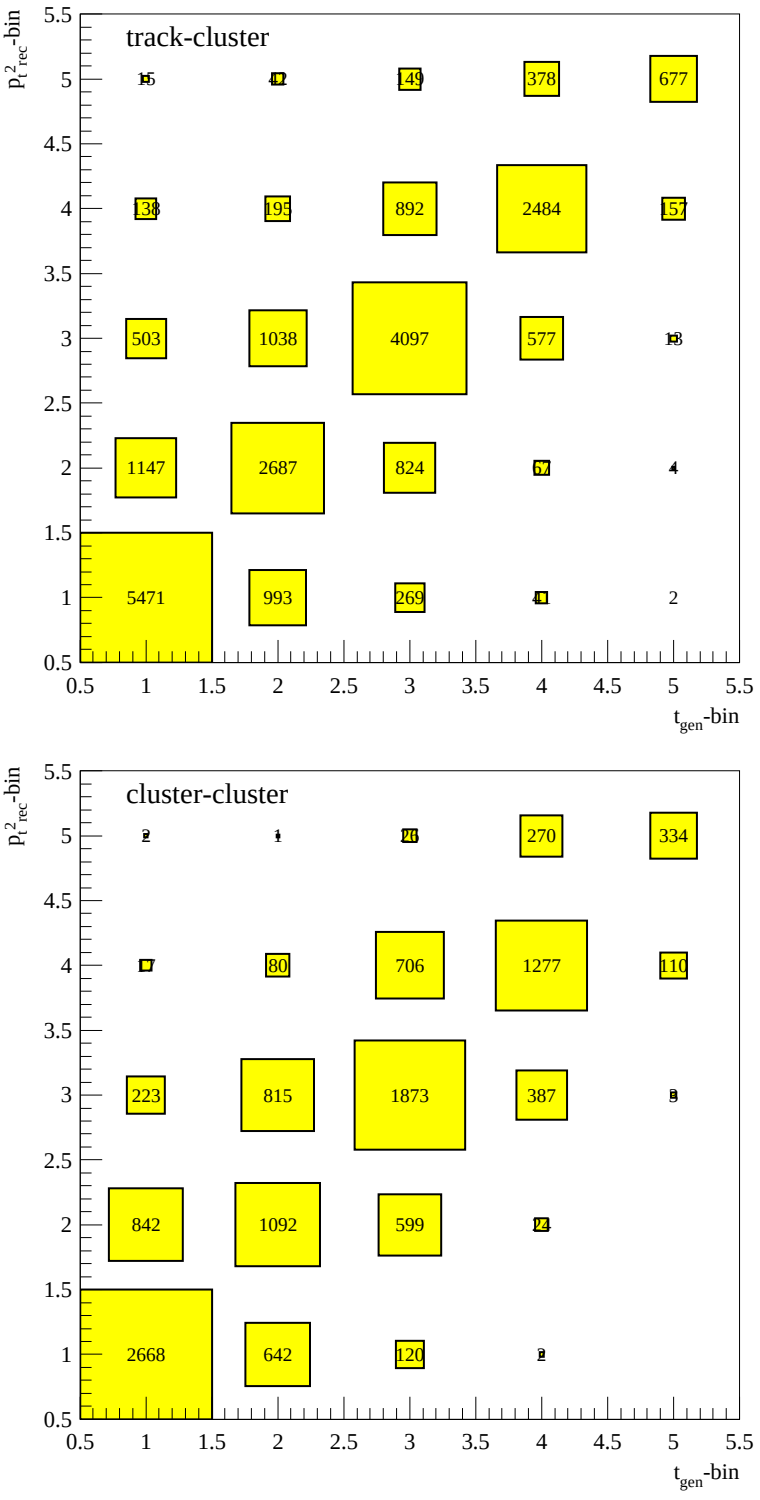

Figure 8.9: The migration or unfolding matrices for the track-cluster and cluster-cluster samples are shown. Each box of a matrix contains the number of proton-elastic J/ψ events, which are generated in the corresponding generated $|t|$ and reconstructed p_t^2 bin. For the binning refer to section 8.2.2.

events from proton-elastic J/ψ photoproduction. Each element of the matrix contains the number of events in the corresponding $(|t|, p_t^2)$ bin.

Let $\vec{N}_{p_t^2}$ be the 'vector'[5] of the measured numbers of events in data for the bins of p_t^2 and let $\vec{N}_{|t|}$ be the 'vector' of the numbers of events in bins of $|t|$. The unfolding matrix $M_{\mathrm{MC}}(|t| \to p_t^2)$ connects these two 'vectors' in the following way

$$\vec{N}_{p_t^2} = \frac{1}{\mathcal{N}} M_{\mathrm{MC}}(|t| \to p_t^2) \cdot \vec{N}_{|t|} \,.$$

Since the unfolding matrix is filled with numbers of events the normalisation $\mathcal{N}$ is needed. In a simplified view the unfolding of the number of events in bins of p_t^2 to the number of events in bins of $|t|$ can be treated as the application of the inverted unfolding matrix $M_{\mathrm{MC}}^{-1}(|t| \to p_t^2)$ to the previous equation:

$$\vec{N}_{|t|} = \mathcal{N} \cdot M_{\mathrm{MC}}^{-1}(|t| \to p_t^2) \cdot \vec{N}_{p_t^2} \,.$$

The matrix inversion picture is only a simple picture for the unfolding. The matrix inversion is numerically instable or impossible in the case of singularities. Therefore the matrix inversion is not used in this analysis.

As a numerically stable method the *Bayes unfolding* [115, 116] is used. This method relies on the Bayes' theorem. The 'vector' $\vec{N}_{|t|}$ is calculated in an iterative procedure. In addition the Bayes' unfolding determines the statistical error of $\vec{N}_{|t|}$ from the statistical errors of the 'vector' $\vec{N}_{p_t^2}$ and the unfolding matrix $M_{\mathrm{MC}}(|t| \to p_t^2)$. Correlations of the errors are taken into account.

In table 8.11 the values of the number of events in the p_t^2 and $|t|$ binning are listed. These values are shown in figure 8.10. It is expected, that the migration between bins results in a shift of events from lower to higher bins due to the exponential behaviour of the distribution. The unfolding method reverses this shift. This is clearly visible in figure 8.10.

	track-cluster					cluster-cluster				
min. $W_{\gamma p}$ [GeV]	135.0					205.0				
max. $W_{\gamma p}$ [GeV]	235.0					305.0				
min. p_t^2 [GeV^2/c^2]	0.000	0.070	0.140	0.300	0.600	0.000	0.070	0.140	0.300	0.600
max. p_t^2 [GeV^2/c^2]	0.070	0.140	0.300	0.600	1.200	0.070	0.140	0.300	0.600	1.200
$N_{p_t^2}^{\mathrm{pelas}}$	475.6	325.6	413.8	220.9	70.8	275.9	170.5	235.3	119.3	35.3
	±29.3	±21.0	±23.5	±17.6	±9.2	±20.8	±14.8	±16.8	±12.6	±6.2
$N_{\|t\|}^{\mathrm{pelas}}$	499.3	378.0	388.0	189.9	51.6	287.7	220.3	202.4	97.4	28.6
	±26.0	±15.8	±17.4	±11.6	±5.4	±18.5	±10.8	±11.1	±7.5	±3.9

Table 8.11: The number of events before (in bins of p_t^2) and after (in bins of $|t|$) unfolding are shown for the track-cluster and cluster-cluster sample.

[5] The 'vectors' of numbers of events are no physics vectors with their transformation features.

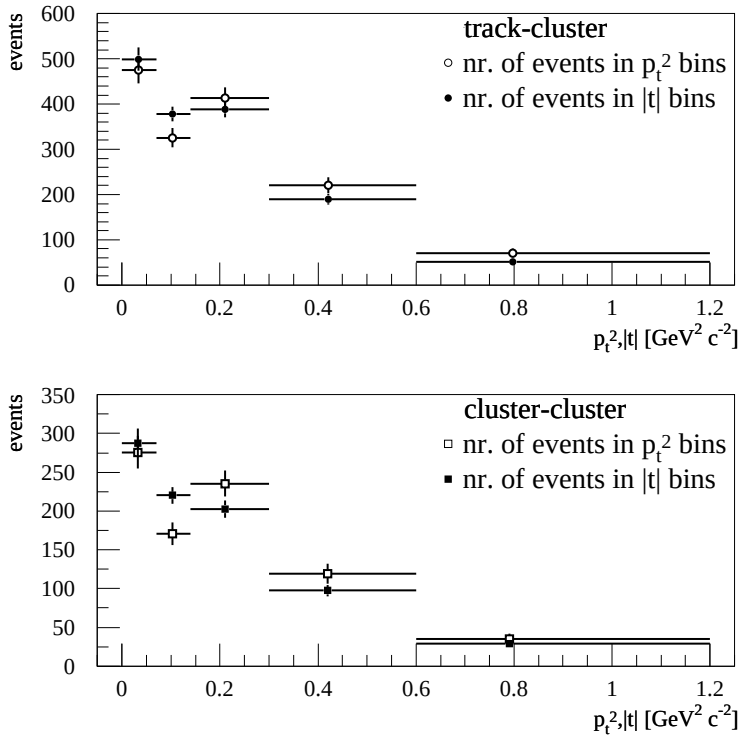

Figure 8.10: The number of events before (in bins of p_t^2) and after (in bins of $|t|$) unfolding are shown for the track-cluster and cluster-cluster sample.

8.7 Systematic Errors

In this section the determination of the systematic uncertainties of the measurement of the cross section $\sigma(W_{\gamma p})$ and the differential cross section $\frac{\mathrm{d}\sigma}{\mathrm{d}t}$ is described. The total systematic error is derived by the quadratic summation of the systematic uncertainties of the individual sources. An overview over the sources, the resulting systematic uncertainties and the total systematic error is given in table 8.12.

The first three systematic uncertainties arise from values which are directly used to calculate the cross section (see equation 8.1). The systematic uncertainty for the cross section arises from the uncertainty of the values. The **branching ratio** for the decay $J/\psi \to e^+e^-$ is $\mathcal{B} = (5.93 \pm 0.10)\%$ [110], which results in a relative systematic uncertainty of 1.7%. The correction factor for the **contamination from $\psi(2S)$ decays** is $f^{\mathrm{TC}}_{\psi(2S)} = 0.012 \pm 0.005$ and $f^{\mathrm{CC}}_{\psi(2S)} = 0.005 \pm 0.005$ for the track-cluster and cluster-cluster sample respectively [99], which gives an uncertainty of 0.5%. The calculation of the luminosity is described in section 8.1 and the values for the uncertainty for the different running periods are listed in table 8.1. For the total uncertainty of the **luminosity measurement** $\delta\mathcal{L}_{\mathrm{tot}} = 1.5\%$ is taken.

The following systematic uncertainties are the consequence of systematic uncertainties of measured angles and energies of the J/ψ decay electron candidates. The effect on the cross section measurement is studied by variation of the MC reconstruction. The different variations are presented in the following.

The systematic uncertainty of the **energy scale for SpaCal clusters** has a linear behaviour from 2.7% at 3 GeV to 0.3% at 27.5 GeV [117]. The variation of the energy

source	$\delta\sigma(W_{\gamma p})_{\rm syst}/\sigma(W_{\gamma p})$ [%]		$\delta\frac{{\rm d}\sigma}{{\rm d}t}_{\rm syst}/\frac{{\rm d}\sigma}{{\rm d}t}$ [%]	
	track-cluster	cluster-cluster	track-cluster	cluster-cluster
branching ratio $\mathcal{B}$	1.7	1.7	1.7	1.7
$\psi(2S)$ background	0.5	0.5	0.5	0.5
luminosity	1.5	1.5	1.5	1.5
cluster energy	0.4 $\rightarrow$ 6.8	5.1, 2.6 $\rightarrow$4.5	2.0 $\rightarrow$ 12.	4.0 $\rightarrow$ 9.5
cluster θ up	—	2.8 $\rightarrow$ 1.3	—	1.2
track energy	0.5	—	0.5	—
track reconstruction	2.0	—	2.0	—
$z_{\rm vtx}$ reweighting	2.6 $\rightarrow$ 0.5	8.5, $\approx$2.0	1.5	2.0
BST coherent loss	—	3.0	—	3.0
BST track finding	—	1.5	—	1.5
trigger level 1	5.0	1.0	5.0	1.0
trigger level 2	4.0	5.0	4.0	5.0
peak fit function	0.8	0.8	0.8	0.8
background subtraction	3.3 $\rightarrow$ 6.6	3.1 $\rightarrow$ 6.1	8.5 $\rightarrow$ 3.7	6.8 $\rightarrow$ 5.2
pelas. correction	4.2 $\rightarrow$ 6.0	5.6	5.7 $\rightarrow$ 6.8	5.3 $\rightarrow$ 7.1
total syst. error	9.7 $\rightarrow$ 13.3	13.5, 10.1 $\rightarrow$11.9	12.7, 10.7 $\rightarrow$ 16.0	11.8 $\rightarrow$ 14.7

Table 8.12: The sources for systematic uncertainties and their effect on the measurement of the cross section $\sigma(W_{\gamma p})$ and the differential cross section $\frac{{\rm d}\sigma}{{\rm d}t}$ are listed. For bin dependent uncertainties explicit values are given for some bins, otherwise the trend ("$\rightarrow$") for the corresponding binning is shown. The single uncertainties are added in quadature to obtain the total relative systematic error.

of SpaCal clusters according to this uncertainty leads to the values listed in table 8.12.

The determination of the **polar angle θ of SpaCal clusters** has a systematic uncertainty of 0.3 mrad $\approx 0.02°$ [117]. The variation of the cluster polar angle θ towards higher values leads to the uncertainties in table 8.12 for the cluster-cluster sample. The main effect arises from the variation of the cluster with large polar angle θ. The variation of the polar angle of the cluster in the track-cluster sample has a negligible effect on the cross section calculation.

The systematic uncertainty of the energy scale in the LAr calorimeter is 0.7% for the polar angle range of the track-cluster sample [118]. The corresponding variation of the **track energy** leads to change in the cross section measurement of 0.5%.

The uncertainty on the measurement of the **polar angle θ of the central track** is 3 mrad, 2 mrad and 1 mrad $\approx 0.06°$ for the following regions $\theta < 120°$, $120° < \theta < 135°$ and $135° < \theta$ [118]. Variations by these values result in a change of the cross section measurement of less than 0.2% and are therefore neglected.

The uncertainty on the **track reconstruction efficiency** is 2% [68]. The distribution of the **position of the vertex** z_{vtx} has to be adjusted in MC in order to describe the distribution in data (see section 6.4.4). The effect on the cross section calculation is determined using adjusted and non-adjusted MC. The systematic uncertainty is listed in table 8.12.

The effect of the **coherent loss in the BST** has several causes and is described in section 6.2.3.5. A systematic uncertainty of 3% is applied for the cross section for the cluster-cluster sample [96].

The systematic effects of the **BST track finding** is studied by variation of the cut value of the track probability (see section 6.2.1) for the cluster-cluster sample. The standard cut value is 1%. For the variation the values 0.2% and 5% are used. The systematic uncertainty on the cross section amounts to 1.5%.

The systematic uncertainty of the **trigger level 1** has been analysed in [68] for the level 1 subtrigger `S40` and a level 1 subtrigger, which is similar to the `S33`. The systematic uncertainties are 1% and 5% respectively.

The efficiency of the **level 2 neural network trigger** for the track-cluster sample can be obtained from data or MC simulation (see section 6.1 and section 8.4). The efficiency for the cross section calculation is determined from data, while the efficiency determined from MC is used to estimate the systematic uncertainty to 4%. For the cluster-cluster sample the efficiency of the L2NN is determined from MC, because it cannot be determined from data since no independent L1ST exist (see section 7.4). Although L1ST validated by other L2 conditions are not suited for the determination of the efficiency of the L2NN, these L1ST are used to estimate the efficiency of the L2NN from data. A systematic uncertainty for the cluster-cluster sample of $\approx 5\%$ is obtained.

For the signal extraction (see section 8.3) there are two sources of systematic uncertainties considered. The shape of the **peak fit function** leads to an uncertainty of less than 0.8%. This is studied by comparing the integral over the peak fit function and the number of events in MC distributions. The second effect arises from the **background**

subtraction. The error of the fit parameter for the background normalisation is taken into account in the determination of the signal events. In table 8.12 the corresponding systematic uncertainties are shown.

The **proton-elastic correction** is the determination of the number of proton-elastic events from the number of events classified as fwd.-untagged and fwd.-tagged. In section 8.5 two methods are described: the MC method and the matrix unfolding method. For the cross section calculation the MC method is used. The matrix unfolding method is used to estimate the systematic uncertainty of the method determining the number of proton-elastic events. The uncertainty of the method ranges from $\approx 1.5\%$ to $\approx 5.9\%$. An additional source of uncertainty is the difference of the description of the forward detectors in MC to the data (see section 6.4.3) which amounts to $\approx 4\%$. The two contributions are added in quadrature and the results are listed in table 8.12.

No additional systematic uncertainty due to the **unfolding** $p_t^2 \to |t|$ is applied since the Bayes' unfolding takes into account the statistical errors of the unfolding matrix.

Chapter 9

Results

The elastic J/ψ photoproduction cross section $\sigma(W_{\gamma p})$ (see section 9.1) and the differential cross section $\frac{\mathrm{d}\sigma}{\mathrm{d}t}$ (see section 9.2) are presented in the range of large $W_{\gamma p}$: $135\,\mathrm{GeV} < W_{\gamma p} < 305\,\mathrm{GeV}$.

The results are compared with previous measurements. The extension in phase space and the improvement in precision are described.

The effective pomeron trajectory (see section 9.2.2) is studied by combining the results at large $W_{\gamma p}$ of this analysis with the results at $40\,\mathrm{GeV} < W_{\gamma p} < 160\,\mathrm{GeV}$ of the analysis in [99].

The results are discussed in section 9.3.

9.1 Cross Section $\sigma(W_{\gamma p})$

The elastic J/ψ photoproduction cross section $\sigma(W_{\gamma p})$ is measured as a function of the photon-proton centre of mass energy $W_{\gamma p}$. The cross section is determined in five and four bins of $W_{\gamma p}$ for the track-cluster and cluster-cluster sample respectively. The results and the inputs for the cross section extraction (see equation 8.1) are listed in table 9.1. Figure 9.1 shows the cross section $\sigma(W_{\gamma p})$ as a function of $W_{\gamma p}$. The inner error bars correspond to the statistical errors and the outer error bars correspond to the total errors, which are the statistical and systematic errors added in quadrature.

In figure 9.2 the results of this analysis are compared with previously published results of H1 [14] [1], ZEUS [119] and the fixed target experiments E516 [120] and E401 [121]. The results of the recent track-track analysis [99] [2] using H1 data are also shown. For the high $W_{\gamma p}$ range the results of this analysis, the published H1 results for the track-cluster and cluster-cluster topology and the published ZEUS results for the decay $J/\psi \to e^+e^-$ are shown in figure 9.3.

[1] The published results of H1 [14] for the decay $J/\psi \to e^+e^-$ were calculated with a wrong branching ratio. The results are corrected accordingly and labeled "H1 $J/\psi \to e^+e^-$ (BR corr.)".

[2] The results of the recent track-track analysis [99] using H1 data are labeled as "$J/\psi \to \mu^+\mu^-$ track-track (PF)".

	track-cluster					cluster-cluster			
min. $W_{\gamma p}$ [GeV]	135.0	155.0	170.0	185.0	205.0	205.0	235.0	255.0	280.0
max. $W_{\gamma p}$ [GeV]	155.0	170.0	185.0	205.0	235.0	235.0	255.0	280.0	305.0
$\langle W_{\gamma p} \rangle$ [GeV]	144.9	162.5	177.3	194.8	219.6	219.6	244.8	267.2	292.3
N_{notag}	318.6 ±21.4	341.2 ±22.5	340.5 ±23.1	309.6 ±21.4	275.9 ±21.3	216.6 ±16.6	221.0 ±16.2	244.9 ±18.2	176.4 ±17.4
f_{ed}	0.962 ±0.007	0.967 ±0.007	0.952 ±0.007	0.954 ±0.008	0.947 ±0.009	0.965 ±0.008	0.981 ±0.009	0.963 ±0.008	0.954 ±0.011
$f_{\psi(2S)}$ [%]	1.2					0.5			
$\mathcal{F}_\gamma/10^{-2}$	0.885	0.545	0.464	0.517	0.607	0.607	0.320	0.329	0.267
$\mathcal{B}$ [%]	5.93					5.93			
$\mathcal{L}$ [pb^{-1}]	30.26					26.90			
ε_{tot}	0.219 ±0.003	0.331 ±0.034	0.353 ±0.015	0.259 ±0.014	0.149 ±0.014	0.161 ±0.003	0.247 ±0.004	0.258 ±0.004	0.203 ±0.004
$\sigma(W_{\gamma p})$ [nb]	87.0	100.7	109.0	121.5	159.4	133.4	171.5	173.3	193.7
$\delta\sigma(W_{\gamma p})_{\text{stat}}$ [nb]	5.8	6.6	7.4	8.4	12.3	10.2	12.6	12.9	19.1
$\delta\sigma(W_{\gamma p})_{\text{syst}}$ [nb]	8.4	9.8	10.8	13.0	21.2	18.0	17.3	18.2	23.0
$\delta\sigma(W_{\gamma p})_{\text{tot}}$ [nb]	10.3	11.8	13.1	15.5	24.5	20.7	21.4	22.3	29.9

Table 9.1: The values of the elastic J/ψ photoproduction cross section $\sigma(W_{\gamma p})$, the statistical error $\delta\sigma(W_{\gamma p})_{\text{stat}}$, the systematic error $\delta\sigma(W_{\gamma p})_{\text{syst}}$ and the total error $\delta\sigma(W_{\gamma p})_{\text{tot}}$ are listed. Equation 8.1 is used to calculate the cross section in bins of $W_{\gamma p}$ for the track-cluster and cluster-cluster sample. The input quantities for equation 8.1 are given in the table. For a description refer to chapter 8.

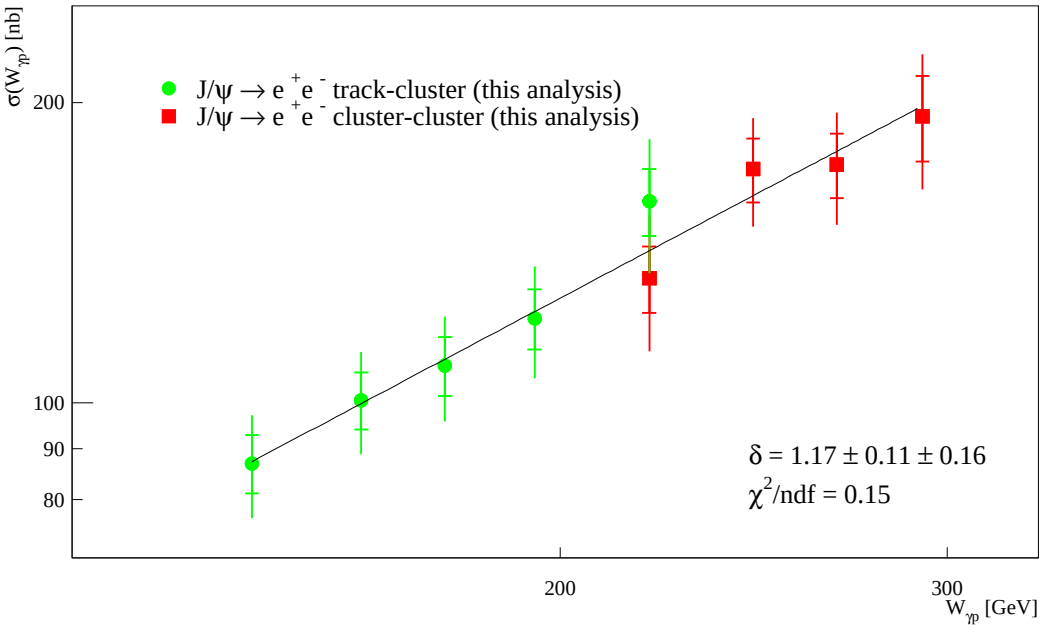

Figure 9.1: The elastic J/ψ photoproduction cross section $\sigma(W_{\gamma p})$ as a function of $W_{\gamma p}$ is shown for the track-cluster and cluster-cluster samples. The inner error bars correspond to the statistical error and the outer error bars to the total error. A fit of the form $\sigma(W_{\gamma p}) \propto {W_{\gamma p}}^{\delta}$ is applied. The fit is described in section 9.1.1.

The data used for the published H1 results were taken with an energy of the proton beam of 820 GeV, while the data for this analysis were taken with an energy of the proton beam of 920 GeV. This results in a higher centre of mass energy (see equation 1.1) and thus in higher accessible photon-proton centre-of-mass energy $W_{\gamma p}$ (see section 1.4). The kinematic limit for $W_{\gamma p}$ changes from ≈ 300 GeV to ≈ 318 GeV.

The published results for the track-cluster and cluster-cluster topology have a reach in $W_{\gamma p}$ of 210 GeV and of 285 GeV respectively. This results in "the highest position" of the measurement at $\langle W_{\gamma p} \rangle = 197.1$ GeV and $\langle W_{\gamma p} \rangle = 272.4$ GeV respectively. This analysis extends the $W_{\gamma p}$ ranges for the track-cluster and cluster-cluster topology to 235 GeV and 305 GeV respectively, which results in extracted values up to $\langle W_{\gamma p} \rangle = 219.6$ GeV and $\langle W_{\gamma p} \rangle = 292.3$ GeV. The extension of the kinematic range for the track-cluster topology allows a common bin with the cluster-cluster sample. The extension of the kinematic range for the cluster-cluster topology provides a measurement in a new kinematic region.

The data analysed in the H1 publication [14] correspond to an integrated luminosity of 20.5 pb^{-1} and 10.0 pb^{-1} for the track-cluster and cluster-cluster topologies respectively. This analysis uses data corresponding to an integrated luminosity of 30.26 pb^{-1} and 26.90 pb^{-1} for the track-cluster and cluster-cluster samples respectively. The statistics in the track-cluster sample is increased with respect to the previous measurement even more than the increase of the integrated luminosity by the usage of an efficient neural-network on trigger level 2. For the cluster-cluster sample the BST consists additional 4 planes with respect to the previous analysis and thus provides higher efficiency and angular acceptance.

The data used for the published ZEUS results are taken in the running periods 1999 and 2000 with an energy of the proton beam of 920 GeV. The results reach up to 290 GeV in the photon-proton centre-of-mass energy $W_{\gamma p}$, which results in measurements up to $\langle W_{\gamma p} \rangle \approx 275$ GeV.

The larger range in $W_{\gamma p}$ of this analysis compared to the published ZEUS data is due to the special detectors — BST and SpaCal — which allow a precise measurement of the polar angle θ and the energy of the J/ψ decay electron candidates in the very backward region of the H1 detector.

The increased statistics allows to increase the number of bins with respect to the published H1 result from 3 to 5 and 4 for the track-cluster and cluster-cluster sample respectively. The statistical errors per bin are reduced to $\approx 80\%$ and $\approx 65\%$ of the errors of the published H1 results for the track-cluster and cluster-cluster sample. The systematic errors are reduced to $\approx 60\%$ of errors of previous measurement per bin for both samples.

9.1.1 $W_{\gamma p}$ Dependence of $\sigma(W_{\gamma p})$

In figure 9.1 a fit of the form $\sigma(W_{\gamma p}) \propto {W_{\gamma p}}^{\delta}$ is applied to the data. The fit function is motivated by Regge theory (see equation 1.48). Using the parameters from the Donnachie-Landshoff fit (see equation 1.50) δ is predicted to be $\delta = 4 \cdot \varepsilon \approx 0.32$.

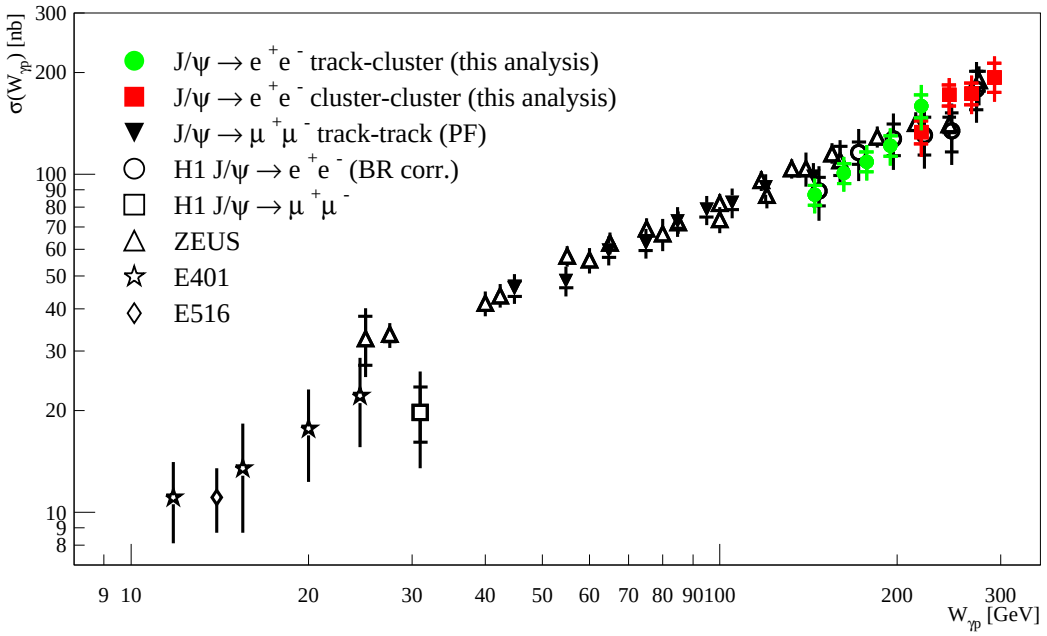

Figure 9.2: The elastic J/ψ photoproduction cross section $\sigma(W_{\gamma p})$ as a function of $W_{\gamma p}$ is shown. The inner error bars show the statistical errors, while the outer error bars show the total errors. The results of this analysis for the track-cluster and cluster-cluster samples are compared to published results from H1 [14] for the track-cluster and cluster-cluster topology. The results of the recent "$J/\psi \to \mu^+\mu^-$ track-track (PF)" analysis [99] are shown instead of the published H1 track-track results [14]. The published results of ZEUS [119] and the fixed target experiments E516 [120] and E401 [121] are shown. A zoomed view of the high $W_{\gamma p}$ region is shown in figure 9.3.

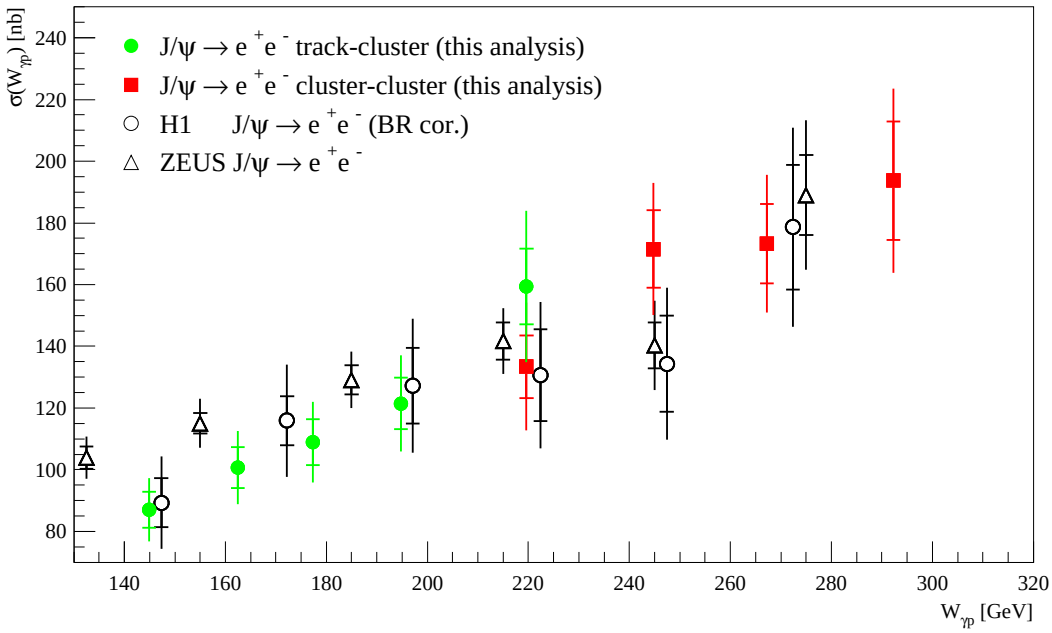

Figure 9.3: The elastic J/ψ photoproduction cross section $\sigma(W_{\gamma p})$ as a function of $W_{\gamma p}$ is shown. The inner error bars show the statistical errors, while the outer error bars show the total errors. The results of this analysis for the track-cluster and cluster-cluster samples are compared to the published results from H1 [14] for the corresponding topologies. The lower and higher three points of the published H1 result are of track-cluster and cluster-cluster topology respectively. Compared to the published data the number of bins and the phase space are extended, while the errors are reduced. A common bin of the track-cluster and cluster-cluster samples exists in this analysis. The published results of ZEUS [119] for the decay $J/\psi \to e^+e^-$ in the high $W_{\gamma p}$ region are also shown.

The fit in figure 9.1 to the data from the track-cluster (TC) and cluster-cluster (CC) samples yields

$$\delta_{\mathrm{TC,CC}}(135\,\mathrm{GeV} < W_{\gamma p} < 305\,\mathrm{GeV}) = 1.17 \pm 0.11 \pm 0.16\,, \tag{9.1}$$

where the first error is the statistical and the second error is the systematic error. The statistical error is the fit error, if the fit is applied to the data with the statistical error of the data only. Applying the fit to the data with the total error of the data yields the total error of δ. The systematic error is obtained by quadratic subtraction.

In order to extend the range in $W_{\gamma p}$ the results of this analysis are combined with published H1 results at low $W_{\gamma p}$ [14] and recent track-track results for the intermediate $W_{\gamma p}$ range [99]. Both analyses use the decay $J/\psi \to \mu^+\mu^-$. For the intermediate $W_{\gamma p}$ range both decay muons are detected by tracks in the central region — track-track (TT) analysis. For the low $W_{\gamma p}$ measurement information of the forward muon detector is used.

The fit $\sigma(W_{\gamma p}) \propto {W_{\gamma p}}^{\delta}$ to the combined data yields

$$\delta := \delta_{\mathrm{TT,TC,CC}}(26\,\mathrm{GeV} < W_{\gamma p} < 305\,\mathrm{GeV}) = 0.76 \pm 0.03 \pm 0.04\,. \tag{9.2}$$

The values of $\delta_{\mathrm{TC,CC}}$ and $\delta_{\mathrm{TT,TC,CC}}$ are in good agreement with the published values of H1 [14] and ZEUS [119] and the recent track-track (TT) analysis using H1 data [99]:

$$\begin{aligned}
\delta_{\mathrm{H1}}(26\,\mathrm{GeV} < W_{\gamma p} < 285\,\mathrm{GeV}) &= 0.84 \pm 0.07\,, & (9.3)\\
\delta_{\mathrm{ZEUS}}(30\,\mathrm{GeV} < W_{\gamma p} < 290\,\mathrm{GeV}) &= 0.69 \pm 0.02 \pm 0.03\,, & (9.4)\\
\delta_{\mathrm{TT}}(40\,\mathrm{GeV} < W_{\gamma p} < 160\,\mathrm{GeV}) &= 0.71 \pm 0.04 \pm 0.07\,, & (9.5)
\end{aligned}$$

where the first errors are the statistical and the second are the systematic errors. For δ_{H1} the total error is given.

The strongly rising cross section $\sigma(W_{\gamma p}) \propto {W_{\gamma p}}^{\delta}$ leads to large values of $\delta \approx 0.7$ which are incompatible with the value of $\delta \approx 0.3$ predicted for single pomeron exchange.

9.1.2 Two Pomeron Fit

In order to describe the steep rise of the cross section Donnachie and Landshoff introduced the hard pomeron (see section 1.6.3). The intercept $\alpha^0_{\mathrm{I\!P}}$ and slope $\alpha'_{\mathrm{I\!P}}$ of the trajectory of the hard pomeron are determined using HERA data [19].

In figure 9.5 the two pomeron fit is applied to the track-cluster and cluster-cluster results of this analysis, the low $W_{\gamma p}$ result of [14] and the track-track results of [99]. In the fit the amplitudes of the two pomeron trajectories are free parameters. The relative contributions of the hard and soft pomeron and the interference term are listed in table 9.2. The relative contribution of the hard pomeron rises with rising $W_{\gamma p}$, while the relative contribution of the soft pomeron decreases with rising $W_{\gamma p}$. The

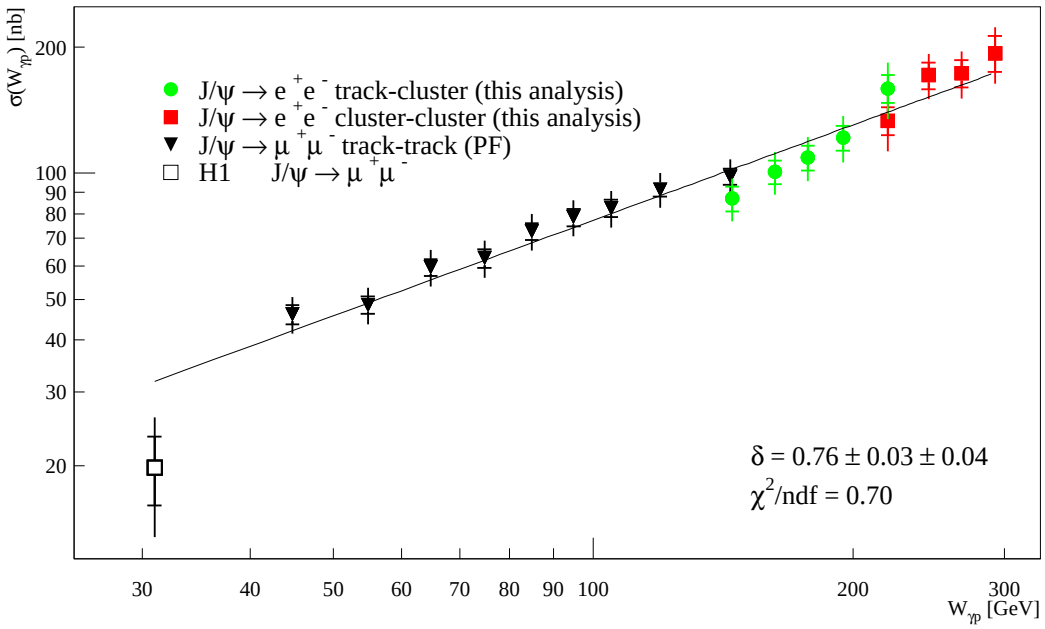

Figure 9.4: The elastic J/ψ photoproduction cross section $\sigma(W_{\gamma p})$ as a function of $W_{\gamma p}$ is shown. The inner error bars correspond to the statistical error and the outer error bars to the total error. In addition to the results for the track-cluster and cluster-cluster samples the results from the low $W_{\gamma p}$ analysis [14] and the track-track analysis [99] are shown. A fit of the form $\sigma(W_{\gamma p}) \propto {W_{\gamma p}}^{\delta}$ is applied to the data of the full $W_{\gamma p}$ range.

fit describes the HERA data well, while it overshoots the results of the fixed target experiments E516 [120] and E401 [121] at low $W_{\gamma p}$.

Including the results of the fixed target experiments into the fit, the two pomeron fit does not describe the data (see figure 9.5). At high $W_{\gamma p}$ the fit is fixed by the track-cluster and cluster-cluster results of this analysis, while at low $W_{\gamma p}$ it is pulled to lower cross section values by the results of the fixed target experiments. Thus the fit undershoots the results of the track-track analysis in the intermediate $W_{\gamma p}$ region.

The two pomeron fit to this combined data set is not able to describe the data. This is a new result compared to [14], where the two pomeron fit described very well the fixed target results and the previous HERA results (see figure 1.9).

$W_{\gamma p}$	hard : soft : inter
30 GeV	0.05 : 0.64 : 0.31
150 GeV	0.23 : 0.31 : 0.46
200 GeV	0.28 : 0.26 : 0.46
250 GeV	0.33 : 0.22 : 0.45
290 GeV	0.36 : 0.20 : 0.45

Table 9.2: The relative contributions of the hard and soft pomeron and the interference term in the two pomeron fit (see figure 9.5) for different values of $W_{\gamma p}$. The relative errors of the contributions are of the order of $5-7\%$. For comparison the published values of H1 [14] are: 0.1 : 0.5 : 0.4 at $W_{\gamma p} = 30\,\text{GeV}$ and 0.5 : 0.1 : 0.4 at $W_{\gamma p} = 250\,\text{GeV}$.

9.1.3 Shape Analysis of $\sigma(W_{\gamma p})$

A characteristic feature of the two pomeron model is the "concave" shape of the cross section $\sigma(W_{\gamma p})$ in the double logarithmic presentation. The QCD predictions have different shape depending on the gluon densities.

In order to study the curvature a polynomial of second order in the double logarithmic presentation is chosen as the basis for the following fit function

$$\ln(\sigma(W_{\gamma p})/\sigma(W_{\gamma p,0})) = \texttt{P1} + \texttt{P2} \cdot \ln(W_{\gamma p}/W_{\gamma p,0}) + \texttt{P3} \cdot (\ln(W_{\gamma p}/W_{\gamma p,0}))^2 \quad (9.6)$$

$$\Rightarrow \sigma(W_{\gamma p}) \propto {W_{\gamma p}}^{\texttt{P2}+\texttt{P3}\cdot\ln(W_{\gamma p}/W_{\gamma p,0})}, \quad (9.7)$$

where P1, P2 and P3 are the free parameters of the fit. The parameter P3 corresponds to the curvature of the fit function in the double logarithmic presentation.

In figure 9.6 and 9.7 the fit function of equation 9.7 is applied to the following data sets of $\sigma(W_{\gamma p})$:

a) "new H1 data", i.e. the results of this analysis for the track-cluster and cluster-cluster sample and the track-track results of [99];

b) "HERA data", i.e. a) and the published H1 low $W_{\gamma p}$ result [14] and the published results from ZEUS [119];

c) "all data", i.e. b) and the results from the fixed target experiments E516 [120] and E401 [121].

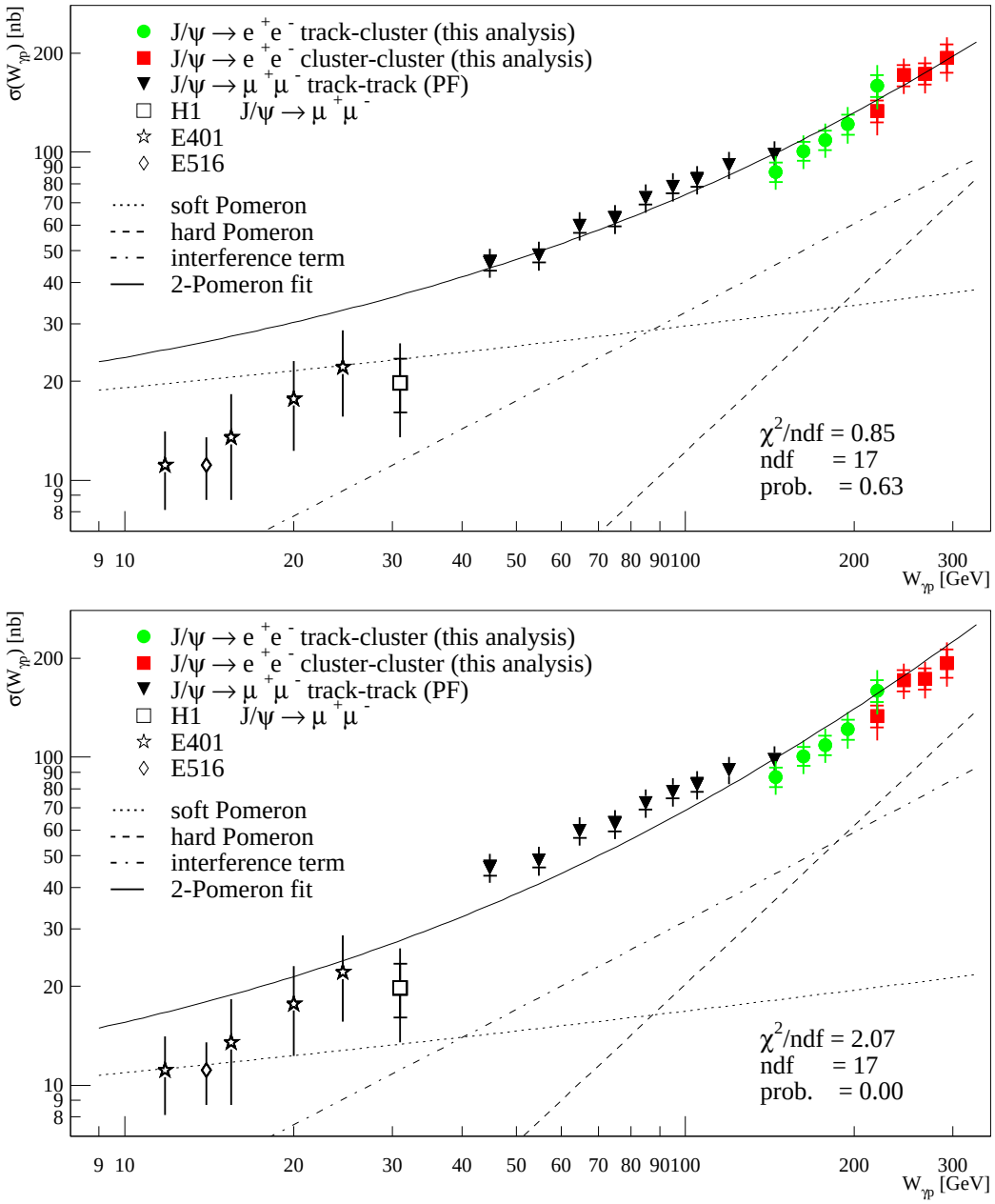

Figure 9.5: The elastic J/ψ photoproduction cross section $\sigma(W_{\gamma p})$ is shown as a function of $W_{\gamma p}$. The inner error bars correspond to the statistical error and the outer error bars to the total error. In the upper figure the two pomeron fit [19] is applied to the track-cluster and cluster-cluster results of this analyis, the low $W_{\gamma p}$ result of [14], the track-track results of [99]. For the fit only the statistical errors are taken into account. The solid line shows the result of the fit, while the dotted and dashed lines correspond to the contribution of the soft and hard pomeron respectively. The dashed-dotted line shows the interference term of the two trajectories. The relative contributions are listed in table 9.2. In the lower plot the results from the fixed target experiments E516 [120] and E401 [121] are included in the fit.

The fits to the different data sets yield the curvature parameters

$$\text{a) P3} = 0.12 \pm 0.05 \pm 0.08\,, \tag{9.8}$$
$$\text{b) P3} = 0.01 \pm 0.02 \pm 0.03\,, \tag{9.9}$$
$$\text{c) P3} = -0.07 \pm 0.02 \pm 0.02\,. \tag{9.10}$$

Within the errors the value of the curvature parameter for a) and b) are consistent with zero. Considering the size of the relative errors no distinct sign of curvature is favoured. While the fit to the data set c) leads to a negative curvature which is ≈ 2.5 standard deviation different from zero. A negative curvature disfavours the two pomeron model.

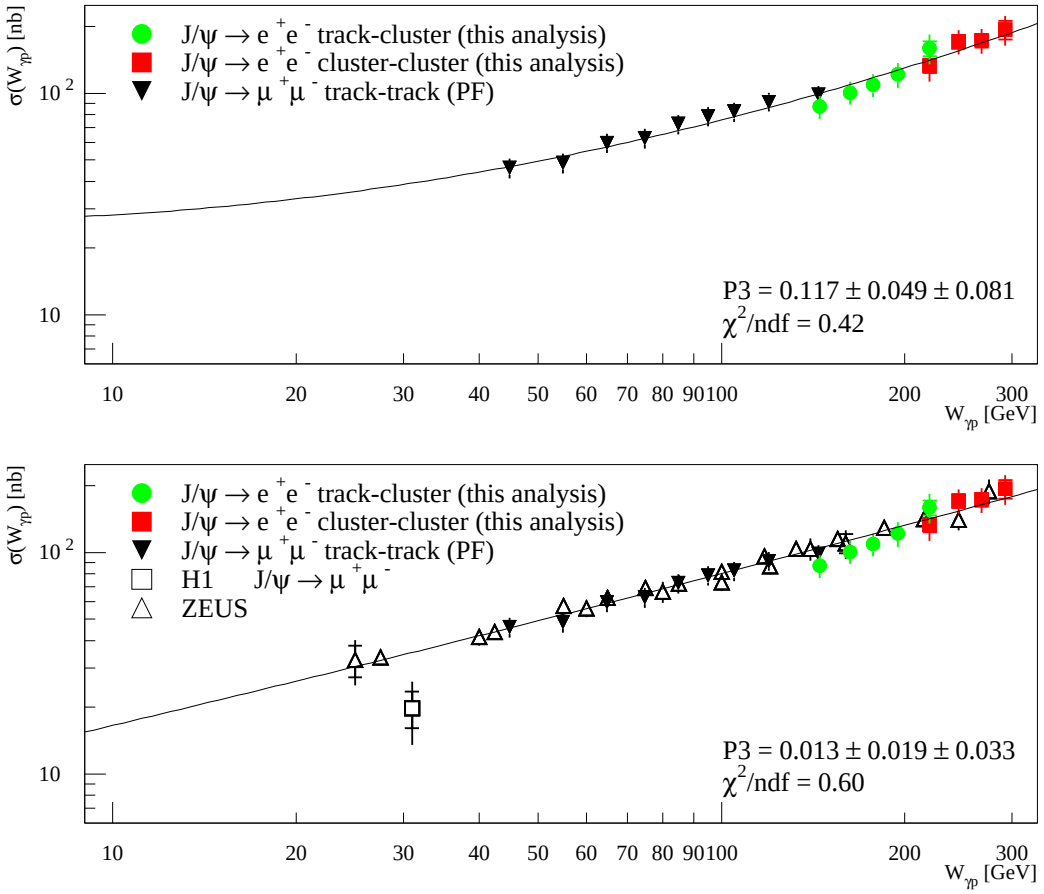

Figure 9.6: The elastic J/ψ photoproduction cross section $\sigma(W_{\gamma p})$ is shown as a function of $W_{\gamma p}$. The inner error bars correspond to the statistical error and the outer error bars to the total error. A fit of the form in equation 9.7 is applied to different data sets in order to study the curvature in the double logarithmic presentation. The fit parameter P3 corresponds to the curvature of the fit. The data sets contain the results of the track-cluster and cluster-cluster sample of this analysis, the track-track results of [99], the published H1 low $W_{\gamma p}$ result [14], the published results of ZEUS [119]. A fit to a data set including also the results of the fixed target experiments E516 [120] and E401 [121] is shown in figure 9.7.

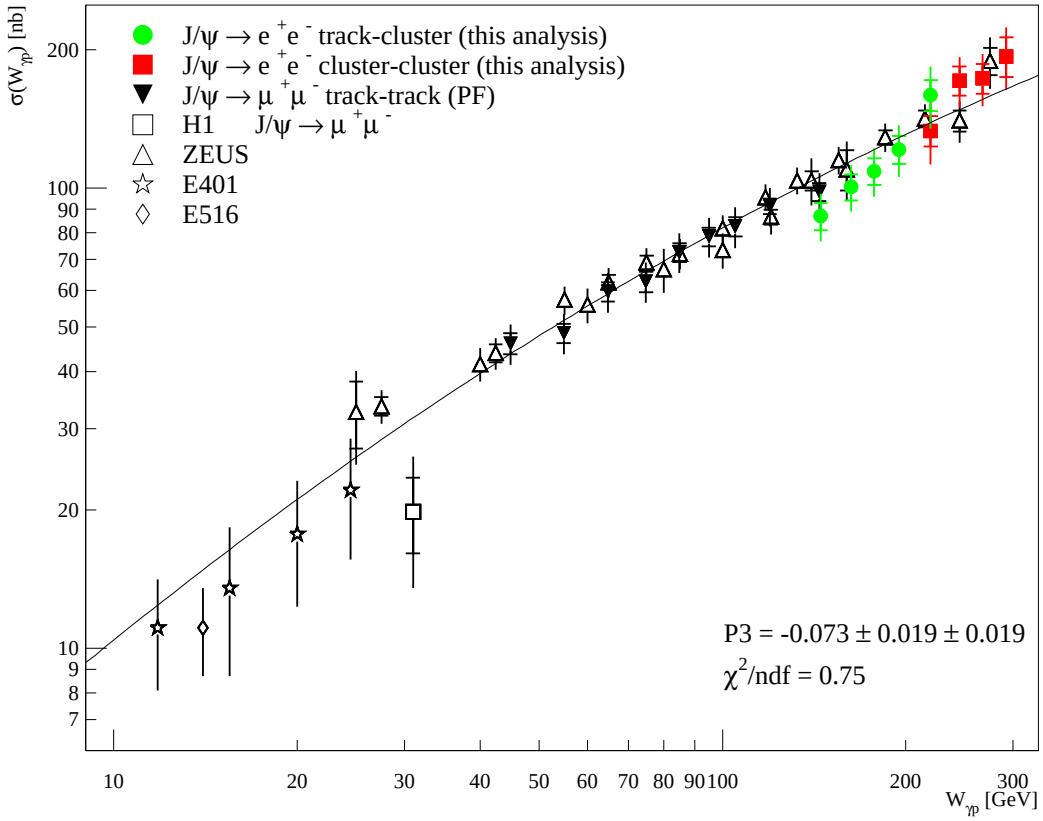

Figure 9.7: The elastic J/ψ photoproduction cross section $\sigma(W_{\gamma p})$ is shown as a function of $W_{\gamma p}$. The inner error bars correspond to the statistical error and the outer error bars to the total error. A fit of the form in equation 9.7 is applied to different data sets in order to study the curvature in the double logarithmic presentation. The fit parameter `P3` corresponds to the curvature of the fit. A fit to the results of the track-cluster and cluster-cluster sample of this analysis, the track-track results of [99], the published H1 low $W_{\gamma p}$ result [14], the published results of ZEUS [119] and the fixed target experiments E516 [120] and E401 [121] is shown in figure 9.7. Fits to two other data sets are shown in figure 9.6

9.1.4 Comparison with QCD Predictions

The QCD predictions are based on the calculations of FMS [10] and MRT [122] using different gluon densities. The gluon densities are determined in an indirect form e.g. from the scaling violation of the proton structure function $F_2(x, Q^2)$ in inclusive measurements, where the gluon density enters the cross section linearly.

The QCD predictions for the $W_{\gamma p}$ dependence of $\sigma(W_{\gamma p})$ are directly based on the gluon densities. Since the gluon density $g(x_g, \tilde{Q}^2)$ enters quadratically in the cross section in equation 1.68 the comparison of the QCD predictions to the data is a good test for the used gluon densities.

The FMS calculation uses the gluon density from CTEQ4L [123], while the MRT calculations use the gluon densities from CTEQ5M [124], CTEQ6M [125], MRST99 [126], MRST02 [127], H1QCD [117], H1PDF2000 [118] and ZEUS-S [128]. The absolute magnitude of the predictions depend on a number of parameters — like the mass of the charm quark — and on non-perturbative effects. The cross section in equation 1.65 is $\propto m_c^{-8} \cdot \mathcal{C}(Q^2)$, where m_c is the mass of the charm quark and $\mathcal{C}(Q^2)$ is determined from the vector meson wave function. Both contribute to the large uncertainty in the normalisation of the prediction. Therefore only the $W_{\gamma p}$ dependence of the predictions is compared to the data, while the normalisation is a free fit parameter.

In figure 9.8 several QCD predictions are compared to the track-cluster and cluster-cluster results of this analysis, the track-track results of [99] and the low $W_{\gamma p}$ result of [14]. The results of the fixed target experiments are not included in the comparison since these QCD predictions do not reach these low energies.

The QCD predictions for the $W_{\gamma p}$ dependence of $\sigma(W_{\gamma p})$ depend strongly on the different gluon densities, since the gluon density $g(x_g, \tilde{Q}^2)$ enters quadratically in the cross section in equation 1.68. The different shapes for the cross section $\sigma(W_{\gamma p})$ (see figure 9.8) are due to the different shapes of the gluon densities.

The fit results including the fit probability for the different predictions are listed in table 9.3. The predictions based on the gluon densities from MRST02, H1QCD and H1PDF2000 predict a shape which is incompatible with the data. The calculations MRT(CTEQ6M) and FMS(CTEQ4L) predict a too shallow and too steep rise respectively. The prediction based on MRST99 gives a better description, than the prediction based on the more recent gluon density from MRST02. The calculations based on CTEQ5M and ZEUS-S give the best description of the measured cross section.

9.2 Differential Cross Section $\frac{\mathrm{d}\sigma}{\mathrm{d}t}$

The differential elastic J/ψ photoproduction cross section $\frac{\mathrm{d}\sigma}{\mathrm{d}t}$ is measured as a function of $|t|$ in the range $0\,\mathrm{GeV}^2/\,\mathrm{c}^2 < |t| < 1.2\,\mathrm{GeV}^2/\,\mathrm{c}^2$. The $|t|$-range is divided into five bins as explained in section 8.2.2. $\frac{\mathrm{d}\sigma}{\mathrm{d}t}$ is measured separately for the track-cluster and cluster-cluster samples in the range of the photon-proton centre-of-mass energy $135\,\mathrm{GeV} < W_{\gamma p} < 235\,\mathrm{GeV}$ and $205\,\mathrm{GeV} < W_{\gamma p} < 305\,\mathrm{GeV}$ respectively.

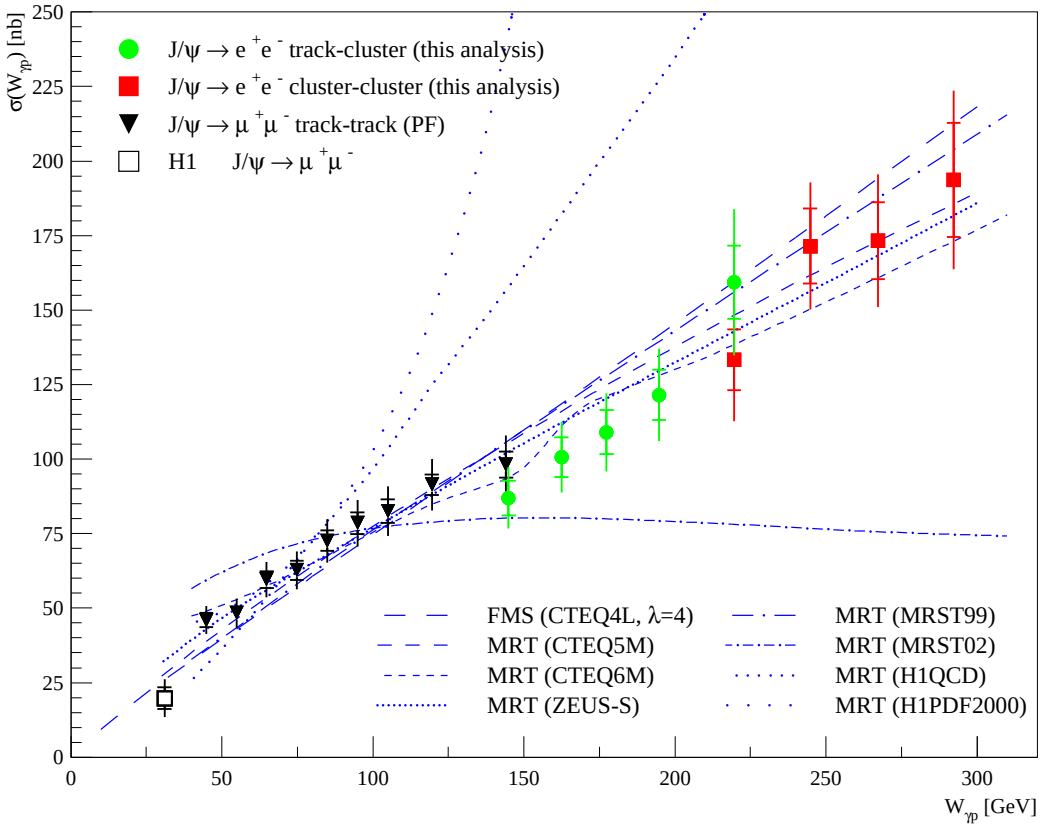

Figure 9.8: The elastic J/ψ photoproduction cross section $\sigma(W_{\gamma p})$ as a function of $W_{\gamma p}$ is shown. The inner error bars show the statistical errors, while the outer error bars show the total errors. The track-cluster and cluster-cluster results of this analyis, the low $W_{\gamma p}$ result of [14] and the track-track results of [99] are shown. The data are compared to two QCD calculations using different parameterisations of the gluon density in the proton. The FMS [10] calculation uses the gluon density from CTEQ4L [123]. MRT [122] calculations are shown for the gluon densities from CTEQ5M [124], CTEQ6M [125], MRST99 [126], MRST02 [127], H1QCD [117], H1PDF2000 [118] and ZEUS-S [128]. The shape of the predictions based on MRST02, H1QCD and H1PDF2000 do not agree with the data. The other predictions are fitted to the data using the normalisation as free parameter. The fit results are listed in table 9.3. The MRT(CTEQ6M) prediction has a bulge at $W_{\gamma p} \approx 150\,\text{GeV}$. In order to verfy the bulge for this $W_{\gamma p}$ range the stepsize in $W_{\gamma p}$ for the calculations was reduced by T. Teubner. The bulge is a result of the used gluon density.

	normalisation			χ^2	ndf	χ^2/ndf	prob.
FMS (CTEQ4L, $\lambda = 4$)	0.89	± 0.01	± 0.02	26.21	18	1.46	0.095
MRT (CTEQ5M)	0.91	± 0.01	± 0.02	15.05	18	0.84	0.659
MRT (CTEQ6M)	2.09	± 0.03	± 0.05	22.08	18	1.23	0.228
MRT (MRST99)	1.24	± 0.02	± 0.03	22.33	18	1.24	0.218
MRT (MRST02)	3.00			– – –	– – –	– – –	– – –
MRT (H1QCD)	0.96			– – –	– – –	– – –	– – –
MRT (H1PDF2000)	3.26			– – –	– – –	– – –	– – –
MRT (ZEUS-S)	1.41	± 0.02	± 0.03	11.56	18	0.64	0.869

Table 9.3: QCD predictions are fitted to the cross section $\sigma(W_{\gamma p})$ (see figure 9.8 and the description there). The normalisation is the free paramter in the fit. From the χ^2 and the number of degrees of freedom the probability for the fit is calculated. For MRT(MRST02), MRT(H1QCD) and MRT(H1PDF2000) no fit is performed, since their shapes do not agree with the data. The normalisation for these predictions is determined in [129] from the Q^2 dependence of the cross section.

For the calculation of the differential cross section $\frac{\mathrm{d}\sigma}{\mathrm{d}t}$ equation 8.1 is used and the result is divided by the bin width of the $|t|$-bin. The result of the unfolding procedure in section 8.6 are the numbers of proton-elastic events $N^{\mathrm{pelas}}_{|t|}$ in bins of $|t|$. Therefore no further f_{ed}-correction is needed. The inputs for the calculation and the results for the differential cross section are listed in table 9.4.

The $|t|$ dependence of the differential cross section $\frac{\mathrm{d}\sigma}{\mathrm{d}t}$ is discussed in section 9.2.1. The measurements of the differential cross section $\frac{\mathrm{d}\sigma}{\mathrm{d}t}$ are used to determine the parameters of an "effective" pomeron trajectory in section 9.2.2.

9.2.1 t Dependence of $\frac{\mathrm{d}\sigma}{\mathrm{d}t}$

In figure 9.9 the differential cross section $\frac{\mathrm{d}\sigma}{\mathrm{d}t}$ as a function of $|t|$ is shown for the track-cluster and cluster-cluster samples. A fit of the form $\frac{\mathrm{d}\sigma}{\mathrm{d}t}(t) \propto \mathrm{e}^{-b\cdot|t|}$ is applied. The fit function is motivated by equation 1.45. Due to the exponential behaviour of the data and the large bin width an iterative fitting procedure is necessary in order to determine the positions t_{pos} within the $|t|$-bins. The procedure is described in section 8.2.2. Equation 8.5 is used to calculate the positions t_{pos} (see table 9.4). For the b-slope of the track-cluster and cluster-cluster samples the fit yields

$$b_{\mathrm{TC}}(135\,\mathrm{GeV} < W_{\gamma p} < 235\,\mathrm{GeV}) = (5.1 \pm 0.3 \pm 0.2)\,\mathrm{GeV}^{-2}\,\mathrm{c}^2\,, \quad (9.11)$$

$$b_{\mathrm{CC}}(205\,\mathrm{GeV} < W_{\gamma p} < 305\,\mathrm{GeV}) = (5.4 \pm 0.4 \pm 0.2)\,\mathrm{GeV}^{-2}\,\mathrm{c}^2\,, \quad (9.12)$$

where the first error is the error of the fit, while the second error is the systematic error. The systematic error is derived from the fit stability. This is studied by excluding the first or last $|t|$ bin from the fit. The track-cluster and cluster-cluster samples correspond to an average photon proton centre of mass energy of $\langle W_{\gamma p}\rangle = 180.6\,\mathrm{GeV}$ and $\langle W_{\gamma p}\rangle = 250.8\,\mathrm{GeV}$ respectively.

	track-cluster					cluster-cluster				
min. $W_{\gamma p}$ [GeV]	135.0					205.0				
max. $W_{\gamma p}$ [GeV]	235.0					305.0				
$\langle W_{\gamma p} \rangle$ [GeV]	180.6					250.7				
min. p_t^2 [GeV^2/c^2]	0.000	0.070	0.140	0.300	0.600	0.000	0.070	0.140	0.300	0.600
max. p_t^2 [GeV^2/c^2]	0.070	0.140	0.300	0.600	1.200	0.070	0.140	0.300	0.600	1.200
$N^{\text{pelas}}_{\lvert t\rvert}$	499.3 ±26.0	378.0 ±15.8	388.0 ±17.4	189.9 ±11.6	51.6 ±5.4	287.7 ±18.5	220.3 ±10.8	202.4 ±11.1	97.4 ±7.5	28.6 ±3.9
$f_{\psi(2S)}$ [%]	1.2					0.5				
$\mathcal{F}_\gamma / 10^{-2}$	3.016					1.522				
$\mathcal{B}$ [%]	5.93					5.93				
$\mathcal{L}$ [pb^{-1}]	30.26					26.90				
$\varepsilon_{\text{tot},\lvert t\rvert}$	0.281 ±0.014	0.267 ±0.019	0.251 ±0.015	0.198 ±0.026	0.167 ±0.030	0.226 ±0.003	0.225 ±0.004	0.210 ±0.003	0.186 ±0.004	0.149 ±0.006
$\frac{d\sigma}{dt}$ [nb c^2 GeV^{-2}]	462.6	369.6	176.1	58.3	9.4	743.7	572.9	246.5	71.6	13.1
$\delta\frac{d\sigma}{dt}_{\text{stat}}$ [nb c^2 GeV^{-2}]	24.1	15.5	7.9	3.6	1.0	47.7	28.1	13.5	5.5	1.8
$\delta\frac{d\sigma}{dt}_{\text{syst}}$ [nb c^2 GeV^{-2}]	58.8	39.5	21.5	7.7	1.5	87.8	75.1	31.8	9.8	1.9
$\delta\frac{d\sigma}{dt}_{\text{tot}}$ [nb c^2 GeV^{-2}]	63.5	42.5	22.9	8.5	1.8	99.9	80.2	34.5	11.3	2.6
t_{pos} [GeV^2/c^2]	0.034	0.104	0.215	0.431	0.829	0.034	0.104	0.214	0.430	0.825
b-slope [GeV^{-2} c^2]	5.059 ±0.289					5.408 ±0.356				

Table 9.4: The values of the differential elastic cross section $\frac{d\sigma}{dt}$ as a function of $|t|$, the statistical error $\delta\frac{d\sigma}{dt}_{\text{stat}}$, the systematic error $\delta\frac{d\sigma}{dt}_{\text{syst}}$ and the total error $\delta\frac{d\sigma}{dt}_{\text{tot}}$ are listed for the track-cluster and cluster-cluster samples. The cross section is calculated in bins of $|t|$ using equation 8.1 and dividing by the width of the $|t|$ bin. The result of the unfolding procedure in section 8.6 are the numbers of proton-elastic events $N^{\text{pelas}}_{|t|}$ in bins of $|t|$. Therefore no further f_{ed}-correction is needed. The input quantities for equation 8.1 are given in the table. For a description refer to chapter 8. In an iterative procedure an exponential fit of the form $\frac{d\sigma}{dt}(t) \propto e^{-b\cdot|t|}$ is applied and the positions t_{pos} within the $|t|$-bins (see equation 8.5) and the slope b are derived.

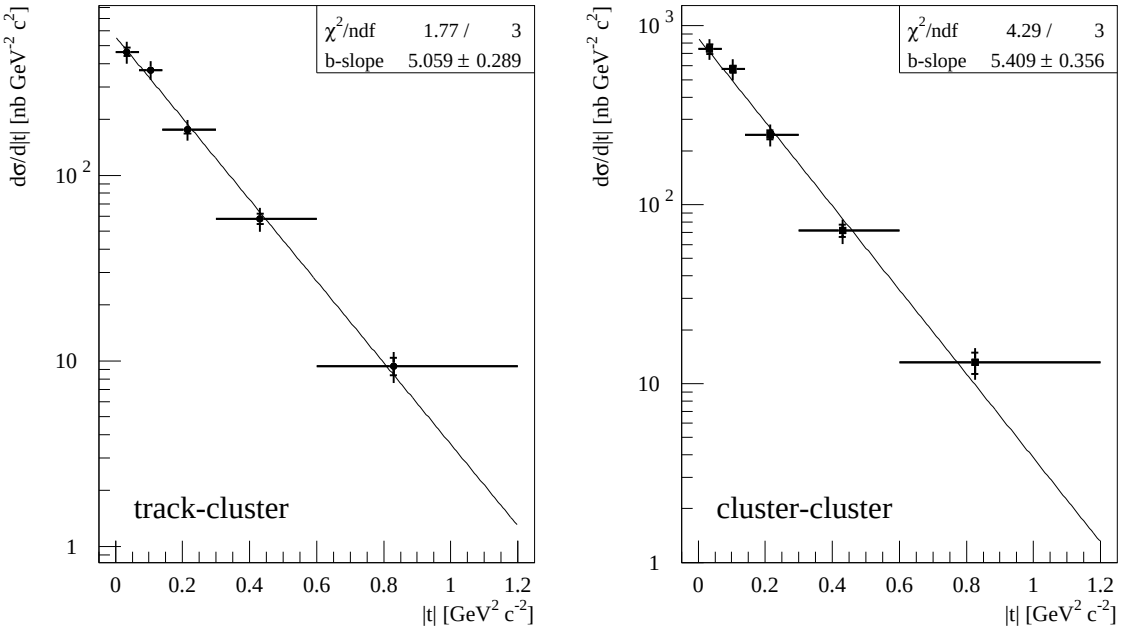

Figure 9.9: The differential cross section $\frac{d\sigma}{dt}$ of the elastic J/ψ photoproduction as a function of $|t|$ is shown for the track-cluster and cluster-cluster samples. An exponential fit of the form $\frac{d\sigma}{dt}(t) \propto e^{-b\cdot|t|}$ is applied.

There exist no published H1 results for the b-slope for the kinematic range in $W_{\gamma p}$ of the track-cluster and cluster-cluster samples. ZEUS has published the following results [119] for the corresponding $W_{\gamma p}$ range:

$$b_{\mathrm{ZEUS}}(125\,\mathrm{GeV} < W_{\gamma p} < 170\,\mathrm{GeV}) = (4.30 \pm 0.19^{+0.31}_{-0.17})\,\mathrm{GeV}^{-2}\,\mathrm{c}^2\,, \quad (9.13)$$

$$b_{\mathrm{ZEUS}}(170\,\mathrm{GeV} < W_{\gamma p} < 230\,\mathrm{GeV}) = (4.65 \pm 0.20^{+0.28}_{-0.21})\,\mathrm{GeV}^{-2}\,\mathrm{c}^2\,, \quad (9.14)$$

$$b_{\mathrm{ZEUS}}(230\,\mathrm{GeV} < W_{\gamma p} < 290\,\mathrm{GeV}) = (4.05 \pm 0.38^{+0.33}_{-0.25})\,\mathrm{GeV}^{-2}\,\mathrm{c}^2\,. \quad (9.15)$$

The results for the b-slope of this analysis for the track-cluster and cluster-cluster samples, the results of the H1 track-track analysis [99] and the ZEUS publication [119] are shown in figure 9.10 as a function of $W_{\gamma p}$. The published ZEUS values are generally lower than the H1 results. The results of this analysis agree very well with an extrapolation of the H1 track-track analysis (see figure 9.11).

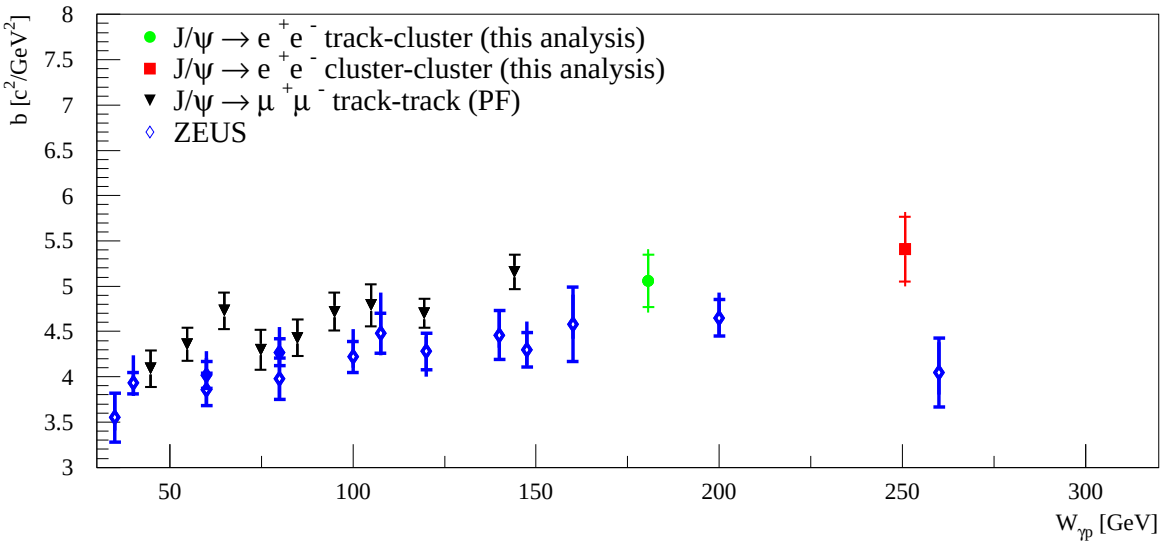

Figure 9.10: The values of the b-slope of the $|t|$ dependence of the differential cross section $\frac{\mathrm{d}\sigma}{\mathrm{d}t}$ as a function of $W_{\gamma p}$ are shown. The results of this analysis for the track-cluster and the cluster-cluster samples, the results of the track-track analysis [99] and the ZEUS publication [119] are presented. The b values are plotted at the mean values $\langle W_{\gamma p} \rangle$ of the corresponding $W_{\gamma p}$ bins.

9.2.2 Effective Pomeron Trajectory

The $W_{\gamma p}$ dependence of the cross section $\sigma(W_{\gamma p})$ is not described by single pomeron exchange (see section 9.1.1). In order to describe the cross section $\sigma(W_{\gamma p})$ for the HERA data (see section 9.1.2) a second, hard pomeron was introduced.

Although two pomerons are needed to describe the $W_{\gamma p}$ dependence of $\sigma(W_{\gamma p})$, only one, "effective" trajectory $\alpha(t) = \alpha_0 + \alpha' \cdot t$ is used for the analysis of the differential cross section $\frac{\mathrm{d}\sigma}{\mathrm{d}t}$. This trajectory corresponds to an *effective pomeron*.

From the $W_{\gamma p}$ dependence of the b-slope of the differential cross section the slope α' of the effective pomeron trajectory is derived in section 9.2.2.1.

The $W_{\gamma p}$ dependence of $\frac{d\sigma}{dt}$ in bins of $|t|$ is used to determine the intercept α_0 and the slope α' (see section 9.2.2.2).

9.2.2.1 Determination of the Slope of the Effective Pomeron Trajectory

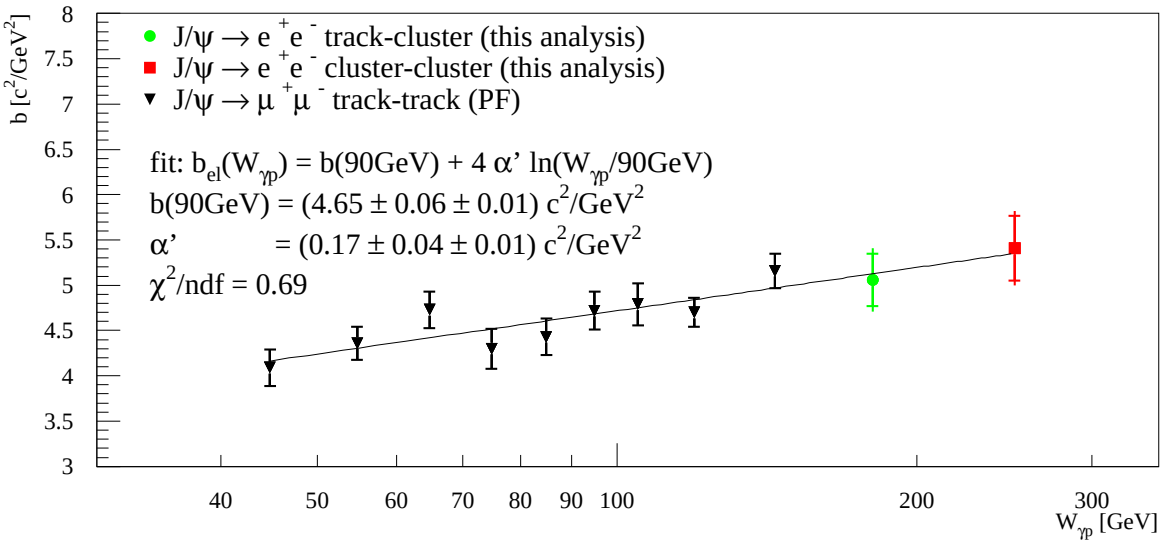

Figure 9.11: The values of the slope b of the t dependence of the differential cross section $\frac{d\sigma}{dt}$ as a function of $W_{\gamma p}$ are plotted at the mean values $\langle W_{\gamma p} \rangle$ of each $W_{\gamma p}$ bin. The results of this analysis for the track-cluster and cluster-cluster samples and the results of the track-track analysis [99] are shown. The inner error bars show the statistical error, while the outer error bars show the total error. A fit $b(W_{\gamma p}) = b(90\,\text{GeV}) + 4\alpha' \ln(W_{\gamma p}/90\,\text{GeV})$ is applied.

In figure 9.11 the b-slope as a function of $W_{\gamma p}$ is shown for the track-cluster and cluster-cluster samples. The results of the track-track analysis [99] are also shown. A fit of the form

$$b(W_{\gamma p}) = b(90\,\text{GeV}) + 4\,\alpha'_b\,\ln(W_{\gamma p}/90\,\text{GeV}) \tag{9.16}$$

is performed using the combined data. The fit function is motivated by equation 1.47. α' is the slope of the effective pomeron trajectory (see equation 1.35). The fit to the combined b-slope results of the track-track, track-cluster and cluster-cluster analysis — covering the $W_{\gamma p}$ range of $40\,\text{GeV} < W_{\gamma p} < 305\,\text{GeV}$ — yields

$$b(90\,\text{GeV})_{\text{TT,TC,CC}} = (4.65 \pm 0.06 \pm 0.01)\,\text{GeV}^{-2}\,\text{c}^2\,, \tag{9.17}$$

$$\alpha'_b := \alpha'_{\text{TT,TC,CC}} = (0.17 \pm 0.04 \pm 0.01)\,\text{GeV}^{-2}\,\text{c}^2\,, \tag{9.18}$$

where the first error is the fit error taking only the statistical errors of the data into account, while the second error is the systematic error calculated by quadratic subtraction from the total fit error taking the total error of the data into account. The results of the track-track analysis alone [99] and the published ZEUS analysis [119] are

$$b(90\,\mathrm{GeV})_{\mathrm{TT}} = (4.648 \pm 0.067 \pm 0.040)\,\mathrm{GeV}^{-2}\,\mathrm{c}^2\,, \tag{9.19}$$
$$\alpha'_{\mathrm{TT}} = (0.172 \pm 0.045 \pm 0.026)\,\mathrm{GeV}^{-2}\,\mathrm{c}^2\,, \tag{9.20}$$

$$b(90\,\mathrm{GeV})_{\mathrm{ZEUS}} = (4.15 \pm 0.05\,^{+0.30}_{-0.18})\,\mathrm{GeV}^{-2}\,\mathrm{c}^2\,, \tag{9.21}$$
$$\alpha'_{\mathrm{ZEUS}} = (0.116 \pm 0.026\,^{+0.010}_{-0.025})\,\mathrm{GeV}^{-2}\,\mathrm{c}^2\,, \tag{9.22}$$

The track-track analysis [99] uses data from $40\,\mathrm{GeV} < W_{\gamma p} < 160\,\mathrm{GeV}$, while the ZEUS analysis [119] covers $30\,\mathrm{GeV} < W_{\gamma p} < 290\,\mathrm{GeV}$.

With the results of the track-cluster and cluster-cluster analyses the determination of the slope α' of the effective pomeron trajectory using H1 data is extended into the kinematic region of $W_{\gamma p}$ beyond 160 GeV and up to 305 GeV.

The merit of the method of determining α' from the $W_{\gamma p}$ dependence of the b-slope is, that the relative normalisation of the differential cross sections $\frac{\mathrm{d}\sigma}{\mathrm{d}t}$ of the different data samples is irrelevant since only the b-slope values are used.

The investigation of the b-slope of the differential cross section $\frac{\mathrm{d}\sigma}{\mathrm{d}t}$ as a function of $W_{\gamma p}$ allows to determine the slope α' of the effective pomeron trajectory only. It gives no handle for the determination of the intercept α_0 of the effective pomeron trajectory. Both, α_0 and α' can be determined from the $W_{\gamma p}$ dependence of the differential cross section $\frac{\mathrm{d}\sigma}{\mathrm{d}t}$ for different values of fixed $|t|$. This method is described in the next section.

9.2.2.2 Effective Pomeron Trajectory

In this section the intercept α_0 and the slope α' of the effective pomeron trajectory are derived from the $W_{\gamma p}$ dependence of the differential cross section $\frac{\mathrm{d}\sigma}{\mathrm{d}t}$ for different values of fixed $|t|$. From the equations 1.35, 1.45 and 1.47 it follows for the differential cross section $\frac{\mathrm{d}\sigma}{\mathrm{d}t}$ as a function of $W_{\gamma p}$ for fixed $|t|$

$$\begin{aligned}
\left.\frac{\mathrm{d}\sigma}{\mathrm{d}t}(W_{\gamma p})\right|_{|t|\mathrm{fixed}} &\propto \mathrm{e}^{-b(W_{\gamma p})|t|} {W_{\gamma p}}^{4\varepsilon} \\
&\propto {W_{\gamma p}}^{4(\alpha_0+\alpha' t-1)} \cdot \underbrace{\mathrm{e}^{-(b_0-4\alpha'\ln W_{\gamma p_0})|t|}}_{=\mathrm{const.}} \\
&\propto \left.{W_{\gamma p}}^{4(\alpha(|t|)-1)}\right|_{|t|\mathrm{fixed}} .
\end{aligned} \tag{9.23}$$

In figure 9.12 the differential cross section $\frac{\mathrm{d}\sigma}{\mathrm{d}t}$ is shown as a function of $W_{\gamma p}$ for five values of $\langle|t|\rangle$. The values $\langle|t|\rangle$ are the positions t_{pos} determined in the exponential fit

to $\frac{d\sigma}{dt}$ (see table 9.4). The results for the track-cluster and cluster-cluster samples are shown. In order to extend the range in $W_{\gamma p}$ also the results of the track-track analysis [99] are included[3].

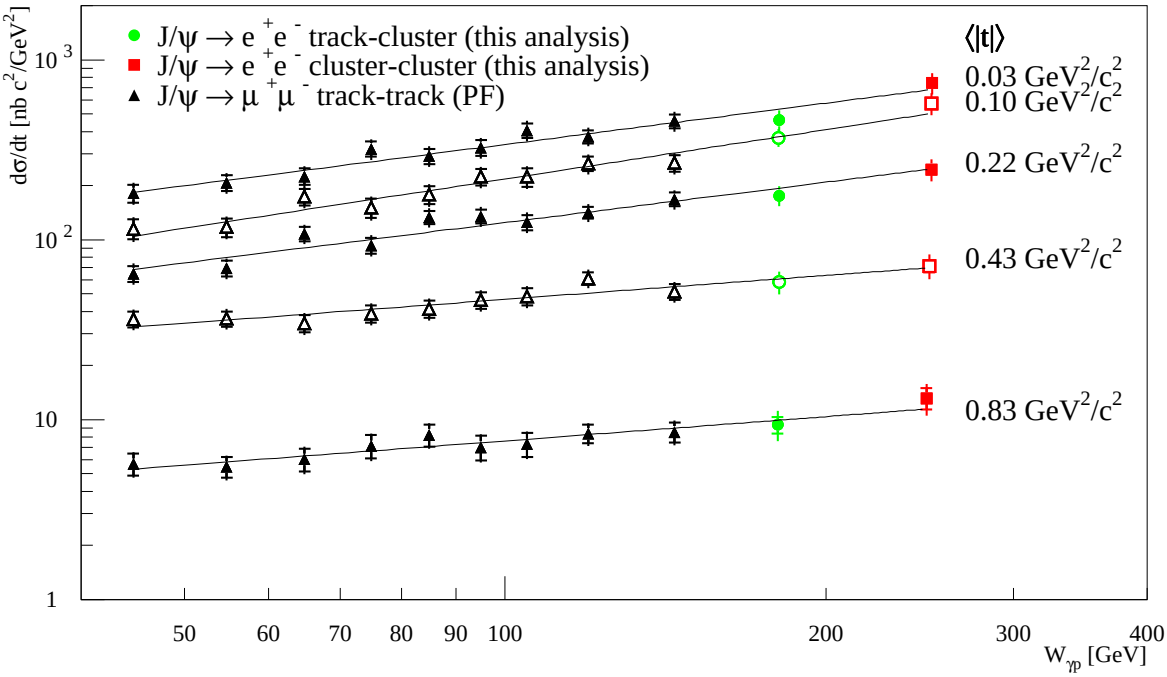

Figure 9.12: The differential elastic photoproduction cross section $\frac{d\sigma}{dt}$ as a function of $W_{\gamma p}$ is measured in five bins in $|t|$ (see section 8.2.2). The values $\langle|t|\rangle$ within the bins are listed. The inner error bars of the data correspond to the statistical error and the outer error bars to the total error. A fit of the form $\frac{d\sigma}{dt} \propto {W_{\gamma p}}^{4(\alpha(|t|)-1)}$ is applied to the five data sets. The fit results are listed in table 9.5.

$\langle\|t\|\rangle$[GeV^2/c^2]	$\alpha(\langle\|t\|\rangle)$		
0.03	1.19	±0.01	±0.02
0.10	1.23	±0.01	±0.02
0.22	1.19	±0.01	±0.02
0.43	1.11	±0.01	±0.02
0.83	1.11	±0.02	±0.02

Table 9.5: The values of the effective pomeron trajectory $\alpha(\langle|t|\rangle)$ for the elastic J/ψ photoproduction for different values of $\langle|t|\rangle$. The values are obtained from the fits in figure 9.12. The statistical and systematic error are listed.

Fits of the form of equation 9.23 are applied to the five data sets, corresponding to the five values of $\langle|t|\rangle$. The fits can be affected by the relative normalisation of the differential cross section values of this analysis and the track-track analysis [99]. Therefore the relative normalisation is studied and the relative normalisation is found to be

[3]The analysis [99] covers the range $0\,\text{GeV}^2/\text{c}^2 < |t| < 1.2\,\text{GeV}^2/\text{c}^2$ with eight bins in $|t|$. As explained in section 8.2.2 the p_t^2 binning of this analysis is adjusted to the bin boundaries of [99], but the highest three bins contain two bins of the bins of [99] each. Therefore the results of [99] for $\frac{d\sigma}{dt}$ were recalculated for the actual binning of this analysis by Philipp Fleischmann, in order to be able to combine the results.

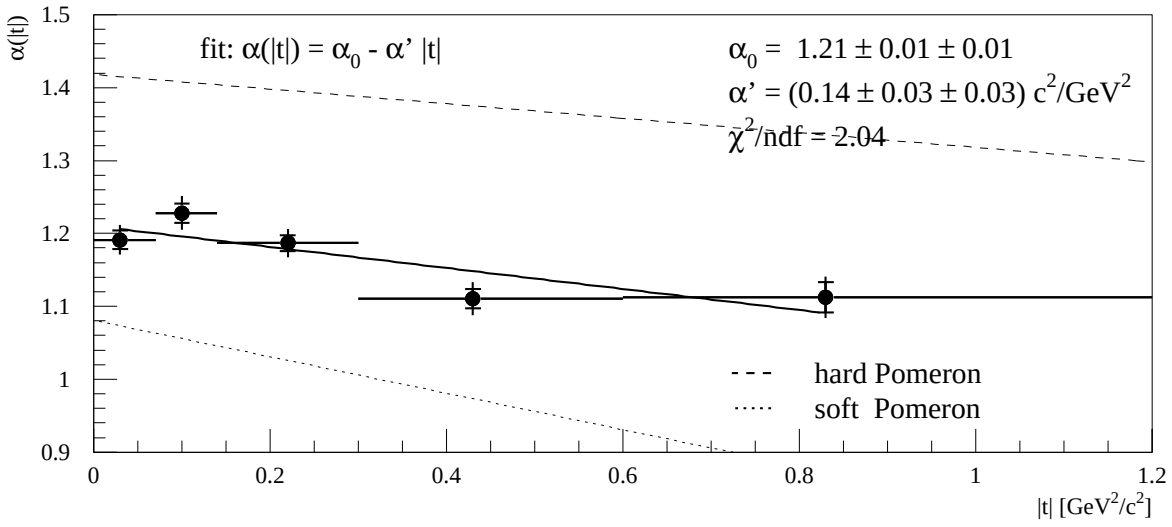

Figure 9.13: The effective pomeron trajectory $\alpha(|t|)$ is shown. The values are taken from table 9.5. The inner error bars correspond to the statistical error and the outer error bars to the total error. A fit of the form $\alpha(|t|) = \alpha_0 - \alpha'|t|$ is applied to the data. The trajectories of the hard pomeron $\alpha_{I\!P}(t) = 1.42 + 0.10\,\mathrm{GeV}^{-2}\,\mathrm{c}^2 \cdot t$ and the soft pomeron $\alpha_{I\!P}(t) = 1.08 + 0.25\,\mathrm{GeV}^{-2}\,\mathrm{c}^2 \cdot t$ are shown.

compatible with 1 within the errors. The fits yield values of $\alpha(\langle|t|\rangle)$, which are listed in table 9.5. The fit results $\alpha(\langle|t|\rangle)$ as a function of $|t|$ are shown in figure 9.13. A fit of the form $\alpha(|t|) = \alpha_0 - \alpha'|t|$ (see equation 1.35) is applied and yields for the intercept α_0 and the slope α' of the effective pomeron trajectory

$$\alpha_0 := \alpha_{0,\mathrm{TT,TC,CC}} = 1.21 \pm 0.01 \pm 0.01\,, \tag{9.24}$$

$$\alpha' := \alpha'_{\mathrm{TT,TC,CC}} = (0.14 \pm 0.03 \pm 0.03)\,\mathrm{GeV}^{-2}\,\mathrm{c}^2\,. \tag{9.25}$$

In figure 9.14 the values of $\alpha(t)$ of the H1 [14] and ZEUS [119] publications are included. The H1 publication [14] uses data from the decay $J/\psi \to \mu^+\mu^-$ of the running periods 1996 and 1997 in the kinematic range $40\,\mathrm{GeV} < W_{\gamma p} < 150\,\mathrm{GeV}$ and $0\,\mathrm{GeV}^2/\,\mathrm{c}^2 < |t| < 1.2\,\mathrm{GeV}^2/\,\mathrm{c}^2$. The published values of H1 for the intercept and the slope of the effective pomeron trajectory are

$$\alpha_{0,\mathrm{H1}} = 1.27 \pm 0.05\,, \tag{9.26}$$

$$\alpha'_{\mathrm{H1}} = (0.08 \pm 0.17)\,\mathrm{GeV}^{-2}\,\mathrm{c}^2\,. \tag{9.27}$$

With respect to previous the H1 results this analysis extends the kinematic range in $W_{\gamma p}$ from 150 GeV to 305 GeV.

The ZEUS publication [119] uses a combined data set of the decay $J/\psi \to e^+e^-$ of the running period 1999 and 2000 and the decay $J/\psi \to \mu^+\mu^-$ of the running periods 1996

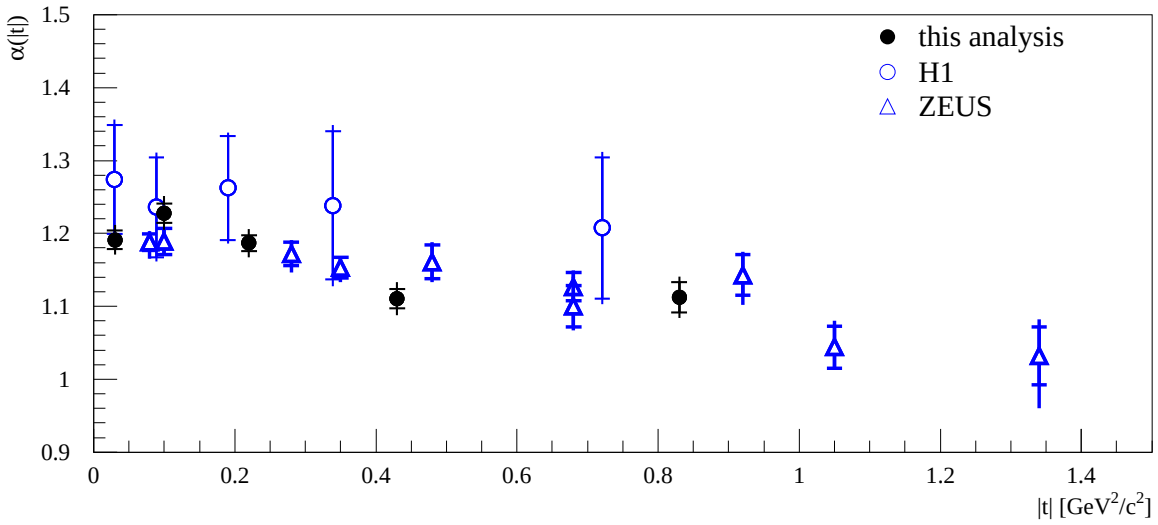

Figure 9.14: The effective pomeron trajectory $\alpha(|t|)$ for the elastic J/ψ photoproduction is shown. The results of this analysis and the published results of H1 [14] and ZEUS [119] are shown. The inner error bars correspond to the statistical error and the outer error bars to the total error.

and 1997. The electron channel covers the kinematic range $35\,\mathrm{GeV} < W_{\gamma p} < 290\,\mathrm{GeV}$ and $0 < |t| < 1.25\,\mathrm{GeV}^2/\,\mathrm{c}^2$, while the muon channel covers the kinematic range $30\,\mathrm{GeV} < W_{\gamma p} < 170\,\mathrm{GeV}$ and $0 < |t| < 1.8\,\mathrm{GeV}^2/\,\mathrm{c}^2$. The published values of ZEUS for the intercept and the slope of the effective pomeron trajectory are

$$\alpha_{0,\mathrm{ZEUS}} = 1.200 \pm 0.009\,^{+0.004}_{-0.010}\,, \tag{9.28}$$

$$\alpha'_{\mathrm{ZEUS}} = (0.115 \pm 0.018\,^{+0.008}_{-0.015})\,\mathrm{GeV}^{-2}\,\mathrm{c}^2\,, \tag{9.29}$$

where the first errors are the statistical errors and the second errors are the systematic errors.

The results for the intercept α_0 and the slope α' of the effective pomeron trajectory of this analysis and the published values of H1 and ZEUS agree very well within the errors. Compared to the published H1 results the errors of the results of this analysis — using the combined results from the track-cluster and cluster samples of this analysis and from the track-track analysis [99] — are reduced by more than a factor 3.

9.3 Discussion

The $W_{\gamma p}$ dependence of the elastic J/ψ photoproduction cross section $\sigma(W_{\gamma p})$ follows a power law ${W_{\gamma p}}^{\delta}$ with $\delta_{\mathrm{TC,CC}} = 1.17 \pm 0.11 \pm 0.16$ for the high $W_{\gamma p}$ region and $\delta = 0.76 \pm 0.03 \pm 0.04$ for the full $W_{\gamma p}$ range accessible to H1. This strong rise of the cross section excludes the single, soft pomeron exchange which would lead to $\delta \approx 0.32$

The two pomeron model describes $\sigma(W_{\gamma p})$ as a function of $W_{\gamma p}$ for the H1 data, but overshoots significantly the low $W_{\gamma p}$ results of the fixed target experiments E516 [120] and E401 [121]. A two pomeron fit to the combined data set of the fixed target and H1 data is incompatible with the data.

The two pomeron model predicts a concave shape of the cross section $\sigma(W_{\gamma p})$ in the double logarithmic presentation. The fit over the full $W_{\gamma p}$ range to the combined data set of the fixed target experiments and the HERA data suggest a negative curvature with ≈ 2.5 standard deviations from zero ($\texttt{P3} = -0.07 \pm 0.02 \pm 0.02$), i.e. a convex shape of $\sigma(W_{\gamma p})$ in the double logarithmic presentation. A negative curvature as found here disfavours the two pomeron model.

This analysis extends the measurement of the differential cross section $\frac{\mathrm{d}\sigma}{\mathrm{d}t}$ using H1 data in the region of the highest $W_{\gamma p}$. For the track-cluster and cluster-cluster samples the following b-slope parameters are determined: $b_{\mathrm{TC}}(\langle W_{\gamma p}\rangle = 180.6\,\mathrm{GeV}) = (5.1 \pm 0.3 \pm 0.2)\,\mathrm{GeV}^{-2}\,\mathrm{c}^2$, $b_{\mathrm{CC}}(\langle W_{\gamma p}\rangle = 250.7\,\mathrm{GeV}) = (5.4 \pm 0.4 \pm 0.2)\,\mathrm{GeV}^{-2}\,\mathrm{c}^2$.

The measurement of the differential cross section $\frac{\mathrm{d}\sigma}{\mathrm{d}t}$ gives access to the parameters of an effective pomeron trajectory in two ways. The t dependence of the differential cross section $\frac{\mathrm{d}\sigma}{\mathrm{d}t}(t) \propto \mathrm{e}^{-b|t|}$ yields a slope parameter b for different values of $W_{\gamma p}$. From the $W_{\gamma p}$ dependence of b in the full kinematic range of the H1 data the slope of the effective pomeron trajectory is obtained: $\alpha'_b = (0.17 \pm 0.04 \pm 0.01)\,\mathrm{GeV}^{-2}\,\mathrm{c}^2$. This method has the advantage, that the relative normalisation of different data sets for the different regions in $W_{\gamma p}$ are irrelevant, since only the slope of the cross section is measured. However, this method gives access only to one of the two parameters of the effective pomeron trajectory.

The $W_{\gamma p}$ dependence of the differential cross section $\frac{\mathrm{d}\sigma}{\mathrm{d}t}$ in bins of $|t|$ enables determination of the intercept $\alpha_0 = 1.21 \pm 0.01 \pm 0.01$ and the slope $\alpha' = (0.14 \pm 0.03 \pm 0.03)\,\mathrm{GeV}^{-2}\,\mathrm{c}^2$ of the effective pomeron trajectory.

The intercept α_0 and the slope α' of the effective pomeron trajectory lie between the corresponding values for the hard $\alpha_{\mathrm{I\!P}}(t) = 1.42 + 0.10\,\mathrm{GeV}^{-2}\,\mathrm{c}^2 \cdot t$ and the soft $\alpha_{\mathrm{I\!P}}(t) = 1.08 + 0.25\,\mathrm{GeV}^{-2}\,\mathrm{c}^2 \cdot t$ pomeron (see section 1.6.3). The slope α' of the effective pomeron trajectory differs from zero by more than four standard deviations and by three and one standard deviations from the slope values of the soft and hard pomeron respectively.

The result for the slope α' agrees very well with the result α'_b determined from the b-slope analysis of the differential cross section $\frac{\mathrm{d}\sigma}{\mathrm{d}t}$.

For both measurements of α' the value is more than three standard deviations different from zero, which confirms the effect of shrinkage. This is a new result compared to the published H1 result $\alpha'_{\mathrm{H1}} = (0.08 \pm 0.17)\,\mathrm{GeV}^{-2}\,\mathrm{c}^2$, where the slope is consistent with zero.

QCD makes no prediction about shrinkage. The two pomeron model predicts almost no shrinkage, although both slope parameters of the hard and soft pomeron are different from zero. Both measurements for the slope parameter α' give a significantly larger value than the slope of the hard pomeron.

Taking into account the measured values of the b-slope b_{TC} and b_{CC} the average over $|t|$ of the effective pomeron trajectory $\alpha(t) = \alpha_0 + \alpha' \cdot t$ amounts to $\langle \alpha(t) - 1 \rangle_{|t|} \approx 0.182$, which leads to $\delta_\alpha = 4 \cdot \langle \alpha(t) - 1 \rangle_{|t|} \approx 0.729$. The calculated value for δ_α agrees very well with the result δ of the fits to the cross section $\sigma(W_{\gamma p})$.

The QCD predictions for the $W_{\gamma p}$ dependence of the cross section $\sigma(W_{\gamma p})$ show a strong dependence on the gluon densities used, since the gluon densities enter quadratically in the cross section. Therefore the comparison of the predicted $W_{\gamma p}$ dependence is a sensitive test for the gluon densities, which are determined in inclusive measurements, where the gluon density is measured indirectly e.g. via scaling violations of the proton structure function $F_2(x, Q^2)$. The predictions based on the gluon densities from MRST02, H1QCD and H1PDF2000 are incompatible with the measured cross section $\sigma(W_{\gamma p})$, while the predictions based on CTEQ6M and CTEQ4L predict a too shallow and too steep rise of the cross section $\sigma(W_{\gamma p})$ respectively. The predictions based on CTEQ5M and ZEUS-S agree with the data.

Summary

In this thesis the elastic J/ψ photoproduction at high photon-proton centre-of-mass energies $W_{\gamma p}$ was studied. The J/ψ was identified through its decay into an e^+e^- pair. Depending on $W_{\gamma p}$ the decay electrons enter different regions in the H1 detector and are registered either in the central detector part ("track") or in the backward calorimeter ("cluster"). This analysis concentrated on the track-cluster and cluster-cluster samples where the data were limited in statistics in previous analysis.

The track-cluster and cluster-cluster samples correspond to the kinematic range 135 GeV $< W_{\gamma p} <$ 235 GeV and 205 GeV $< W_{\gamma p} <$ 305 GeV, respectively. The experimental signature of photoproduction events is the absence of the scattered beam electron in the main detector, which corresponds to the kinematic range $Q^2 < 1\,\mathrm{GeV}^2/\,\mathrm{c}^2$. The data is selected with a transverse momentum $p_t^2 < 1.2\,\mathrm{GeV}^2/\,\mathrm{c}^2$ of the J/ψ, which corresponds to the kinematic range $|t| \leq 1.2\,\mathrm{GeV}^2/\,\mathrm{c}^2$.

The data for the track-cluster and cluster-cluster samples have been collected with the H1 detector at the ep-collider HERA during the years 1999 and 2000 resulting in an integrated luminosity of 30.26 pb^{-1} and 26.90 pb^{-1} for the analysed data, respectively.

High efficiency in the online event selection during data taking was achieved by the use of the level 2 neural network trigger. For the track-cluster selection a feed forward neural network was used for the first time. For the cluster-cluster selection a parallel algorithm was used exploiting the back-to-back topology of the J/ψ decay electrons. The trigger efficiency was determined from data and MC simulation.

For cluster-cluster events the backward silicon tracker (BST) is the only source for track and vertex information. Only this information in combination with the precise energy measurement in the SpaCal allows the reconstruction of the J/ψ mass with sufficient precision. With the upgrade the BST provides hit information from eight planes. Based on the hit information a new track finding algorithm was developed. The MC simulation of the BST detector and the track finding was studied and adjusted to data on different levels, starting from the BST hit information up to the efficiency of the track finding.

The final selected event samples are still contaminated by background events. The main background contributions arise from the electron-pair-production and the QED-Compton process, varying with $W_{\gamma p}$. The contributions are studied with MC simulations.

The signal extraction uses the distribution of the invariant mass of the two J/ψ decay electron candidates in the final selected event samples. The different shape of the signal

and of the background contributions for the track-cluster and cluster-cluster samples are taken into account in a multi step fit procedure. In the fit procedure the background is subtracted and the number of signal events is determined.

The number of elastic J/ψ candidates has been derived using two different methods. The first method uses events without activity in the forward region of the detector only and corrects for remaining proton dissociation. The second method uses in addition a data sample with activity in the forward region in the detector and $p_t^2 < 5.0\,\mathrm{GeV}^2/\,\mathrm{c}^2$. It uses an unfolding technique to derive the number of elastic J/ψ candidates. While the first method is numerically stable and it relies more on MC, the second method is based on data but is numerically instable due to necessary matrix inversions. The results of both methods agree well within the statistical errors.

For the measurement of the differential cross section $\frac{\mathrm{d}\sigma}{\mathrm{d}t}$ the number of proton-elastic events in bins of $|t|$ is necessary. Experimentally the events are observed in bins of p_t^2 of the J/ψ meson and the kinematic variable $|t|$ is directly not accessible. Because of detector effects there is significant migration between bins and the approximation $|t| \approx p_t^2$ cannot be used. In order to determine the number of events in bins of $|t|$ from the number of events in bins of p_t^2 an unfolding method is used.

The elastic J/ψ photoproduction cross section $\sigma(W_{\gamma p})$ was measured almost up to the kinematic limit and extends therefore the kinematic range of H1 measurements to $W_{\gamma p} = 305\,\mathrm{GeV}$. Due to the higher integrated luminosity and the efficient event selection during the data taking the statistics is increased compared to previous measurements by a factor of 2 to 3. This allows an increase in the number of bins and an additional reduction of the statistical and systematic errors.

The $W_{\gamma p}$ dependence of the elastic J/ψ photoproduction cross section $\sigma(W_{\gamma p})$ follows a power law ${W_{\gamma p}}^{\delta}$ with $\delta_{\mathrm{TC,CC}} = 1.17 \pm 0.11 \pm 0.16$ for the high $W_{\gamma p}$ region and $\delta = 0.76 \pm 0.03 \pm 0.04$ for the full $W_{\gamma p}$ range accessible to H1. This strong rise of the cross section excludes the single, soft pomeron exchange.

The two pomeron model is not able to describe the combined results of fixed target experiments and H1, although it describes the results of H1 alone. The two pomeron model predicts a "concave" shape of $\sigma(W_{\gamma p})$ in the double logarithmic presentation. While a fit to the combined results of fixed target data, H1 and ZEUS leads to a "convex" shape, i.e. a negative curvature, which is ≈ 2.5 standard deviations different from zero.

This analysis provides first measurements of the differential cross section $\frac{\mathrm{d}\sigma}{\mathrm{d}t}$ using H1 data up to the highest values of $W_{\gamma p}$. The $|t|$ dependence of $\frac{\mathrm{d}\sigma}{\mathrm{d}t}$ is described by $\frac{\mathrm{d}\sigma}{\mathrm{d}t} \propto \mathrm{e}^{-b\cdot|t|}$. From the track-cluster and cluster-cluster samples the following slope parameters are derived: $b_{\mathrm{TC}}(\langle W_{\gamma p}\rangle = 180.6\,\mathrm{GeV}) = (5.1 \pm 0.3 \pm 0.2)\,\mathrm{GeV}^{-2}\,\mathrm{c}^2$, $b_{\mathrm{CC}}(\langle W_{\gamma p}\rangle = 250.8\,\mathrm{GeV}) = (5.4 \pm 0.4 \pm 0.2)\,\mathrm{GeV}^{-2}\,\mathrm{c}^2$.

The measurement of the differential cross section $\frac{\mathrm{d}\sigma}{\mathrm{d}t}$ gives access to the parameters of an effective pomeron trajectory in two ways. The t dependence of the differential cross section $\frac{\mathrm{d}\sigma}{\mathrm{d}t}(t) \propto \mathrm{e}^{-b\cdot|t|}$ yields slope parameter b for different values of $W_{\gamma p}$. From the $W_{\gamma p}$ dependence of b the slope of the effective pomeron trajectory is obtained as $\alpha'_b = (0.17 \pm 0.04 \pm 0.01)\,\mathrm{GeV}^{-2}\,\mathrm{c}^2$. This method has the advantage, that the relative

normalisation of different data sets for the different regions in $W_{\gamma p}$ are irrelevant, since only the slope of the cross section is measured. However, this method gives access only to one of the two parameters of the effective pomeron trajectory.

The $W_{\gamma p}$ dependence of the differential cross section $\frac{\mathrm{d}\sigma}{\mathrm{d}t}$ in bins of $|t|$ enables determination of the intercept $\alpha_0 = 1.21 \pm 0.01 \pm 0.01$ and the slope $\alpha' = (0.14 \pm 0.03 \pm 0.03)\,\mathrm{GeV}^{-2}\,\mathrm{c}^2$ of the effective pomeron trajectory. The two determined slope parameters α'_b and α' are compatible within errors.

The measured values of the intercept α_0 and α' slope of the effective pomeron trajectory lie between the values for the hard and soft pomeron. The measured values for the slope α' are more than three standard deviations different from zero, which confirms the effect of shrinkage. This is in mild contradiction to the two pomeron model prediction, which predicts almost no shrinkage.

Prediction from QCD were compared to the cross section $\sigma(W_{\gamma p})$. The $W_{\gamma p}$ dependence of the predictions is a direct consequence of the used gluon densities, which makes the comparison a sensitive test for the gluon densities, which are determined in indirect way from inclusive measurements. While some of these analyses result in gluon distributions consistent with the J/ψ measurements presented here, others can definitely be excluded. For future QCD analyses the exclusive production of J/ψ mesons is therefore a very sensitive tool to directly access the gluon distribution in the nucleon.

Appendix A

Signal Extraction

This appendix contains the full set of figures of the fits used for the signal extraction. For the different samples and binnings the fits are shown in the figures listed in the following table:

sample		binning	figure
track-cluster	fwd.-untagged	$W_{\gamma p}$ binning	A.1
track-cluster	fwd.-tagged	$W_{\gamma p}$ binning	A.2
cluster-cluster	fwd.-untagged	$W_{\gamma p}$ binning	A.3
cluster-cluster	fwd.-tagged	$W_{\gamma p}$ binning	A.4
track-cluster	fwd.-untagged	p_t^2 binning	A.5
track-cluster	fwd.-tagged	p_t^2 binning	A.6
cluster-cluster	fwd.-untagged	p_t^2 binning	A.7
cluster-cluster	fwd.-tagged	p_t^2 binning	A.8

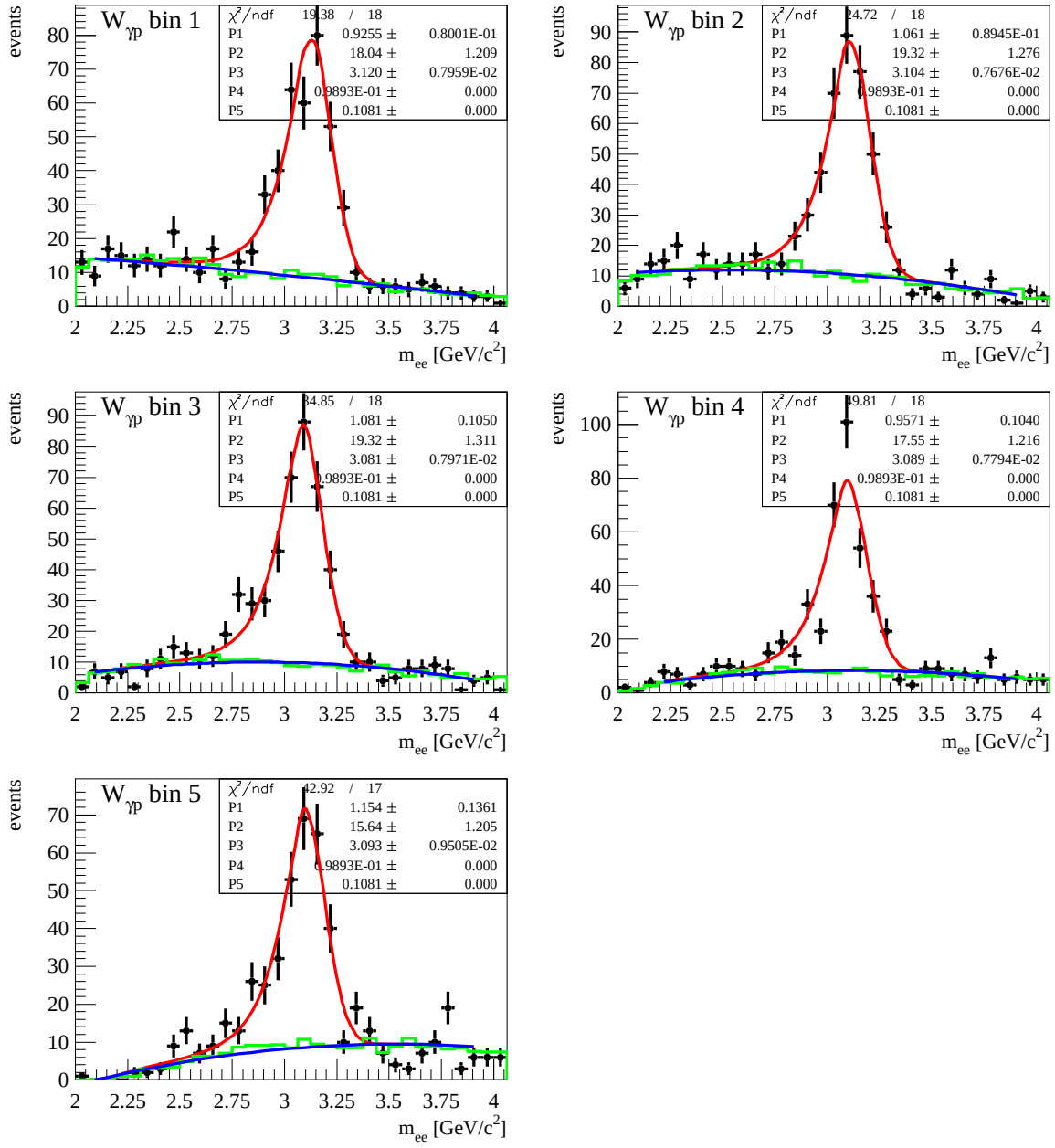

Figure A.1: The signal extraction fits for the fwd.-untagged track-cluster sample are shown in bins of $W_{\gamma p}$.

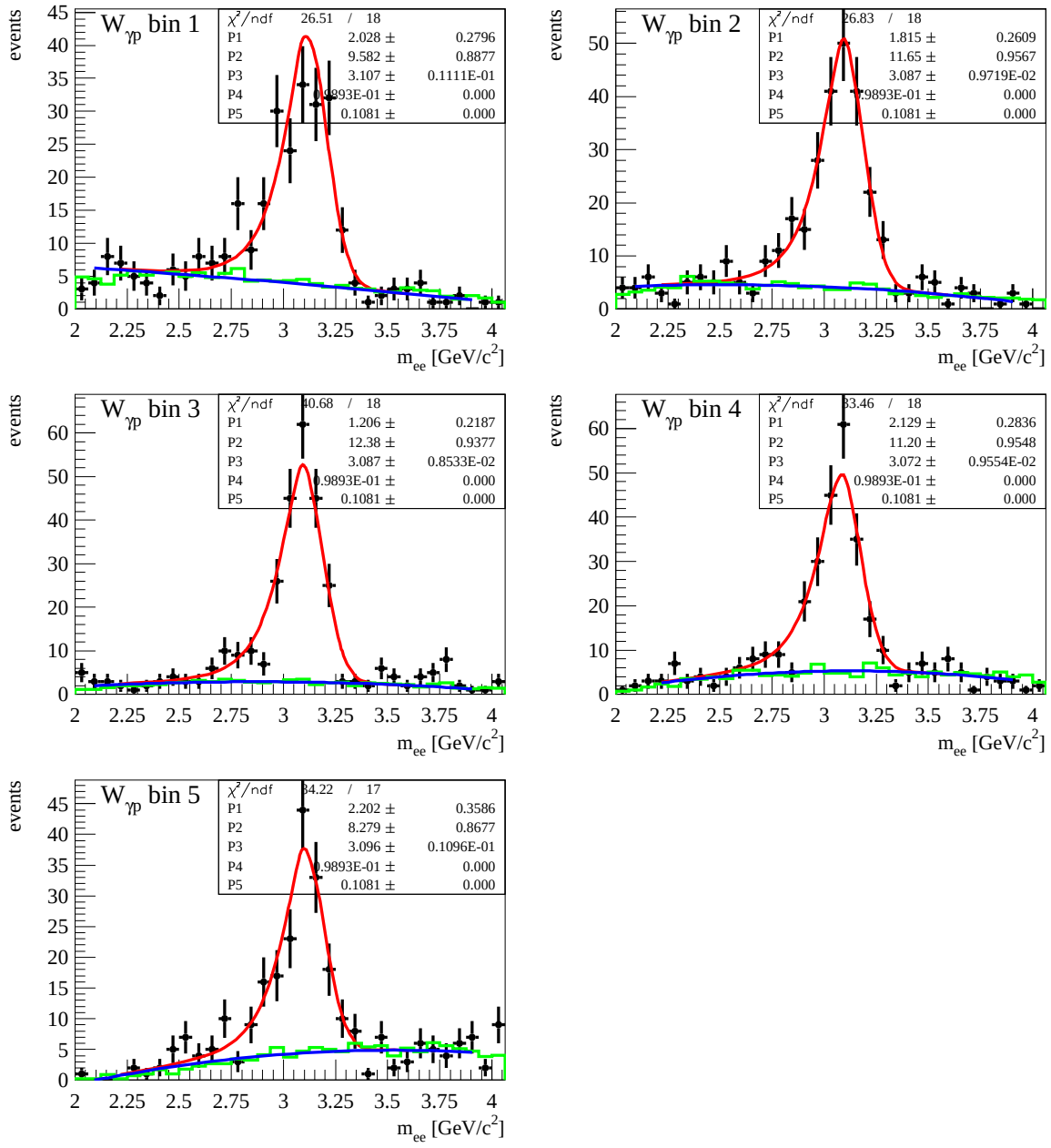

Figure A.2: The signal extraction fits for the fwd.-tagged track-cluster sample are shown in bins of $W_{\gamma p}$.

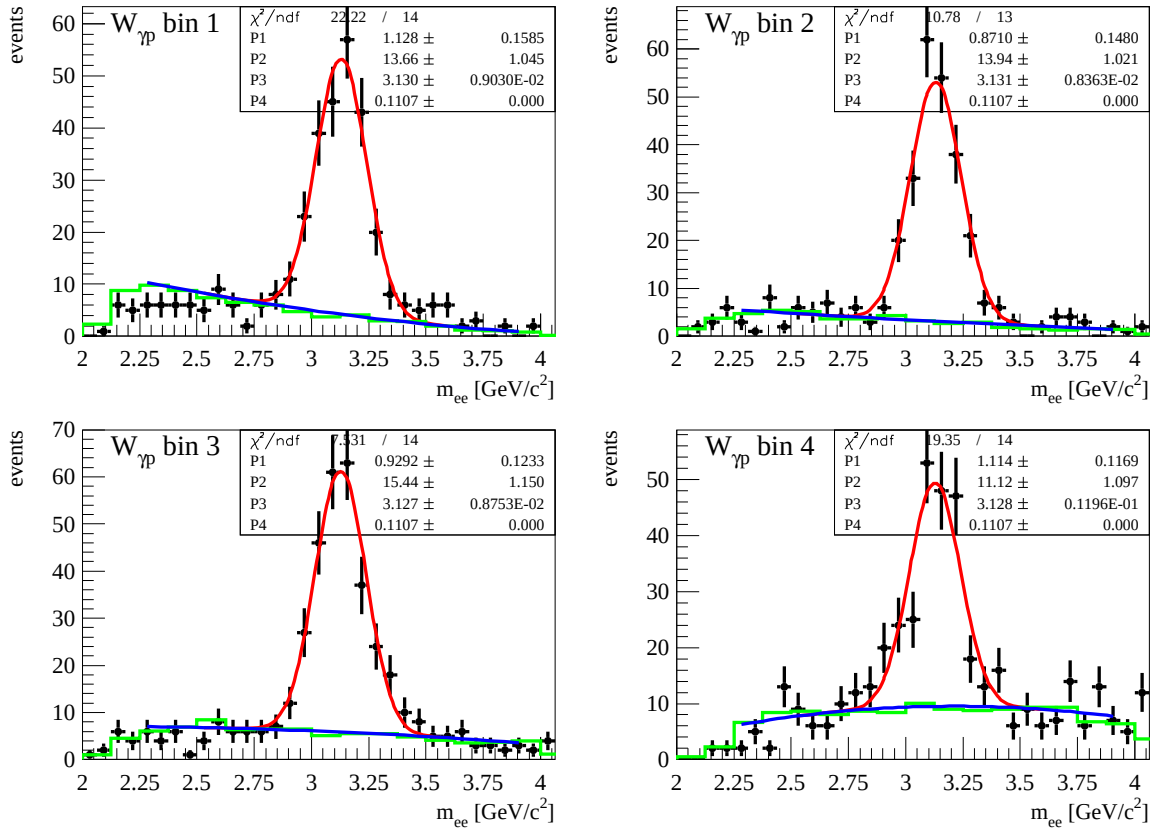

Figure A.3: The signal extraction fits for the fwd.-untagged cluster-cluster sample are shown in bins of $W_{\gamma p}$.

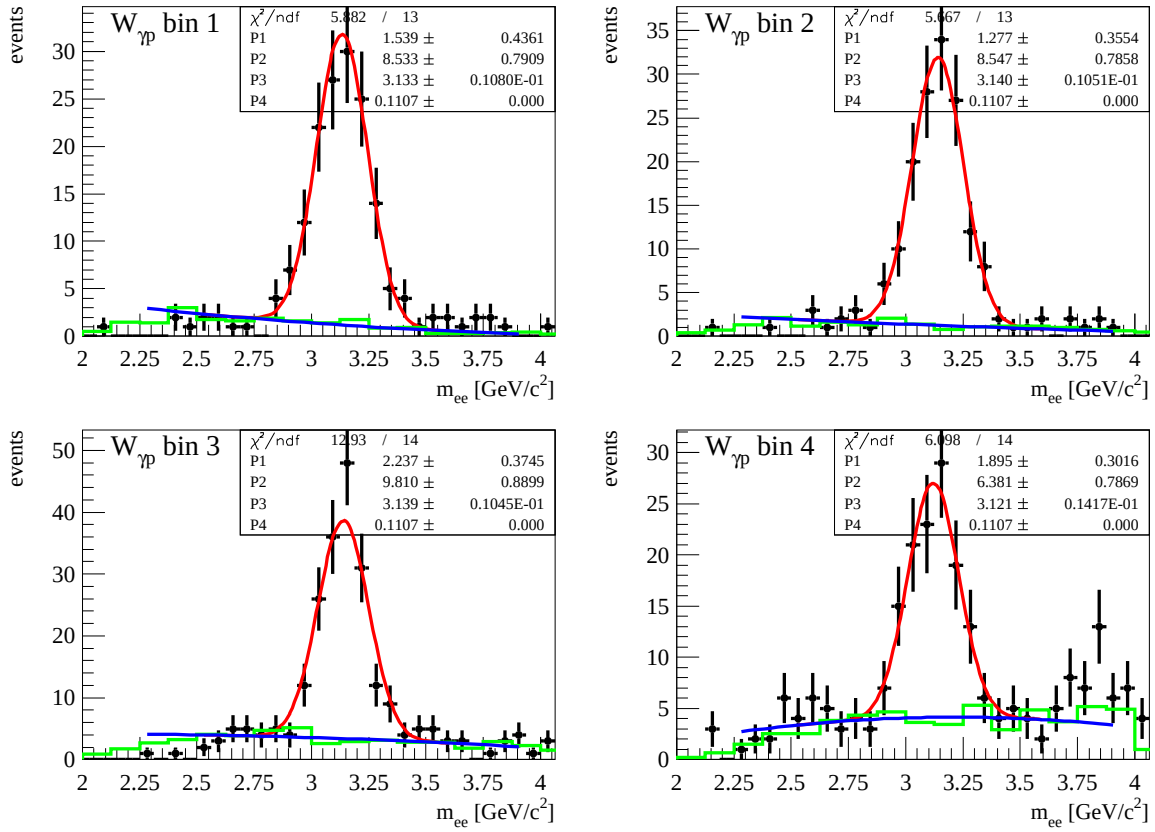

Figure A.4: The signal extraction fits for the fwd.-tagged cluster-cluster sample are shown in bins of $W_{\gamma p}$.

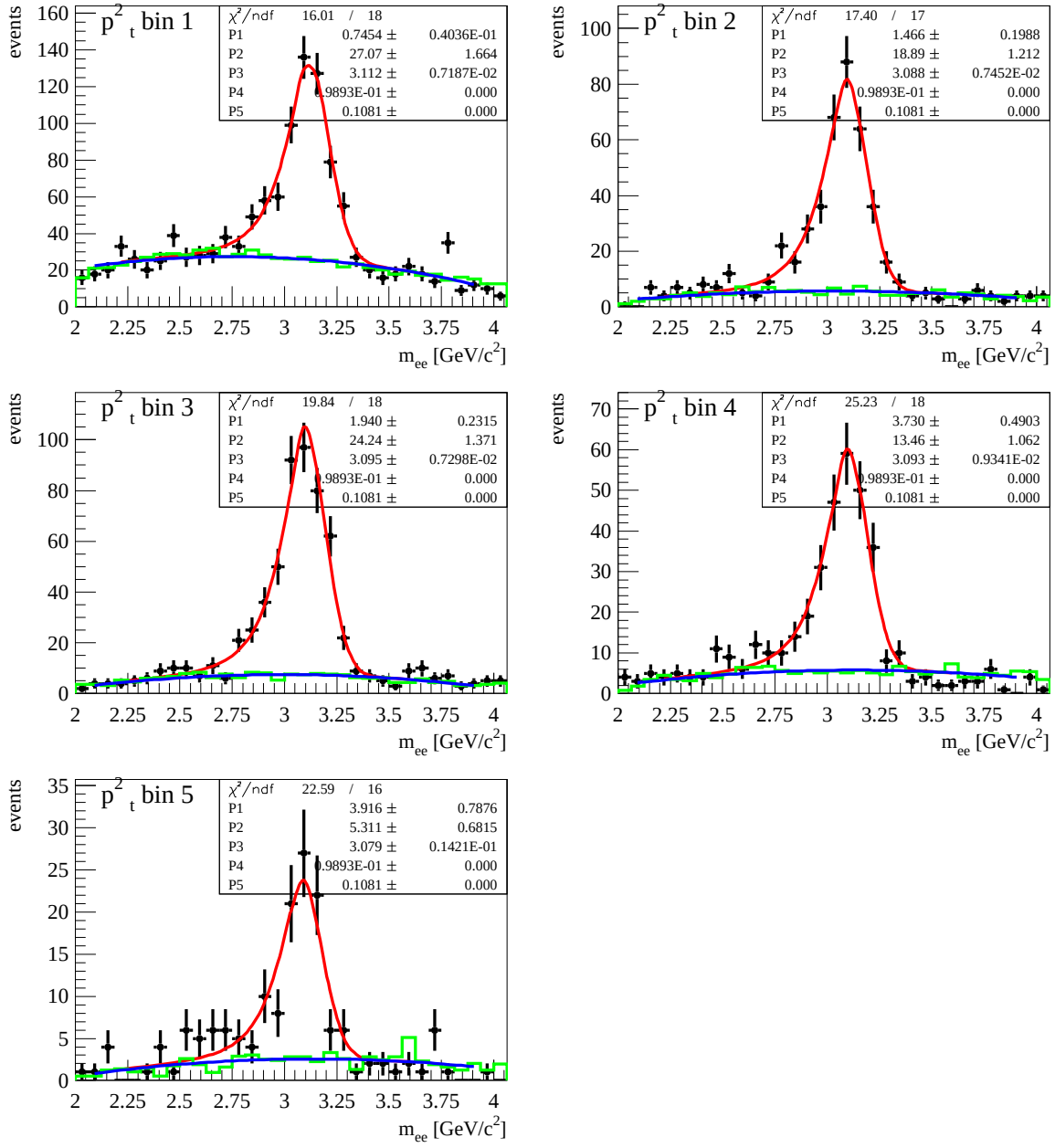

Figure A.5: The signal extraction fits for the fwd.-untagged track-cluster sample are shown in bins of p_t^2.

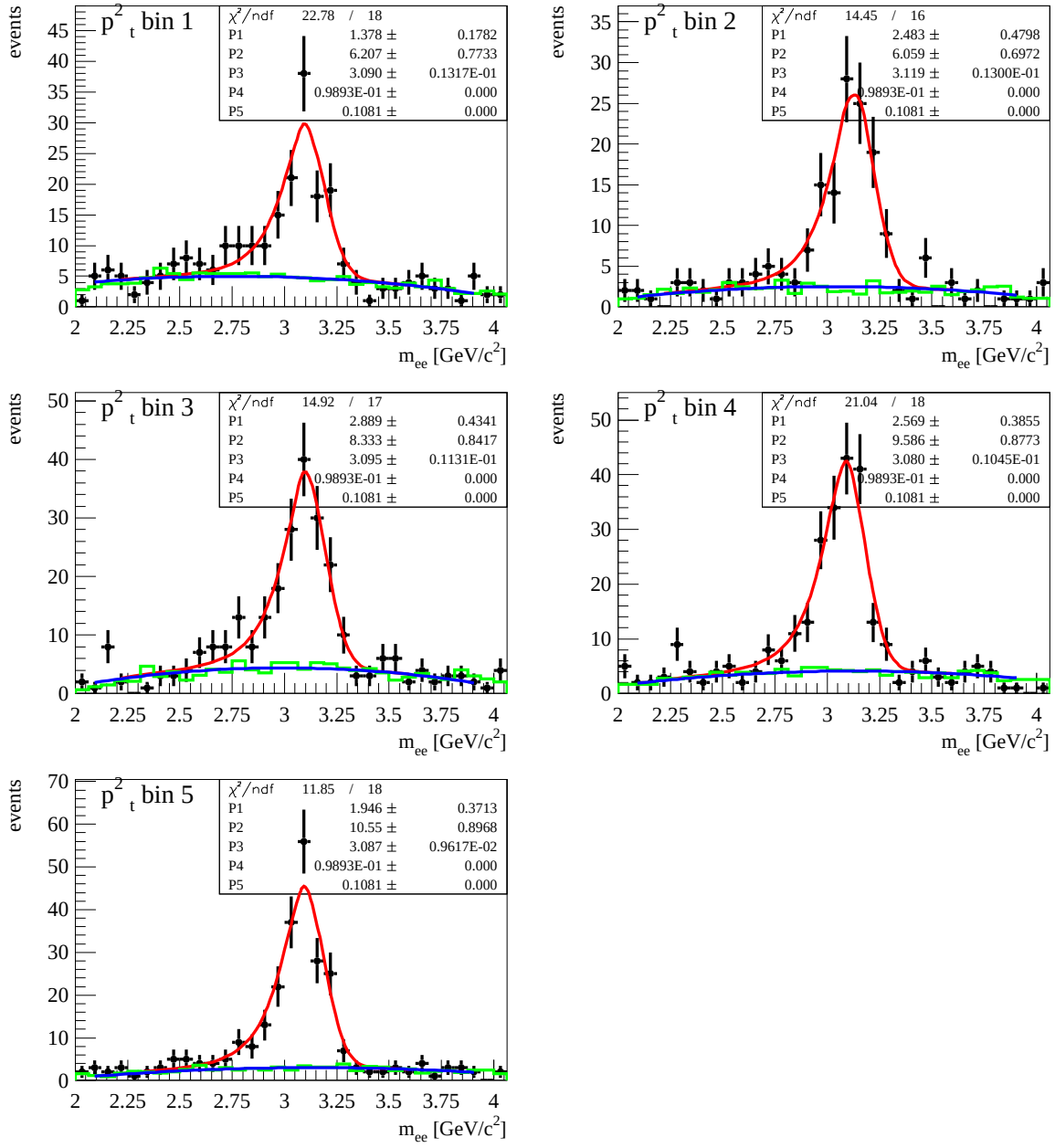

Figure A.6: The signal extraction fits for the fwd.-tagged track-cluster sample are shown in bins of p_t^2.

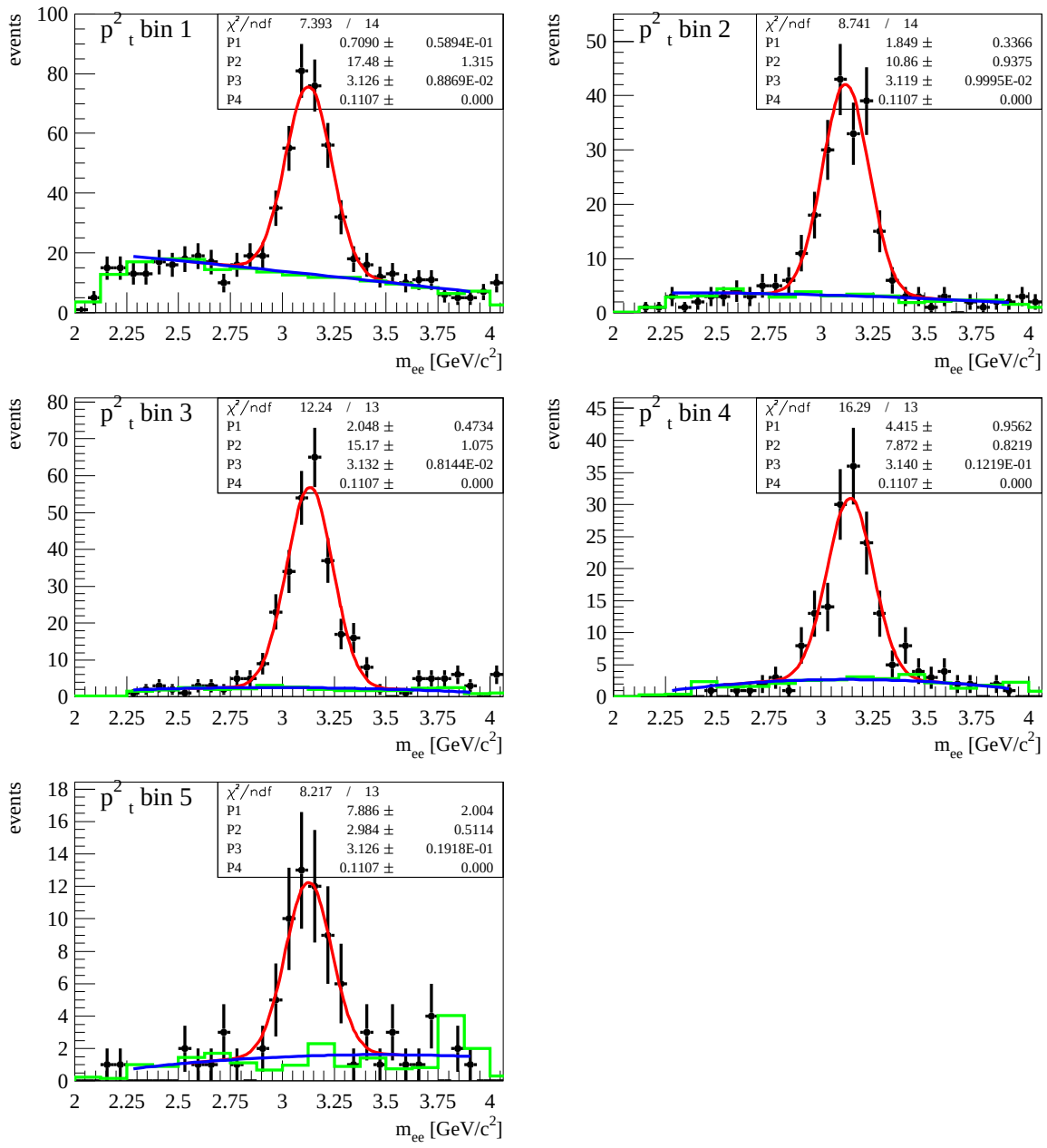

Figure A.7: The signal extraction fits for the fwd.-untagged cluster-cluster sample are shown in bins of p_t^2.

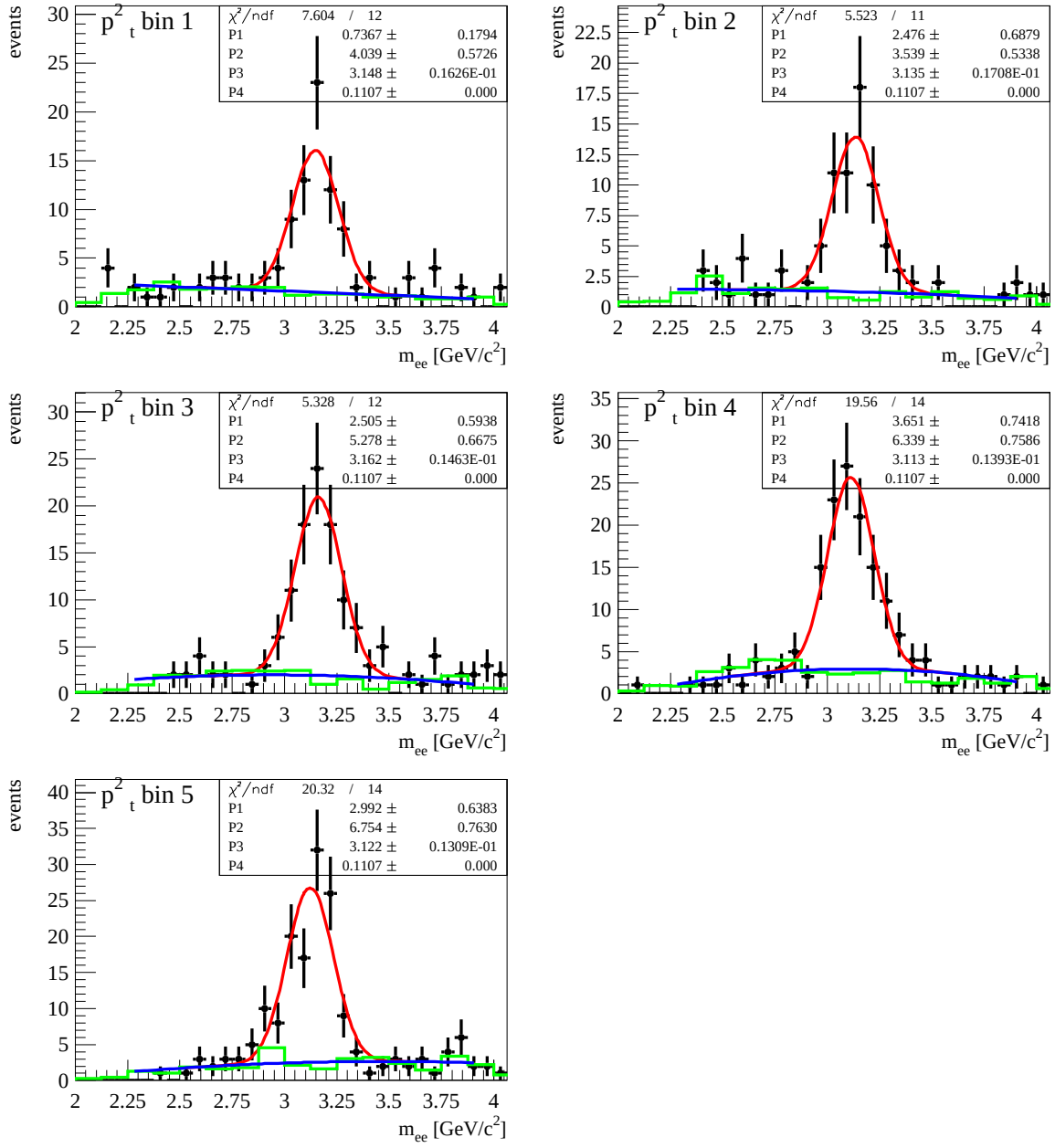

Figure A.8: The signal extraction fits for the fwd.-tagged cluster-cluster sample are shown in bins of p_t^2.

Bibliography

[1] Francis Halzen and Alan D. Martin. QUARKS AND LEPTONS: An Indroductory Course in Modern Particle Physics. John Wiley & sons, 1984.

[2] P. Schmüser. The Electron Proton Colliding Beam Facility HERA. *Nucl. Instrum. Meth.*, **A235**, pages 201–208, 1984.

[3] Deutsches Elektronen-Synchrotron, http://www.desy.de.

[4] D.A. Andrews, R. Golub, and G. Newton. Some estimates of the proton charge radius from measurements of the Lamb-shift interval in hydrogen. *J. Phys. G: Nucl. Phys.*, **3**, pages L91–L92, May 1977.

[5] A. Donnachie and P.V. Landshoff. Total cross sections. *Phys. Lett.*, **B 296**, pages 227–232, 1992.

[6] S.J. Brodsky et al. Diffractive Leptoproduction of Vector Mesons in QCD. *Phys. Rev*, **D 50**, page 3134, 1994.

[7] M.G. Ryskin. Diffractive J/ψ Electroproduction IN LLA QCD. *Z. Phys.*, **C 57**, page 89, 1993.

[8] M.G. Ryskin, R.G. Roberts, A.D. Martin, and E.M. Levin. Diffractive J/ψ photoproduction as a probe of the gluon density. *Z. Phys.*, **C 76**, page 231, 1997.

[9] L. Frankfurt, W. Koepf, and M. Strikman. Hard diffractive electroproduction of vector mesons in QCD. *Phys. Rev.*, **D 54**, pages 3194–3214, 1996.

[10] L. Frankfurt, W. Koepf, and M. Strikman. Diffractive heavy quarkonium photoproduction and electroproduction in QCD. *Phys. Rev.*, **D 57**, page 512, 1998. hep-ph/9702216.

[11] H1 Collaboration, S. Aid et al. Elastic photoproduction of ρ^0 mesons at HERA. *Nucl. Phys.*, **B 463**, pages 3–32, 1996. hep-eq/9601004.

[12] ZEUS Collaboration, M. Derrick et al. Measurement of elastic omega photoproduction at HERA. *Z. Phys.*, **C 73**, page 73, 1996. hep-ex/9608010.

[13] H1 Collaboration, S. Aid et al. Elastic and inelastic photoproduction of J/ψ mesons at HERA. *Nucl. Phys.*, **B 472**, pages 3–31, 1996. hep-ex/9603005.

[14] C. Adloff et al. Elastic Photoproduction of J/ψ and Υ Mesons at HERA. *Phys. Lett.*, **B 483**, pages 23–35, 2000. hep-ex/0003020.

[15] H1 Collaboration, S. Aid et al. Elastic electroproduction of ρ^0 and J/ψ mesons at large Q^2 at HERA. *Nucl. Phys.*, **B 468**, pages 3–36, 1996. hep-ex/9602007.

[16] H1 Collaboration, C. Adloff et al. Proton dissociative ρ and elastic ϕ electroproduction at HERA. *Z. Phys.*, **C 75**, page 607, 1997. hep-eq/9705014.

[17] H1 Collaboration, I. Ahmed et al. A Measurement of the Proton Structure Function $F_2(x, Q^2)$. *Nucl. Phys.*, **B 439**, pages 471–502, 1995.

[18] ZEUS Collaboration, M. Derrick et al. Measurement of the Proton Structure Function F_2 from the 1993 HERA Data. *Z. Phys.*, **C 65**, page 379, 1995.

[19] A. Donnachie and P.V. Landshoff. Small x: two pomerons! *Phys. Lett.*, **B 437**, pages 408–416, 1998. hep-ph/9806344.

[20] Particle Data Group. Review of Particle Physics. *Eur. Phys. J.*, **C 3**, pages 1–794, 1998.

[21] T.H. Bauer, R.D. Spital, D.R. Yennie, and F.M. Pipkin. The Hadronic Properties of the Proton in High-Energy Interactions. *Rev. Mod. Phys.*, **50**, page 261, 1978.

[22] J.J. Sakurai. Vector-meson Dominance and High-Energy Electron-Proton inelastic Scattering. *Phys. Rev. Lett.*, **22**, pages 981–984, 1969.

[23] H1 Collaboration, S. Aid et al. Measurement of the total photon-proton cross section and its decomposition at 200 GeV centre-of-mass energy. *Z. Phys.*, **C 69**, pages 27–38, 1995.

[24] C.W. von Weizsäcker. Ausstrahlung bei Stößen sehr schneller Elektronen. *Z. Phys.*, **88**, page 612, 1934.

[25] E.J. Williams. Nature of high energy particles of penetrating radiation and status of ionisation and radiation formulae. *Phys. Rev.*, **45**, page 729, 1934.

[26] V.M. Budnev et al. Equivalent Photon Approximation. *Phys. Rept.*, **C 15**, page 181, 1975.

[27] J.R. Smith. Polarization decomposition of fluxes and kinematics in ep reactions. H1–Note H1-04/93-282, DESY, 1993.

[28] J.R. Smith and B.D. Burow. Photon fluxes with particle beam mass effects and polarizations. H1–Note H1-01/94-338, DESY, 1994.

[29] S. Frixione, M.L. Mangano, P. Nason, and G. Ridolfi. Improving the Weizsäcker-Williams approximation in electron-proton collisions. *Phys. Lett.*, **B 319**, pages 339–345, 1993.

[30] C. Kiesling. Pomeron and Odderon at HERA. Talk presented on LOW X 2003, Navplion, Greece, June 2-5 2003.

[31] P. D. B. Collins. An Introduction to Regge Theory & High Energy Physics. Cambridge University Press, Cambridge, 1977.

[32] T. Regge. Bound States, Shadow States and Mandelstam Representation. *Nuovo Cimento*, **18**, page 947, 1960.

[33] G.F. Chew and S.C. Frautschi. Principle of Equivalence for all Strongly Interacting Particles within S-Matrix Framework. *Phys. Rev. Lett.*, **7**, page 394, 1961.

[34] S. Udluft. Protondissoziative Photoproduktion von ϕ-Mesonen am H1-Experiment bei HERA. Dissertation, Ludwig-Maximilians-Univerität München, 2000.

[35] A. Donnachie and P.V. Landshoff. Charm production at HERA. *Phys. Lett.*, **B 470**, pages 243–246, 1999.

[36] A. Donnachie and P.V. Landshoff. New data and the hard pomeron. *Phys. Lett.*, **B 518**, pages 63–71, 2001.

[37] A. Donnachie and P.V. Landshoff. Fit Function derived from the Two Pomeron Model. Private communication, 2003.

[38] L. Frankfurt, W. Koepf, and M. Strikman. Diffractive heavy quarkonium photoproduction and electroproduction in QCD. *Phys. Rev.*, **D 57**, pages 512–526, 1998.

[39] K. Goulianos. Diffractive Interactions of Hadrons at High-Energies. *Phys. Rept.*, **101**, page 169, 1983.

[40] T. Teubner. Theory of Elastic Vector Meson Production. In G. Grindhammer, B. A. Kniehl, and G. Kramer, *New Trends In Hera Physics 1999*, pages 349–360. Springer Verlag, 2000.

[41] C. Kiesling. Heavy Quarkonium Production at HERA. In G. Grindhammer, B. A. Kniehl, and G. Kramer, *New Trends In Hera Physics 1999*, pages 303–324. Springer Verlag, 2000.

[42] H1 Collaboration, I. Abt et al. The H1 detector at HERA. *Nucl. Instrum. Meth.*, **A386**, pages 310–347, 1997.

[43] H1 Collaboration, I. Abt et al. The tracking calorimeter and muon detectors of the H1 experiment at HERA. *Nucl. Instrum. Meth.*, **A386**, pages 348–396, 1997.

[44] D. Pitzl et al. The H1 silicon vertex detector. *Nucl. Instrum. Meth.*, **A 454**, pages 334–349, 2000.

[45] B. List. The H1 central silicon tracker. *Nucl. Instrum. Meth.*, **A501**, pages 49–53, 2001.

[46] H1 Collaboration, H. Behrend et al. Technical Proposal to build Silicon Tracking Detectors for H1. PRC 92/01 H1-06/92-226, DESY Hamburg, IfH Zeuthen, PSI Villigen, ETH Univ. Zürich, 1992.

[47] BST Homepage. http://www.ifh.de/H1-BST.

[48] T. Naumann. BST II ϕ-strip detectors. Private communication.

[49] V. V. Arkadov. Measurement of Deep-Inelastic ep Scattering Cross Section using the Backward Silicon Tracker at the H1 Detector at HERA. Dissertation, Humboldt-Universität Berlin, 2000.

[50] J. Katzy. Messung der Strukturfunktion F_2 bei kleinen Bjorken-x und kleinen Impulsüberträgen am H1-Experiment bei HERA. Dissertation, Universiät Heidelberg, Inaugural-dissertation, June 1997.

[51] H1 Calorimeter Group, B. Andrieu et al. The H1 Liquid Argon Calorimeter System. *Nucl. Instrum. Meth.*, **A 336**, pages 460–498, 1993.

[52] H1 Calorimeter Group, B. Andrieu et al. Beam tests and calibration of the H1 liquid argon calorimeter with electrons. *Nucl. Instrum. Meth.*, **A350**, pages 57–72, 1994.

[53] H1 Calorimeter Group, B. Andrieu et al. Results from Pion Calibration Runs for the H1 Liquid Argon Calorimeter and Comparisons with Simulations. *Nucl. Instrum. Meth.*, **A336**, pages 499–509, 1993.

[54] H1 SPACAL Group, R.-D. Appuhn et al. The H1 Lead/Scintillating-Fibre Calorimeter. Technical Report DESY-96-171, DESY, August 1996.

[55] H1 SPACAL Group. The LED based Calibration System of the H1 Lead/Scintillating-Fibre Calorimeter. Technical report.

[56] H1 SPACAL Group, T. Nicholls et al. Performance of an Electromagnetic Lead/Scintillating Fiber Calorimeter for the H1 Detector. *Nucl. Instrum. Meth.*, **A 374**, pages 149–156, 1996.

[57] H1 SPACAL Group, R.-D. Appuhn et al. Hadronic response and e/pi separation with the H1 lead/fibre calorimeter. *Nucl. Instrum. Meth.*, **A382**, pages 395–412, 1996.

[58] I. Kenyon et al. The H1 Forward Muon Spectrometer. *Nucl. Instr. and Meth.*, **A 340**, pages 304–308, 1994.

[59] K. L. Hewitt. The Detection and Triggering of Forward Muons using the H1 Detector. Diploma Thesis, Univerity of Birmingham, 1996.

[60] K. L. Hewitt. Elastic J/ψ Photoproduction and the Detection and Triggering of Muons at Low $W_{\gamma p}$ using the H1 Detector. Dissertation, Univerity of Birmingham, March 1998.

[61] H1 Collaboration, T. Ahmed et al. First measurement of the deep inelastic structure of proton diffraction. *Phys. Lett.*, **B 348**, pages 681–696, 1995.

[62] B. List. Diffractive J/ψ-Produktion in Elektron-Proton-Stößen am Speicherring HERA. Diploma Thesis, Berlin, 1993.

[63] I. Herynek and J. Hladký. VLQ-TOF system. H1 Note H1-05/99-572, Institute of Physics of the Academy of Sciences of the Czech Republic, Prague, May 1999.

[64] H1 Collaboration. Luminosity Measurement in the H1 Experiment at HERA. In *Proceedings of the XXVIII International Conference on High Energy Physics, Warsaw*, pages 17–26, 1996.

[65] B. Reisert. Elektron-Proton-Streuung bei hohen Impulsüberträgen am H1-Experiment bei HERA. Dissertation, Ludwig-Maximilians-Universität München, 2001. MPI-PhE/2000-26.

[66] J. Dichtl. Neuronale Trigger für Heavy-Quarkonium-Produktion bei HERA. Diploma Thesis, Ludwig-Maximilians-Universität München, 1999.

[67] V. Boudry et al. The Inclusive Electron Trigger for the SPACAL: Design and CERN-test Results. H1 Note H1-03/95-430, DESY, 1995.

[68] J. Möck. Untersuchung diffraktiver J/ψ-Ereignisse im H1-Experiment bei HERA und Entwicklung neuronaler Triggeralgorithmen. Dissertation, Fakultät für Physik der Technischen Universität München, München, September 1997.

[69] L1 subtrigger changes. http://www-h1.desy.de/icgi-trigger/trigchange.cgi.

[70] Raúl Rojas. Theorie der neuronalen Netze; eine systematische Einführung. Springer, Berlin, Heidelberg, New York, London, Paris, Tokyo, Hong Kong, Barcelona, Budapest, 1993.

[71] Prof. Dr. Berndt Müller and Dr. Joachim Reinhardt. Neural Networks — An Introduction. Springer-Verlag, 1990.

[72] D. E. Rummelhart, G. E. Hinton, and R. J. Williams. Learning Representations by Back-propagating Errors. *Nature*, **323**, page 533, 1986.

[73] L. Janauschek. Untersuchungen zur Untergrundreduktion mit einem neuronalen Trigger beim H1-Experiment bei HERA. Diploma Thesis, Ludwig-Maximilians-Universität, München, 1998.

[74] J.K. Köhne et al. Realization of a second level neural network trigger for the H1 experiment at HERA. *Nucl. Instrum. Meth.*, **A 389**, pages 128–133, 1997.

[75] Inc. Adaptive Solutions. CNAPS Release Notes 2.0. Technical report, 1993. Beaverton Or.

[76] A. Gruber. Untersuchung von $D^{*\pm}$-Ereignissen am H1-Experiment unter Berücksichtigung des Level-2-Triggers. Dissertation, Ludwig-Maximilians-Universität München, 1997.

[77] Interactive cgi-based Web-Interface for the Monitoring of the Level 2 Neural Network Trigger, http://www-l2nn.desy.de.

[78] B. List and A. Mastroberardino. DiffVm: A Monte Carlo generator for diffractive processes in ep scattering. Technical report, DESY, 1999. DESY-PROC-1999-02.

[79] B. List. Diffraktive $J\psi$-Produktion in Elektron-Proton-Stößen am Speicherring HERA. Diploma Thesis, Technische Universität Berlin, 1993.

[80] T. Sjöstrand. High-energy-physics event generation with PYTHIA 5.7 and JETSET 7.4. *Comp. Phys. Comm.*, **82**, pages 74–89, 1994.

[81] W. Bethe and W. Heitler. On the stopping of fast particles and on the creation of positive electrons. *Proceedings of the Royal Society*, **A 146**, pages 83–112, 1934.

[82] S. P. Baranov, O. Duenger, H. Shooshtari, and J. A. M Vermaseren. LPAIR: A Generator for Lepton Pair Production. In W. Buchmüller and G. Ingelmann, *Proceedings of the Workshop: Physics at HERA*, volume 3, pages 1478–1482. DESY, October 1991.

[83] D. Hoffmann and L. Favart. Lepton Pair Monte Carlo Generators for HERA Physics. In T. Doyle, G. Grindhammer, G. Ingelman, and H. Jung, *Proceedings of the Workshop: Monte Carlo Generators for HERA Physics 1998/99*, pages 576–595. DESY, 1999.

[84] D. Schmidt. Diffraktive Photoproduktion von Charmonium im H1-Detektor bei HERA. Dissertation, Univerität Hamburg, 2001.

[85] T. Carli, A. Courau, S. Kermiche, and P. Kessler. In *Proceedings of the Workshop: Physics at HERA*, volume 3, page 1468, Hamburg, 1992. DESY.

[86] S. Kermiche. Etude du QED Compton a HERA: Luminosite et Calibration du Detecteur H1. Dissertation, University of Paris-Sud, LAL Orsay, 1994.

[87] V. Lendermann. Measurement of the QED Compton Scattering Cross Section with the H1 Detector at HERA. Dissertation, University of Dortmund, 2001.

[88] M. Kasprzak. Dissertation, Warsaw, DESY-F35D-96-16, 1996.

[89] T. Sjöstrand. PYTHIA 5.6 and JETSET 7.3: Physics and manual. CERN-TH-6488-92.

[90] R. Brun et al. GEANT3 User's Guide, 1987. CERN-DD/EE-84-1.

[91] R. Brun, R. Hagelberg, M. Hansroul, and J. C. Lassalle. Geant: Simulation Program for Particle Physics Experiments. User Guide and Reference Manual. CERN-DD-78-2-REV.

[92] J. Meyer. Guide for the H1 simulation program H1SIM. Internal Software–Note 03-11/89, DESY, 1989.

[93] H1REC9 - The H1 Reconstruction Program. http://www-h1.desy.de/icas/imanuals/h1rec/h1rec9/h1rec.html.

[94] T. Naumann. Number of BST-II planes hit by a track. Private communication.

[95] P. Kostka. BST readout problems. Private communication.

[96] T. Naumann. BST coherent losses. Private communication.

[97] A. Blondel and F. Jacquet. In U. Amaldi, *Proceedings of the Study of an ep Facility for Europe*, page 391. DESY 79/48, 1979.

[98] V. Lendermann. Calibration of SpaCal at low energies. Private communication.

[99] P. Fleischmann. Elastic J/ψ production at HERA. Dissertation, Universität Hamburg, 2004.

[100] Dr. B. Struck (Company). STR722 VME-TAXI — VME Crate Interconnect. Technical report.

[101] J. Olsson and F. Sefkow. HV bit information. Minutes of the Data Quality Meetings 05.03.1996 and 26.03.1996, 05.03.1996 and 26.03.1996.

[102] Lee West. How to use the Heavy Flavour Working Group Track, Muon and Electron Selection Code. https://www-h1.desy.de/h1/iww/iwork/ihq/sw-doc/track_doc30000.ps.gz, December 1997.

[103] S. Schmidt. Cut against inefficient SpaCal trigger cells. Private communication, April 2004.

[104] B. Naroska. p_t^2-cut and the proton elastic and proton dissociative J/ψ photoproduction cross section. Private communication, March 2004.

[105] Arnd Meyer. Charmonium Production in Deep Inelastic Scattering at HERA. Dissertation, Universität Hamburg, 1998.

[106] M. Dirkmann. Untersuchung an einem Spaghetti-Kalorimeter unter besonderer Berücksichtigung des inneren Randbereiches und des Nachweises von Pi-Mesonen. Diploma Thesis, Universität Dortmund, 1995.

[107] Andreas Meyer. Discussion about hadronic SpaCal. Private communication, March 2004.

[108] H1 'Inclusive' Physics Working Group. SpaCal Noise. http://www-h1.desy.de/ispacal/escale.html, 2003.

[109] R. Sütterlin. Untersuchung der Compton-Streuung bei der Elektron-Proton Reaktionen bei HERA. Diploma Thesis, Ludwig-Maximilians-Universität München, 1998.

[110] K. Hagiware et al. Particle Data Group. Review of Particle Properties. *Phys. Rev.*, **D 66**, page 010001, 2002. http://pdg.lbl.gov.

[111] P. Fleischmann. Contamination of the J/ψ sample by ψ(2S) decays. Private communication.

[112] S. Levonian and A. Panitch. Treatment of the Proton Satellite Bunches in 1994 Data. H1 Note H1-09/95-454, 1995.

[113] S. Levonian. Luminosity Summary Tables. http://www-h1.desy.de/h1det/lumi/summary_tables/.

[114] G. D. Lafferty and T. R. Wyatt. Where to stick your data points: The treatment of measurements within wide bins. *Nucl. Instrum. Meth.*, **A 355**, pages 541–547, 1995.

[115] G. D'Agostini. A multidimensional unfolding method based on Bayes' therorem. *Nucl. Instrum. Meth.*, **A 362**, pages 487–498, 1995.

[116] G. D'Agostini. Probability and Measurement Uncertainty in Physics - a Bayesian Primer. 1995. DESY-95-242, hep-ph/9512295.

[117] H1 Collaboration, C. Adloff et al. Deep-Inelastic Inclusive ep Scattering at Low x and a Determination of α_s. *Eur. Phys. J.*, **C21**, page 33, 2001. hep-ex/0012053.

[118] H1 Collaboration, C. Adloff et al. Measurement and QCD analysis of neutral and charged current cross sections at HERA. *Eur. Phys. J.*, **C30**, pages 1–32, 2003. hep-ex/0304003.

[119] ZEUS Collaboration, S. Chekanov et al. Exclusive photoproduction of J/ψ mesons at HERA. *Eur. Phys. J.*, **C 24**, page 345, 2002. hep-ep/0201043.

[120] E516 Collaboration, B. H. Denby et al. Inelastic and Elastic Photoproduction of J/ψ (3097). *Phys. Rev. Lett.*, **52**, page 795, 1984.

[121] E401 Collaboration, M. Binkley et al. J/ψ Photoproduction from 60-GeV/c to 300-GeV/c. *Phys. Rev. Lett.*, **48**, page 73, 1982.

[122] A.D. Martin, M.G. Ryskin, and T. Teubner. Q^2 dependence of diffractive vector meson electroproduction. *Phys. Rev.*, **D 62**, page 014022, 2000. hep-ph/9912551.

[123] H. L. Lai et al. Improved Parton Distributions From Global Analysis of Recent Deep Inelastic Scattering and Inclusive Jet Data. *Phys. Rev.*, **D 55**, page 1280, 1997. hep-ph/9606399.

[124] CTEQ, H. L. Lai et al. Global QCD analysis of parton structure of the nucleon: CTEQ5 parton distributions. *Eur. Phys. J.*, **C 12**, page 375, 2000. hep-ph/9903282.

[125] J. Pumplin, D.R. Stump, J. Huston, H.L. Lai, P. Nadolsky, and W.K. Tung. New generation of parton distributions with uncertainties from global QCD analysis. *JHEP*, **07**, page 012, 2002. hep-ph/0201195.

[126] A. D. Martin, R. G. Roberts, W. James Stirling, and R. S. Thorne. Parton distributions and the LHC: W and Z production. *Eur. Phys. J.*, **C14**, pages 133–145, 2000. hep-ph/9907231.

[127] A. D. Martin, R. G. Roberts, W. J. Stirling, and R. S. Thorne. Uncertainties of predictions from parton distributions. I: Experimental errors. ((T)). *Eur. Phys. J.*, **C28**, pages 455–473, 2003. hep-ph/0211080.

[128] ZEUS Collaboration, S. Chekanov et al. A ZEUS next-to-leading-order QCD analysis of data on deep inelastic scattering. *Phys. Rev.*, **D67**, page 012007, 2003. hep-ex/0208023.

[129] H1 Collaboraton. Diffractive Elastic J/ψ Production at HERA in Photoproduction and Deep Inelastic Scattering. in preparation.

Danksagung

Zu allererst möchte ich mich bei meinen Eltern und meiner Schwester Barbara für ihre ungebrochene Motivation und Unterstützung aller Art bedanken.

Meinem Doktorvater Herrn Prof. Dr. Chr. Kiesling gilt mein Dank für die Ermöglichung dieser Arbeit und die Unterstützung und Betreuung wäherend der Durchführung. Insbesondere möchte ich ihm danken, für die tiefen Einblicke in die Hardware und den Betrieb des Neuronalen Netzwerktriggers. Damit wurde mir ermöglicht, den gesamten Weg der Datennahme nachzuvollziehen und die Bedeutung des Triggersystems für die Physikanalyse zu erkennen. Für seinen uneingeschränkten Optimismus, seine unzählbaren Ideen und die klaren Physikdiskussionen möchte ich mich herzlich bedanken.

Herrn Prof. Dr. M. Faessler danke ich für die Übernahme des Zweitguachtens.

Den Herrn Direktoren Prof. Dr. G. Buschhorn und Prof. Dr. A. Caldwell des Max-Planck-Instituts für Physik München spreche ich meinen Dank aus für die uneingeschränkte Nutzung der Infrastruktur des Instituts.

Für das große Interesse am Fortgang meiner Analyse bedanke ich mich bei den Hamburger Kollegen der Heavy Flavour Working Group des H1-Experimentes insbesonders bei Herrn Dr. Andreas Meyer, Herrn Dr. Ph. Fleischmann. Ganz speziell bedanke ich mich bei Frau Prof. Dr. B. Naroska, für ihre immer konstruktiv-kritische Art und ihren aufbauenden Zuspruch in der Endphase. Den H1-Physikkoordinatoren Herrn Dr. P. Newman und Herrn Dr. V. Chekelian danke ich für ihr Interesse und bei Dr. Th. Naumann für die zahlreichen Diskussionen über BST.

Alle ehemaligen und aktuellen Mitglieder der H1-Gruppe am MPI München ermöglichten ein angenehmes Arbeitsklima und gute Diskussionen über *life, the universe and everything.* Kurzweilig waren die Gespräche mit Herrn J. Zimmermann über alle Arten von progressieven Programmiertechniken. Mein spezieller Dank gilt Frau Dr. A. Dubak für Motivation und für Diskussionen über technische Herausforderungen bei der Fertigstellung der Analyse.

Der ehemaligen HERA-III Arbeitsgruppe des MPI München danke ich für ihr großes Interesse an meiner Physikanalyse und anregenden Fragen aus der Sicht von Außenstehenden. Mein Dank gilt dabei Herrn Dr. R. Galea, Herrn Dr. X. Liu und insbesondere speziell Frau Dr. Iris Abt.

Die Mitarbeiten des MPI München Frau Marlene Schaber, Herrn Joseph (Sepp) Huber, Herrn Uwe Leuphold, Dr. Denis Salihagicic und Herrn Michael Vidal haben mich bei der Erstellung dieser Arbeit in unterschiedlichster Weise unterstützt. Marlene hat in administrativen Dingen geholfen und immer ein aufbauendes Wort gefunden. Mit Sepp habe ich das Büro während meiner gesamten MPI-Zeit geteilt — es hätte niemand besseren geben können. Für ihren unverzüglichen und unermüdlichen Einsatz zum Behufe der schnellstmöglichen Lösung aller Probleme, die Rechner und Netzwerk betreffen, danke ich Uwe, Denis und Michael.